Modeling the hydrogen distribution accompanying electron injection in SiO_2 films in strong electric fields

G. V. Gadiyak

Institute of Computer Technologies, Siberian Section, Russian Academy of Sciences,
630090 Novosibirsk, Russia

(Submitted April 19, 1995; accepted for publication May 12, 1996)
Fiz. Tekh. Poluprovodn. **31**, 257–263 (March 1997)

A new theoretical model is proposed for describing the behavior of hydrogen when electrons are injected from contacts in thin-film SiO_2 in strong fields. Hot electrons dislodge hydrogen from dangling SiO_{-} and Si_{-} bonds, creating traps for electrons and holes. Computations have been carried out for hydrogen redistribution and charge accumulation in SiO_2. The experimental data of D.A. Buchanan *et al.* [J. Appl. Phys. **76**, 3595 (1994)] are used to determine the hydrogen-formation reaction cross section $\sigma_H \simeq 6\times10^{-20}$ cm^2 and the hydrogen-photogeneration frequency $\nu_{ph}=2\times10^{-6}$ sec^{-1}. An explanation is given for the accumulation of an anomalous positive charge in the SiO_2 film. © *1997 American Institute of Physics.* [S1063-7826(97)00103-8]

Hydrogen plays an important role in the growth of the thermal oxide SiO_2 as a passivating impurity in silicon metal–oxide–semiconductor (MOS) structures.[1,2] By saturating the dangling bonds of silicon or oxygen, hydrogen eliminates defect states in the bulk and at the Si/SiO_2 and SiO_2/Me interfaces. It is assumed that defect states play a key role in the degradation of devices based on silicon MOS structures, and the possibility of predicting the evolution of the hydrogen profile in the subgate insulator therefore has great significance. Buchanan *et al.*[3] suggested that electrons heated in SiO_2 can cause redistribution of the hydrogen as a result of its being dislodged from the bonds and migration to the boundary, so that it creates defects in the bulk and at the Si/SiO_2 boundary. They also experimentally studied the hydrogen distribution in a film for various values of the transmitted charge Q. The formation of defects accompanying the injection of hot carriers has been considered in Refs. 4–8, and the migration of hydrogen atoms was studied in Ref. 9. In this case, the main role was played by hole injection, which weakened the SiH bonds at the silicon surface and in the SiO_2 layer adjacent to it. In Ref. 10, as in Ref. 3, the hydrogen distribution in SiO_2 was experimentally studied, and two maxima of the hydrogen concentration were obtained—on the SiO_2 surface and at the Si/SiO_2 interface. The limiting hydrogen concentrations in SiO_2 films grown by various means have been determined. Unfortunately, there are no data in the literature on the theoretical study of the hydrogen redistribution in a $Si/SiO_2/Al$ structure, and no comparison has been made with the experimental data. We propose here a computational model that takes into account the hydrogen redistribution, reactions with hydrogen in the solid state, the creation of new trapping centers, the capture of carriers on them, recombination of free carriers with the carriers captured at the traps, and the effect of the electric field on electron heating.

PHYSICAL MODEL

We assume that there is an inhomogeneous hydrogen distribution in the SiO_2 film, with two maxima, in the Si/SiO_2 region and in the SiO_2/Al region.[3,10] The hydrogen saturates dangling bonds of the SiH or SiOH form, which can arise during the thermal oxidation of silicon or during its hydrogen processing. When free hydrogen migrates in a film, reactions of the form

$$\mathrm{SiH}+\mathrm{H}\xrightarrow{k_1}\mathrm{Si}_{-}+\mathrm{H}_2 \tag{1}$$

or

$$\mathrm{SiOH}+\mathrm{H}\xrightarrow{k_1}\mathrm{SiO}_{-}+\mathrm{H}_2$$

are possible, where Si_{-} or SiO_{-} are dangling bonds, which are neutral traps for carriers. The possibility of reactions of the form of Eq. (1) was verified by a quantum molecular dynamics calculation carried out by Yu. N. Morokov using the semiempirical MINDO method. When hydrogen approaches a SiH complex, a new H_2 bond appears. When this happens, the kinetic energy evolved is sufficient to break the SiH bond. The reaction constant of Eq. (1) can be estimated from

$$k_1(x,T)=4\pi D_H(T)r_H\cdot\xi_1(x), \tag{2}$$

where D_H is the diffusion coefficient of atomic hydrogen, r_H is the interaction radius of atomic hydrogen with SiH or SiOH complexes, ($\sim$1.0–2.0 Å), and $\xi(x)$ is a parameter that distinguishes the reactions in the bulk and on the surface. Free hydrogen atoms are generated by electrons injected into the SiO_2 or created by photogeneration and collected in an electric field with energy $\varepsilon \geqslant \varepsilon_{cr}=1.5$ eV, or by high-energy photons. Here ε_{cr} is the threshold energy needed to break a SiH or SiOH bond in reactions of the form

$$\mathrm{SiH}+e\underset{k_3}{\overset{k_2}{\rightleftarrows}}\mathrm{Si}+\mathrm{H}+e \tag{3}$$

or

$$\mathrm{SiOH}+e\underset{k_3}{\overset{k_2}{\rightleftarrows}}\mathrm{SiO}_{-}+\mathrm{H}+e$$

with reaction constants

$$k_3(T,x)=4\pi D_{\mathrm{H}}(T)r_{\mathrm{H}}\cdot\xi_3(x) \tag{4}$$

and

$$k_2(T,x)=\sigma_{\mathrm{H}}(\varepsilon,x)v_d^e, \tag{5}$$

where v_d^e is the electron-drift velocity, and $\sigma_{\mathrm{H}}(\varepsilon,x)$ is the decay reaction cross section of the SiH bond, which depends on the electron energy by the threshold relationship

$$\sigma_{\mathrm{H}}(\varepsilon,x)=\begin{cases}\sigma_{\mathrm{H}}^0 & \text{for } \varepsilon(x)\geqslant\varepsilon_{\mathrm{cr}}, \\ 0 & \text{for } \varepsilon(x)<\varepsilon_{\mathrm{cr}}.\end{cases} \tag{6}$$

Here we have taken into account the dependence of the mean electron energy on the distance x from the injection site according to a linear law

$$\varepsilon(x)\simeq a\cdot x$$

before the instant of reaching saturation $\varepsilon_{\mathrm{sat}}$ at a given electric field E. The saturation energy $\varepsilon_{\mathrm{sat}}$ also increases linearly with field E:

$$\varepsilon_{\mathrm{sat}}\simeq b\cdot E.$$

Both laws follow from the calculations of Refs. 11 and 12, and the approximation constants are adjusted to these calculated results. By the reverse reaction in Eq. (3) is understood the possibility that the dangling bonds become saturated with hydrogen atoms, where it is assumed that these reactions occur differently in the bulk and on the surface [parameter $\xi_3(x)$ has a different value for the reaction in the bulk and on the surface]. However, we should point out here that the binding energy of the SiH complex is about 1.5 eV, whereas it is much greater for the SiOH complex. Therefore, in what follows, we shall consider only SiH complexes and the processes in them.

The system of equations for the model described above has the form

$$\frac{\partial C_{\mathrm{H}}}{\partial t}=\frac{\partial}{\partial x}\left(D_{\mathrm{H}}\frac{\partial C_{\mathrm{H}}}{\partial x}\right)+\sigma_{\mathrm{H}}(\varepsilon,x)v_d^e nC_{\mathrm{SiH}}+\nu_{\mathrm{ph}}C_{\mathrm{SiH}} -k_1(x)C_{\mathrm{SiH}}C_{\mathrm{H}}-k_3(x)C_{\mathrm{H}}C_{\mathrm{Si\_}}, \tag{7}$$

$$\frac{\partial C_{\mathrm{SiH}}}{\partial t}=-\sigma_{\mathrm{H}}(\varepsilon,x)v_d^e nC_{\mathrm{SiH}}-\nu_{\mathrm{ph}}C_{\mathrm{SiH}}-k_1(x)C_{\mathrm{SiH}}C_{\mathrm{H}} +k_3(x)C_{\mathrm{H}}C_{\mathrm{Si\_}}, \tag{8}$$

$$\frac{\partial C_{\mathrm{H_2}}}{\partial t}=\frac{\partial}{\partial x}\left(D_{\mathrm{H_2}}\frac{\partial C_{\mathrm{H_2}}}{\partial x}\right)+k_1(x)C_{\mathrm{SiH}}C_{\mathrm{H}}, \tag{9}$$

$$\frac{\partial C_{\mathrm{Si\_}}}{\partial t}=\sigma(\varepsilon,x)v_d^e nC_{\mathrm{SiH}}+\nu_{\mathrm{ph}}C_{\mathrm{SiH}}+k_1(x)C_{\mathrm{SiH}}C_{\mathrm{H}} -k_3(x)C_{\mathrm{H}}C_{\mathrm{Si\_}}. \tag{10}$$

Hydrogen can also be generated by irradiating the sample with light, as was done, for example, in Ref. 3, where ν_{ph} is the frequency of generation of hydrogen atoms by light. The next problem to be solved is that of the charge-accumulation kinetics in $\mathrm{SiO_2}$. To solve this problem, information is needed on the nature of the electron- and hole-capture centers (trapping centers). Unfortunately, no generally accepted physical models for these centers yet exist.[1,2,13,14] As a rule, they are associated with lattice defects, which can be conventionally divided into those present in the starting material after synthesis and those that result from repeated treatment with a field or with other external perturbations.

We assume that the neutral dangling bonds that appear are traps for both electrons

$$\mathrm{Si}_-+e\xrightarrow{\sigma^n{}_{\mathrm{Si}}}\mathrm{Si}_-^-,$$

$$\mathrm{SiO}_-+e\xrightarrow{\sigma^n{}_{\mathrm{Si}}}\mathrm{SiO}_-^-, \tag{11}$$

and for holes,[14]

$$\mathrm{Si}_-+p\xrightarrow{\sigma^p{}_{\mathrm{Si}}}\mathrm{S}i_{/\text{-}}^+, \tag{12}$$

$$\mathrm{SiO}_-+p\xrightarrow{\sigma^p{}_{\mathrm{Si}}}\mathrm{SiO}_-^+.$$

Free carriers can recombine with carriers already captured at the traps:

$$\mathrm{Si}^++e\xrightarrow{\sigma^{rn}{}_{\mathrm{Si}}}\mathrm{Si}_-, \tag{13}$$

$$\mathrm{SiO}^++e\xrightarrow{\sigma^{rn}}\mathrm{SiO}_-$$

$$\mathrm{Si}^-+p\xrightarrow{\sigma^{rn}{}_{\mathrm{Si}}}\mathrm{Si}_-, \tag{14}$$

$$\mathrm{SiO}^-+p\xrightarrow{\sigma^{rn}{}_{\mathrm{Si}}}\mathrm{SiO}_-.$$

The charge-accumulation and current-relaxation equations are

$$j_n=j_{inj}^n+j_{\mathrm{ph}}^n, \tag{15}$$

$$j_p=g\cdot j_n+j_{\mathrm{ph}}^p, \tag{16}$$

$$j_{inj}^n=A\cdot E^2\ \exp(-\alpha\phi^{3/2}/E), \tag{17}$$

$$\frac{\partial C_{\mathrm{Si\_}}}{\partial t}=\sigma_{\mathrm{H}}(j_n/e)C_{\mathrm{SiH}}-k_3(x)C_{\mathrm{Si\_}}C_{\mathrm{H}}+k_1(x)C_{\mathrm{SiH}}C_{\mathrm{H}} -\sigma_{\mathrm{Si}}^n(j_n/e)C_{\mathrm{Si\_}}+\sigma_{\mathrm{Si}}^{rn}(j_n/e)C^++\sigma_{\mathrm{Si}}^{rp}(j_p/e)C^-, \tag{18}$$

$$\frac{\partial C^+}{\partial t}=\sigma_{\mathrm{Si}}^p(j_p/e)C_{\mathrm{Si\_}}-\sigma_{\mathrm{Si}}^{rn}(j_n/e)C^+, \tag{19}$$

$$\frac{\partial C^-}{\partial t}=\sigma_{\mathrm{Si}}^n(j_n/e)C_{\mathrm{Si\_}}-\sigma_{\mathrm{Si}}^{rp}(j_p/e)C^-, \tag{20}$$

where the electron current is determined by the conditions at the contacts (the injection current is computed from the formulas for tunneling through a triangular barrier, ϕ is the barrier height at the interfaces for electrons with a mean energy that exceeds the conduction-band edge, and A and α are tunneling constants) and by the generation of electrons by photons. For the hole current j_p [Eq. (16)], the model of

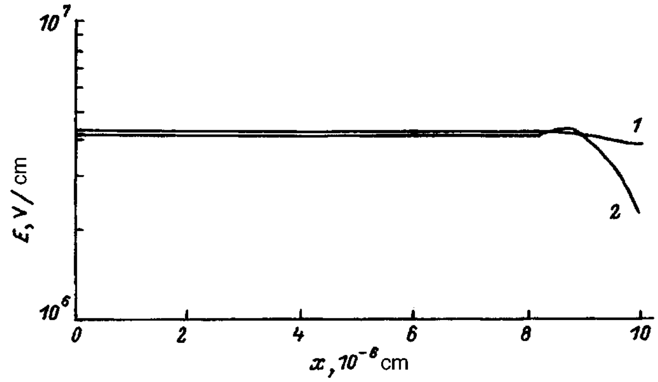

FIG. 1. Electric-field distribution profiles in the film. $V_g = -42$ V for different values of the charge flux: *1*—5×10^{-2} C/cm^2; *2*—5×10^{-1} C/cm^2.

Ref. 15 for the generation of holes from the contact by hot electrons is adopted. Since for holes there are large barrier heights at the Si/SiO$_2$ or SiO$_2$/*Me* boundaries, the hole-generation probability constant was assumed to be[16] 10^{-3}. The quantities C^+ and C^- in Eqs. (18)–(20) are the concentrations of holes and electrons, respectively, which are trapped at dangling bonds, and $C_{\mathrm{Si\_}}$ is the concentration of dangling bonds in the neutral state. The free-carrier concentrations were computed from

$$n = j_n/(e\cdot v_d^e)$$

and

$$p = j_p/(e\cdot v_d^p).$$

In writing Eqs. (15) and (16), instead of using the continuity equations for electrons and holes, we considered the following points: (1) The free electron and hole concentrations were usually several orders of magnitude (as many as six) lower than the electron or hole concentration at the traps ($n\sim10^5-10^8$, $p\sim10^4-10^7\,\mathrm{cm}^{-3}$, C^-, C^+, $C_{\mathrm{Si}}\sim10^{15}-10^{19}\,\mathrm{cm}^{-3}$) and were uniformly distributed over the thickness of the insulator, with the exception of thin ~50 to 100-Å-thick layers near the electrode.[17–19] (2) The electric field distribution was also fairly uniform over the sample (Fig. 1) and began to vary only when a charge of about 5.3×10^{-2} C/cm^2 passed through unit area of the structure, screening the applied voltage. (3) The fields existing in the structure did not exceed 10^7 V/cm, and therefore avalanche multiplication processes can be disregarded.[1] (4) The photocurrent in Eqs. (15) and (16) can be disregarded, since special filters were used in the experiments to cut off the spectra of photons whose energy exceeded[3] 5.0 eV. (5) Current variations due to capture processes can also be ignored because of the smallness of the free-carrier concentrations. Note that the role of the constant exposure used here reduced only to exciting the electron subsystem at the contacts (Al or Si), and that the already excited electrons with a mean energy above the conduction band edge then tunneled into the SiO$_2$.[20] Since no current value was given in Ref. 3, it was impossible to estimate the reduction of the barrier height in Eq. (17). The current was estimated from a charge of about 1.0 C/cm^2 passing through unit area in a time of about 10^5 sec. The causes indicated above make it possible to use Eqs. (15) and (16) instead of the continuity equations with an accuracy no worse than 0.1–1.0%. A similar approximation has been used in the literature (see, for example, Refs. 16, 21, and 22). In the same way, we can write the equations of the charge kinetics at the trapping centers that appear during the synthesis of SiO$_2$ and Poisson's equation:

$$\frac{\partial n_t}{\partial t} = \sigma_n(j_n/e)(N_t-n_t) - \sigma_{rn}(j_p/e)n_t, \tag{21}$$

$$\frac{\partial p_t}{\partial t} = \sigma_p(j_p/e)(P_t-p_t) - \sigma_{rp}(j_n/e)p_t - p_t/\tau_p, \tag{22}$$

$$\frac{\partial E(x)}{\partial x} = (e/\varepsilon)(p_t - n_t + C^+ - C^-), \tag{23}$$

where N_t and P_t are the concentrations of neutral traps for electrons and holes, n_t and p_t are the concentrations of electrons and holes captured at the traps, and σ_n, σ_p, σ_{rn}, and σ_{rp} are the electron- and hole-capture cross sections and the recombination cross sections of the electrons and holes captured at the traps, respectively. The free electron and hole concentrations are omitted from Eq. (23) because they are small.

The boundary conditions for the reduced system of equations have the form

$$\frac{\partial C_{\mathrm{H}}}{\partial x}(x=0,t)=0, \quad \frac{\partial C_{\mathrm{H}}}{\partial x}(x=L,t)=J_{\mathrm{H}},$$

$$C_{\mathrm{H}_2}(x=0,t)=0, \quad \frac{\partial C_{\mathrm{H}_2}}{\partial x}(x=L,t)=0,$$

$$\varphi(0)=0, \quad \varphi(L)=V_g.$$

Here we have used the conditions of nonflow and semitransparency for hydrogen and the possibility of transmitting voltage to the structure. Other versions of the boundary conditions were also used in the numerical calculations. The initial conditions for the system of equations are

$$C_{\mathrm{SiH}}(x,t=0)=C^0_{\mathrm{SiH}}, \quad C_{\mathrm{Si\_}}(x,t=0)=C^0_{\mathrm{Si\_}},$$

$$C_{\mathrm{H}}(x,t=0)=C^0_{\mathrm{H}}, \quad C_{\mathrm{H}_2}(x,t=0)=C^0_{\mathrm{H}_2},$$

$$C^+(x,t=0)=0, \quad C^-(x,t=0)=0,$$

$$n_t(x,t=0)=0, \quad p_t(x,t=0)=0.$$

Gaussian functions were used to approximate the initial profile, C^0_{SiH}, $C^0_{\mathrm{Si\_}}$, C^0_{H}, $C^0_{\mathrm{H}_2}$, of the concentrations of trapped hydrogen, as well as for the concentration of trapping centers that appear during synthesis. We shall consider samples in which, in strong electric fields, electrons are accumulated at neutral traps.[3]

METHOD OF CALCULATION

We used an implicit technique to numerically solve the system of equations (7)–(10) and (15)–(22). The time derivatives were approximated with first-order accuracy. The step in time was chosen to increase over time with a growth increment of $\delta t^n/\delta t^{n-1}=1.1$. A conservative technique of second-order accuracy on a nonuniform grid was used to approximate the spatial derivatives. The nonlinear system of difference equations was solved by successive scalar passes, using the solutions from the previous iteration. The accuracy of the calculations was no worse than 0.1%.

RESULTS OF CALCULATIONS AND DISCUSSION

Despite the well-known object of this study—hydrogen in silicon oxide—until now the question considered in the literature has been in what form does hydrogen diffuse, as a neutral particle or as a positively charged particle. For atoms, this is in the form of protons, and for molecules in the form of positive H_2^+ ions. What boundary conditions can be used for the atoms or molecules at the SiO_2/Al and SiO_2/Si boundary: reflecting boundaries $(\partial C/\partial x=0)$, adsorbing boundaries $(C=0)$, or transparent boundaries for the penetration of particles from one material to the other (the condition that the fluxes are equal at the interface, $D_1\,\partial C_2/\partial x=D_2\,\partial C_2/\partial x$? To answer these questions, calculations were carried out with various types of boundary conditions, and the drift component of positive ions of atomic or molecular hydrogen was taken into account in the expression for the flow, Eq. (24). The results of the calculations were compared with the experimental data of Ref. 3. An analysis of these data shows that molecular hydrogen does not penetrate into the silicon substrate. Therefore, at the Si/SiO_2 interface, the Neumann condition can be used for mobile molecular hydrogen and the condition of equality of the fluxes for atomic hydrogen, since the latter penetrates into the Si. Both types of boundary conditions, $\partial C/\partial x=0$ and $C=0$, were tested at the Al/SiO_2 interface.

It follows from the calculations that, for molecular hydrogen, using Neumann conditions at both boundaries makes it possible to have unbounded growth of the H_2 concentration in the SiO_2. It is easy to see this result from the form of Eq. (9), where the right side contains only the generation term $\sim k_1 C_{\mathrm{SiH}} C_{\mathrm{H}}$, whereas the reflection condition is valid at both boundaries. As a result, for characteristic times of $t\sim 10^6$ sec, a charge flow through unit area of $Q\simeq 1$ C/cm^2, and the chosen parameters σ_{H} and σ_{ph}, concentrations of $H_2\sim 10^{20}$ cm^{-3} were obtained, which are not observed in experiment. It follows from this that either sinks for molecular hydrogen exist in the bulk, or the adsorption condition, $C_{\mathrm{H}_2}=0$, is valid, or H_2 emerges from one of the boundaries. We have used in our calculations the condition that mobile molecular hydrogen equals zero. This limits the growth of the H_2 concentration in the bulk. This type of boundary condition corresponds to the case in which part of the molecular hydrogen emerges from the film. In order to bring the calculations into agreement with the experiment of Ref. 3, the parameter $\xi_1(x)$ in the reaction constant $k_1(2)$ was set equal to $\sim 10^{-3}$. The latter is evidence that not every attempt of the mobile hydrogen to approach the Si–H or SiO–H complexes is accompanied by H_2-molecule formation; i.e., the reaction occurs with a certain activation barrier. A calculation by the semiempirical MINDO method of a reaction in the Si–H+H system is evidence that it has a nonactivation nature. Consequently, the SiO–H complexes apparently predominate in the system, reactions with which involve overcoming a reaction barrier.

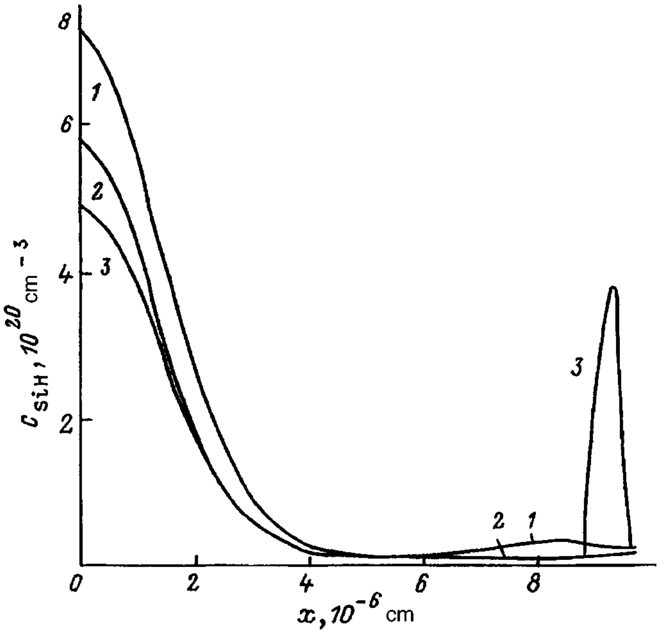

FIG. 2. Distribution profiles of bound hydrogen in a SiO_2 film, $V_g=-42$ V, $k_1=10^{-3}$. *1*—calculation with $k_3\neq 0$ in the SiO_2 bulk; *2*—calculation taking into account the positive charge of atomic hydrogen, $q=1$; *3*—calculation with $k_3=0$ in the bulk and $k_3\neq 0$ close to the SiO_2/Si boundary, $q=0$.

We assume that mobile atomic and molecular hydrogen moves through the insulator in the form of ions. We therefore added a drift term to the flux term in the diffusion equations (7) and (9) in the form

$$j_{\mathrm{H}^+}=-D_{\mathrm{H}^+}\frac{\partial C_{\mathrm{H}^+}}{\partial x}+E\cdot q\cdot \mu_{\mathrm{H}^+}\cdot C_{\mathrm{H}^+}, \tag{24}$$

where the mobility μ_{H^+} is associated with the diffusion coefficient D_{H^+} by the Einstein relation. In addition, the charge of the particles (molecules and atoms) was taken into account in Poisson's equation, Eq. (23)

$$\frac{\partial E(x)}{\partial x}=(e/\varepsilon)(p_t-n_t+C^+-C^-+C_{\mathrm{H}^+}+C_{\mathrm{H}_2^+}).$$

As follows from Fig. 2, with a negative bias V_g^- on the gate, the electric field of about 4×10^6 V/cm does not allow the protons to drift to the Si/SiO_2 interface, and the hydrogen concentration at this site does not increase with time. It can therefore be concluded that hydrogen atoms in SiO_2 diffuse in neutral form. The situation with molecular hydrogen is somewhat more complex. Its diffusion in the form of an H_2^+ ion does not disturb the qualitative picture of the process and gives fairly good agreement with experiment[3] in both cases (Fig. 2). In our subsequent calculations, we assumed that the molecules diffuse as neutral H_2.

As shown by the calculations, reactions such as Eq. (3) occur in only one direction in the bulk (Fig. 2) [the parameter is $\xi_3(x)=0$], and the dangling bonds (the surface states) are saturated with hydrogen atoms only close to the Si/SiO_2 interface. The cause of this behavior is that, after a hydro-

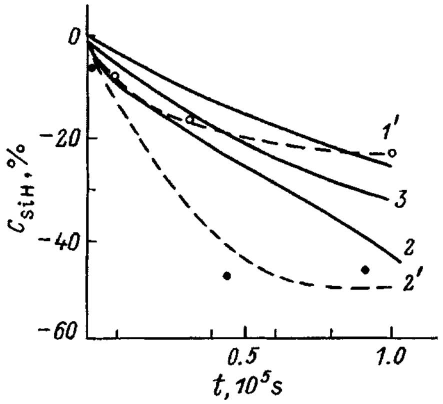

FIG. 3. Decrease of the percentage of bound hydrogen at the SiO_2/Al boundary vs time: *1,1'*—$E=0$, $\sigma_{ph}=2\times10^{-6}$; *2,2'*—$E=+4\times10^6$ V/cm, $\sigma_H=6\times10^{-20}$ cm^2, $\nu_{ph}=2\times10^{-6}$ sec^{-1}, *3*—$E=-4\times10^6$ V/cm, $\sigma_H=6\times10^{-20}$ cm^2, $\nu_{ph}=6\times10^{-6}$ sec^{-1}. *1–3*—calculation; *1'−2'*—experimental values from Ref. 3.

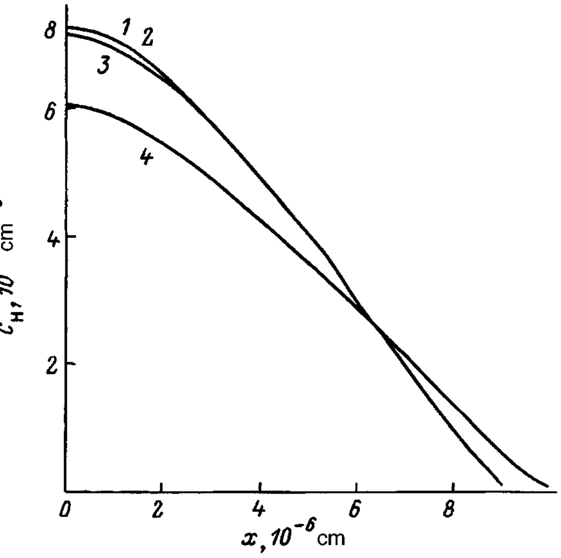

FIG. 4. Distribution profiles of atomic hydrogen for various times, sec: *1*—10^1, *2*—10^2, *3*—10^4, *4*—10^5.

gen atom is extracted from a bond, reclosure of the bonds and geometrical relaxation of the defect occurs at this site.[2,14] These defect complexes do not participate in charge accumulation, as follows from the data of Ref. 3.

After we adjusted the parameters of the cross section σ_H of the reaction of Eq. (3) and the generation frequency ν_{ph} at which hydrogen atoms are ejected by light from Si–H or SiO–H bonds by high-energy phonons, we obtained $\sigma_H \simeq 6\times10^{-20}$ cm^2 and $\nu_{ph} \simeq 2\times10^{-6}$ sec^{-1}. The results of a comparison of the calculated values and the experimental results of Ref. 3 are shown in Fig. 3. Here we have the dependence of the H concentration close to the Al/SiO_2 boundary in a field of $\sim 4\times10^6$ V/cm and without a field ($E=0$) when the sample is irradiated by light for about 10^5 sec. The same figure also shows a curve (*3*) in which the polarity of the applied voltage was changed. A smaller amount of hydrogen was evolved from the SiO_2/Al region, since the electrons are injected from the Al, and they need a certain distance x in order to attain enough energy to eject hydrogen from the bonds. When the injection is from the Si, all the electrons have high energy when they reach the region with high hydrogen concentration (the neighborhood of the SiO_2/Al boundary). Figures 4–6 show the evolution of the atomic, molecular, and bound hydrogen profiles for various times. As can be seen from Fig. 4, as time passes, the concentration of atomic hydrogen first increases, then saturates, and finally decreases; this occurs because it is lost through the boundaries and is consumed in the reaction in which molecular hydrogen is formed, and because the hydrogen generation rate decreases. For molecular hydrogen, a maximum is formed close to the SiO_2/Al boundary during the initial interval; this increases with time because of the reaction in Eq. (1), and then the H_2 molecules diffuse toward the boundary with Si. Because of the reflection condition at this boundary, the H_2 concentration increases, so that the maximum shifts from the boundary with the Al to the boundary with the Si. For hydrogen, the dangling bonds of the SiO_2/Al boundary become saturated, and a second maximum appears close to the SiO_2/Si boundary. The dependence of the hydrogen concentration at this boundary as a function of the transmitted charge is shown in Fig. 7, which also shows the experimental data of Ref. 3. As can be seen from these data, good agreement with experiment is observed.

For instrumental applications, it is essential to predict how the charge accumulation evolves in SiO_2. It was noted in Ref. 3 that, for small fields, when small amounts of charge, 0.1 C/cm^2, are transmitted through unit area into SiO_2, negative charge is accumulated at neutral traps. When large amounts of electrons are transmitted into SiO_2, negative or positive charge (anomalous positive charge) is accumulated, depending on the polarity. The region of trapped charge is rather extensive, being about 100 Å, and this charge does not disappear by tunneling through the interface. Buchanan *et al.*[3] conclude that there are no holes on the

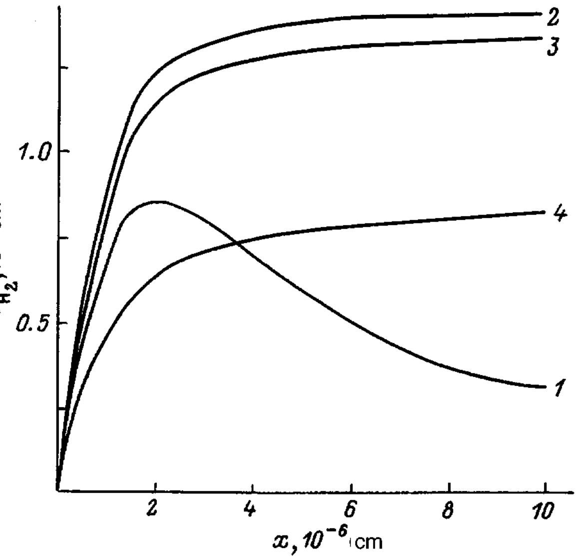

FIG. 5. Distribution profiles of molecular hydrogen for various times, sec: *1*—10^1, *2*—10^2, *3*—10^4, *4*—10^5.

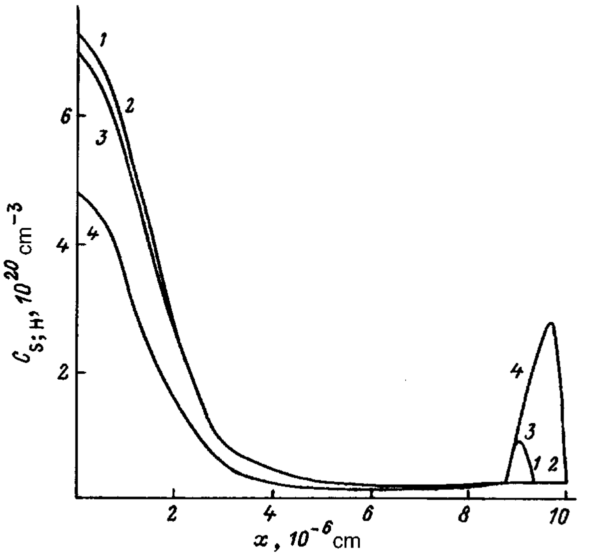

FIG. 6. Distribution profiles of bound hydrogen for various times, sec: *1*—10^1, *2*—10^2, *3*—10^4, *4*—10^5.

traps. The accumulation of positive charge in SiO_2 was noted for the first time by Withan and Lenahan[23] and Bender *et al.*[22] attempted to model its accumulation. They assumed that an external stimulation gives rise to defects in which positive charge accumulates. This situation involves dangling bonds as a result of the generation of hydrogen. An important point here is the method of appearance of holes in the insulator, since the SiO_2/Al and SiO_2/Si barrier heights are too large for holes to appear by tunneling. However, in our case, we have, first, high-energy electrons (with an energy of >2 eV plus the barrier height of 3–4 eV) and, second, external irradiation by light, which excites a hole subsystem and reduces the barrier height for hole tunneling from the contacts—the Fischetti mechanism for hole injection into SiO_2.[15] We used this mechanism with a hole-generation parameter g from Si equal to 10^{-3} (Refs. 16 and 20) and from Al equal to 3×10^{-4}. We assumed that both positive and negative charge can accumulate at the dangling bonds, but with different values of the capture and recombination cross sections. We used the following values in our calculations: $\sigma_{\text{Si}}^{n}=10^{-19}$ cm^2, $\sigma_{\text{Si}}^{rp}=10^{-15}$ cm^2, $\sigma_{\text{Si}}^{p}=10^{-15}$ cm^2, $\sigma_{\text{Si}}^{rn}=10^{-18}$ cm^2, and, for traps of the second type, as noted in Ref. 3, values of $\sigma_n=4\times10^{-18}$ cm^2, $\sigma_{rn}=5\times10^{-15}$ cm^2, $\sigma_p=0$, $\sigma_{rp}=0$. Figure 8 shows the behavior of the trapped charge as a function of the transmitted charge for both polarities. For a positive voltage on the gate, $V_g>0$ in SiO_2, a negative charge is accumulated, whereas, for a negative voltage, a positive charge is accumulated. If we disregard the accumulation of charge at the traps N_t (the case $V_g>0$), the accumulated charge Q is always positive (Fig. 8, curve *3*). If we take into account the accumulation of electrons at neutral traps N_t, then, for small values of the transmitted charge, we have negative values of the accumulated charge, whereas, for large values of the transmitted charge, we have positive values. This behavior is caused by competition between the capture of holes and electrons at the traps and the recombination of the trapped carriers with free carriers. An important element in this model is the hole-generation parameter g, which determines the value of the hole current in the insulator. As can be seen from the figure, extremely good agreement was obtained between the calculated results and the experimental data of Ref. 3.

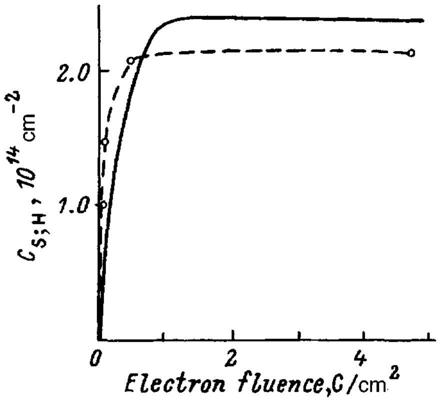

FIG. 7. Concentration of bound hydrogen at the SiO_2/Si interface vs the transmitted charge density: the solid curve shows the calculated results, and the dotted curve shows the experimental results of Ref. 3, $V_g<0$, $E=4\times10^6$ V/cm.

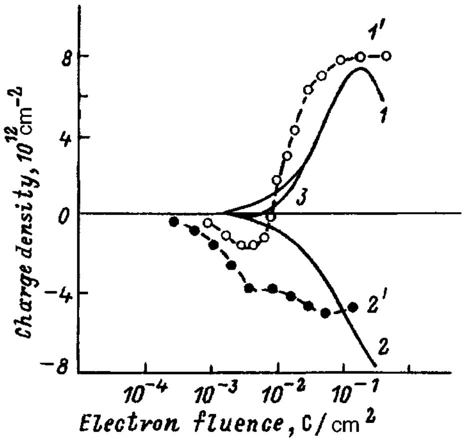

FIG. 8. Trapped charge density at the SiO_2/Si interface vs transmitted charge density: *1,1′,3*—$V_g<0$; *2,2′*—$V_g>0$; *1–3*—calculation; *1′,2′*—experimental results of Ref. 3.

The author would like to express his appreciation to E. G. Sal'man and V. A. Gritsenko for many useful discussions of the problem and its results, to Yu. N. Morokov for carrying out the quantum calculations of the interaction of hydrogen with hydrogen complexes, and to I. I. Gadiyak for help in putting together the manuscript. The author would also like to thank the referee for careful reading of the manuscript and for constructive comments, which made it possible to substantially improve the text of the article.

[1] A. P. Baraban, V. V. Bulavinov, and P. P. Konorov, *The Electronics of SiO_2 Layers on Silicon* (Leningradskiĭ Gos. Univ., Leningrad, 1988).

[2] V. A. Gritsenko, *Construction and Electronic Structure of Amorphous Insulators in Silicon MOS Structures* (Nauka, Novosibirsk, 1993).

[3] D. A. Buchanan, D. J. DiMaria, A. D. Marwick, and L. Dory, J. Appl. Phys. **76**, 3595 (1994).

[4] C. Bulucea, Solid-State Electron. **18**, 467 (1975).

[5] M. Fischetti, R. Gastaldi, F. Maggioni, and A. Modelli, J. Appl. Phys. **53**, 3129 (1982).
[6] M. Fischetti, R. Gastaldi, F. Maggioni, and A. Modelli, J. Appl. Phys. **53**, 3135 (1982).
[7] S. K. Lai, J. Appl. Phys. **54**, 2540 (1983).
[8] C. T. Sah, Y. C. Cun, and J. T. Tzou, J. Appl. Phys. **54**, 2547 (1983).
[9] R. Gale, F. J. Feigle, and C. W. Magge, J. Appl. Phys. **54**, 6938 (1983).
[10] Yu. V. Gorelkinskii, N. N. Nevinnyĭ, and E. A. Lyuts, Poverkhnost' **6**, 79 (1994).
[11] M. V. Fischetti, D. J. DiMaria, S. D. Brorson, T. N. Theis, and J. R. Kirtley, Phys. Rev. B **31**, 8124 (1985).
[12] G. V. Gadiyak, S. P. Sinitsa, and I. V. Travkov, Mikroelektronika **15**, 448 (1988).
[13] C. T. Sah, Solid–State Electron. **33**, 147 (1990).
[14] V. O. Sokolov and V. B. Sulimov. Phys. Status Solidi B **135**, 369 (1986).
[15] M. V. Fischetti, Phys. Rev. B, **31**, 2099 (1985).
[16] G. V. Gadiyak, V. A. Gritsenko, K. A. Nasyrov, and Yu. A. Perchilo, Technical Digest 1993, International Conference on VLSI and CAD, Taejon, Korea, November 15–17, 1993, p. 159.
[17] J. N. Churchill, F. E. Holmstrom, and T. W. Collins, Adv. Electron. and Electron Phys. **58**, 1 (1981).
[18] V. A. Gurtov, A. I. Nazarov, and I. V. Travkov, Fiz. Tekh. Poluprovodn, **24**, 969 (1990) [Semiconductors **24**, 611 (1990)].
[19] G. V. Gadiyak, Avtometriya **4**, 31 (1995).
[20] K. F. Schuegraft and C. Hu, IEEE Trans. Electron. Dev. **41**, 761 (1994).
[21] D. A. Buchanan, M. V. Fischetti, and D. J. DiMaria, Phys. Rev. B **43**, 1471 (1991).
[22] A. E. Bender, G. B. Semushkin, and K. L. Temnikov, Elektron. Tekhn. **6**, 53 (1988).
[23] H. S. Withan and P. M. Lenahan, Appl. Phys. Lett. **51**, 1007 (1987).

Translated by W. J. Manthey

Effect of electron irradiation on the electrical properties of *n*-type $Pb_{1-x}Sn_xTe$ ($x \simeq 2$) alloys

E. P. Skipetrov and A. N. Nekrasova

M. V. Lomonosov Moscow State University 119899, Moscow, Russia

(Submitted February 26, 1996; accepted for publication April 8, 1996)
Fiz. Tekh. Poluprovodn. **31**, 264–267 (March 1997)

The effect of electron bombardment ($T_{\mathrm{irr}} \simeq 300$ K, $E=6$ MeV, $\Phi \leqslant 4\times10^{17}$ cm^{-2}) on the electrical properties of *n*-type $Pb_{1-x}Sn_xTe$ has been studied. Electron bombardment decreases the electron concentration and produces conductivity-type $n-p$ conversion. The difference rate of the donor- and acceptor-type defect generation as a result of bombardment has been determined. Anomalies are detected in the temperature and magnetic-field dependences of the electrical parameters of the bombardment samples. These anomalies are associated with the appearance of a hole-enriched surface layer as a result of electron bombardment. *© 1997 American Institute of Physics.* [S1063-7826(97)00203-2]

A fairly well-established model of the energy spectrum of electron-irradiated $Pb_{1-x}Sn_xTe$ ($x=0.2$) alloys is now available. This model satisfactorily describes the reconstruction of the spectrum of undoped *p*-type alloys during electron bombardment and subsequent hydrostatic compression.[1,2] According to this model, electron bombardment results in the appearance in the energy spectrum of the alloy of a resonance donor level E_d in the conduction band and a band of acceptor-type resonance states E_a, which is located close to the top of the valence band and which stabilizes the Fermi level in irradiated crystals. It has been established that the character of the variation of the charge-carrier concentration as a result of bombardment with electrons and the limiting characteristics of irradiated crystals are determined by a number of parameters, including the energy position and width of the resonance band E_a, as well as the ratio of the generation rates of donor- and acceptor-type defects, $dN_d/d\Phi$ and $dN_a/d\Phi$. In particular, for definite values of these parameters, deep electron irradiation of *p*-type crystals can result in ‘‘soft’’ stabilization of the Fermi level in the valence band, or can induce an extended insulating state in which the Fermi level is stabilized within the band gap.

At the same time, experimental data obtained by studying *p*-type crystals does not make it possible to predict with adequate reliability how the parameters of *n*-type alloys vary as a result of bombardment with electrons: depending on the ratio of the generation rates of defects of donor and acceptor character, irradiation of *n*-type crystals can either cause $n-p$ conversion of the conductivity type ($dN_d/d\Phi < dN_a/d\Phi$) or can increase the electron concentration in the conduction band to the point that the Fermi level is stabilized at the energy level of the donor-type defects ($dN_d/d\Phi > dN_a/d\Phi$). Moreover, the question of the energy position of the donor-type radiation level and the character of the reconstruction of the energy spectrum of the irradiated alloys as the tin concentration in the alloy is varied remain undecided.

Our overall goal therefore was to study how the electrical properties of undoped single-crystal *n*-type $Pb_{1-x}Sn_xTe$ ($x \simeq 0.2$) are affected by deep irradiation by electrons, in order to determine the parameters of the energy spectrum of the charge carriers for these materials, to explain how their properties vary, and, in particular, to see what limiting characteristics of the materials can be attained as a result of irradiation. In this paper we discuss single-crystal samples of *n*-$Pb_{1-x}Sn_xTe$ ($x \simeq 0.2$) grown by the Czochralski method. To obtain *n*-type crystals with low electron concentrations, we used prolonged annealing in lead and tin vapors (doping by deviation from stoichiometry) and doping with zinc during diffusion annealing. The parameters of the samples studied here before subjecting them to electron bombardment are given in Table I.

The original samples were irradiated at room temperature on an Élektronika ÉLU-6 linear electron accelerator ($E=6$ MeV, $d\Phi/dt \simeq 10^{12}$ cm$^{-2}\cdot$sec^{-1}, $\Phi \leqslant 8.4\times10^{17}$ cm^{-2}). The temperature dependences of the resistivity ρ and the Hall coefficient R_H ($4.2 \leqslant T \leqslant 300$ K, $B \leqslant 0.04$ T), as well as the Shubnikov–de Haas effect and the field dependences of the Hall coefficient ($T=4.2$ K, $B \leqslant 6$ T, $\mathbf{B}\|\langle 100\rangle$), were studied in each sample before and after irradiation.

It was established that, in all our samples, a slow decrease first occurs during electron bombardment, followed by an increase of the resistivity ρ at liquid-helium temperatures, with the greatest variations characterizing the samples with the lowest initial electron concentration. The temperature dependences of the resistivity of the original samples have a ‘‘metallic’’ character, which indicates that there are no local levels in the band gap of the alloys (Fig. 1). In samples with high initial electron concentration, the character of the $\rho(1/T)$ dependences does not change after irradiation, whereas, in sample *C*-22, the $\rho(1/T)$ dependences acquire a semiconductor form. An activation section associated with intrinsic ionization of the charge carriers appears in the temperature region close to room temperature, whereas, at low temperatures ($T<20$ K), there is an activation section with an activation energy of $\Delta E_a \simeq 0.2$ meV.

The behavior of the Hall coefficient in our samples during irradiation was more complicated. A rapid falloff of the absolute value of R_H occurs in the low temperature region of

TABLE I. Parameters of n-$Pb_{1-x}Sn_xTe$ samples at $T=4.2$ K.

Sample	Composition, x	n, 10^{17} cm^{-3}	ρ, 10^{-4} $\Omega\cdot cm$	μ_H, 10^5 $cm^2/(V\cdot s)$	Φ_{max}, 10^{17} cm^{-2}
Nn-3	0.2	0.76	1.1	6.2	7.5
Nn-4	0.2	1.23	0.7	6.0	7.9
Nn-5	0.2	1.20	0.6	6.8	8.4
C-22	0.22	0.15	4.8	7.3	7.7

the $R_H(T)$ dependences, and a broad maximum ($T>30$ K), whose amplitude monotonically increases with increasing irradiation flux, appears (Fig. 2). The subsequent behavior of the Hall coefficient during irradiation evidently depends on the initial electron concentration in the samples. In samples with a high initial electron concentration, the Hall coefficient retains a negative sign and increases in absolute value to values that exceed $|R_H|$ in unirradiated crystals. At the same time, in sample C-22, with a minimal initial electron concentration, the Hall coefficient changes sign at low temperatures when the electron flux is $\Phi^*\simeq 6\times 10^{17}$ cm^{-2}, and inversion of the sign of the Hall coefficient as temperature increases is observed on the temperature dependences of R_H (Fig. 2). Finally, at the maximum irradiation fluxes, the temperature dependences of the Hall coefficient acquire a ''normal'' form typical of undoped p-type crystals.

In the neighborhood of the $n-p$ conversion point during irradiation, the dependences of the Hall coefficient on magnetic field at $T=4.2$ K also have an anomalous character (Fig. 3). For irradiation fluxes of $\Phi<\Phi^*$, the absolute magnitude R_H rapidly decreases as the magnetic flux increases, and sign inversion occurs. After the $n-p$ conversion point ($\Phi>\Phi^*$), the Hall coefficient remains positive in the entire range of the magnetic fields studied here, slowly decreasing with increasing field.

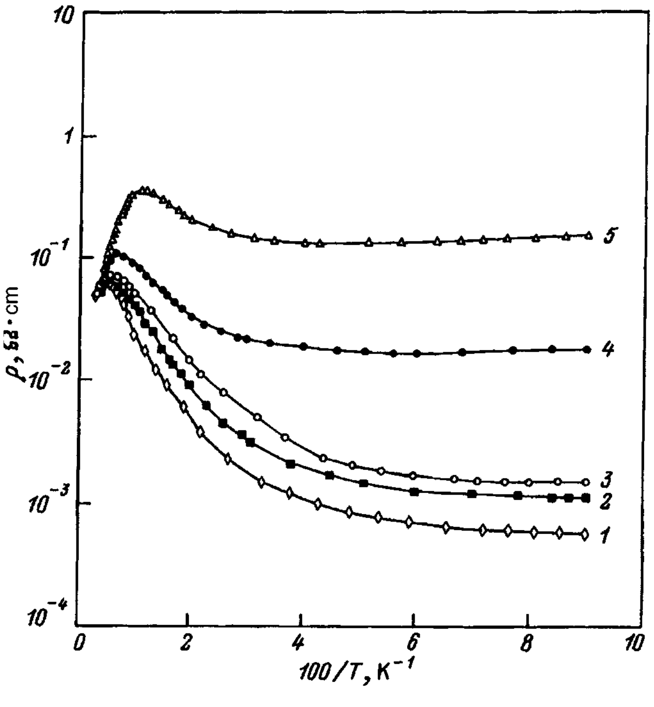

FIG. 1. Temperature dependences of resistivity ρ for sample C-22 for various irradiation fluxes Φ, 10^{17} cm^{-2}: *1*—0, *2*—4.4, *3*—5.5, *4*—6.5, *5*—7.7.

As a whole, except for the anomalous character of the temperature and field dependences of the Hall coefficient, the results (increasing resistivity, sign inversion of R_H during irradiation) indicate, from our viewpoint, a decrease in electron concentration during irradiation all the way to inversion of the conductivity type in the sample with the smallest initial electron concentration. According to the model of the energy spectrum proposed in Refs. 1 and 2 for electron-irradiated p-$Pb_{1-x}Sn_xTe$ ($x=0.2$) alloys, this means that, in our n-type samples, the generation rate of acceptor-type defects during irradiation exceeds that of donor-type defects ($dN_a/d\Phi>dN_d/d\Phi$). Therefore, as the irradiation flux is increased, the electron concentration slowly decreases, and the Fermi level moves downward along the conduction band. In samples with a relatively high initial electron concentration, the fluxes used in the experiment cause only an insignificant (10%–15%) decrease in the electron concentration, whereas, in sample C-22, whose initial electron concentration is an order of magnitude lower, it causes $n-p$ conversion and stabilizes the Fermi level in a resonance band located in the valence band at the level E_a.

In sample C-22, the hole concentration for the maximum irradiation flux, calculated from the Hall coefficient at $T=4.2$ K, is $p_{max}\simeq 10^{15}$ cm^{-3}, while the difference rate of the generation of radiation defects, determined from the position of the point where the sign of R_H inverts on the dependences of the Hall coefficient on the irradiation flux is

$$d(N_a-N_d)/d\Phi\simeq 0.02\ cm^{-1}.$$

Unfortunately, these data were insufficient to calculate the position and width of the acceptor-type resonance band E_a in terms of the model of the energy spectrum of the electron-irradiated $Pb_{1-x}Sn_xTe$ ($x=0.2$) alloy.[2] To determine these parameters of the model, experimental data are needed on how the hole concentration in the irradiated sample varies when the spectrum is reconstructed under pressure.

In samples with high initial electron concentration (such as Nn-3–Nn-5; see Table I), the defect generation rate was

$$d(N_a-N_d)/d\Phi\simeq 0.04\ cm^{-1}.$$

It was estimated from the variation of the period of the Shubnikov–de Haas oscillations after irradiation. Distinct oscillations of the transverse magnetoresistance are maintained all the way to the maximum irradiation fluxes in these samples, indicating a high uniformity of the generation of radiation defects during irradiation and high charge-carrier mobilities in the irradiated crystals. The appearance of broad maxima in the $R_H(T)$ dependences can be associated with

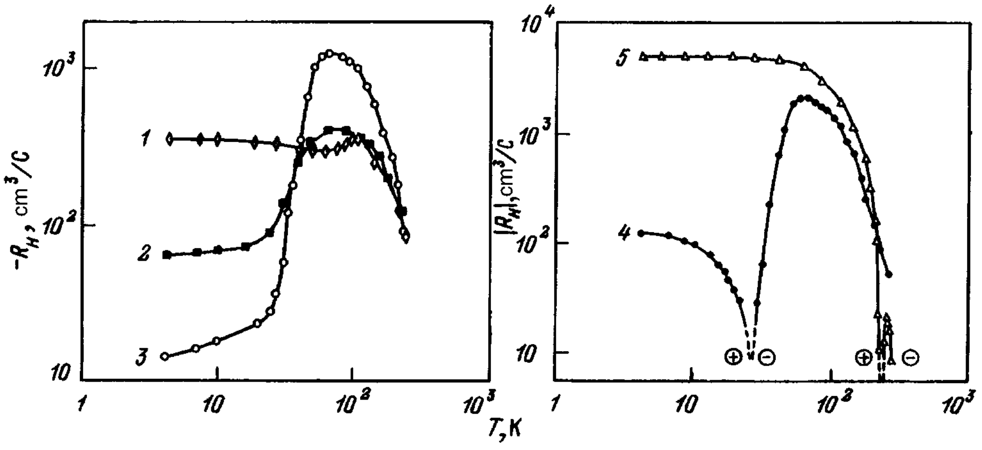

FIG. 2. Temperature dependences of the Hall coefficient R_H for sample C-22 for various irradiation fluxes Φ, 10^{17} cm^{-2}: *1*—0, *2*—3.4, *3*—5.5, *4*—6.5, *5*—7.7.

the appearance of a donor-type defect level E_d located above the Fermi level in the irradiated crystals and thermal generation of electrons from the conduction band to this level. An increase of the amplitude of the maximum in this case could be associated with an increase in the density of resonance states as the irradiation flux increases. However, in this case, the appearance of the maximum should more likely be accompanied by an increase and not by a decrease of the absolute value of the Hall coefficient at low temperatures. It is also not clear how the appearance of a resonance donor level in the conduction band can be connected with sign inversion of R_H in the magnetic-field dependences of the Hall coefficient.

Another possible explanation of the anomalies observed in this work can be that a p-type layer appears on the surface of the irradiated crystals. The possibility for the appearance of a p-type surface layer as a result of electron irradiation of $Pb_{1-x}Sn_xTe$ alloys has been discussed in Refs. 2 and 3. It was assumed that its formation can be caused by intense surface oxidation when the sample is irradiated in ozone-enriched air. Clearly, the effect of this layer on the parameters of irradiated samples measured at low temperatures must increase as the electron concentration decreases in the bulk of the crystals. Here the Hall coefficient in classical magnetic fields must be computed in terms of a model of a bilayer structure:[4,5]

$$\sigma=(\sigma_1 d_1+\sigma_2 d_2)/d, \tag{1}$$

$$R_H=d\,\frac{\mu_1\sigma_1 d_1+\mu_2\sigma_2 d_2+\mu_1\mu_2(\mu_2\sigma_1 d_1+\mu_1\sigma_2 d_2)B^2}{(\sigma_1 d_1+\sigma_2 d_2)^2+(\mu_2\sigma_1 d_1+\mu_1\sigma_2 d_2)^2 B^2}, \tag{2}$$

where $d=d_1+d_2$ is the sample thickness, and d_i, μ_i, and σ_i are the thickness, charge-carrier mobility, and conductivity, respectively, for the ith layer.

The Hall coefficient at low temperatures must then be determined not only by the electron concentration in the bulk of the sample, but must also depend on the hole concentration in the skin layer, on the electron and hole mobilities, and on the magnetic induction B. When a p-type layer appears on the surface of the sample, n–p conversion as a result of electron irradiation should start from the surface of the sample, and, as the irradiation flux increases, the p-type layer must gradually occupy the entire volume of the crystal. It is possible that this is why the point where the sign of the Hall coefficient R_H inverts for sample C-22 shifts toward higher temperatures as the irradiation flux increases (Fig. 2).

In conclusion, we should point out that the nature of the low-temperature activation section on the temperature dependences of the resistivity of electron-irradiated sample C-22 is not yet clear. Starting from the model of the energy spectrum of the electron-irradiated $Pb_{1-x}Sn_xTe$ ($x=0.2$) alloy and the value of ΔE_a, it can be hypothesized that hopping conductivity along the resonance band E_a exists in the low-temperature region in the irradiated crystal. However, to conclusively solve this problem, additional studies of irradi-

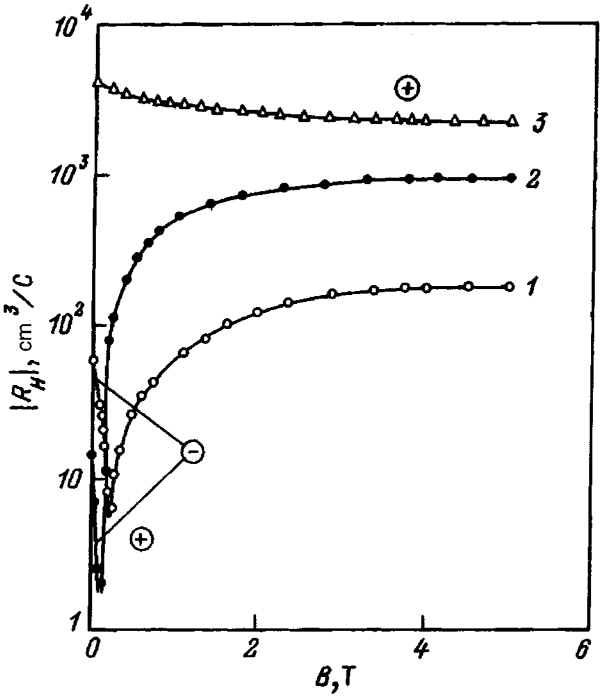

FIG. 3. Hall coefficient vs magnetic field for sample C-22 at $T=4.2$ K for various irradiation fluxes Φ, 10^{17} cm^{-2}: *1*—3.4, *2*—4.4,*3*—7.7.

ated crystals in strong magnetic fields and also under pressure are needed.

The authors are grateful to D. B. Chesnokova and A. V. Nikorich for providing the samples for study, and also to A. M. Musalitin for irradiating the samples with fast electrons.

This work was carried out with the partial financial support of the Russian Fund for Fundamental Research (Grant 96-02-18325a).

[1] N. B. Brandt, E. P. Skipetrov, and A. G. Khorosh, Fiz. Tekh. Poluprovodn. **24**, 51 (1990) [Semiconductors **24**, 31 (1990)].
[2] N. B. Brandt, E. P. Skipetrov, and A. G. Khorosh, Fiz. Tekh. Poluprovodn. **26**, 888 (1992) [Semiconductors **26**, 500 (1992)].
[3] A. N. Nekrasova, D. V. Pelekhov, V. I. Sidorov, and E. P. Skipetrov, Neorg. Mater. **28**, 2272 (1992).
[4] R. L. Petritz, Phys. Rev. **110**, 1254 (1958).
[5] V. I. Petrovskiĭ, N. N. Solov'ev, E. M. Omel'yanovskiĭ, and V. S. Ivleva, Fiz. Tekh. Poluprovodn. **12**, 1904 (1978) [Semiconductors **12**, 1132 (1978)].

Translated by W. J. Manthey

Transport phenomena in n-$Mn_xHg_{1-x}Te/Cd_{0.96}Zn_{0.04}Te$ epitaxial films

G. V. Beketov, A. E. Belyaev, S. A. Vitusevich, S. V. Kavertsev, and S. M. Komirenko

Institute of Semiconductor Physics, Ukrainian National Academy of Sciences, 252650 Kiev, Ukraine

(Submitted March 11, 1996; accepted for publication April 8, 1996)
Fiz. Tekh. Poluprovodn. **31**, 268–272 (March 1997)

The results of an experimental study of samples of $Mn_xHg_{1-x}Te$ films grown by liquid-phase epitaxy on a $Cd_{0.96}Zn_{0.04}Te$ substrate are presented. It shows that, as a result of the diffusion of cadmium from the substrate, a $Cd_xMn_yHg_{1-x-y}Te$ film with a variable band-gap layer is formed close to the ⟨epitaxial-film⟩–substrate interface. The appearance of this variable band gap is revealed by the transport phenomena. The temperature dependence of the band gap $E_g(T)$ is determined in a linear approximation on T from the results of a theoretical analysis of the temperature dependences of the free-carrier concentration and mobility. It is shown that averaging the semiempirical dependences for the ternary compounds with the extreme compositions, using the virtual-crystal approximation, can produce large errors when determining $E_g(T)$ in a specific semiconductor. © *1997 American Institute of Physics.* [S1063-7826(97)00303-7]

By comparison with the well-known semiconductors $Cd_xHg_{1-x}Te$, which are widely used in modern microelectronics, the semimagnetic semiconductors of the $Mn_xHg_{1-x}Te$ (MMT) system possess a number of advantages. MMT crystals are characterized by relatively high stability of the bulk and surface properties. The presence of magnetic Mn ions in the lattice makes it possible to efficiently control the band parameters of the material by means of a magnetic field. However, there are many questions regarding the technology and use of a set of components based on narrow-gap semimagnetic semiconductors that have not been sufficiently studied. These questions include, in particular, the problem of liquid-phase epitaxy of MMT films on a wide-band substrate. It is a rather complex task to synthesize an ideal (MnTe) substrate for the growth of such films. Therefore, substrates are made from other materials, which possess the optimum parameters for this purpose. To successfully predict the properties of the indicated structures, it is therefore necessary to determine the degree to which the ''nonideality'' of the substrate affects the parameters of the as-grown epitaxial film. In this paper we consider a solution of this problem, in the particular case of a CdZnTe substrate.

The MMT layers were grown by liquid-phase epitaxy on chemically and mechanically polished $Cd_{0.96}Zn_{0.04}Te$ (111) *A* substrates. Single crystals of $Cd_{0.96}Zn_{0.04}Te$ were grown by the vertical Bridgman method. The dislocation density in these crystals did not exceed 5×10^5 cm^{-2}. The epitaxial films were grown at a temperature of 848 K, with a cooling interval of 5–15 K. The films were then annealed in mercury vapor at 523 K for 100 h. After annealing, the electron concentration at liquid-helium temperature was about 10^{15} cm^{-3}. The Hall coefficient and the resistivity were measured by the van der Pauw method. Before the measurements, the surface of the films was etched in a 2% solution of Br in dimethylformamide. The uniformity in composition was monitored by a Kamskan x-ray microanalyzer. The film thickness was also monitored by means of an MII-4 interference microscope.

Studies of the distribution profiles of the components over the thickness of the structure showed that cadmium was uniformly distributed in the epitaxial film. Here the percentage of cadmium is so great that, strictly speaking, the resulting films should be regarded as four-component solid solutions of $Cd_xMn_yHg_{1-x-y}Te$ (CMMT). Figure 1 shows the distribution profile of the components in one of our structures ($x\approx0.04$, $y\approx0.07$), which will be used in what follows as a characteristic example. At the substrate–film interface, this structure contains a transition layer about 30 μm thick, with a large composition gradient. Here the variation of the percentage of Cd qualitatively reflects the variation of the band gap through the thickness of the structure. Thus, in contrast with bulk crystals, in the epitaxial films studied here, the band gap E_g (the energy gap between the extremes of the Γ_6 and Γ_8 bands) is a function not only of composition and temperature, but also of the thickness.

It is hard to predict *a priori* to what extent the presence

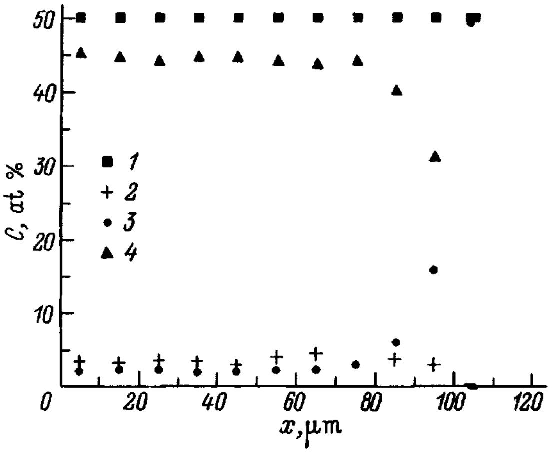

FIG. 1. Distribution of the concentration *C* of the components of the solid solution through the thickness of the structure. The components are *1*—Te, *2*—Mn, *3*—Cd, *4*—Hg; *x* is the distance from the surface.

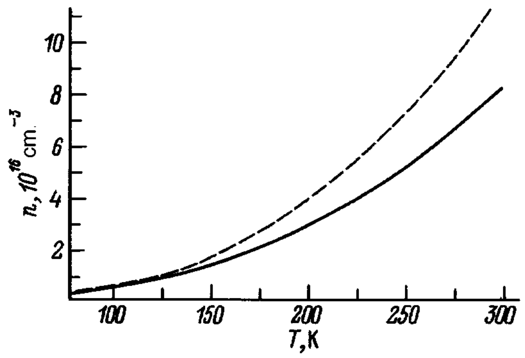

FIG. 2. Temperature dependences of the conduction−electron concentration n in a variable band−gap structure (dashed curve) and in an epitaxial film after removing the substrate along with the variable band−gap layer (solid curve).

of a variable band-gap layer will manifest itself in the transport phenomena at the temperatures that are critical for the use of CMMT-based devices. Therefore, after measuring the annealed structures, the substrate was removed by chemical–dynamic polishing to a film thickness of about 10 μm, in order to eliminate the possible influence of the film–substrate transition layer on the measured quantities. It was found that, in the temperature region $T>70$ K, the temperature dependences of the Hall concentration $n(T)$ differed appreciably in films with a variable band-gap layer and without it (Fig. 2). Similar differences are also observed on the temperature dependences of the Hall mobility $\mu(T)$ (Fig. 3). At lower temperatures, these two dependences virtually coincide.

The observed differences in the $n(T)$ dependences can be qualitatively explained in the following way: At low temperature, the Fermi level is close to the bottom of the conduction band; consequently, the effective addition to the density of the electronic states caused by the presence of a variable band-gap layer is negligible. As temperature increases, the contribution of the variable band-gap part increases because the Fermi level increases and because E_g increases more rapidly in the narrow-band part of the structure.[1] This shows up on the $n(T)$ dependence as an increase of the slope in the intrinsic-conductivity region, reflecting the fact that the density of electronic states in the conduction band of such a variable band-gap structure increases more rapidly than in an ordinary semiconductor.

This assertion can be illustrated by using the self-consistent approach to a combined description of the $n(T)$ and $\mu(T)$ dependences. Even in bulk samples of CMMT, such a problem is nontrivial, which is mainly attributable to difficulties in determining the $E_g(T)$ dependence. As will be shown below, the use for these purposes of the well-known procedure of averaging the available semiempirical dependences for the ternary compositions[2] can produce rather large errors. Therefore, to solve this problem, we have used the approach described in Ref. 3, where the temperature dependence of the energy gap

$$E_g=E_{\Gamma_6}^{k=0}-E_{\Gamma_8}^{k=0}$$

is determined from measurements of $n(T)$ on the given crystal. The resulting dependence is then used to theoretically describe the mobility. It can now be considered as established[3–6] that, when μ is calculated in the range 4 K$\leqslant T \leqslant$300 K for semiconductors of the given class, it is sufficient to take into account three main scattering mechanisms: scattering at ionized impurities and at holes, scattering at the disordering potential, and inelastic scattering at optical phonons. Since the density of electron states in the conduction band has a substantial effect on the efficiency of the indicated mechanisms at each temperature, although in a different way, agreement of the theoretically calculated curve with experiment serves as a good criterion that the $E_g(T)$ values thus obtained are correct.

The details of a mobility calculation carried out by a variational method[4,7] and also a calculation of the main energy parameters are given in Ref. 3. The parameters that were used for the materials and the results of the calculations are given in Table I. In calculating the mobility, we took into account the three-mode character of the phonon spectrum, as well as the temperature dependence of the contribution to the high-frequency part of the permeability from virtual interband transitions over the entire Brillouin zone,[8] $\kappa_{BG}=10.4-10.37y-3x$ for $T<100$ K and $\kappa_{BG}=6.24+0.017(300-T)$ in the range 100 K$\leqslant T \leqslant$300 K, assuming $\kappa_{BG}=10.4-10.37f$ for $\text{Mn}_f\text{Hg}_{1-f}\text{Te}$.[9] The frequencies are $\omega_{\text{LO}}^{(i)} \approx \omega_{\text{LO}}^{(i)}(k_F)$, where k_F is the wave vector of the electrons at the Fermi level. The scattering efficiency at the disordering potential was calculated in terms of the coherent-phase approximation,[5] using the averaging

$$\mu_{\text{dis}}=\text{W}[xyd_1^2+xzd_2^2+yzd_3^2]^{-1},$$

where W is a function that depends on the energy parameters of the crystal;[5] the d_i are the values of the disordering potentials for the ternary solutions CdMnTe $(i=1)$, CdHgTe $(i=2)$ and MnHgTe $(i=3)$; $z=1-x-y$; and μ_{dis} is the electron mobility, limited by the scattering at the disordering potential.

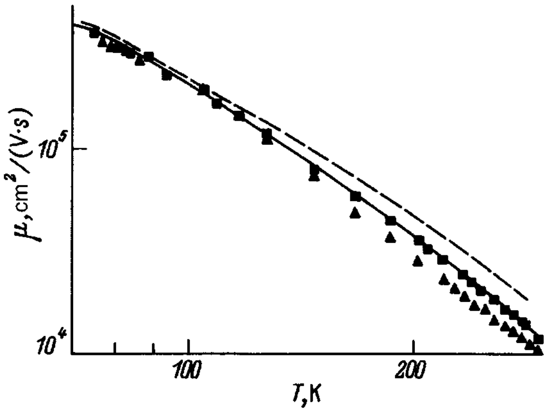

FIG. 3. Temperature dependences of the Hall mobility and the calculated mobility of the conduction electrons, respectively, in a variable band−gap structure (triangles and dashed curve) and in an epitaxial film after the substrate is removed along with the variable band−gap layer (squares and solid curve).

TABLE I. Parameters used for the materials.

Lattice parameter, 10^{-8} cm	$a_0=(6.4605x+6.3300y+6.4820z)$	Refs. 9 and 14
Matrix element of the Kane model, eV·cm	$P=8.1\times10^{-8}$	Ref. 2
Spin-orbit splitting, eV	$\Delta=1.08$	Ref. 4
Luttinger parameters	$\gamma_1=2;\ \gamma_2=\gamma_3=0$	
$\hbar\omega_{TO}^{(i)}$, meV	CdTe: $17.3+1.1(1-x)$,	Ref. 4
	MnTe: 23.1,	Ref. 6
	HgTe: $14.5+1.5x$	Ref. 4
Insulator lattice constants	CdTe: $3.1x$	Ref. 4
	MnTe: $4.5y$	Ref. 15
	HgTe: $4.7(1-x-y)$	Ref. 4
Disordering potential, eV	$d_1=d_3-d_2=1.9$	
	$d_2=1.6$	Ref. 5
	$d_3=3.5$	Ref. 6
Constants of nonpolar deformation potential, eV	$p_0=29.3$	Ref. 4
	$p_1=5$	

Calculational parameters.

Sample without a variable band−gap layer	Variable band−gap structure
$E_g(T)=0.010819+2.41569e-4xT$, eV	$E_g(T)=0.023324+9.187e-5xT$, eV
$N_D=2.53\times10^{15}\text{cm}^{-3}$	$N_D=2.1\times10^{15}\text{cm}^{-3}$
$N_A=1.27\times10^{15}\text{cm}^{-3}$	$N_A=0.9\times10^{15}\text{cm}^{-3}$

As can be seen from Fig. 3, the theory gives a fairly good description of the experiment in a sample without a variable band-gap layer, whereas, a variable band-gap structure reveals a substantial discrepancy, which increases with temperature. Such a discrepancy is a good confirmation of the qualitative remarks made above, since it is observed in a temperature range where scattering at optical phonons is dominant, and this can be correctly calculated only if the $E_g(T)$ dependence is taken into account correctly. Since $E_g(T)$ was calculated in each case using Kane's three-band model, in which the dependence of the band gap on the coordinate is disregarded, it can be asserted that the indicated discrepancy is associated with the effect of the variable band-gap layer on the transport phenomena.

It should be pointed out that, for a variable band-gap structure, it is possible to make the experimental and theoretically calculated mobilities agree in the temperature region $T<70$ K by simply adjusting the total concentrations of ionized donors, N_{D^-}, and acceptors, N_{A^+}. However, the error in determining $E_g(T)$ causes this concentration to be about 25% less than the concentration of ionized impurities calculated for an epitaxial film without a variable band-gap layer.

Figure 4 shows the temperature dependence of the electron mobility in the entire temperature interval studied here for the case in which there is no variable band-gap layer. As

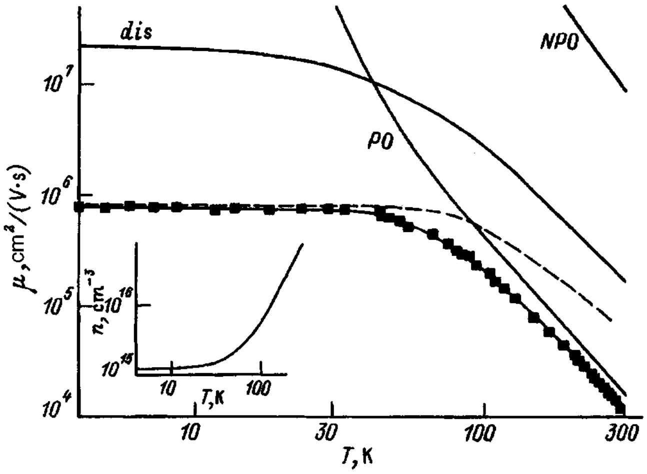

FIG. 4. Experimental (squares) and theoretically calculated (solid curve without symbols) dependences of $\mu(T)$ in a film without a variable band−gap layer. The calculations included scattering at charged impurities and holes (dashed curve), at the disordering potential (dis), and at polar (PO) and nonpolar (NPO) optical phonons. The inset shows the $n(T)$ dependence used in the calculation.

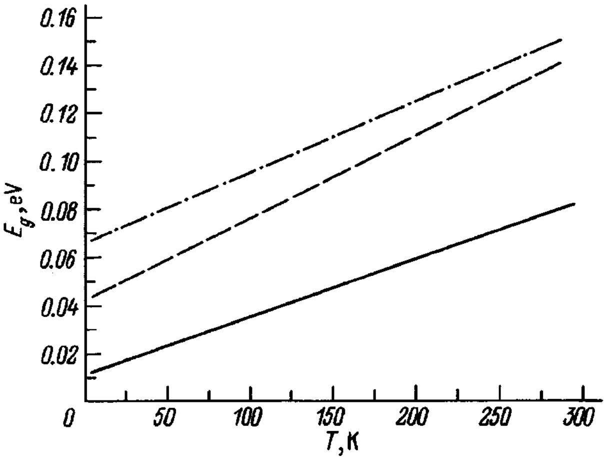

FIG. 5. $E_g(T)$ dependences: the solid curve shows the dependence obtained in this paper; the dot-dashed and dashed lines show the dependences calculated in the virtual-crystal approximation (see text).

was assumed for samples of the given composition, it is sufficient to take into account scattering at charged centers, at the disordering potential, and at polar optical phonons. The agreement of theory and experiment in this case is also evidence that there is no deep resonance acceptor center capable of affecting the observed values. Thus, the approach used here makes it possible not only to describe the set of experimental data, but also to establish the temperature dependence of the parameter E_g.

It can be seen in Fig. 5 that the values of $E_g(x,y,T)$ calculated from different semiempirical dependences in the virtual-crystal approximation are substantially different not only from each other (dashed and dot–dashed straight lines) but also from the dependences that we obtained (solid curve). The dependence indicated in the figure by the dot–dashed line is obtained by using formulas for the extreme ternary compounds, given in Ref. 2. The $E_g(x,y,T)$ values shown by the dashed line are obtained using the data of Ref. 10 for CdHgTe, Ref. 11 for MnHgTe, and Ref. 12 for CdMnTe. Different experimental methods were used to determine the semiempirical dependences of E_g on composition and temperature (for example, see the review articles in Refs. 10 and 13), and the sensitivity of these methods partially depends on the temperature and the parameters of the specific samples. On the other hand, these formulas, as a rule, are not universal with respect to composition. It is therefore not surprising that the averaging of such dependences by the virtual-crystal method can result in significant errors when one attempts to determine $E_g(T)$ in a real semiconductor.

The results of this work lead to the following conclusions:

1) As a result of the diffusion of Cd during the liquid-phase epitaxial growth of $Mn_xHg_{1-x}Te$ films on substrates of type CdTe, four-component $Cd_xMn_yHg_{1-x-y}Te$ epitaxial layers are formed.

2) In the temperature region where intrinsic conductivity predominates, the presence of a variable band-gap layer close to the ⟨epitaxial-film⟩–substrate interface manifests itself in the transport phenomena. This circumstance must be taken into account when calculating the energy parameters of the structure.

3) Even in the absence of a variable band-gap layer, the temperature dependence of the parameter E_g in narrow-band n-$Cd_xMn_yHg_{1-x-y}Te$ semiconductors must be self-consistently determined in each specific case from experimental data, since the averaging of known semiconductor dependences for ternary compounds for these purposes in the framework of the virtual-crystal approximation can result in large errors.

[1] J. M. Pawlikowski and E. Popko, Solid State Commun. **22**, 4231 (1977).

[2] Shojiro Takeyama and Shin−ichiro Narita, J. Phys. Soc. Japan **55**, 1, 274 (1986).

[3] S. M. Komirenko, Semicond. Sci. Techn. **9**, 19 (1994).

[4] J. J. Dubowski, T. Dietl, W. Shymanska, and R. R. Galazka, J. Phys. Chem. Sol. **42**, 351 (1981).

[5] D. S. Montgomery, J. Phys. C **16**, 2923 (1985).

[6] A. G. Wafaa, J. D. Patterson, and S. L. Lehoczky, Infrared Phys. **34**, 311 (1993).

[7] W. Szymanska and T. Dietl, J. Phys. Chem. Solids **39**, 1025 (1978).

[8] M. Grynberg, R. Le Toullec, and M. Balkanski, Phys. Rev. B **9**, 517 (1974).

[9] N. N. Berchenko, V. E. Krevs, and V. G. Sredin, *II-VI Semiconductor Solid Solutions and Their Application* (Voenizdat, Moscow 1982).

[10] M. H. Weiler, Semicond. Semimet. **16**, 119 (1981).

[11] J. Kaniewski, A. Mysielski, Solid State Commun. **41**, 959 (1982).

[12] T. Kendelwicz, Solid State Commun. **36**, 127 (1980).

[13] R. Dornhaus and G. Nimtz, *The Properties and Applications of the CdHgTe Alloy System. Narrow Gap Semiconductors* (Springer, Berlin, 1983).

[14] S. M. Durbin, J. Han, O. Sungki, M. Kobayachi, D. R. Menke, R. L. Gunshor, Q. Fu, N. Pelekanos, A. V. Nurmikko, D. Li, J. Gonsalves, and N. Otsuka, Appl. Phys. Lett. **55**, 2087 (1989).

[15] P. I. Baranskii, O. P. Gorodnichii, and N.V. Shevchenko, Infrared Phys. **30**, 259 (1990).

Translated by W. J. Manthey

Scaling in the regime of the quantum Hall effect and hole localization in *p*-Ge/Ge$_{1-x}$Si$_x$ heterostructures

Yu. G. Arapov, N. A. Gorodilov, V. N. Neverov, G. I. Kharus,
and N. G. Shelushinina

Institute of the Physics of Metals, Ural Branch, Russian Academy of Sciences, 620219 Ekaterinburg, Russia

(Submitted January 29, 1996; accepted for publication April 17, 1996)
Fiz. Tekh. Poluprovodn. **31**, 273–280 (March 1997)

For multilayer Ge/Ge$_{1-x}$Si$_x$ ($x \simeq 0.03$) heterostructures with two-dimensional p-type conductivity over the Ge layers, the temperature and magnetic dependences of the longitudinal resistivity ρ_{xx} and the Hall resistivity ρ_{xy} have been studied in fields up to 12 T in the temperature interval of $T=(0.1–15)$ K. The observed decrease of the amplitude of the ρ_{xx} peaks with decreasing temperature for $T \leqslant 2$ K corresponds to a transition to the scaling regime under the conditions of the quantum Hall effect. Scaling diagrams in the (σ_{xy}, σ_{xx}) coordinates have been constructed for the region of fields and temperatures of interest. It is found that, on the whole, the form of the diagrams corresponds to the theoretical predictions. It is shown that the character of the flux lines on the scaling diagrams is directly connected with such a parameter as the width of a band of delocalized states at the center of the Landau level. *© 1997 American Institute of Physics.* [S1063-7826(97)00403-1]

1. INTRODUCTION

The phenomenon of the integral quantum Hall effect (QHE), detected by Von Klitzing *et al.*,[1] is closely associated with the problem of electron localization in a two-dimensional (2D) system in a quantizing magnetic field B. Laughlin[2] and Halperin[3] showed that, for the QHE to exist, narrow bands of delocalized states must be present close to the middle of each of the Landau subbands (provided that all the other states are localized). On the other hand, for $B=0$, an earlier paper of Abrahams *et al.*[4] used the theory of one-parameter scaling to conclude that quantum diffusion is absent in $2D$ disordered systems; i.e., there are no delocalized states in $2D$ systems in the presence of even a small degree of disorder. The conclusions of Laughlin[2] and Halperin[3] thus contradicted the consequences of the theory of single-parameter scaling of Ref. 4.

To explain the QHE, Pruisken[5–7] and also Khmel'nitskiĭ[8] proposed the hypothesis of two-parameter scaling, which results in the existence of both localized and delocalized states (close to the middle of the Landau subbands) in the spectrum of a disordered $2D$ system in a quantizing magnetic field. The consequences of the theory of two-parameter scaling in the QHE regime were experimentally verified by Wei *et al.*[9] for InGaAs/InP heterostructures, by Kawaji *et al.*[10] for n channels in a silicon MOS transistor, and by Dolgopolov *et al.*[11] for silicon MOS structures and for AlGaAs/GaAs heterostructures.

In this paper we analyze the scaling diagrams for multilayer Ge/Ge$_{1-x}$Si$_x$ heterostructures with p-type conductivity over the germanium layers.

2. THEORY

According to the hypothesis of single-parameter scaling,[4,12] the variation of the conductance (the inverse total resistance) G as the macroscopic size L of the system varies is determined by

$$\frac{d \ln g}{d \ln L}=\beta(g), \qquad (1)$$

where $g=hG/e^2$, and β is a function of the single variable g (a function of the scaling). If the conductance is represented as $g=\sigma L^{d-2}$, where σ is the conductivity in units of e^2/h, and d is the dimension, metallic behavior of the system corresponds to the condition $\sigma=\text{const}$ as $L\rightarrow\infty$. For $2D$ systems, the concepts of conductance and conductivity coincide, and the condition of delocalization of the electronic states corresponds to the condition $\beta(\sigma)=0$.

As shown in Refs. 4 and 12, when $B=0$, the function $\beta(\sigma)$ is always negative for a $2D$ gas, and only when $\sigma\rightarrow\infty$, which corresponds to the absence of disorder, does it asymptotically tend to 0. When $\sigma\gg1$, it is $\beta(\sigma)=-1/2\pi\sigma$. Thus, for an electron in a disordered $2D$ system, no true delocalized states (states with an infinite localization radius x) exist. In the framework of the hypothesis of single-parameter scaling, for dissipative conductivity σ_{xx}, the conclusion that all the states in an infinite $2D$ system are localized is maintained even in a magnetic field; i.e., $\beta(\sigma_{xx})<0$ for all finite values of σ_{xx}.[6,7] In the limit $\sigma_{xx}\gg1$, the scaling function has the form $\beta(\sigma_{xx})=-1/2\pi^2\sigma_{xx}^2$.

Pruisken[5] was the first to express the idea that, in a quantizing magnetic field, it is necessary to consider renormalization for variations of L of both components of the conductivity tensor—the dissipative component σ_{xx} and the Hall component σ_{xy}. The dependence of σ_{xy} on L shows up when one takes into account the closed currents at the boundaries of the sample that unavoidably arise in an external magnetic field (edge currents). As a result, for noninteracting electrons in a chaotic impurity potential, we have the following system of equations of two-parameter scaling:

$$\frac{d\ln\sigma_{xx}}{d\ln L}=\beta_{xx}(\sigma_{xx},\sigma_{xy}), \qquad (1)$$

$$\frac{d\ \ln \sigma_{xy}}{d\ \ln L}=\beta_{xy}(\sigma_{xx},\sigma_{xy}). \tag{2}$$

Each of the scaling functions β_{xx} and β_{xy} is a function of the two parameters σ_{xx} and σ_{xy}; i.e., the variations of σ_{xx} and σ_{xy} are mutually dependent when L is varied. In the weak-localization limit $\sigma_{xx}\gg 1$, Pruisken obtained the specific form of the scaling functions:[6,7]

$$\begin{aligned}\beta_{xx}&=-\frac{1}{2\pi^2\sigma_{xx}^2}-D\exp(-2\pi\sigma_{xx})\cos 2\pi\sigma_{xy},\\ \beta_{xy}&=-D\ \exp(-2\pi\sigma_{xx})\sin 2\pi\sigma_{xy},\end{aligned} \tag{3}$$

where σ_{xx} and σ_{xy} are given in units of e^2/h, and D is a positive constant that contains information on the microscopic behavior of the system (for example, on the character of the chaotic impurity potential).

It is convenient to study the consequences of the scaling equations by considering the motion of the points on the (σ_{xy}, σ_{xx}) plane as L increases (scaling diagrams). It directly follows from Eqs. (2) and (3) that two types of fixed points exist on a phase diagram in (σ_{xy}, σ_{xx}) coordinates. When $\sigma_{xy}=i$, where i is an integer, we have

$$\beta_{xy}=0,\quad \beta_{xx}=-\frac{1}{2\pi^2\sigma_{xx}^2}-D\ \exp(-2\pi\sigma_{xx})<0. \tag{4}$$

Consequently, σ_{xy} does not change as L varies, while $\sigma_{xx}\to 0$ as $L\to\infty$, which indicates that the sample behaves like an insulator. Thus, for an infinite sample, we have a fixed point (i,0) that describes a plateau of the QHE.

When $\sigma_{xy}=i+1/2$, we have

$$\beta_{xy}=0,\quad \beta_{xx}=-\frac{1}{2\pi^2\sigma_{xx}^2}+D\ \exp(-2\pi\sigma_{xx}). \tag{5}$$

It thus follows that σ_{xy}, as in the preceding case, is not renormalized as L varies. It is further assumed[6] that there is a finite value of $\sigma_{xx}=\sigma^*$, which is determined by the condition

$$(\sigma^*)^2\ \exp(-2\pi\sigma^*)=\frac{1}{2\pi^2 D}, \tag{6}$$

for which $\beta_{xx}=0$. In this case, $\beta_{xx}<0$ for $\sigma_{xx}>\sigma^*$ and $\beta_{xx}>0$ for $\sigma_{xx}<\sigma^*$. Then, as $L\to\infty$, we have $\sigma_{xx}\to\sigma^*$ (metallic behavior), and the fixed point ($i+1/2$, σ^*) corresponds to a delocalized state in the center of the Landau subband.

By extrapolating Eq. (3) into the region of the strong localization regime $\sigma_{xx}\ll 1$, Pruisken[6,7] obtained the qualitative form of the scaling diagrams on the (σ_{xy}, σ_{xx}) plane, i.e., the form of the trajectories of the matched transformation of the conductivities σ_{xx} and σ_{xy} as L varies from a value of the order of the magnetic length to $L\to\infty$. These diagrams have been repeatedly reproduced in the literature (see, for example, Refs. 6–9 and 11). In Fig. 1, we show a section of the scaling diagram for one Landau level (the zero level) from Ref. 6. The main features of the scaling diagrams are as follows: The presence of two types of fixed points, as well as the existence of a universal trajectory (a separatrix), along which points on the (σ_{xy}, σ_{xx}) plane ''flow'' from the neighborhood of the point ($i+1/2,\sigma^*$) to the points (i, 0) and ($i+1$, 0) as L increases, were obtained by Khmel'nitskiĭ[8] from the general properties of the symmetry and periodicity of the functions β_{xx} and β_{xy}. The numerical calculations of Ando[13] for a δ-form impurity potential confirm the strong variation of σ_{xy} as L varies (renormalization of σ_{xy}) and the mutual dependence of the renormalization of the quantities σ_{xx} and σ_{xy}.

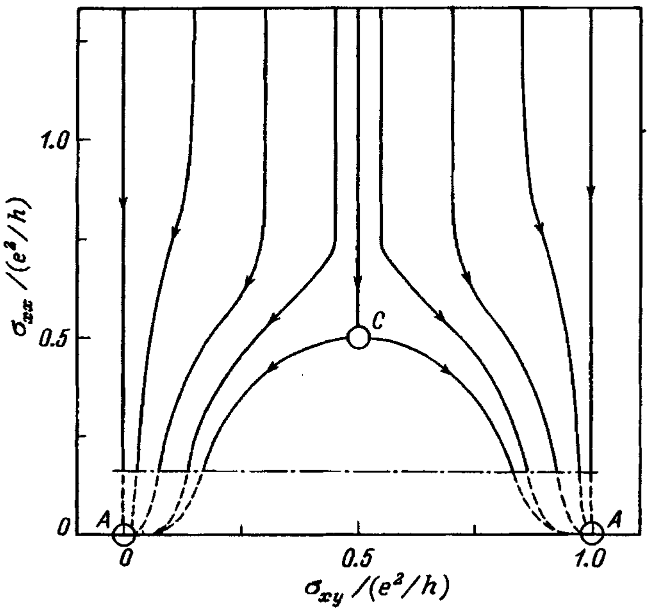

FIG. 1. Integral curves of the system of equations of two−parameter scaling (2) according to the theory of Ref. 6. The arrows indicate the direction of motion of the (σ_{xy}, σ_{xx}) points as L increases. The symbol A marks stable fixed points corresponding to plateaus of the QHE; C is an unstable fixed point, corresponding to a delocalized state at the center of the Landau subband.

Theoretical representations developed for $T=0$ are ordinarily compared with experimental data at finite temperatures using the concept of the Thouless length L_{in}—the path length of an electron from one inelastic collision event to another.[14] The loss of phase coherence of the electron wave function does not occur at this length, and scaling considerations are consequently applicable, with L_{in} playing the role of the effective size of the sample. It is well known that $L_{\text{in}}\sim T^{-p/2}$ at low temperatures. For electron–electron scattering in 2D systems, $p=2$ for pure samples and $p=1$ for samples with impurities when processes with small energy transfer are substantial (the Nyquist mechanism).[15] Since $L_{\text{in}}\to\infty$ as $T\to 0$, under certain conditions the experimental $\sigma_{xx}(T)$ and $\sigma_{xy}(T)$ dependences, as $T\to 0$, can be compared with the $\sigma_{xx}(L)$ and $\sigma_{xy}(L)$ dependences as $L\to\infty$.

3. EXPERIMENTAL RESULTS AND DISCUSSION

We have measured the dependences of the longitudinal resistance ρ_{xx} and the Hall resistance ρ_{xy} on magnetic field B in multilayer, selectively doped Ge/Ge$_{1-x}$Si$_x$ ($x=0.03$) heterostructures with p-type conductivity along the Ge layers. The heterostructures studied here contain from 15 to 30 periods, with Ge and Ge$_{1-x}$Si$_x$ layers (200–230) Å thick. The Ge layers are undoped, but the GeSi layers are doped

TABLE I. Parameters of the samples.

Sample	p, 10^{11} cm^{-2}	μ_p, 10^4 cm^2/(V·s)	B_0, T
1	3.3	1.4	9.5
2	2.4	1.1	6.9
3	2.6	1.5	7.6
4	2.3	1.2	6.6

Note: B_0 is the field at which the ρ_{xx} 0^- peak is observed at $T=0.1$ K.

with boron in such a way that spacers about 50 Å thick remain between the doped part of the solid solution and the germanium layers. The top of the valence band in the Ge layer is located higher in energy than the top of the valence band in the $Ge_{1-x}Si_x$ layer. As a result, holes from the doped part of the solid solution pass into the Ge layers. The growth methods and the properties of the p-Ge/$Ge_{1-x}Si_x$ heterostructures are described in more detail in earlier papers (see Ref. 16 and the bibliography cited there).

Samples in the form of Hall bridges with a size of 0.27 cm×0.05 cm were fabricated for the measurements. The measurements were carried out in a superconducting solenoid in magnetic fields B up to 12 T in a temperature interval $T=(0.1\text{–}15)$ K. The hole concentration p and mobility μ_p at $T=0.1$ K are shown in Table I for the samples studied here. The hole concentration was determined from Hall measurements in a weak magnetic field and from the period of the Shubnikov–de Haas oscillations for large Landau level numbers.

Figure 2 shows the ρ_{xx} (B) and ρ_{xy} (B) dependences at $T=0.1$ K for sample 1 (see Table I). The ρ_{xy} (B) curve shows well-developed quantum plateaus $\rho_{xx}^i=ie^2/h$ with numbers $i=1$, 2, 3 and 5. The absence of a plateau with $i=4$ means that the 1^- and 2^+ levels are not split (they overlap). The first two magnetoresistance peaks (from the side of large fields) 0^- and 1^+ correspond to spin-nondegenerate (with ± directions) Landau levels with numbers $N=0$ and $N=1$. The inset shows the ρ_{xx} (B) and ρ_{xy} (B) dependences in the region of the 0^- peak at other temperatures.

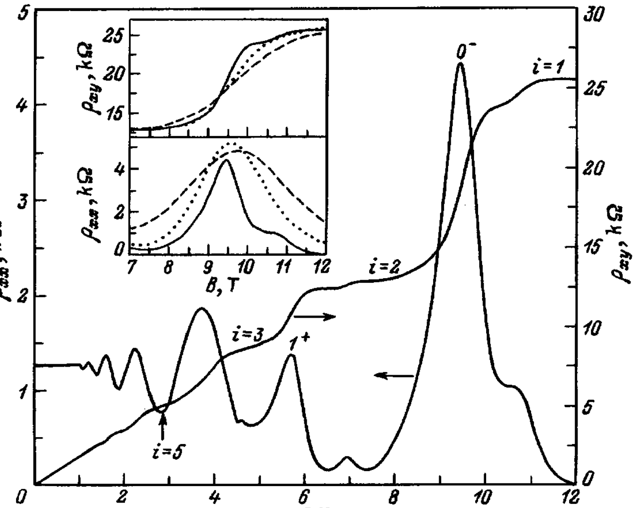

FIG. 2. ρ_{xx} and ρ_{xy} vs magnetic field B for sample 1 (see Table I) at $T=0.1$ K. The inset shows parts of the $\rho_{xx}(B)$ and $\rho_{xy}(B)$ dependences at $T=4.2$ K (dashed curves), $T=1.7$ K (dotted curves), and $T=0.1$ K (solid curves).

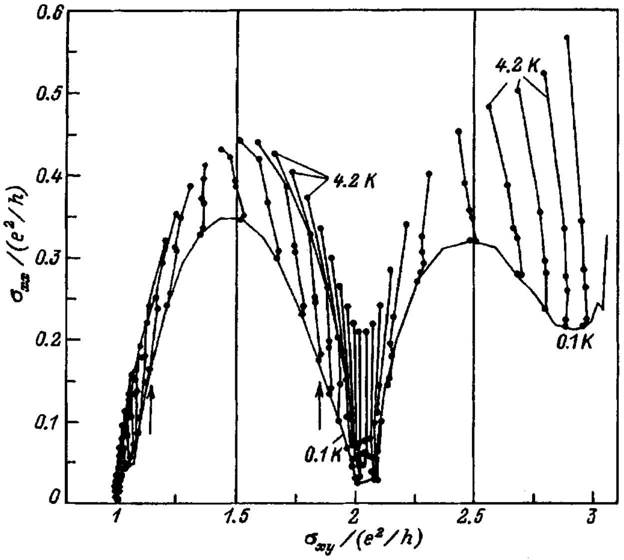

FIG. 3. Scaling diagram in (σ_{xy}, σ_{xx}) coordinates for sample 1. The flux lines are shown for fixed B with a constant step of $\Delta=0.2$ T. The data are for $T=0.1$, 0.36, 0.9, 1.1, 1.7 and 4.2 K. The arrows show the boundaries of the band of delocalized states for the 0^- peak when $T=0.1$ K.

The scaling diagram in the (σ_{xy}, σ_{xx}) coordinates for the same sample is shown in Fig. 3. The data are given for the interval $1 \leqslant \sigma_{xy} \leqslant 3$ (in units of e^2/h), which corresponds to the filling of the Landau sublevels 0^- ($1 \leqslant \sigma_{xy} \leqslant 2$) and 1^+ ($2 \leqslant \sigma_{xy} \leqslant 3$). The points corresponding to a fixed magnetic field (or to a degree of filling of $r=p/n_B$, where $n_B=eB/hc$) for six different temperatures in the interval (0.1–4.2) K are combined so as to form a set of broken lines (flux lines). The envelope curve is also shown for a temperature of 0.1 K.

Figure 4 shows the ρ_{xx} and ρ_{xy} dependences on magnetic field B for sample 2, which has a lower hole concentration than sample 1. QHE plateaus with numbers $i=1$, 2, and 4 are seen on the $\rho_{xy}(B)$ curve for this sample. No spin splitting of the Landau levels with $N=1$ (and, consequently, of the QHE plateau with $i=3$) is observed all the way to the lowest temperatures. As shown in Ref. 17, the qualitative difference of the pattern of quantum oscillations for small Landau-level numbers in Ge/$Ge_{1-x}Si_x$ samples with different hole concentrations p is caused by the presence (for comparatively large p) or the absence (for small p) of filling of the second quantum-well subband. Figure 5 shows the scaling diagram for sample 2 only for the spin-nondegenerate Landau level 0^- ($1 \leqslant \sigma_{xy} \leqslant 2$).

It can be seen from Figs. 3 and 5 that, for the samples studied here, the motion of the points on the (σ_{xy}, σ_{xx}) plane as temperature decreases corresponds, on the whole, to the predictions of the theory of two-parameter scaling: the flux lines tend to the fixed points (1, 0), (2, 0) and (3, 0). The formation of a quantum plateau with $i=3$ [point (3, 0)] as the temperature is lowered is clearly seen in sample 1.

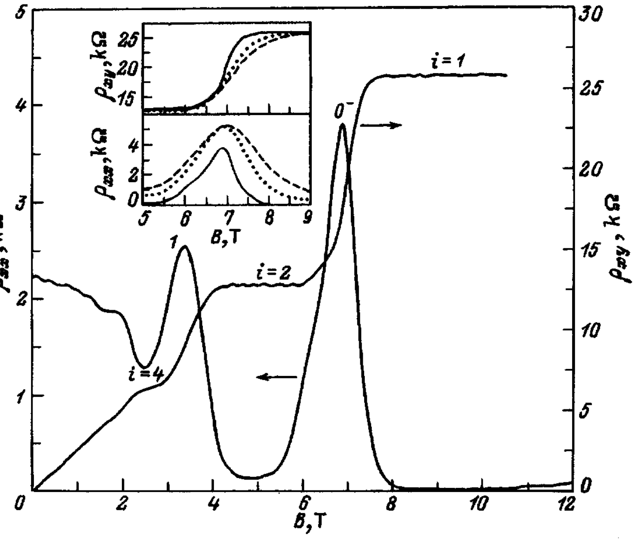

FIG. 4. ρ_{xx} and ρ_{xy} vs magnetic field B for sample 2 at $T=0.09$ K. The inset shows sections of the $\rho_{xx}(B)$ and $\rho_{xy}(B)$ dependences at $T=4.2$ K (dashed curves), $T=2.0$ K (dotted curves), and $T=0.09$ K (solid curves).

A certain asymmetry of the envelope of the curve relative to the line $\sigma_{xy}=1.5$ is seen in Fig. 3 for sample 1. For sample 2, the asymmetry of the envelope for the 0^- peak is much more pronounced (Fig. 5). Asymmetry of this sort is associated with partial overlap of adjacent Landau levels and is caused by a shift of the position of a delocalized state relative to the center of the Landau level because of mixing of the states of overlying or underlying levels toward states of the given level.[18] According to Ref. 13, the degree of asymmetry is determined by the parameter $\hbar\omega_c/\Gamma$, where ω_c is the cyclotron frequency, and Γ is the width of the Landau level caused by interaction with impurities. By using the formula for the width Γ in the case of a short-range impurity potential,

$$\Gamma=\sqrt{\frac{2}{\pi}\hbar\omega_c\frac{\hbar}{\tau}}, \tag{7}$$

where τ is the relaxation time of the pulse, we find

$$\frac{\hbar\omega_c}{\Gamma}=\sqrt{\frac{\pi\mu_p B}{2c}}, \tag{8}$$

where $\mu_p B/c=\omega_c\tau$. Estimates show that, for the 0^- peak, the parameter $\hbar\omega_c/\Gamma=4.5$ in sample 1 and $\hbar\omega_c/\Gamma=3.3$ in sample 2. Thus, smaller values of the parameter $\hbar\omega_c/\Gamma$ increase the asymmetry of the scaling diagrams.

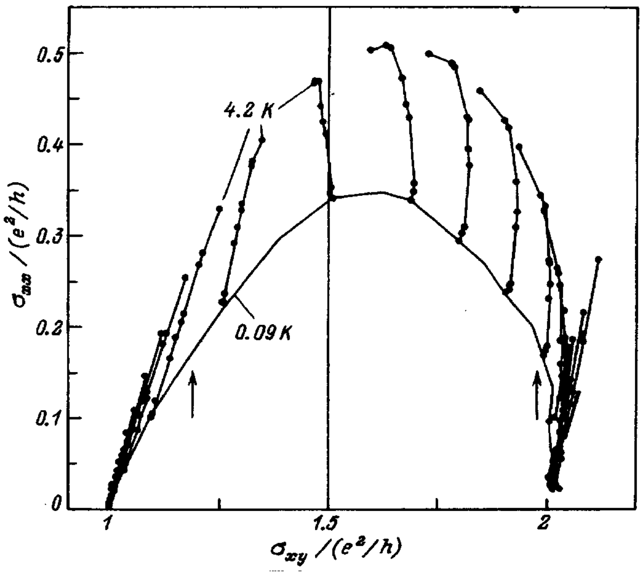

FIG. 5. Scaling diagram in $(\sigma_{xy},\sigma_{xx})$ coordinates for sample 2. The flux lines are shown for fixed B values with constant step $\Delta=0.2$ T. Data for $T=0.09$, 0.13, 0.17, 0.27, 0.37, 0.85, 1.15, 1.4, 2.0, 2.2 and 4.2 K are used. The arrows indicate the boundary of the band of delocalized states at $T=0.09$ K.

It can be seen from the graphs in Figs. 3 and 5 that, at $T=0.1$ K, the 0^- peak of σ_{xx} in sample 1 shifts in the direction of smaller σ_{xy} relative to the point $\sigma_{xy}=1.5$, whereas, in sample 2, it shifts toward larger σ_{xy}. This difference is caused by the nonlinear dependence on B, and hence by the inequivalence of the Landau levels for holes in the 2D structures studied here, in agreement with the numerical calculation of the energy spectrum in a quantizing magnetic field.[17]

The maximum (peak) value of $\sigma_{xx}(B)$ is reached when the Fermi level coincides with the energy E_c of the delocalized states at the center of the Landau subband. The equation $E_F=E_c$ corresponds to half-integral values of the degree of filling $r=i+1/2$ (and also to half-integral values of σ_{xy}). Let us consider the temperature dependence of σ_{xx} in the neighborhood of the fixed point $(i+1/2,\sigma^*)$, corresponding to a delocalized state (point C in Fig. 1). When $T=0$ in an infinite sample, all the states of the Landau subband other than states with $E=E_c$ are localized. As $E\rightarrow E_c$, the localization radius ξ approaches infinity according to the law[19]

$$\xi(E)\sim|E-E_c|^{-\nu}, \tag{9a}$$

where $\nu>0$ is the critical index. For the short-range impurity potential, the estimate[20]

$$\xi(E)\cong\lambda\left(\frac{\Gamma}{|E-E_c|}\right)^{\nu} \tag{9b}$$

is valid, where $\lambda=(c\hbar/eB)^{1/2}$ is the magnetic length. According to theory (Ref. 21 and the bibliography cited there) and the experimental results of Ref. 22, $\nu=2.3$ for the lower Landau level. It is clear that, in a sample of finite size L, states with $\xi>L$ can be regarded as delocalized. At finite temperatures, the role of the size of the sample is played by the Thouless length L_{in}. Therefore, at $T\neq 0$, we see a band of delocalized states $|E-E_c|\leqslant\gamma$, whose width γ is determined by

$$\xi_\gamma=L_{\text{in}}, \tag{10}$$

where $\xi_\gamma\equiv\xi(E_c\pm\gamma)$. Since $L_{\text{in}}(T)\sim T^{-p/2}$, we have from Eqs. (9b) and (10) that $\gamma\sim T^{\varkappa}$, where $\varkappa=p/2\nu$. The experimental value of this parameter for the lower Landau level is[23] $\varkappa=0.4$.

To analyze the temperature dependence of the conductivity, it is convenient to start from[19,24]

$$\sigma_{xx}(T)=-\int dE\,\frac{\partial f(E-E_F)}{\partial E}\,\sigma(E), \tag{11}$$

where $f(E-E_c)$ is the Fermi–Dirac distribution function, and $\sigma(E)$ is the partial contribution to the dissipative conductivity of the states with energy E. Since only delocalized states in the energy interval $|E-E_c|\leqslant\gamma$ contribute to the conductivity, we can write the partial conductivity as

$$\sigma(E)=\sigma_c\frac{\gamma^2}{(E-E_c)^3+\gamma^2}. \tag{12}$$

When $E_F=E_c$, we find from Eqs. (11) and (12) that

$$\sigma_{xx}(T)=\frac{\pi}{4}\sigma_c\frac{\gamma}{kT}\ (kT>\gamma),$$

$$\sigma_{xx}(T)=\sigma_c(kT<\gamma).$$

The quantity $\sigma_c\equiv\sigma(E_c)$ in Eqs. (12) and (13) at zero temperature depends only on the linear size L of a 2D system. This dependence is determined by the system of equations of two-parameter scaling, [Eqs. (2)], which for $\sigma_{xy}=i+1/2$ reduces to two independent equations. We introduce the symbol σ^* for the zero of the function $\beta_{xx}(i+1/2,\sigma^*)=0$, and we expand β_{xx} close to the point $\sigma_c=\sigma^*$. We then obtain the following expression from Eq. (5):

$$\frac{d\ln\sigma_c}{d\ln L}=-\eta(\sigma_c-\sigma^*), \tag{14}$$

where $\eta>0$. Integrating Eq. (14), we find

$$\sigma_c-\sigma^*\sim L^{-\eta}. \tag{15}$$

It is clear from Eq. (15) that η is the scale dimension of the longitudinal conductance close to the fixed critical point $(i+1/2,\sigma^*)$.[25] When $T\neq 0$, replacing L with L_{in} and using the dependence $L_{\text{in}}\sim T^{-p/2}$, we find

$$\sigma_c-\sigma^*\sim T^{p\eta/2}. \tag{16}$$

Two regions can therefore be distinguished in the temperature dependence of the peak amplitude of $\sigma_{xx}(T)$. In low-temperature regions $kT\ll\gamma$ we realize the scaling regime, in which the temperature dependence $\sigma_{xx}(T)$ is completely determined by the Thouless length L_{in}, and σ_{xx} increases with temperature according to Eq. (16). The limiting value of σ^* corresponds to $T=0$ in an infinite sample. When $kT>\gamma$, the scaling dependence of Eq. (16) does not hold, and, according to Eq. (13), the relationship of the width of the interval of delocalized states $\gamma\sim T^{\varkappa}$ and the thermal smearing of the Fermi step kT becomes the main factor. Since the parameter $\varkappa$ is ~0.4, σ_{xx} decreases with temperature. The maximum $\sigma_{xx}(T)$ is reached at $kT\cong\gamma$.

Let us examine the experimental results. Figure 6 shows the $\sigma_{xx}(T)$ dependence for three samples. Curves *1* and *2* relate to the magnetoresistance peaks 0^- ($\sigma_{xy}=3/2$) and 1^+ ($\sigma_{xy}=5/2$) in sample 1, and curves *3* and *4* relate to peak 0^- ($\sigma_{xy}=3/2$) in samples 3 and 4. It can be seen that, in the samples studied here, the transition to the scaling regime of Eq. (16), in which the amplitude of the peaks begins to decrease with decreasing temperature, occurs at $T\cong 2$ K. As $T\rightarrow 0$, the $\sigma_{xx}(T)$ dependence is close to linear, which corresponds to a value of $\eta p/2\cong 1$ in Eq. (16). If it is assumed that the main mechanism at low temperatures is the Nyquist mechanism for the loss of phase coherence,[15] using $p=1$, we find $\eta\cong 2$. Extrapolating the $\sigma_{xx}(T)$ dependences to $T=0$, we found the limiting values of $\sigma^*\cong 0.33$ and $\sigma^*\cong 0.30$ for the 0^- and 1^+ peaks in sample 1 and $\sigma^*\cong 0.23$ in samples 3 and 4 (Fig. 6). A theoretical calculation in the model of the short−range impurity potential gives a value of $\sigma^*=0.5$ for the lowest Landau level (see, for example, Ref. 26 and the bibliography cited there).

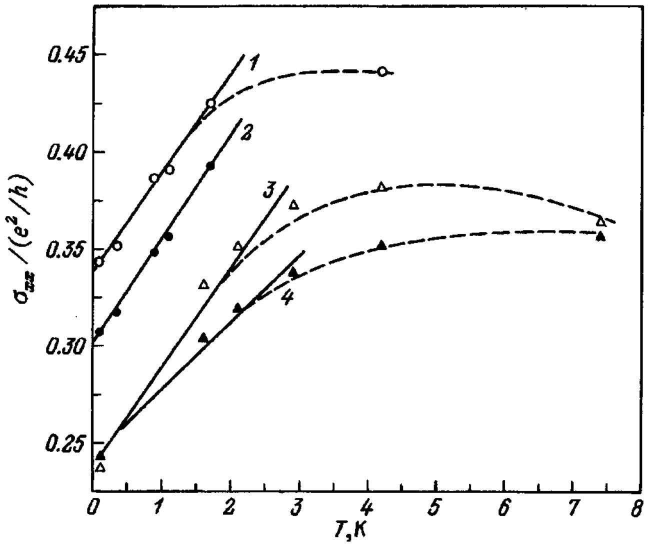

FIG. 6. Temperature dependence of the peak value of σ_{xx} for the Landau levels 0^- (*1*) and 1^+ (*2*) in sample 1, and also for the 0^- peaks in sample 3 (*3*) and 0^- in sample 4 (*4*).

Let us estimate the parameters that characterize the localization-delocalization effects in the samples studied here. Let ΔB be the magnetic−field interval corresponding to the region of a QHE plateau on the $\rho_{xy}(B)$ dependence and δB be the field interval corresponding to the transition region between adjacent plateaus. It is easy to show that the ratio of the quantities δB and ΔB, within a factor of the order of unity, equals the ratio of the width of the band of delocalized states and the total width of the Landau subband: $\delta B/\Delta B\cong\gamma/\Gamma$. In the samples studied here, at the lowest temperature $T\sim 0.1$ K, the fraction of delocalized states for the 0^- peak is about 10% ($\gamma/\Gamma=0.1$ for sample 1, and $\gamma/\Gamma=0.12$ for sample 2).

According to Eq. (9b), the localization radius at the boundary of the band of delocalized states ($E=E_c\pm\gamma$) is determined by

$$\xi_\gamma\cong\lambda\left(\frac{\Gamma}{\gamma}\right)^{2.3}. \tag{17}$$

In the samples studied here, $\lambda\cong 100$ Å and $\xi_\gamma\cong 10^{-4}$ cm for the 0^- peak. According to Eq. (10), this also gives an estimate of the inelastic scattering length at $T=0.1$ K. Thus, at the lowest temperature of the measurements, L_{in} remains much less than the geometrical size of the sample (5×10^{-2} cm).

As the temperature is lowered, the quantum plateaus on the $\rho_{xy}(B)$ dependence become increasingly wider, while the transitions between them become increasingly sharper, in accordance with the decrease of the parameter γ. On the scaling diagram, this process is expressed by the fact that, as T decreases (and L increases), the density of the points on the $(\sigma_{xy}, \sigma_{xx})$ plane close to fixed points of the type of A (Fig. 1) increases, while, close to fixed point C, it decreases. As $T \to 0$ $(L \to \infty)$, all the $(\sigma_{xy}, \sigma_{xx})$ points, except the one in the region of the maximum of σ_{xx}, should cluster around the points $(i, 0)$ corresponding to the QHE plateaus. As noted above, on the scaling diagrams for the samples studied here, a tendency is actually seen for the experimental points to cluster close to the points (1, 0), (2, 0) or (3, 0) as T decreases. However, by comparison with the theoretical diagram of Fig. 1, this tendency is far less clearly expressed in the middle part of each of the diagrams (in the neighborhood of $\sigma_{xy} = 1.5$ or 2.5). This difference of the real and ideal scaling diagrams is undoubtedly caused by the existence at $T \neq 0$ of a band of delocalized states of finite width γ. The point $\sigma_{xy} = 1.5$ in Fig. 3 corresponds to the field $B_0 = 9.5$ T (see Fig. 2). We can estimate the interval of magnetic fields corresponding to the band of delocalized states from the half-width of the 0^- peak of ρ_{xx}: $\delta B \cong 0.5$ T. On the diagram (Fig. 3), the boundaries thus determined for the band of delocalized states are indicated by arrows. It can be seen that the band of delocalized states on the scaling diagram corresponds to a wide interval $\delta\sigma_{xy}$. This property of scaling diagrams is virtually independent of temperature: as the temperature decreases, the absolute value of the half-width δB decreases and the transition region of the variation of σ_{xy} between adjacent plateaus narrows, but the interval $\delta\sigma_{xy}$ remains nearly constant, which is attributable to the quantization of the Hall conductivity. It can be seen from the diagram that the existence of states with nonzero σ_{xx} values as $T \to 0$ leads to a pattern of almost parallel vertical flux lines in the interval $\delta\sigma_{xy}$. The density of flux lines, shown with a fixed step Δ in magnetic field, is very close to the half-integer values of σ_{xy} and sharply increases in the neighborhood of the boundary points $\sigma_{xy} = 1, 2, \ldots$. Note that a similar pattern of flux lines was observed all the way to 80 mK on perfect InGaAs/InP heterostructures, where the scaling regime was attained at $T < 4.2$ K.[9]

4. CONCLUSIONS

The study of scaling diagrams in $(\sigma_{xy}, \sigma_{xx})$ coordinates for multilayer $p-\mathrm{Ge/Ge}_{1-x}\mathrm{Si}_x$ heterostructures confirms the main conclusion of the theory of two−parameter scaling: the presence of self−consistent variation of σ_{xx} and σ_{xy} as $L \to \infty$ $(T \to 0)$. A consideration of the motion of the points on the $(\sigma_{xy}, \sigma_{xx})$ plane makes it possible to distinctly observe fixed points corresponding to the plateaus of the QHE. An image of the plot of the dependence of σ_{xx} on σ_{xy} is an extremely sensitive method for studying the formation of the QHE plateaus as the external conditions change.[27]

For $T \leqslant 2$ K, we observed a decrease in the amplitude of the σ_{xx} (ρ_{xx}) peaks 0^{-1} and 1^+ as the temperature was lowered, which corresponds to a transition to the scaling regime. For the samples studied here, the dependence of the peak value of σ_{xx} on T in this temperature region was close to linear, and the σ_{xx} value, as $T \to 0$, tended to a finite limiting value $\sigma^* \cong 0.3e^2/h$. The finite conductivity within a band of delocalized states of appreciable width of $\gamma \sim 0.1\Gamma$ even at the lowest temperature $T \cong 0.1$ K does not allow us to decide between the presence or absence of the separatrix whose existence is predicted by certain versions of scaling theory.[8]

This work was supported by the Russian Fund for Fundamental Research, Projects No. 94-02-05769a and 95-02-04891 and the Russian program on the ''Physics and Technology of Nanostructures,'' Project No. 1-065/3.

[1] K. Von Klitzing, G. Dorda, and M. Pepper, Phys. Rev. Lett. **45**, 494 (1980).
[2] R. B. Laughlin, Phys. Rev. B **23**, 5632 (1981).
[3] B. I. Halperin. Phys. Rev. B **25**, 2185 (1982).
[4] E. Abrahams, P. W. Anderson, D.C. Licciardello, and T. V. Ramakrishnan, Phys. Rev. Lett. **42**, 673 (1979).
[5] A. M. M. Pruisken, Nucl. Phys. B **235** [FS 11], 277 (1984).
[6] A. M. M. Pruisken, Phys. Rev. B **32**, 2636 (1985).
[7] A. Pruisken, in *The Quantum Hall Effect*, edited by R. Prendzha and S. Girvina (Mir, Moscow, 1989), p. 127.
[8] D. E. Khmel′nitskiĭ, JETP Lett. **38**, 552 (1983).
[9] H. P. Wei, D. C. Tsui, and A. M. M. Pruisken, Phys. Rev. B **33**, 1488 (1985); H.P. Wei, D.C. Tsui, and A. M. M. Pruisken, in *High Magnetic Fields in Semiconductor Physics*, edited by G. Landwehr (Springer, Berlin, 1987), p. 11.
[10] S. Kawaji and J. Wakabayashi, J. Phys. Soc. Jpn. **56**, 21 (1987); M. Yamane, J. Wakabayashi, and S. Kawaji, J. Phys. Soc. Jpn. **58**, 1899 (1989).
[11] V. T. Dolgopolov, A. A. Shashkin, B. K. Medvedev, and V. G. Mokerov, Zh. Eksp. Teor. Fiz. **99**, 201 (1991) [JETP **72**, 113 (1991)].
[12] P. A. Lee and T. V. Ramakrishnan, Rev. Mod. Phys. **57**, 287 (1985).
[13] T. Ando, Surface Science **170**, 243 (1986); J. Phys. Soc. Jpn. **55**, 3199 (1986).
[14] D. J. Thouless, Phys. Rev. Lett. **39**, 1167 (1977).
[15] E. Abrahams, P. W. Anderson, P. A. Lee, and T. V. Ramakrishnan, Phys. Rev. B **24**, 6738 (1981); B. L. Altshuler, A. G. Aronov, and D. E. Khmelnitsky, J. Phys. C **15**, 7367 (1982).
[16] B. F. Aronzon, N. K. Chumakov, J. Leotin, J. Galibert, L. Essaleh, A. L. Chernov, O. A. Kuznetsov, L. K. Orlov, R. A. Rubtsova, and O. A. Mironov, Superlat. Microstr. **13**, 159 (1993).
[17] Yu. G. Arapov, N. A. Gorodilov, V. N. Neverov, M. V. Yakunin, A. V. Germanenko, G. M. Min′kov, O. A. Kuznetsov, R. A. Rubtsova, A. L. Chernov, and L. K. Orlov, JETP Lett. **59**, 268 (1994).
[18] A. Cheng, in *The Quantum Hall Effect*, edited by R. Prendzha and S. Girvina (Mir, Moscow, 1989), p. 180.
[19] S. Das Sarma and D. Liu, Phys. Rev. B **48**, 9166 (1993−II).
[20] D. G. Polyakov and B. I. Shklovskii, Phys. Rev. Lett. **73**, 1150 (1994).
[21] D. Liu and S. Das Sarma, Phys. Rev. B **49**, 2677 (1994−II).
[22] S. Koch, R. J. Haug, K. von Klitzing, and K. Ploog, Phys. Rev. B **46**, 1596 (1992).
[23] H. P. Wei, D. C. Tsui, M. A. Paalanen, and A. M. M. Pruisken, Phys. Rev. Lett. **61**, 1294 (1988).
[24] Y. Katayama, D. C. Tsui, and M. Shayegan, Phys. Rev. B, **49**, 7400 (1991−I).
[25] A. M. M. Pruisken, Phys. Rev. Lett., **61**, 1297 (1988.)
[26] Y. Huo, R. E. Hentzel, and R. N. Bhatt, Phys. Rev. Lett. **70**, 481 (1993).
[27] Yu. G. Arapov, N. A. Gorodilov, V. N. Neverov, G. I. Kharus, N. G. Shelushinina, O. A. Kuznetsov, L. K. Orlov, R. A. Rubtsova, and A. L. Chernov, JETP Lett. **59**, 245 (1994).

Translated by W. J. Manthey

Defects in intrinsic and pseudodoped amorphous hydrated silicon

O. A. Golikova

A. F. Ioffe Physicotechnical Institute, Russian Academy of Sciences, 194021 St. Petersburg, Russia

(Submitted April 12, 1996; accepted for publication April 24, 1996)
Fiz. Tekh. Poluprovodn. **31**, 281–284 (March 1997)

The data on the dark conductivity and photoconductivity of a-Si:H films obtained by various methods in the soft-deposition regime are presented. It is shown that, regardless of the substrate temperature, the material obtained in this regime is intrinsic. Deviation from the soft-deposition regime results in the growth of pseudodoped a-Si:H, with an increased density of defects (dangling Si–Si bonds) and with inhomogeneous structure. The defects in intrinsic and pseudodoped a-Si:H are found, respectively, in D^0 and D^+ states. *© 1997 American Institute of Physics.* [S1063-7826(97)00503-6]

1. INTRODUCTION

The conditions for obtaining intrinsic amorphous hydration of silicon (a-Si:H) in a standard diode reactor ($f=13.56$ MHz) using undiluted silane (SiH_4) are well known: The optimal temperatures for depositing the films are $T_s=230-250\,°C$, and the deposition rates are $r=1-2$ Å/sec. Intrinsic a-Si:H has the following parameters at room temperature: a dark conductivity of $\sigma_d=10^{-11}-10^{-10}\ \Omega^{-1}\cdot\text{cm}^{-1}$, a photoconductivity (AMI) of $\sigma_{\text{ph}}=10^{-5}-10^{-4}\ \Omega^{-1}\cdot\text{cm}^{-1}$, and a defect density, determined by the constant photocurrent method (CPM), of $N_D=(5-10)\times10^{15}\ \text{cm}^{-3}$. Here the activation energy σ_d is close to $\Delta E=\varepsilon_c-\varepsilon_F|_{T=0}=0.85$ eV (ε_c is the conduction band edge, and ε_F is the Fermi level). This ΔE value corresponds to $(\varepsilon_c-\varepsilon_F)_{300\,\text{K}}=kT\ \ln\sigma_0/\sigma_d=0.72$ eV ($T=300$ K, $\sigma_0=150\ \Omega^{-1}\cdot\text{cm}^{-1}$).

Increasing T_s to 400 °C or decreasing it to 100 °C, as is well known, increases the defect density.[1,2] In this case, ε_F shifts, respectively, toward ε_c or ε_v (the valence band edge); i.e., a pseudodoping effect is observed.[3]

On the other hand, the pseudodoping effect opens up possibilities of controlling the position of the Fermi level in the mobility gap of a-Si:H not only by introducing electrically active impurities, but also without introducing them: entirely by creating defects in the film-deposition process. It is evident that the defects in the second case formally play the role of a dopant. In this connection, the question arises of the nature of the defects in intrinsic and pseudodoped a-Si:H. The experimental results presented in this paper, in our opinion, should help to answer this question.

2. EXPERIMENTAL RESULTS

We indicated above the conditions for obtaining intrinsic a-Si:H, a deviation from which makes the material only pseudodoped. However, Golikova *et al.*[4] were the first to show that this depends on the type of reactor: the pseudodoping effect can be avoided if the film is deposited in a triode reactor ($f=13.56$ MHz) when the anode–grid distance is optimized and when the cathode and grid have the same potential. In this case, since the substrate is at the cathode, the discharge region is spatially remote from the growing film. This means, first, that only long-lived SiH_3 radicals that have high mobility at the film surface participate in the film growth.[5] Second, the intensity with which the surface of the growing film is bombarded by the charged particles of the plasma is minimized. The so-called soft-deposition regime is thereby implemented: with no increase of the defect density with increasing T_s.

Many other methods were subsequently developed that provided a ''soft'' regime for depositing a-Si:H films: a remote silane–hydrogen plasma,[1,6] catalytic breakdown of SiH_4 at a hot tungsten filament,[7,8] and high-frequency (70 MHz) breakdown of SiH_4 in a diode reactor.[9] It was recently shown that the method of SiH_4 breakdown in a chamber for magnetron sputtering in a constant electric field also makes it possible to provide a soft-deposition regime.[10] Figure 1 shows rather good agreement of the data on a-Si:H films deposited by the indicated methods: regardless of T_s, the material is intrinsic. At the same time, Fig. 1 illustrates the result of pseudodoping for films deposited in a standard diode reactor.[11]

Let us consider how the (CPM) defect density correlates with the position of the Fermi level $(\varepsilon_c-\varepsilon_F)_{300\,\text{K}}$ of pseudodoped a-Si:H. Figure 1 shows our data for films deposited in a triode reactor at constant temperature $T_s=300\,°C$, but with varying V and P, where $V=0-200$ V is the cathode–grid bias, and $P=50-120$ mT is the pressure of SiH_4 in the chamber. In addition, Fig. 2 shows data for a-Si:H films obtained at a number of European scientific centers: Philips University, Marburg (FRG); the Polytechnic School, Palaiseau (France); BARI (Italy); and PATRAS (Greece).[12] The deposition conditions of these films were different (reactor type, temperature, composition of gas mixture, etc.), but the resulting data are in good agreement with each other, regardless of this circumstance. We should also point out the agreement with the data obtained for films deposited in the Electrotechnical Laboratory, Tsukuba (Japan).[13] We therefore conclude that the correlation between $\varepsilon_c-\varepsilon_F$ and N_D shown in Fig. 2 is universal.

Based on the above discussion, we shall next consider the Fermi level (ε_F) and also the photoconductivity (σ_{ph}) of pseudodoped a-Si:H as a function of the defect density N_D in the same way as is done for doped a-Si:H, where N_D equals $N_{\text{P,B}}$, the atomic density of introduced impurities of phosphorus or boron (Figs. 3 and 4). It can be seen that ε_F

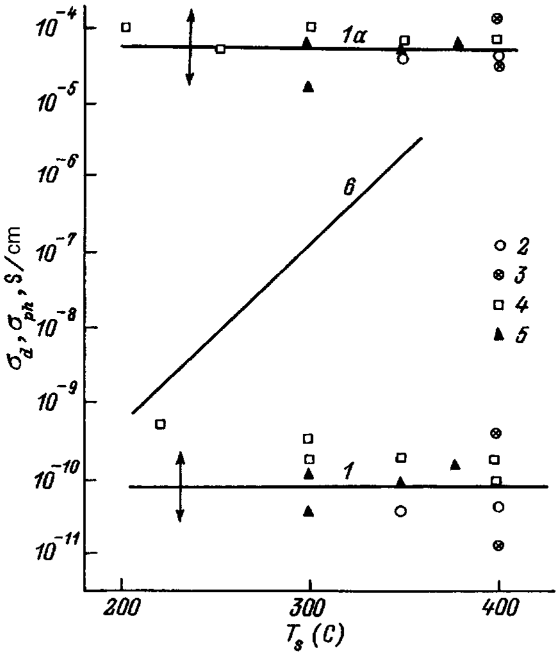

FIG. 1. Dark conductivity and photoconductivity (AMI), measured at room temperature for undoped a-Si:H films obtained by various methods, vs deposition temperature: in a triode reactor (*1* and *1a*; the arrows show the scatter of the experimental data), by the remote-plasma method (*2*), by catalytic breakdown at a hot filament (*3*) and in a high-frequency (70 MHz) diode reactor (*4*), and by the SiH_4-breakdown method in a chamber for magnetron sputtering in a constant electric field (*5*). The dark conductivity of a-Si:H films deposited in a standard diode reactor is shown by curve (*6*).

and σ_{ph} are not one-to-one functions of N_D; i.e., the same value of N_D corresponds to two states of pseudodoped a-Si:H that differ in the position of the Fermi level and the value of the photoconductivity. We should point out that, for $N_D = \text{const}$, the differences between ε_F and σ_{ph} increase with increasing value of N_D. Note also that the maximum values of N_D in pseudodoped a-Si:H films do not exceed 10^{17} cm^{-3}.

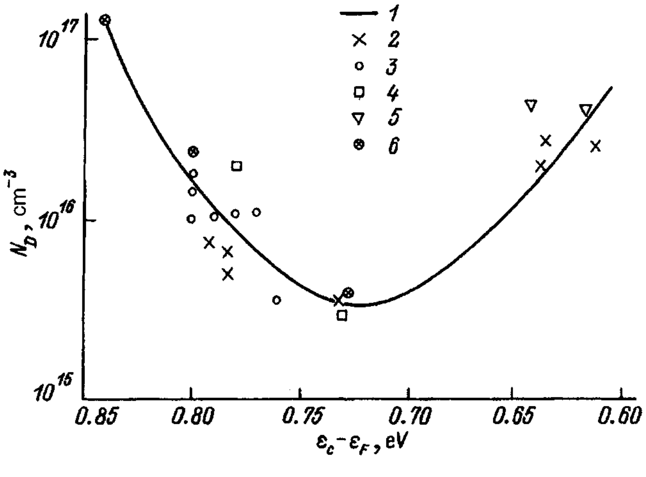

FIG. 2. Correlation between the defect density in undoped a-Si:H and the position of the Fermi level in the mobility gap. The films were obtained at A. F. Ioffe Physicotechnical Institute (*1*), Philips University (*2*), The Polytechnic School (*3*), BARI (*4*), and PATRAS (*5*). The measurements for (*2–5*) were made at Philips University. *6*—data for films obtained at the Electrotechnical Laboratory.

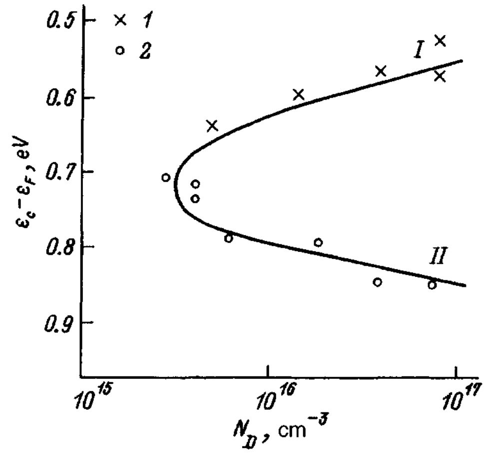

FIG. 3. The Fermi level as a function of defect density. The solid curve is for pseudodoped a-Si:H. Points *1* and *2* are for a-Si:H doped with phosphorus and boron, respectively. *I* and *II* denote the two different branches of the curve.

3. DISCUSSION

Let us consider the curve of $\varepsilon_c - \varepsilon_F = f(N_D)$ shown in Fig. 3. Samples belonging to branches I and II of this curve are, respectively, analogs of samples doped with phosphorus and boron. In this case, the limiting values of $\varepsilon_c - \varepsilon_F$ in each of the branches correspond to the densities of phosphorus or boron atoms $N_{P,B} \simeq 10^{17}$ cm^{-3} (for doping from the gas phase);[14] i.e., $N_{P,B}$ corresponds in order of magnitude to the maximum defect density in pseudodoped a-Si:H. Note that the points belonging to doped samples lie on the curve shown in Fig. 3.

It follows from a consideration of the $\sigma_{ph} = f(N_D)$ curve (Fig. 4) that the defects in the samples of pseudodoped a-Si:H belonging to branches I and II are in different charge

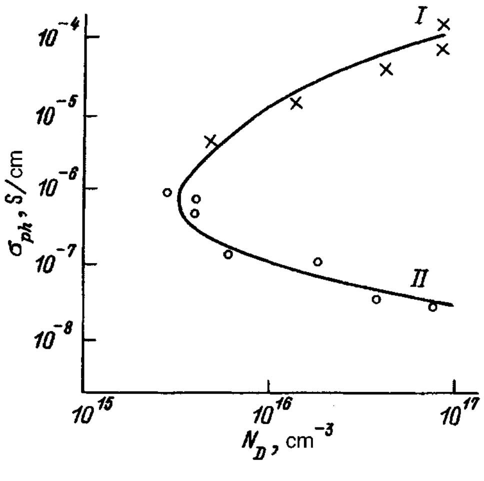

FIG. 4. Photoconductivity $G \simeq 10^{19}$ cm$^{-3}\cdot$sec^{-1}, $h\nu = 2$ eV, $T = 300$ K as a function of the defect density. The notation is the same as in Fig. 3.

states: for $N_D=$const, the $\mu\tau$ value of the electrons (the product of mobility and lifetime) differs, and the difference increases with increasing value of N_D.

Since we can assume $\mu\simeq$const, it is obvious that, as N_D increases, the difference between the electron-capture cross sections increases, as in a-Si:H doped with phosphorus and boron, where the defects—dangling Si–Si bonds—are predominantly in the charge states D^- and D^+. Therefore, if the defect density is minimal in intrinsic a-Si:H, and all the defects are in the D^0 state, then, in pseudodoped a-Si:H, the $N_{D^-,D^+}/(N_{D^0}+N_{D^-,D^+})$ value increases at the same time that the defect density increases. We should point out that the points that belong to doped samples lie on a reduced curve (Fig. 4).

A long intense exposure of a-Si:H films, as is well known, increases the defect density, but the Fermi level approaches a point corresponding to the intrinsic material (the Stabler–Wronski effect). It is also well known that the photoinduced defects are in the D^0 state. Thus, for a defect density formed during the deposition of an a-Si:H film that is the same as the photoinduced defect density, the Fermi level shifts in the opposite direction. We also conclude from this result that defects formed during film growth are in charge states that differ from D^0.

We also note in this connection the results of Hata and Matsuda,[15] who showed that laser annealing affects the density of photoinduced defects and the density of defects formed during film growth differently. These authors associate this behavior with structural differences in the neighborhoods of the defects. Actually, different charge states of defects should have different effects on their local surroundings. Thus, in Ref. 16, it is concluded that the formation of photoinduced defects (D^0) reduces the variance of the angles between the Si–Si bonds. At the same time, increasing the density of the defects formed during film deposition, in our opinion D^- or D^+, has the opposite result.[17]

If it is assumed that pseudodoping of a-Si:H is accompanied by the formation of charged defects, will the local neutrality condition be satisfied? In other words, in addition to the formation of a charged defect (a dangling Si:Si bond), one should expect the formation of an oppositely charged center. It was natural to assume that there may be an effect from associated O, C, N, and possibly W and Cr defects, which are neutral if the film structure is formed in the soft-deposition regime. They become electrically active when deviations from this regime occur. Our samples obtained in a triode reactor and in a magnetron chamber were therefore studied by reverse Rutherford scattering. As a result, it was shown that the O, C, and N concentrations are lower than 10^{20} cm^{-3} (i.e., they correspond to the level of the leading foreign laboratories[18]), while no W and Cr impurities were detected in our films.

As already indicated (Fig. 1), if different methods providing soft deposition are used, intrinsic a-Si:H is always obtained. It was shown in Ref. 17 that only films of intrinsic a-Si:H can be considered completely homogeneous. The density of defects (dangling Si–Si bonds) in such films is minimal, all defects are in the D^0 state, and the question of electrical neutrality does not arise. As far as pseudodoped a-Si:H is concerned, it was established in Ref. 17 that an increase in defect density is accompanied by changes in a number of structural characteristics: an increase in the concentration of bound hydrogen in the film, in the microstructural parameter, and in the Urbach energy; a shift of the Raman frequency ω_{TO}; and an increase in the half-width of the TO peak ($\Delta\omega_{TO}$). Moreover, in such a-Si:H films, the total content of hydrogen, determined by the proton-recoil method, substantially exceeds the concentration of bound hydrogen. It is apparently the inhomogeneity of the films that makes it possible to satisfy the condition of local electrical neutrality. Thus, for example, in the opinion of Favre *et al.*,[19] the predominance of D^- centers that they detected in nonintrinsic a-Si:H films is compensated for by the existence of positively charged traps—tailing levels of the valence band. It is evident that other models can be proposed, but further structural studies are needed for their development.

We hypothesize that, in the inhomogeneous structural network of a-Si:H, which contains additionally, unbound hydrogen, it is impossible in principle to expect defects to exist in only the D^0 state. At the same time, it is evident that we do not have in mind the formation of pairs of defects, $D^- - D^+$, as was done in the model of Branz and Silver:[20] in this case, the Fermi level does not shift; i.e., the indicated model is not applicable to pseudodoped a-Si:H.

4. CONCLUSIONS

There is thus a close association of the defect density in films of pseudodoped a-Si:H, the structural inhomogeneity of these films at different levels (from close order to microstructure), the predominance in them of charged defects of one sign, and the shift of the Fermi level in the mobility band. Both in intrinsic and in pseudodoped a-Si:H, the defects are dangling Si–Si bonds; however, in the first case, they are in a D^0 state and, in the second case, they are in a D^- or a D^+ state. Intrinsic a-Si:H in which the defect density is minimal, while its structure is homogeneous, is obtained in a soft-deposition regime, regardless of T_s. When deviations from this regime occur, the material becomes pseudodoped.

This work was supported by INTAS Grant No. 931916 and was carried out in cooperation with the Joint Research Program. The author thanks the coordinator of the program, Prof. V. Fuhs, for providing results of studies of a-Si:H films obtained in the scientific centers of the FRG, France, Italy, and Greece. The author also thanks the colleagues of Prof. Fuhs's group (IP1), who actively carry out the research program.

[1] N. M. Johnson, P. V. Santsos, C.E. Nebel, W. B. Jackson, R. A. Street, K. S. Stevens, and J. Walker, J. Non-Cryst. Solids **137/138**, 235 (1991).
[2] N. Hata and S. Wagner, J. Appl. Phys. **72**, 2357 (1992).
[3] O. A. Golikova, Fiz. Tekh. Poluprovodn. **25**, 1517 (1991) [Sov. Phys. Semicond. **25**, 915 (1991)].
[4] O. A. Golikova, M. M. Kazanin, M. M. Mezdrogina, K. L. Sorokina, and U. S. Babakhodzhaev, Fiz. Tekh. Poluprovodn. **23**, 1737 (1989) [Sov. Phys. Semicond. **23**, 1076 (1989)].
[5] A. Matsuda and K. Tanaka, J. Appl. Phys. **60**, 2351 (1986).

[6] V. L. Dalal, M. Leonard, and G. Baldwin, J. Non-Cryst. Solids **164–166**, 71 (1993).
[7] M. Vanecek, B. P. Nelson, A. H. Mahan, and R. S. Crandall, J. Non-Cryst. Solids **137/138**, 91 (1991).
[8] R. Zeidlitz, F. Kessler, and M. Heintze, J. Non-Cryst. Solids, **164–166**, 83 (1993).
[9] U. Kroll, J. Meier, M. Goetz, A. Howling, J.-L. Dorier, J. Dutla, A. Shan, and Ch. Holenstein, J. Non-Cryst. Solids **164–166**, 60 (1991).
[10] O. A. Golikova, A. N. Kuznetsov, V. Kh. Kudoiarova, and M. M. Kazanin, Fiz. Tekh. Poluprovodn. **30**, 1879 (1996) [Semiconductors **30**, 983 (1996)].
[11] R. M. A. Dawson, C. M. Fortmann, M. Gunes, Y. M. Li, S. S. Nag, R. M. Collins, and C. R. Wronski, J. Appl. Phys. Lett. **63**, 955 (1993).
[12] W. Fuhs (private communication).
[13] T. Kamei, G. Ganguly, N. Hata, and A. Matsuda, Proc. ICAS-15 (Cambridge, UK, 1993), p. 15.
[14] P. G. LeComber and W. E. Spear, J. Non-Cryst. Solids **35–36**, 327 (1980).
[15] N. Hata and A. Matsuda, Abstracts ICAS-15 (Cambridge, UK, 1993), p. 125.
[16] C. M. Fortmann, R. M. Dawson, H. Y. Liu, and C.R. Wronski, J. Appl. Phys. **76**, 2841 (1994).
[17] O. A. Golikova and V. Kh. Kudoiarova, Fiz. Tekh. Poluprovodn. **29**, 1128 (1995) [Semiconductors **29**, 584 (1995)].
[18] M. Nakata, S. Wagner, and T. M. Peterson, J. Non-Cryst. Solids **164–166**, 179 (1993).
[19] M. Favre, A. Shan, J. Hubin, E. Bustarret, M. A. Hachicha, and S. Basrour, J. Non-Cryst. Solids **137/138**, 335 (1991).
[20] H. M. Branz and V. Silver, Phys. Rev. B **42**, 7420 (1990).

Translated by W. J. Manthey

Structural perfection of epitaxial layers of 3*C*-SiC grown by vacuum sublimation on 6*H*-SiC substrates

A. N. Andreev, N. Yu. Smirnova, A. S. Tregubova, M. P. Shcheglov,
and V. E. Chelnokov

A. F. Ioffe Physicotechnical Institute, Russian Academy of Sciences, 194021, St. Petersburg, Russia

(Submitted April 17, 1996; accepted for publication April 24, 1996)
Fiz. Tekh. Poluprovodn. **31**, 285–290 (March 1997)

This paper discusses how the processing parameters affect the structural perfection of epitaxial layers of 3*C*-SiC grown on 6*H*-SiC substrates by vacuum sublimation. It shows that, at constant temperature and using virtually undisoriented substrates, decreasing the growth rate increases the size of the twinning regions in the films and reduces the total defect concentration of the 3*C*/6*H* structures. Epitaxial layers of 3*C*-SiC with a defect density of 10^1-10^2 cm^{-2} and a twinning area of up to 6 mm^2 have been obtained. © *1997 American Institute of Physics.* [S1063-7826(97)00603-0]

1. INTRODUCTION

The high mobility [1000 cm^2/(V·s)] and drift saturation rate (2.7×10^7 cm/sec) of the electrons and the large value of the electric breakdown field (4×10^6 V/cm),[1,2] in combination with a rather large band gap, have aroused interest in using silicon carbide in the cubic modification to fabricate semiconductor devices for various purposes (high-frequency devices, power devices, devices for high temperatures, etc.). To implement the high potentialities of this material, epitaxial layers (ELs) of satisfactory quality are needed. They are difficult to produce because of the need for heteroepitaxial growth, which is usually done on silicon or silicon carbide substrates of various crystal modifications (usually the commonest modification, 6*H*). The use of silicon substrates causes the resulting ELs to have a high defect level because of the large differences in the crystal lattice constants (~20%) and the thermal expansion coefficients (~0.08%) of Si and 3*C*-SiC.[3,4]

In the case of growth on 6*H*-SiC substrates, the structural imperfection of 3*C*-SiC ELs is mainly determined by the presence of a twin structure[5–7] and is usually characterized by the density of intertwin boundaries (dislocation-pair boundaries, DPBs). Some decrease in the DPB density with increasing thickness of the epitaxial layer was observed in Refs. 6 and 7, but it was accompanied by an increase in the transverse size of these boundaries. The complete disappearance of DPBs has not been experimentally observed.1) Moreover, in certain cases, the growth of fairly thick layers has caused the formation of a polycrystalline structure.[7] Powell *et al.*[9] used deposition from the gas phase to grow ELs with a maximum twinning area of about 1 mm^2.

A decrease of the DPB density can also be achieved by using 15*R*-SiC substrates,[6] but this modification, like 3*C*, is an uncommon one. To avoid DPB formation in ELs of 3*C*-SiC, another, comparatively complicated method was proposed in Refs. 10 and 11: growing layers on 6*H*-SiC and 4*H*-SiC substrates with a specially chosen surface orientation—$(0114)_{6H}$ and $(0113)_{4H}$, respectively.

Our goal was to study the degree of structural perfection of ELs of 3*C*-SiC grown by vacuum sublimation on silicon carbide substrates of modification 6*H*, to determine how the processing conditions affect the size of the twin formations in the ELs and the defect density formed at the heteroboundary of 3*C*-SiC/6*H*-SiC structures. It should be pointed out that the question of the study of the transition layers at the heteroboundary and the structural perfection of the interface of SiC-3*C*/SiC-6*H* structures is almost never mentioned in most papers.

2. THE TECHNOLOGY OF GROWING 3*C*-SiC EPITAXIAL LAYERS

The ELs were grown at temperatures of 1800–1900 °C by vacuum sublimation in a closed growth system[12,13] on the (0001)Si-face of substrates obtained by the Lely method. Their surface-disorientation angle relative to the base plane did not exceed 10–20″. Immediately before growth, the substrate was sublimation etched *in situ* to remove the layer disturbed by mechanical polishing and to clean the substrate surface. The 6*H*→3*C* transformation of the modifications was achieved by two methods: (1) by high growth rates ($v_g>3-4$ μm/min), and (2) by substantial enrichment of the vapor phase with silicon (i.e., with silicon vapor pressures in the growth cell corresponding to its equilibrium pressure over a silicon melt) for low values of v_g (0.4–0.8 μm/min). The growth rate was increased or decreased by varying the temperature gradient between the vapor sources and the substrate[14] and by varying the composition of the vapor phase in the growth cell.[15,16]

3. METHODS OF STUDYING THE STRUCTURE OF 3*C*-SiC EPITAXIAL LAYERS

In most papers connected with the growth of ELs of 3*C*-SiC, either etching in an alkali solution[6–8] or oxidation[17] is used to reveal the DPBs and other defects; this allows the defects to be observed by optical microscopy. These techniques make it possible to obtain information on the distribution of twin formations only on the surface of the ELs.

The degree of structural perfection of the as-grown ELs was studied by x-ray topography not only in the Laue geometry by the Lang method, using Mo$K\alpha_1$ radiation, and by the

1063-7826/97/030232-05$10.00

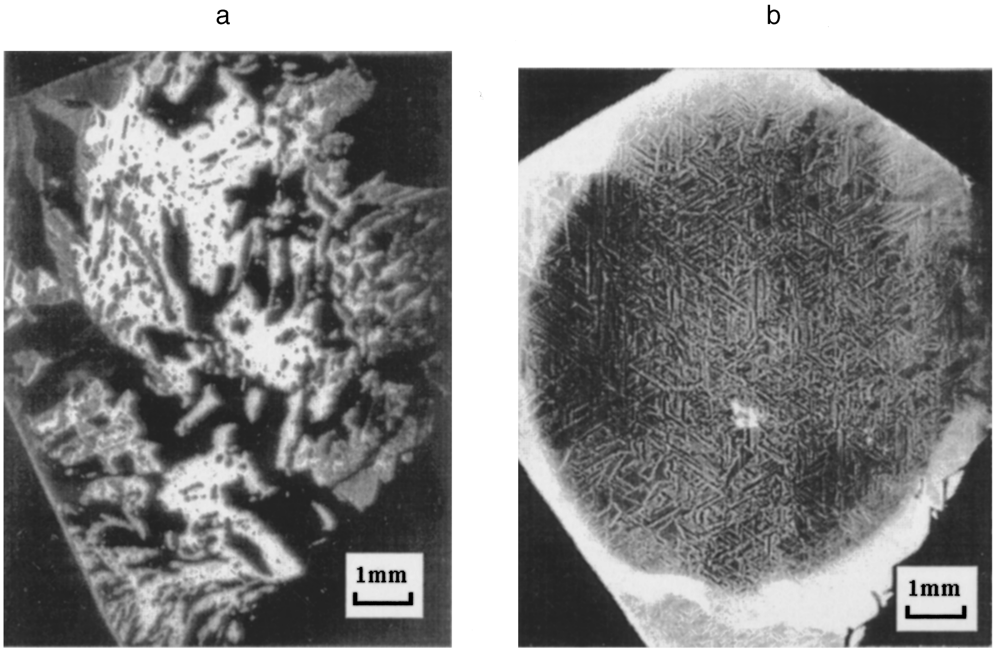

FIG. 1. X-ray topograms of a $3C/6H$ structure ($v_g = 3.2\ \mu$m/min) in the Bragg geometry. Cu $K\alpha$ radiation. Reflections from a—$(113)_{3C}$ and b—$(1.0.\bar{1}.15)_{6H}$.

method of anomalous transmission of x rays (ATXR), using Cu$K\alpha_1$ radiation, but also in the Bragg geometry by the method of skew-symmetric Barett–Newkirk reflections in Cu$K\alpha_1$ radiation. The quantitative characteristics of the degree of perfection of the $3C/6H$ structures were determined from the half-widths of the two-crystal rocking curves in $(111)_{3C}$ and $(0006)_{6H}$ reflections on Cu$K\alpha_1$ radiation, respectively.

To identify the twin structure on the topograms, we used skew-symmetric diffraction spots of the type $(113)_{3C}$ in the Bragg geometry. They have the characteristic that the diffraction conditions corresponding to the maximum intensity of a diffraction spot cannot simultaneously be satisfied for twins of different types, and the diffraction image is formed only by twin regions of the same modification. As a result, regions of black and white contrast that correspond to two possible types of twins are observed on the topograms. These conditions are implemented for twin regions of another type by rotating the test sample by 60% relative to the $[111]_{3C}$ direction (which corresponds to $[0001]_{6H}$); this reverses the image contrast of the twin regions.

To study the degree of structural perfection of the EL–substrate interface, we used $(1.0.\bar{1}.15)_{6H}$ Bragg reflection. Reflections from planes with such indices have no analogs for the cubic SiC lattice, and this makes it possible to obtain the diffraction image of layers of a noncubic structure that lie directly under a $3C$-SiC EL. Note that, on such topograms, the DPB outlines are maintained over the entire thickness of the EL.

4. RESULTS AND DISCUSSION

Our studies showed that twin regions were present in all our $3C$-SiC ELs, but their size varied significantly, depending on the growth conditions (Figs. 1–3). The degree of structural perfection of the transition layers formed at the EL–substrate boundary was also substantially different. As can be seen from the topograms in Figs. 1b and 3b, the defect structure of the transition layer is mainly determined by the presence of stacking faults, which are formed along the faces of the growth pyramids that appear at the initial stage of growth on the surface of the substrate from separate nuclei of the cubic phase of $3C$. For heteroepitaxial growth, the main cause for the formation of such defects is the difference of the crystal lattice parameters of the substrate and the EL. On the topograms, the stacking faults appear as characteristic triangles or elements corresponding to cross sections of the faces of the growth pyramids with a $(111)_{3C}$ plane. Growth pyramids oriented with respect to each other at 60° relative to the $(111)_{3C}$ direction form twins of a different type (Fig. 4), which can be seen on the topograms from the analogous orientation of the stacking defects associated with them (for example, *A* and *B* in Fig. 2b). The distribution and size of the twin regions in the resulting ELs of $3C$-SiC mainly correspond to the defect structure of the transition layer, which is evidence of the determining role of the growth centers that appear on the substrate surface: decreasing the number of such centers promotes the formation of ELs with relatively large twins. Thus, by influencing the nucleation processes, is possible to predetermine the character of the twin structure and, consequently, the degree of structural perfection of the growing ELs.

One of the parameters that can substantially influence these processes is the growth rate. Starting from this premise, several experiments were carried out with the goal of optimizing the growth conditions of the $3C$-SiC ELs. At high growth rates, caused by increasing the temperature gradient between the vapor source and the substrate and by enriching the vapor phase in the growth cell with silicon, ELs were formed with a high DPB density and, consequently, with twins of small size. The $3C/6H$ structures obtained under these conditions had a high defect density at the heterojunction. Typical topograms of such structures are shown in Figs.

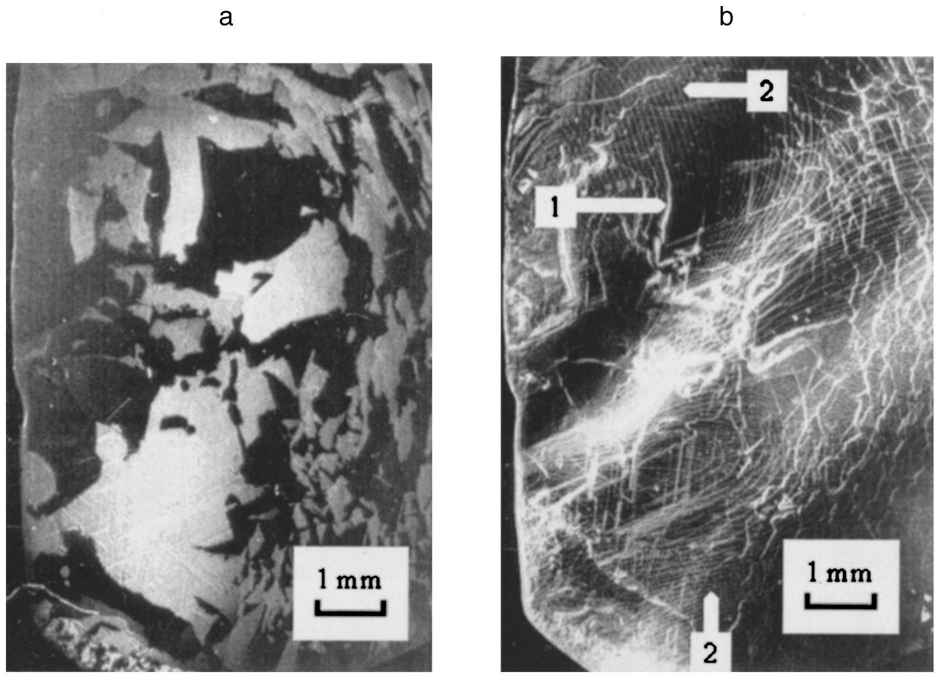

FIG. 2. X-ray topograms of a $3C/6H$ structure ($v_g = 0.9$ μm/min) obtained a—in the Bragg geometry. Cu $K\alpha$ radiation, $(331)_{3C}$ reflection, b—by the Lang method, Mo $K\alpha_1$ radiation, $(1.1.\bar{2}.0)_{6H}$ reflection. 1—intertwin boundaries, 2—dislocation structure of original $6H$-SiC substrate.

1a and 1b. No appreciable decrease in the DPB density was observed all the way to the maximum thicknesses of the ELs (35–40 μm). Their substantial defect concentration is confirmed by x-ray diffraction data: the measured half-widths of the rocking curves ($\omega_{\theta B}$) was 40–90″ for various samples.

Most ELs obtained as the growth rate was decreased to $v_g = 0.4$–0.8 μm/min were characterized by comparatively large twins (Figs. 2a and 3a) and a lower defect density in the transition layer (Fig. 2b). For $v_g < 0.6$ μm/min, the area of the twins in the resulting films reached 5–6 mm^2. We should point out that increasing the area of the twins is associated in a number of cases with processes by which they are obliterated. Thus, for example, it can be seen by comparing the topograms in Figs. 3a and 3b that, while stacking faults corresponding to the growth pyramids of twins of various types (A and C) are observed in the transition layer, only one twin is present on the surface of the EL in the same section.

An increase in the size of the twinning regions produced a significant increase in the structural perfection of the ELs as a whole; this is confirmed by x-ray topograms obtained by the Lang and ATXR methods. The defect density in such epitaxial films was 10^1–10^2 cm^{-2}, with stacking faults (and not DPBs) being predominant. On the topogram in Fig. 2b, the dislocation structure of the original $6H$-SiC substrate is clearly seen under the $3C$-SiC EL, and this is evidence of a high degree of perfection of the interface of $3C/6H$ structures obtained at small v_g. These structures were characterized by small half-widths of the rocking curves (14–30″).

In a number of cases, less perfect films were obtained

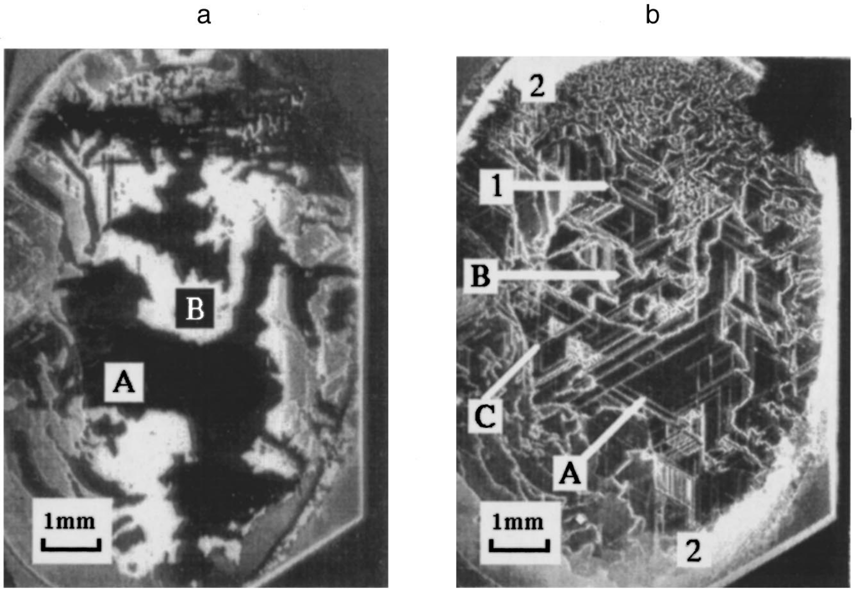

FIG. 3. X-ray topograms of a $3C/6H$ structure ($v_g = 0.6$ μm/min) in the Bragg geometry. Cu $K\alpha$ radiation. a—$(113)_{3C}$ reflection; regions corresponding to twins of different type (A and B) reverse the contrast when the crystal is rotated by 180° relative to the C axis. b—$(1.0.\bar{1}.15)_{6H}$ reflection. A, B, and C are stacking faults; 1—intertwin boundaries; 2—location of a step at the periphery of the sample, formed during preliminary sublimation etching.

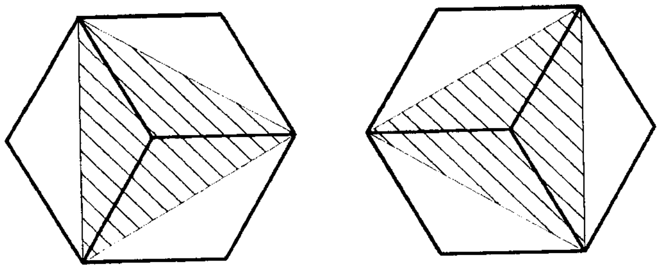

FIG. 4. Formation of various types of twins. The $[111]_{3C}$ direction is perpendicular to the plane of the figure.

under the same conditions, which indicates that other factors affect the nucleation processes. Examples of such factors are the specific state of the surface, i.e., the presence of traces of mechanical polishing (scratches) after insufficiently deep sublimation etching; relief; or dislocations reaching the substrate surface. The effect of these kinds of defects on the nucleation processes during the growth of 3C-SiC ELs was studied in Ref. 17. A characteristic example of the effect of relief is the presence of smaller twins and larger defect concentration in the transition layer close to a step formed at the substrate periphery after preliminary sublimation etching (see, for example, Fig. 2).2)

According to the model proposed in Ref. 18, the number of growth centers that appear on the substrate surface during homoepitaxial growth is determined by the following parameters: temperature, growth rate, and degree of disorientation of the substrate surface.[18] Here, depending on the relationship of the indicated parameters, the growth process is controlled either by the incorporation of adatoms into the crystal structure at terraces whose size and number are determined by the degree of substrate disorientation (''step-flow controlled epitaxy'') or by processes of random ''two-dimensional nucleation.'' In the first case, the structural perfection of the resulting ELs is high, and this fact is confirmed by studies of homoepitaxial-growth processes of silicon carbide in Refs. 19–21. Other conditions being equal, increasing the growth rate strengthens the influence of uncontrolled nucleation. Small growth rates at high temperatures, on the other hand, reduce its probability. Accordingly, when we grew layers in the large-v_g regime, we obtained structures characterized by high defect density in the transition layer, whereas there were far fewer defects when there was excess silicon in the growth cell, and we consequently obtained 3C-SiC ELs with twins of large size. Our results are thus in qualitative agreement with the model concepts described here.

It should be pointed out that this model probably can be valid only if the growth occurs on a fairly perfect planar surface (with a low density of structural defects), from which possible contamination has been removed. Otherwise, first, additional effective nucleation centers arise close to various kinds of inhomogeneities; second, the growth is interrupted in directions parallel to the substrate surface.[17] These processes unavoidably increase the DPB density in 3C-SiC ELs. Thus, the factors that are essential for obtaining comparatively perfect 3C-SiC/6H-SiC structures in our experiments must include the following: first, the use of substrates obtained by the Lely method, which to date have the most nearly perfect structure; second, the use of fairly deep polishing sublimation etching *in situ* immediately before the growth of the 3C-SiC ELs.

5. CONCLUSION

Based on the fact that the characteristics of the twin structure of 3C-SiC ELs that arises when the layers are grown on 6H-SiC substrates are determined by nucleation processes at the initial growth stage, an attempt has been made to optimize the growth conditions. It has been shown that, at a constant temperature and using virtually undisoriented substrates, reducing the growth rate of the ELs increases the area of the twinning areas and decreases the total defect concentration of the structures. As a result, at small growth rates $(0.4-0.8\ \mu\text{m/min})$, silicon carbide ELs are obtained in a cubic modification with a low defect density $(10^1-10^2\ \text{cm}^{-2})$ and a twinning area of up to 6 mm^2.

This work was carried out with the partial support of the University of Arizona.

1) The work of Furukawa *et al.*[8] is an exception. They described the production by a sublimation method of bulk single crystals of 3C-SiC that were characterized by the absence of DPBs on the growth surface, but the linear size was not indicated.

2) The growth cell is constructed in such a way that the etching and growth processes do not occur on the entire substrate surface, since its peripheral region is covered by graphite fittings.

---

[1] Yu. A. Vodakov, G. A. Lomakina, E. N. Mokhov, V. G. Oding, V. V. Semenov, and V. I. Sokolov, in *Wide-Band Semiconductors* (Leningrad, 1979), p. 164.
[2] D. K. Ferry, Phys. Rev. B **12**, 2361 (1979).
[3] V. Shields, K. Fekade, and M. Spencer, *Proceedings of the fifth* SiC *and Related Materials Conf.* (Washington, D.C., 1993) [Inst. Phys. Conf., Ser. **137**, 21 (Bristol and Philadelphia, 1994)].
[4] H. Matsunami, S. Nishino, and H. Ono, IEEE Trans. Electron. Dev. **ED-28**, 1235 (1981).
[5] J. A. Powell, J. B. Petit, L. G. Matus, and S. E. Lempner, *Proc. 3rd Int. Conf. on Amorph. and Cryst.* SiC [Springer Proc. Phys. **56**, 313 (1992)].
[6] K. Nishino, T. Kimoto, and H. Matsunami, *Proceedings of the fifth* SiC *and Related Materials Conf.* (Washington, D.C., 1993) [Inst. Phys. Conf. Ser. **137**, 33 (Bristol and Philadelphia, 1994)].
[7] J. Yang, S. Nishino, J. Powell, and D. Pizouz, *Proceedings of the fifth* SiC *and Related Materials Conf.* (Washington, D.C., 1993) [Inst. Phys. Conf. Ser., **137**, 25 (Bristol and Philadelphia, 1994)].
[8] K. Furukawa, Y. Tajima, H. Saito, and Y. Fujii, Japan. J. Appl. Phys. **32**, L645.
[9] J. A. Powell, D. J. Larkin. J. B. Petit, and J. H. Edgar, *Proceedings of the fourth Int. Conf. on Amorph. and Cryst.* SiC [Springer Proc. Phys. **71**, 23 (1993)].
[10] H. Matsunami, *Proceedings of the fifth* SiC *and Related Materials Conf.* (Washington, D.C., 1993) [Inst. Phys. Conf. Ser. **137**, 45 (Bristol and Philadelphia, 1994)].
[11] A. Yu. Maksimov, A. A. Mal'tsev, and N. K. Yushin, Pis'ma Zh. Tekh. Fiz. **20**, 50 (1994) [*sic*].
[12] M. M. Anikin, A. A. Lebedev, S. N. Pyatko, and A. M. Strel'chuk, Mater. Sci. Eng. B **11**, 113 (1992).
[13] M. M. Anikin, N. B. Guseva, V. A. Dmitriev, and A. L. Syrkin. Izv. AN SSSR. Neorg. Mater. **10**, 1768 (1984).
[14] M. G. Ramm, E. N. Mokhov, and R. G. Verenchikova, Izv. AN SSSR. Neorg. Mater. **15**, 2233 (1979).
[15] A. O. Konstantinov and E. N. Mokhov, Pis'ma Zh. Tekh. Fiz. **7**, 247 (1981) [Sov. Tech. Phys. Lett. **7**, 106 (1981)].
[16] A. N. Andreev, N. Yu. Smirnova, A. S. Tregubova, M. P. Scheglov, and

V. E. Chelnokov. *Proc. 6th* SiC *and Related Materials Conf.* (Kyoto, 1995).

[17] J. A. Powell, J. B. Petit, J. B. Edgar, I. G. Jenkins, L. G. Matus, J. W. Yang, P. Pirouz, W. J. Choyke, L. Clemen, and M. Yoganathan, Appl. Phys. Lett. **59**, 333 (1991).

[18] T. Kimoto and H. Matsunami, *Proceedings of the fifth* SiC *and Related Materials Conference* (Washington, D.C., 1993) [Inst. Phys. Conf. Ser. **137**, 95 (Bristol and Philadelphia, 1994)].

[19] H. Matsunami, *Proceedings of the fifth* SiC *and Related Materials Conference* (Washington, D.C., 1993) [Inst. Phys. Conf. Ser. **137**, 45 (Bristol and Philadelphia, 1994)].

[20] T. Kimoto and H. Matsunami, *Proceedings of the fifth* SiC *and Related Materials Conference* (Washington, D.C., 1993) [Inst. Phys. Conf. Ser. **137**, 55 (Bristol and Philadelphia, 1994)].

[21] A. Iton, H. Akita, T. Kimoto, and H. Matsunami, *Proceedings of the fifth* SiC *and Related Materials Conference* (Washington, D.C., 1993) [Inst. Phys. Conf. Ser. **137**, 5 (Bristol and Philadelphia, 1994)].

Translated by W. J. Manthey

Structure and electrical conductivity of polycrystalline silicon films grown by molecular-beam deposition accompanied by low-energy ion bombardment of the growth surface

D. A. Pavlov, A. F. Khokhlov, D. V. Shungurov, and V. G. Shengurov

N. I. Lobachevskiĭ State University of Nizhniĭ Novgorod, 603600 Nizhniĭ Novgorod, Russia

(Submitted March 12, 1996; accepted for publication May 5, 1996)
Fiz. Tekh. Poluprovodn. **34**, 291–295 (March 1997)

This paper discusses how the structure and electrical conductivity of polycrystalline silicon films grown by molecular-beam deposition are affected by the growth conditions. It shows that the films can be improved by applying to the substrate a voltage in the range 50–300 V, negative with respect to the silicon source. Such films also have higher conductivity. The results are explained in terms of bombardment of the growing film by dopant ions. © *1997 American Institute of Physics.* [S1063-7826(97)00703-5]

INTRODUCTION

Polycrystalline silicon films (PSFs) are widely used in integrated circuits and solar cells.[1,2] Among the various methods of obtaining PSFs, molecular-beam deposition (MBD) has attracted the attention of researchers because it can be used to obtain films at low temperatures, to eliminate background impurities, and to controllably introduce dopants.[3] Another advantage of this method is that the film-deposition conditions can be varied within very wide limits.

Additional control of the parameters of the growing film can be provided by bombarding the growth surface with low-energy ions.[4–8] This has been demonstrated during the growth of silicon[4,5] and metal films[6] in high vacuum, where a reduction of the epitaxial growth temperature was observed, and continuity of the films was attained at an earlier stage. Electron-beam sputtering of amorphous silicon films with a potential applied to the substrate resulted in the formation of large clusters (from 20 to 100 nm in diameter).[7]

Polycrystalline silicon films have been virtually ignored in those studies. At the same time, additional monitoring of the growth parameters is needed in order to obtain such films with given properties. Moreover, in establishing a connection between the ion-beam parameters (the ion density and energy) and the film properties, the film-growth mechanism under the action of low-energy ions must be determined.

Our goal in this study was to analyze the structure and electrical conductivity of thin PSFs grown by MBD by the sublimation of silicon when a negative potential with respect to the silicon source is applied to the substrate.

RESEARCH METHODS

Polycrystalline films were grown by silicon sublimation, using the technique described in detail in Ref. 3. A rectangular plate cut from a single crystal of silicon doped with gallium to a concentration of about $\sim 5\times 10^{19}$ cm^{-3} was used as the source of the silicon and dopant vapors. This dopant was chosen because it has been established[4,5,9] that there is an ionic component in the molecular flux from sublimating single-crystal gallium-doped silicon. The (Ga) dopant concentration in the layer increases if the epitaxial layers are grown while a negative potential with respect to the source is applied to the substrate, whereas it decreases if the potential is positive.[5] The layers for this project were grown with a negative potential $V_b = -(50-300)$ V applied to the substrate.

The experimental setup is shown in Fig. 1. The substrate holder and the substrate, were cut from single-crystal silicon, were heated by an electric current. The voltage drop between the ends of the plate was about ~ 10 V. The films were 0.1–0.5 μm thick. The substrate temperature was varied between 300 and 600 °C.

The grain size in the films and the size of the blocks were calculated from the size of the coherent scattering regions using electron diffraction (diffraction of a transmitted electron beam) and transmission electron microscopy. The surface morphology of the films was studied by a replica method.

A coplanar configuration of contacts with a 1-mm gap was used in measuring the layer resistance. The electric field during the measurements did not exceed 10^2 V/cm.

RESULTS

Film structure. Our studies showed that the grain size of the PSFs increases linearly with increasing deposition temperature (Fig. 2a). At a substrate temperature of $T_s \geqslant 500$ °C, it is almost comparable with the film thickness. At such temperatures, the size of the coherent scattering region[1)] saturates (Fig. 2b).

One can judge how the substrate temperature and potential affect the film structure from the variation of the diffraction patterns. Figure 3 shows diffraction patterns of films grown at 300, 400, and 450 °C with a potential of $V_b = -300$ V applied to the substrate. This figure also shows diffraction patterns from films grown with no potential applied.

When a potential was applied at low deposition temperatures ($T_s \leqslant 300$ °C), the film structure remained amorphous. Only a certain sharpening of the diffraction peaks was noted in this case (Fig. 3, curves a and b). When a negative potential of $V_b = -300$ V is applied to the substrate, the size of the coherent scattering region increases from 2.8 to 3.3 nm. Since this parameter for an amorphous material characterizes

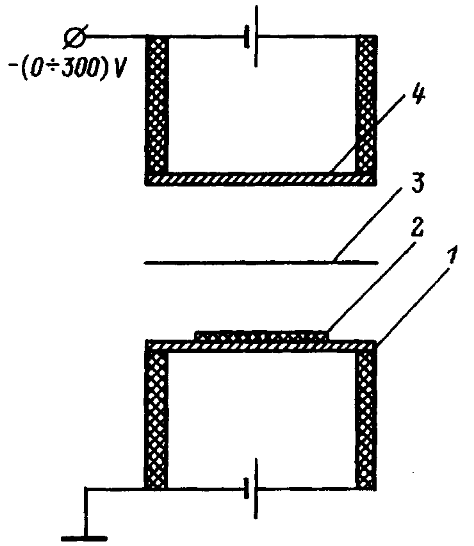

FIG. 1. System for growing silicon films by subliming silicon while the growth surface is irradiated with low-energy ions. *1*—substrate holder, *2*—substrate, *3*—screen, *4*—source.

the short-range ordering region, it can be concluded that bombardment by low-energy ions during the formation of an amorphous structure causes the structure to become ordered.

Figure 3 also shows the diffraction patterns of films grown at $T_s = 450$ °C. Both films (curves *1*c and *2*c) are polycrystalline. The potential affects the substrate by making the diffraction peaks narrower and more intense. In films grown with an applied potential, the size of the coherent scattering region, which in this case should be identical to the size of the blocks inside the grain, increases from 10 to 12 nm. The additional irradiation thus plays a positive role in forming the film structure.

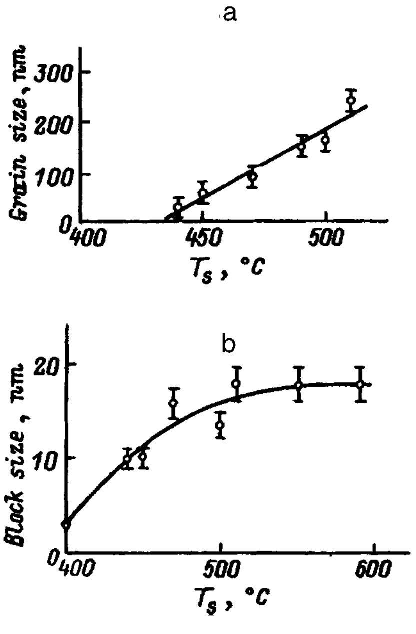

FIG. 2. Grain size (a) and block size (b) vs the deposition temperature of polysilicon films.

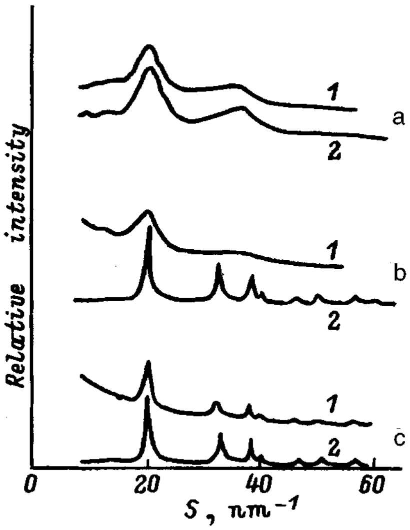

FIG. 3. Diffraction patterns of silicon films at various temperatures T_s °C: a—300, b—400, c—450. *1*—with no bias on the substrate, *2*—$V_b = -300$ V.

The result obtained at a growth temperature of $T_s = 400$ °C is the most interesting result, in our opinion. In this case, the film structure in the absence of bias is amorphous (Fig. 3, curve *1*b), whereas a polycrystalline structure is formed with bias (curve *2*b). The differences in the material's structure can be clearly seen from micrographs of carbon replicas of the surface of these films. The surface of the amorphous film (Fig. 4a) is characterized by small irregularities, while we see a well-developed grain relief on the surface of the polycrystalline film (Fig. 4b).

It should be pointed out that varying the negative potential from 50 to 300 V did not cause any additional differences in the film structure. The fact that there is additional irradiation is apparently more important than the energy of the bombarding ions.

Electrical conductivity of the films. Measured results for the layer resistance R_s of the films at room temperature as a function of deposition temperature, the potential applied to the substrate, and the film thickness are shown in Table I. It can be seen that the resistance decreases with increasing substrate temperature. Films grown with an applied negative potential have a resistance one or two orders of magnitude lower than do those grown with no potential.

DISCUSSION

The effect of substrate temperature on the PSF structure. An analysis of the experimental results indicates that increasing the growth temperature improves the film structure. This is consistent with the existing model of PSF growth by the vacuum method and by gas-transport deposition.[10] According to this model, the adatom mobility is low at a low growth temperature, and the film grows from virtually rigidly fixed nuclei. As the growth temperature increases, the silicon adatoms become more mobile, and the coalescence of the nuclei increases. As a result, the films grow with larger grain size.

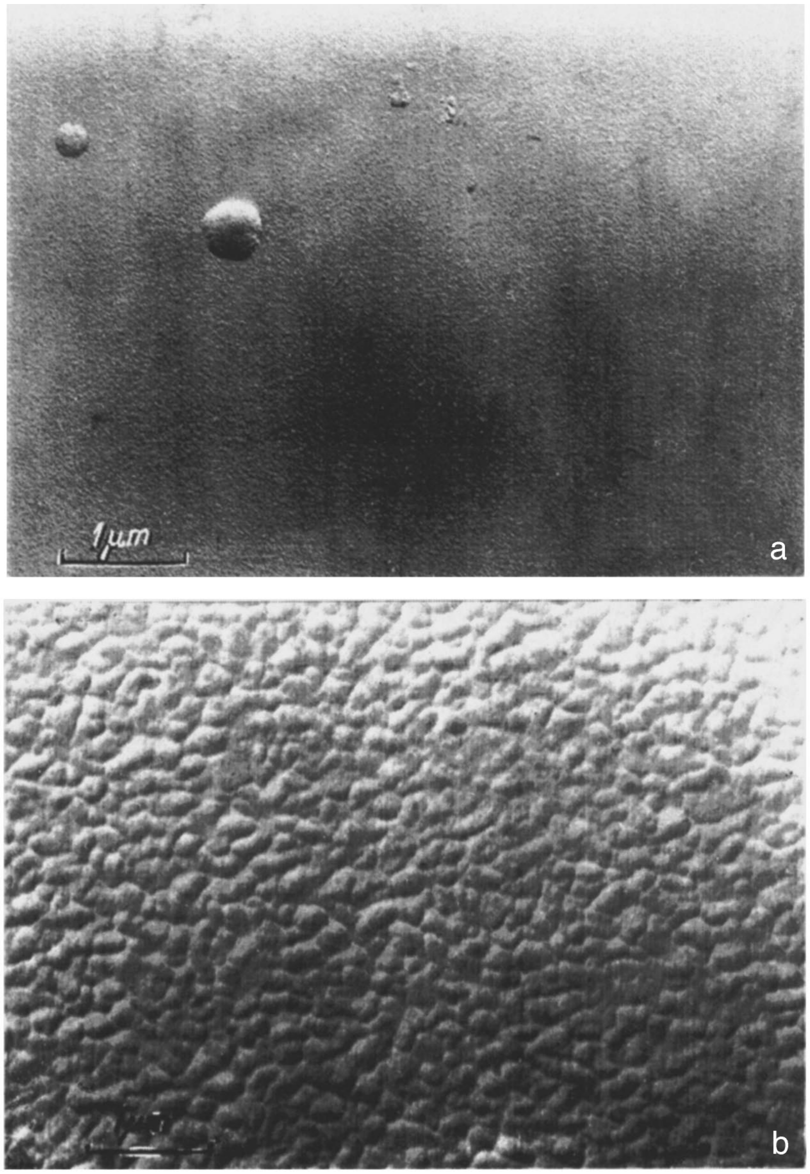

FIG. 4. Micrograph of carbon replicas of the surface of silicon films grown at $T_s = 400$ °C with no bias on the substrate (a) and with $V_b = -300$ V. Magnification 16 000.

New nuclei are generated on the bare sections of the substrate, and they either migrate to larger nuclei or expand independently.

How the application of a potential to the substrate affects the PSF structure. Our experimental results show that applying a negative potential to the substrate when the films are being grown improves their structure, as does increasing the substrate temperature. The application of a negative potential accelerates the ions in the molecular flux toward the substrate. From the various qualitative concepts in the literature concerning the mechanisms by which ionic bombardment affects the structure of deposited films, we can select strengthening of the surface diffusion of adatoms.[11] At the early stages of film growth, ions incident on the surface cause the formation of nuclei (clusters) of larger size than when deposition is carried out without the action of ions. The increase in the cluster size is probably caused by the increase of the adatom mobility and by the breakdown or decay of small nuclei as a result of ion bombardment. Clusters with a certain subcrystalline size decay into free adatoms under the action of incident ions.[12]

TABLE I. Layer resistance of silicon films grown in different deposition regimes.

No.	T_s, °C	d, μm	V_b, V	R_s, $\Omega/\square$
256	400	0.1	300	2.9×10^9
257	450	0.1	300	1.1×10^8
258	450	0.1	0	9.3×10^9
259	400	0.1	0	1.2×10^{10}
260	400	0.1	150	3.5×10^9
262	400	0.1	0	3.0×10^{10}
263	450	0.5	300	5.7×10^7

The surface diffusion of the adatoms can itself be accelerated by the formation of small collision cascades on the surface. The film growth with uniform-size grains observed in our experiments when ions act on the growth surface is apparently caused by the fact that virtually no new nuclei are generated on the intercluster sections.

Other mechanisms for the effect of ion bombardment on the film structure are also possible, but are less significant for our experiments. For example, the ion flux striking the growth surface has a thermal effect, which is usually appreciable if the energy contributed by the ions exceeds 1 $W/cm^2 \cdot sec$.[11]

How the application of a potential to the substrate affects the electrical conductivity of the films. The experimental observation that the films show reduced resistance when they are grown while a potential is applied to the substrate is associated, in our opinion, with a change in the mechanism by which the dopant (gallium) is captured by the growing silicon layer. When films are grown without applying a potential to the substrate, as in the case of the growth of epitaxial silicon layers, the gallium segregates on its growth surface, and only a small part of it is incorporated into the growing crystal.[13] The application of a potential to the substrate strengthens the bombardment of the growth surface by low-energy ions. When this occurs, some of the gallium ions that appear on the growth surface are incorporated into a grain as recoil atoms.[5] Moreover, the probability that the dopant is incorporated into the crystal is also increased by the strengthening of the surface diffusion of the gallium adatoms. The impurity-capture process can also be activated by the generation of defects when the film surface is bombarded by the incident ions.

CONCLUSIONS

1. Amorphous and polycrystalline silicon films grown by the sublimation of gallium-doped single-crystal silicon on a substrate with a small negative bias have a more nearly perfect structure than do films grown with no bias. The limiting growth temperature that determines the transition from the formation of an amorphous to a polycrystalline structure is reduced in this case. The improvement of the film structure is attributable largely to the strengthening of the surface diffusion of adatoms as a result of ion bombardment of the growth surface.

2. The experimentally observed increase of the electrical conductivity of PSFs grown with a negative potential applied to the surface can be explained by the increase of the probability that the growing layer will capture gallium as a result of bombardment with ions and by the improvement of the structural characteristics of the material.

[1)] The coherent scattering region in polycrystalline materials is often smaller than the grain size and is usually identical with the average size of the blocks into which the grains break up. This size D is computed from the angular broadening of the diffraction maxima Δs, using the Scherrer formula $D = 4\pi k/\Delta s$, where k is the Scherrer constant (≈ 1).

---

[1] F. L. Édel'man, *The Structure of LSI Components* (Nauka, Novosibirsk, 1980).
[2] V. M. Koleshko and A. A. Kovalevskiĭ, *Polycrystalline Semiconductor Films in Microelectronics* (Nauka, Minsk, 1978).
[3] D. A. Pavlov, V. G. Shengurov, D. V. Shengurov, and A. F. Khokhlov, Fiz. Tekh. Poluprovodn. **29**, 286 (1995) [Semiconductors **29**, 142 (1995)].
[4] P. V. Pavlov, V. N. Shabanov, V. G. Shengurov, and A.V. Kozhukhov, Poverkhnost' No. 11, 153 (1990).
[5] V. G. Shengurov and V. N. Shabanov, Poverkhnost' No. 12, 98 (1993).
[6] V. S. Postnikov, I. V. Zolotukhin, V. N. Morgunov, and V. M. Ievlev, Fiz. Met. Metalloved. **29**, 441 (1970).
[7] R. V. Kruzelecky, D. Racansky, S. Zukotynski, Y. C. Koo, and J. M. Peza, J. Non-Cryst. Solids **104**, 237 (1988).
[8] F. S. Lyutovich, Rost Kristallov **14**, 34 (1983).
[9] A. V. Kozhukhov, B. Z. Kanter, S. I. Stenin, B. M. Turovskiĭ, and S. A. Chesnokov, Poverkhnost' No. 3, 160 (1989).
[10] Yu. D. Chistyakov, I. V. Korobov, V. O. Filipenko *et al.*, Elektron. Tekhn. No. 9, 38 (1975).
[11] M. Marinov, Thin Sol. Films **46**, 267 (1977).
[12] H. R. Kaufmann and R. S. Robinson. J. Vac. Sci. Technol. **16**, 179 (1979).
[13] G. E. Beoker and J. C. Bean, J. Appl. Phys. **48**, 3395 (1977).

Translated by W. J. Manthey

Quasi-static capacitance of a MOS-FET upon saturation of the carrier drift velocity

M. V. Cheremisin

A. F. Ioffe Physicotechnical Institute, Russian Academy of Sciences, 194021 St. Petersburg, Russia

(Submitted March 29, 1996; accepted for publication May 5, 1996)
Fiz. Tekh. Poluprovodn. **31**, 296–301 (March 1997)

The effect of the saturation of the carrier drift velocity on the voltage-capacitance characteristics of the gate capacitances C_{gs} and C_{gd} of a MOS transistor has been examined. The voltage-capacitance characteristics are studied analytically for three different approximations of the dependence of the carrier drift velocity on the field, $\nu(E)$. It is shown that the voltage-capacitance characteristic can be computed with satisfactory accuracy by means of a very simple piecewise-linear approximation. On the other hand, the voltage-capacitance characteristics must be computed on the basis of more realistic analytical dependences of $\nu(E)$, since a crude piecewise-linear approximation in this case results in serious errors. A comparison of the experimental voltage-capacitance characteristics with the theoretical results can serve as a criterion for estimating the actual law of saturation of the drift velocity. © *1997 American Institute of Physics.* [S1063-7826(97)00803-X]

1. INTRODUCTION

The analytical modeling of the capacitance characteristics of metal–oxide–semiconductor (MOS) transistors plays an important role in the design and creation of logic circuits and analog circuits. An analysis of the equivalent circuit of an MOS transistor in the small-signal approximation[1,2] shows that the total capacitance $C_{gs}+C_{gd}$, where C_{gs} is the gate–source capacitance and C_{gd} is the gate–drain capacitance, determines its most important parameter—the cutoff frequency. A model of the capacitance in terms of a quasi-static approximation was first proposed by Meyer[1] in 1971. Ward and Datton[3] improved this model by taking into account the charge of the depletion region of the inversion channel of the transistor. The charge induced in the channel was taken into account separately for the source and the drain of the transistor. The calculational technique of Ward and Datton[3] made it possible to achieve the best convergence and accuracy with numerical modelling of the voltage-capacitance characteristics of short-channel transistors.

The most complete and consistent approach to computing capacitance was developed by Shur[4] on the basis of a unified model of charge control.[5] The proposed model made it possible to compute the voltage-capacitance characteristics of a transistor in all the regimes of its operation, from the subthreshold regime to the saturation regime. At the same time, the drift-velocity saturation for carriers in an electric field was consistently disregarded as indicated by Rho *et al.*[4]

The drift-velocity saturation of the carriers is most important in short-channel FETs, where the longitudinal electric field E in the channel can greatly exceed the characteristic saturation field of the carrier drift velocity, E_{sat}. The distribution of the potential, the electric field, and the surface carrier concentration in the transistor channel is completely determined by the $\nu(E)$ dependence. The very simple and widely used piecewise-linear approximation of the carrier drift velocity $\nu(E)$ gives a qualitatively good description of the current-voltage characteristics of a transistor. More accurate analytical dependences only provide quantitative refinements.

As will be shown in this article, the voltage-capacitance characteristics of a transistor, in contrast with the I–V characteristics, are more sensitive to the form of the $\nu(E)$ function. Expressions for the voltage-capacitance characteristics of a transistor operating in the triode regime are obtained on the basis of Meyer's simple model. Three different approximations of $\nu(E)$ are considered, including the piecewise-linear approximation. The use of Meyer's very simple model stems from the fact that it allows one to obtain a clear physical picture and simple analytical expressions for the gate capacitances C_{gs} and C_{gd}. Taking into account the charge of the depletion region of the inversion channel, as in the case of the I–V characteristics, can only slightly refine the resulting voltage-capacitance characteristics.

2. CAPACITANCE OF AN FET IN TERMS OF THE SATURATION MODEL OF THE CARRIER DRIFT VELOCITY

We consider an FET with a channel directed in the x direction with a length of l (Fig. 1, inset). The transistor operates in the triode regime (the substrate is grounded). The thickness d of the subgate insulation layer is much less than the characteristic scale of variation of the potential, l. Under this condition, the approximation of the smooth Schottky channel is applicable. In this approximation the transverse component of the electric field in the channel is much greater than the longitudinal component. The surface concentration n_s of the carriers induced in the channel for the above-threshold regime of operation of the transistor can be written as

$$n_s=\frac{CU}{e}, \tag{1}$$

where e is the elementary charge, $U=U_{gs}(x)-U_t$, $U_{gc}(x)$ is the local voltage between the gate and the channel, U_t is the threshold voltage, and C is the capacitance of the insu-

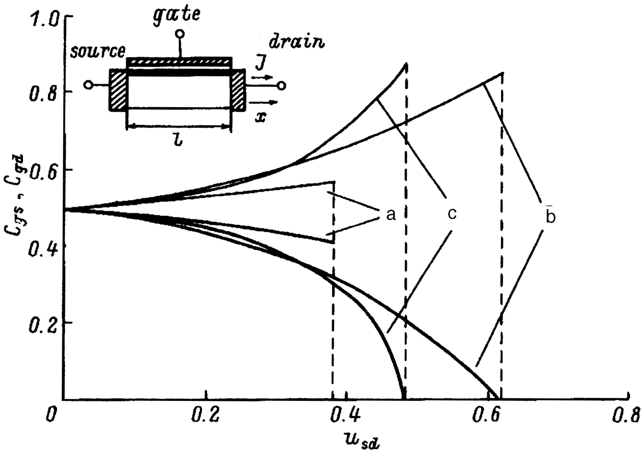

FIG. 1. Voltage–capacitance characteristics of the capacitances C_{gs} (upper curves) and C_{gd} (lower curves) with a parameter value of $\chi=1$ for a—a piecewise−linear approximation ($u_{sd}^{\mathrm{sat}}=0.38$), b—Eq. (8) ($u_{sd}^{\mathrm{sat}}=0.62$), and c—Eq. (14) ($u_{sd}^{\mathrm{sat}}=0.51$).

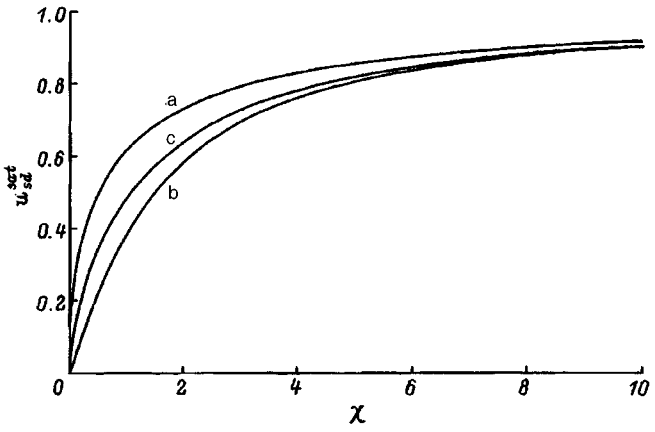

FIG. 2. Source-drain voltage drop u_{sd}^{sat} in the I–V characteristic–saturation regime vs parameter χ for a—the piecewise−linear approximation, b—Eq. (8), c—Eq. (14).

lating layer under the gate per unit area. The current in the conducting channel, using Eq. (1), has the form

$$J=wC\cdot\mu(E)U\cdot E, \tag{2}$$

where w is the width of the device, and $\mu(E)=\nu(E)/E$ is the field dependence of the carrier mobility. Substituting into Eq. (2) the relationship that connects the potential and the field, $E=-dU/dx$, and taking into account the boundary condition at the source, $U(0)=U_s$, it is easy to write the equation for the potential distribution $U(x)$ along the channel. The character of this distribution is completely determined by the form of the approximation of the carrier mobility $\mu(E)$. The dependence of the current in the channel on the source–drain voltage drop $U_{sd}=U_s-U_d$ [where $U_d=U(l)$ is the voltage at the drain] determines the I–V characteristic of the transistor. This dependence can be represented, in general, as a function of the contact voltages—$J=J(U_s,U_d)$.

Following Meyer's model, the total induced charge Q of the inversion layer can be found by integrating the surface concentration n_s of this charge along the channel in the form

$$Q=-wC\int_{U_s}^{U_d}\frac{U}{E}dU, \tag{3}$$

where the longitudinal electric field $E=E(U,J)$ is a function of the current and the local voltage in accordance with Eq. (2). Using Eq. (3), it is easy to find general expressions for the two independent differential gate capacitances C_{gs} and C_{gd}, reduced to the total capacitance of the insulating layer under the gate, $C_0=wCl$.

$$C_{gs}=\left.\frac{\partial Q}{\partial U_s}\right|(U_d=\mathrm{const})=\frac{1}{l}\left[\frac{U_s}{E_s}-\int_{U_s}^{U_d}\frac{\partial}{\partial U_s}\left(\frac{U}{E}\right)dU\right], \tag{4}$$

$$C_{gd}=\left.\frac{\partial Q}{\partial U_d}\right|\Big(U_s=\mathrm{const}\Big)=\frac{1}{l}\left[\frac{U_d}{E_d}-\int_{U_s}^{U_d}\frac{\partial}{\partial U_d}\left(\frac{U}{E}\right)dU\right], \tag{5}$$

where E_s and E_d are the electric fields at the source and the drain, respectively. The computation of the capacitances C_{gs} and C_{gd} from Eqs. (4) and (5) assumes that the spatial distribution of the potential along the channel and the I–V characteristic of the transistor are known. Substituting into Eqs. (4) and (5) the dependence of the local electric field $E=E(U,J)$ following from Eq. (2) and the I–V characteristic in the form $J=J(U_s,U_d)$, it is easy to obtain the voltage-capacitance characteristics of the transistor. These dependences are usually constructed as functions of the voltage U_s on the source for a fixed source–drain voltage drop U_{sd}. In this paper we will use another representation of the voltage-capacitance characteristics, computed for constant voltage U_s on the source and for a variable U_{sd}. The computations will be carried out for two different analytical dependences of mobility $\mu(E)$.

The voltage-capacitance characteristics for the model of a smooth Schottky channel with constant carrier mobility $\mu(E)=\mu_0$ were obtained by Meyer.[1] These characteristics have the form

$$C_{gs}=\frac{2}{3}\left[1-\frac{(1-u_{sd})^2}{(2-u_{sd})^2}\right],\quad C_{gd}=\frac{2}{3}\left[1-\frac{1}{(2-u_{sd})^2}\right], \tag{6}$$

where $u_{sd}=U_{sd}/U_s$. The piecewise-linear approximation[2] of the carrier mobility results in a limitation of these voltage-capacitance characteristics by the source–drain voltage drop u_{sd}^{sat} when the I–V characteristic reaches saturation:

$$u_{sd}^{\mathrm{sat}}=1-\left[1-\frac{(\sqrt{\chi^4+4\cdot\chi^2}-\chi^2)}{2}\right]^{1/2}, \tag{7}$$

where $\chi=2lE_{\mathrm{sat}}/U_s$ is the saturation parameter. Figure 1 (curves a) shows the voltage-capacitance characteristics for a fixed value of the parameter $\chi=1$. The dependences of the voltage u_{sd}^{sat} and the gate capacitances C_{gs}^{sat} and C_{gd}^{sat} in the saturation regime of the transistor on parameter χ are shown in Figs. 2 and 3 (curves a), respectively.

1. Let us consider a more realistic approximation of the mobility $\mu(E)$ in the form

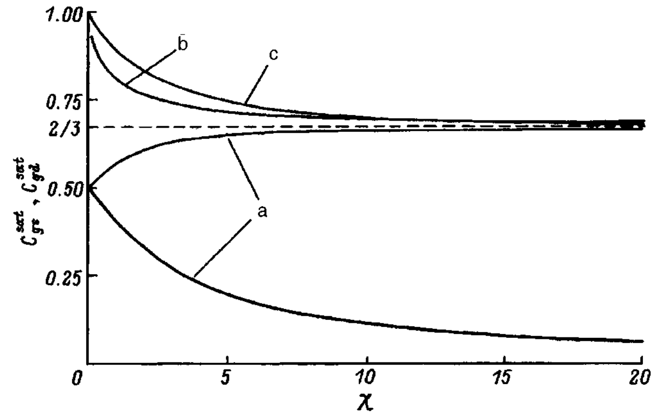

FIG. 3. The dependences of the capacitances C_{gs}^{sat} and C_{gd}^{sat}, (lower curve) in the I-V characteristic—saturation regime vs parameter χ for a–a piecewise-linear approximation of $\mu(E)$, b–Eq. (8), c–Eq. (14).

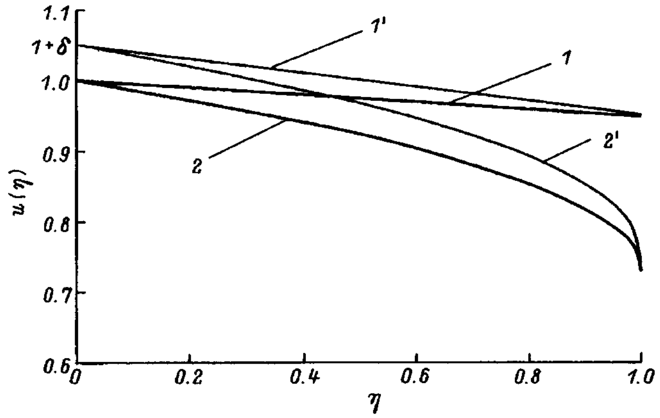

FIG. 4. Potential distribution (*1, 2*) and its redistribution (*1′, 2′*) under the action of a voltage fluctuation δ at the source and a fixed voltage on the drain with $\chi=1$ for an approximation of $\mu(E)$ [Eq. (8)]: *1, 1′*—with $i=0.01$, *2, 2′*—in the saturation regime.

$$\mu(E)=\frac{\mu_0}{(1+E/E_{\text{sat}})}. \tag{8}$$

We introduce the dimensionless values of the local voltage $u=U/U_s$, the length $\eta=x/l$, and the current $i=J/J_0$, where $J_0=CU_s^2w/2l$. Equation (2) can be written as

$$\frac{du}{d\eta}=-\frac{i}{2}\frac{1}{u-u_{\text{sat}}}, \tag{9}$$

where $u_{\text{sat}}=i/\chi$ is the saturation voltage at a given current i. The solution of this equation with the boundary condition at the source of $u(0)=1$ determines the potential distribution along the channel:

$$u(\eta)=u_{\text{sat}}+\left[(1-u_{\text{sat}})^2-i\cdot\eta\right]^{1/2}. \tag{10}$$

Saturation of the carrier drift velocity occurs at the source, where the electric field has the greatest value, approaching infinity as the expression under the radical in Eq. (10) goes to zero. This condition determines the current i_{sat} and the voltage drop u_{sd}^{sat} (Fig. 2, curve *b*) in the saturation regime as a function of parameter χ in the form

$$i_{\text{sat}}=\frac{\chi^2+2\cdot\chi-\sqrt{\chi^4+4\cdot\chi^3}}{2},\qquad u_{sd}^{\text{sat}}=\sqrt{i_{\text{sat}}}. \tag{11}$$

We emphasize that, in the model of Ref. 2, with a piecewise-linear approximation of the mobility, the electric field along the channel actually cannot exceed the value E_{sat}. On the other hand, in the case of the approximation given by Eq. (8), the electric field exceeds this value. This gives a different form of the voltage–capacitance characteristics. Using Eq. (1), we obtain the expression for the I–V characteristic:

$$i=\frac{1-(1-u_{sd})^2}{1+\dfrac{2u_{sd}}{\chi}}. \tag{12}$$

Computing the capacitances C_{gs} and C_{gd} by the procedure described above and the use of Eqs. (9) and (12) gives the result

$$C_{gs}=\frac{2}{3}\left[1-\frac{(1-u_{sd})^2}{(2-u_{sd})^2}+\frac{1+2(1-u_{sd})^3-3(1-u_{sd})^2}{\chi(2-u_{sd})^2}\right],$$

$$C_{gd}=\frac{2}{3}\left[1-\frac{1}{(2-u_{sd})^2}+\frac{1-3u_{sd}-(1-u_{sd})^3}{\chi(2-u_{sd})^2}\right]. \tag{13}$$

These dependences differ from Eq. (6) for a model with constant mobility by the presence of additional terms associated with saturation of the carrier drift velocity. Figure 1 (curves b) shows the voltage–capacitance characteristics for a fixed value of the saturation parameter χ. They are substantially different from the case of piecewise−linear approximation of the mobility. The greatest differences are observed in the saturation regions, which differ for these two cases. Figure 3 (curves b) shows the dependences of the gate capacitances C_{gs}^{sat} and C_{gd}^{sat} in the saturation regime on the saturation parameter χ. The difference, by comparison with the case of the piecewise−linear approximation, is that the gate-drain capacitance is identically equal to zero, while the gate-source capacitance in the case of a short−channel transistor ($\chi\ll1$) has a different limiting value: $C_{gs}^{\text{sat}}=1$. Let us carry out a qualitative treatment of the resulting voltage-capacitance characteristics, based on a simple geometrical interpretation (Fig. 4).

For small current values $i\ll1$, the potential along the channel falls off linearly (Fig. 4, curve *a*). The gate-source capacitance C_{gs} can be found as the ratio of the increment of the total charge Q induced in the channel for fixed drain voltage and source voltages varying by a small amount δ. A simple geometrical construction results in an obvious result: $C_{gs}=1/2$. It can be shown in the same way that $C_{gd}=1/2$.

In short-channel ($\chi\ll1$) transistors in the saturation regime, the potential distribution is virtually uniform (Fig. 4, curve *b*). Therefore, $C_{gs}^{\text{sat}}=1$. At the same time, because of saturation of the drift velocity, the character of this distribution sharply changes close to the drain, where $E_d=du/d\eta|_1=\infty$. This leads to the obvious result that $C_{gd}^{\text{sat}}\equiv0$. Actually, a small variation of the voltage on the drain for a fixed source voltage makes virtually no change in the potential distribution along the channel, $u(\eta)$.

2. Let us consider an approximation of the mobility $\mu(E)$ of the form

$$\mu(E)=\frac{\mu_0}{(1+E^2/E_{\mathrm{sat}}^2)^{1/2}}. \tag{14}$$

In this case, Eq. (2) can be written as

$$\frac{du}{d\eta}=-\frac{i}{2}\,\frac{1}{\sqrt{u^2-u_{\mathrm{sat}}^2}}. \tag{15}$$

The solution of this equation jointly with the boundary condition on the source determines the potential distribution along the channel:

$$F\left(\frac{u}{u_{\mathrm{sat}}}\right)-F\left(\frac{1}{u_{\mathrm{sat}}}\right)=-\frac{\chi\cdot\eta}{u_{\mathrm{sat}}}, \tag{16}$$

where $F(y)=y\sqrt{y^2-1}-\ln(y+\sqrt{y^2-1})$. The I–V characteristic is found by solving Eq. (16) after substituting $\eta=1$. When the potential on the drain reaches values of u_{sat}, the transistor enters the saturation regime. The saturation current i_{sat} can be found in this case from

$$F\left(\frac{\chi}{i_{\mathrm{sat}}}\right)=\frac{\chi^2}{i_{\mathrm{sat}}}. \tag{17}$$

The dependence of the voltage drop at the device vs parameter χ in the saturation regime (Fig. 2, curve *c*) can be found as

$$u_{sd}^{\mathrm{sat}}=1-\frac{i_{\mathrm{sat}}}{\chi}. \tag{18}$$

It can be seen that it differs very little from the case of piecewise-linear approximation of the mobility.

Using Eqs. (4) and (5), the voltage-capacitance characteristics can be obtained only numerically and are shown in Fig. 1 (curves c) for a parameter value of $\chi=1$. The dependence of the gate—source capacitance C_{gs}^{sat} (whereas $C_{gd}^{\mathrm{sat}}\equiv 0$) in the saturation regime vs parameter χ is shown in Fig. 3 (curve c). The form of this dependence substantially differs only from the case of the piecewise-linear approximation.

3. Let us consider the criterion for the applicability of the model of a smooth Schottky channel with a piecewise-linear approximation of the mobility. The condition that the longitudinal field is small by comparison with the transverse field E_y is written as

$$E=-\frac{U_s}{l}\frac{du}{d\eta},\quad E_y=\frac{U_s}{d\cdot\varepsilon_i}\left[u+\frac{U_t}{U_s}\right],\quad E\ll E_y, \tag{19}$$

where ε_i is the permittivity of the subgate layer. The condition given by Eq. (19) determines the limiting value of the voltage drop u_{sd}^{lim} along the channel, up to which the Schottky approximation is valid:

$$u_{sd}^{\mathrm{lim}}=1-\frac{\sqrt{\beta^2+\alpha(1+\alpha)}-\beta}{1+\alpha}, \tag{20}$$

where $\beta=U_t/2U_s$ and $\alpha=\varepsilon_i d/2l$ are dimensionless parameters. The parameter values $\alpha\ll 1$ correspond to a transistor with an infinitely thin insulating layer, in which the Schottky approximation is applicable all the way to the saturation regime. It is easy to write the condition for which the I–V characteristic in the model with a piecewise−linear approximation of the mobility saturates earlier than the Schottky model reaches its limit of applicability; i.e., $u_{sd}^{\mathrm{sat}}<U_{sd}^{\mathrm{lim}}$:

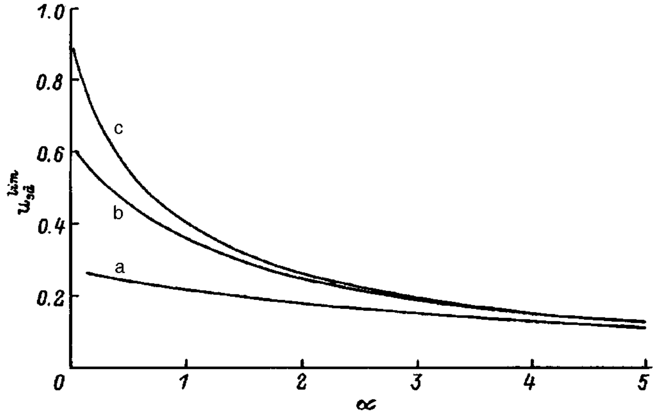

FIG. 5. Limiting voltage drop u_{sd}^{lim} vs parameter α with $\beta=0.25$ for an approximation of $\mu(E)$ [Eq. (8)] with: a—$\chi=0.1$, b—$\chi=1$, and c—$\chi=10$. u_{sd}^{sat}: a—0.27, b—0.62, c—0.92.

$$\chi<\chi_{\mathrm{cr}}=\frac{1-(1-u_{sd}^{\mathrm{lim}})^2}{1-u_{sd}^{\mathrm{lim}}}, \tag{21}$$

where χ_{cr} is the critical value of the saturation parameter, which satisfies the equation $u_{sd}^{\mathrm{sat}}=U_{sd}^{\mathrm{lim}}$.

Using the characteristic parameters of the transistor: $l=1$ μm, $d=350$ Å, and $\varepsilon=4$, the saturation field $E_{\mathrm{sat}}=1.25\times10^6$ V/m, and the voltages $U_s=1$ V and $U_t=0.5$ V, the following estimates can be made: $\beta=0.25$, $\chi=2.5$, $\chi_{\mathrm{cr}}=8.7$, and $\alpha=0.07$. It can be seen that saturation of the drift velocity is extremely important for modern transistors and that Eq. (21) is satisfied. The Schottky approximation is applicable virtually all the way to the saturation regime; i.e., $u_{sd}^{\mathrm{sat}}\approx u_{sd}^{\mathrm{lim}}$.

Let us carry out similar computations for the approximation of the mobility determined by Eq. (8). Using Eqs. (9) and (19), for a given value of the parameters α, β, and χ, we

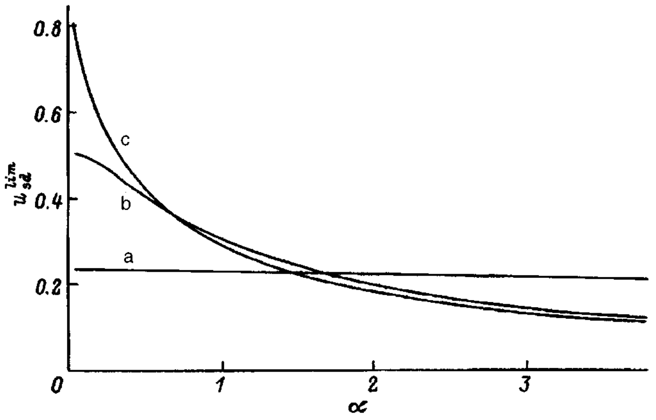

FIG. 6. Limiting voltage drop u_{sd}^{lim} vs parameter α with $\beta=0$ for an approximation of $\mu(E)$ [Eq. (14)] with: *a*—$\chi=0.1$, *b*—$\chi=1$, and *c*—$\chi=10$. u_{sd}^{sat}: *a*—0.24, *b*—0.51, *c*—0.79.

can find the limiting value of the voltage drop u_{sd}^{lim}. Figure 5 shows the dependence of this voltage on parameter α for three fixed values of parameter χ. Note that the Schottky approximation in this case always is inapplicable earlier than the I–V characteristic saturates; i.e., $u_{sd}^{\text{lim}} < u_{sd}^{\text{sat}}$. Despite this circumstance, in an actual transistor $(\alpha \ll 1)$, it can be used virtually all the way to the saturation regime, i.e., $u_{sd}^{\text{sat}} \approx \mathrm{u}_{\mathrm{sd}}^{\mathrm{lim}}$.

For the approximation of the mobility determined by Eq. (14), the results are shown in Fig. 6. For simplicity, the threshold voltage was assumed equal to zero $(\beta = 0)$. In this case, the Schottky approximation is also applicable virtually all the way to the saturation regime, i.e., $u_{sd}^{\text{sat}} \approx u_{sd}^{\text{lim}}$.

3. CONCLUSIONS

Our analysis has shown that the I–V characteristic of an MOS transistor can be computed by using a piecewise−linear approximation of the mobility, whereas analytical dependences provide only a slight quantitative refinement. On the other hand, the voltage–capacitance characteristics are different in these cases. This shows up especially strongly in the saturation region (Fig. 3) for short-channel transistors. In this case, $C_{gs}^{\text{sat}} = 1/2$ and $C_{gd}^{\text{sat}} = 1/2$ for the piecewise-linear approximation, whereas $C_{gs}^{\text{sat}} = 1$ and $C_{gd}^{\text{sat}} = 0$ for the other two approximations of the mobility. It was shown that this is attributable to the qualitative differences in the potential distribution along the channel. Our analysis has shown that the use of a crude piecewise-linear approximation is applicable. Comparison of the experimental voltage–capacitance characteristics with the theoretical results can make it possible to estimate the actual dependence of the carrier mobility on the field.1) It is interesting to determine the cutoff frequency of a transistor on the basis of the resulting voltage–capacitance characteristics.

A study of the criterion for the applicability of the approximation of a smooth Schottky barrier has shown that, for modern transistors with a thin subgate insulating layer, this approximation is valid virtually all the way to the saturation regime for all the approximations used for the mobility.

The author is grateful to M. I. D′yakonov, M. Shur, and M. E. Levinshtein for fruitful discussions and support.

---

1)This possibility was brought to the author′s attention by M. Shur.

[1] J. K. Meyer, RCA Rev. **32**, 42 (1971).

[2] M. Shur, *Physics of Semiconductor Devices* (Prentice−Hall, Englewood Cliffs, N.J., 1990).

[3] D. E. Ward and R. W. Datton, IEEE J. Solid State Circuits, **SC−12** (1978).

[4] K. M. Rho, K. Lee, M. Shur, and T. A. Fjeldly, IEEE Trans. Electron Devices **40**, 131 (1993).

[5] M. Shurm, T. A. Fjeldly, and T. Ytterdal, K. Lee, Solid State Electron. **35**, 1795 (1992).

Translated by W. J. Manthey

Binding energy of shallow donors in asymmetrical systems of quantum wells

V. I. Belyavskiĭ, M. V. Gol'dfarb, and S. V. Shevtsov

Voronezh State Pedagogical University, 394043 Voronezh, Russia

Yu. V. Kopaev

P. N. Lebedev Physical Institute, Russian Academy of Sciences, 117924 Moscow, Russia

(Submitted October 18, 1995; accepted for publication May 14, 1996)
Fiz. Tekh. Poluprovodn. **31**, 302–307 (March 1997)

The dependence of the binding energy of a shallow donor impurity on its position in an asymmetrical system of tunnel-coupled quantum wells is mainly determined by the structure of the one-electron envelope functions and the difference between the dielectric constants of the quantum-well and barrier materials. An effective technique is suggested for calculating the binding energies and envelope functions of the shallow donor states in type-I heterostructures with narrow wells and barriers. We present the results of calculations for $\mathrm{Al}_x\mathrm{Ga}_{1-x}\mathrm{As}$–GaAs structures with two or more quantum wells without imposing any restrictions on the ratios of their sizes. © *1997 American Institute of Physics.* [S1063-7826(97)00903-4]

1. The possibility of fabricating low-dimensional structures in the form of quasi-two-dimensional systems of quantum wells (QW), quasi-one-dimensional quantum wires and quasi-zero-dimensional quantum dots leads to highly diversified and comparatively easily obtained spectra of elementary excitations, both for such systems in isolation and in combination, integrated into nanostructure devices.[1] Additional possibilities in the fabrication of heterostructures (HS) with prescribed properties have been offered by the technology of selective doping.[2] The nature of the arising impurity states is in many ways determined by the peculiarities of the quantum-well electron states inherent to the given heterostructure.

A general qualitative analysis of shallow (Coulomb) impurity states in a two-dimensional ($2D$) system was carried out by Chaplik and Éntin.[3] They obtained an estimate of the binding energy with allowance for the modification of the Coulomb interaction taking place in the $2D$ system. They also estimated the energies and lifetimes of the quasi-stationary impurity states split off from the $2D$ quantum-well subbands (except the lowest). The first theoretical study of a hydrogen-like donor impurity state in an isolated quantum well with infinitely high barriers[4] was later refined in connection with the finite barrier height of the quantum well and the difference in the effective masses and dielectric constants of the materials of the quantum wells and the barrier layers.[5–9] In individual cases more complicated structures have been investigated. They consist, for example, of two identical quantum wells separated by a barrier transparent to tunneling.[10]

Of especial interest, however, are asymmetrical systems of quantum wells. In such structures an effective redislocation of the electron envelope functions in the quantum-well subbands is possible under the action of external fields,[11] which makes it possible to use these structures as multifunctional elements of integrated electronic nanocircuits.[12] Redislocation of the envelopes affects the impurity states[13] and, as a consequence, also affects the position of the Fermi quasi-levels and the filling of the electron subbands.[13] Deep impurity states formed by a maximally localized potential were considered in Ref. 13. In the present paper we examine shallow donor states in asymmetrical heterostructures with quantum wells.

2. As a rule, in the solution of the problem of impurity states in quantum-well heterostructures the variational method is used in the effective mass approximation. This simple, yet convenient approach to the study of shallow (and sometimes quite deep) impurity states in the volume of a semiconductor, where the symmetry of the spatial distribution of the electron density is evident, has substantial limitations when used to calculate impurity states in heterostructures. Indeed, in an asymmetrical heterostructure with two or more quantum wells the electron wave functions can have a very exotic form; for this reason the choice of test functions in the case of such heterostructures is inevitably associated with an increase in the number of variational parameters and a complication of the calculational procedure.

Here, bearing in mind applications to heterostructures with quite narrow quantum wells and barriers, we make use of a technique that has been applied earlier[14,15] to describe exciton states in similar structures. This technique reduces to an expansion of the impurity envelope functions over the $2D$ Wannier basis of electron envelopes in the given heterostructure. Such an approach makes it possible to effectively separate the motion of the electron into transverse and longitudinal (along the heterostructure axis) motion, which significantly facilitates the choice of test envelope functions in the variational procedure. The main details of the design of the heterostructure are taken into account in the calculation: the differences in the effective masses and dielectric constants of the materials of the quantum wells and the barriers, and also effects of nonparabolicity of the conduction band. As usual,[16] the quantum well is represented as a square potential well, and for the effective masses and dielectric constants in the quantum wells and barrier layers we adopt their values in the corresponding bulk semiconductors. This approximation is linked with the presence of two natural and highly different characteristic length scales: it is assumed[16,17] that the effective thickness of the heteroboundary is of the order of magnitude of the interatomic distance, which is several orders of magnitude smaller than the characteristic scale of variation of the external fields applied to the heterostructure. Thus, the effective-mass method is completely applicable in each element of the heterostructure. The solutions in the regions separated by a jump in the potential are joined together with the help of the corresponding boundary conditions. The most commonly used[16,17] are conditions ensuring continuity at the heterojunctions of the envelope functions and the probability flux density calculated in these envelopes.

None of these commonly used approximations, of course, is designed to provide quantitative information about the energy spectrum of the quantum-well system; however, its qualitative analysis within the framework of the envelope-function method in the effective mass approximation almost always leads to completely satisfactory results.[16,17] In particular, it is generally held that the method is quite effective if the characteristic dimensions of the quantum well and barriers exceed about ten angstroms.[17]

3. To classify the electron states in planar quantum-well heterojunctions we may use the set of quantum numbers $\{n,k\}$, where n is the index of the $2D$ quantum-well subband of the conduction band, and k is the quasimomentum of transverse motion. The envelopes of the one-electron wave functions can be represented in the form[17]

$$|n,k\rangle=\frac{1}{\sqrt{S}}\,f_{nk}(z)\exp(ik\rho), \tag{1}$$

where S is the normalization area of the heterostructure, ρ is the transverse component of the radius vector r, the z axis points in the direction of the heterostructure axis, and the $1D$ envelope functions $f_{nk}(z)$ are solutions (for given k) simultaneously of the Schrödinger equation with potential in the form of rectangular quantum wells.[17] These envelope functions (1), which describe single-particle elementary excitations in the electronic subsystem of the heterostructure, can be considered as a set of eigenfunctions of some effective Hamiltonian H_0 which also defines the electron energy spectrum $E_n(k)$ of the given heterostructure:[18]

$$H_0|nk\rangle=E_n(k)|nk\rangle. \tag{2}$$

The presence in the heterostructure of a donor impurity adds an impurity potential $U(r)$ to H_0. The electron envelope function $|\rangle$ is therefore a solution of the equation

$$H|\rangle=E|\rangle, \tag{3}$$

where $H=H_0+U$. As a suitable basis over which to expand the desired function $|\rangle$ we may use the two-dimensional Wannier basis, whose elements are expressed in terms of the wave functions (1) as

$$|n\beta\rangle=\frac{1}{\sqrt{N}}\sum_k \exp(-ik\beta)|nk\rangle. \tag{4}$$

Here the discrete vector index β defines the position of the given unit cell, and N is the number of unit cells in the heterostructure plane.

Expanding the envelope $|\rangle$ over the basis (4)

$$|\rangle=\sum_\beta |n\beta\rangle\langle n\beta|\rangle, \tag{5}$$

we easily obtain a system of equations for the expansion coefficients $\langle n\beta|\rangle$. We easily see that

$$\sum_{n'\beta'}\langle n\beta|H_0|n'\beta'\rangle\langle n'\beta'|\rangle\Rightarrow E_n(-i\nabla)\langle n\beta|\rangle, \tag{6}$$

where ∇ is the gradient operator with respect to the $2D$ variable β, which now is considered as a continuous quantity. To determine the Coulomb interaction energy of the electron with an impurity center, we introduce the electrostatic Green's function $G(r,r')$, which has the meaning of the potential at the point r of a single positive charge located at the point r'. Noting that the effective localization radius of the shallow donors in semiconductors substantially exceeds the lattice constant a and, consequently, the defining contribution to the formation of the envelopes $|\rangle$ comes from a very small region of quasimomenta in the vicinity of the center of the two-dimensional Brillouin zone, $ka\ll 1$, Altarelli[17] points out that the dependence of the one-dimensional envelopes in (1) on k can be disregarded, denoting them simply as $f_n(z)$. It is easy to see that in this case the basis (4) degenerates to a point basis (in the heterostructure plane) layer-modulated by the envelope functions $f_n(z)$. The Coulomb matrix elements between the basis functions (4) can now be represented in the form

$$\langle n\beta|U|n'\beta'\rangle=-\delta_{\beta\beta'}W_{nn'}(\beta,z_0), \tag{7}$$

where

$$W_{nn'}(\beta,z_0)=\int dz f_n^*(z)G(\beta,z,z_0)f_n(z). \tag{8}$$

Here z_0 is the position of the impurity in the heterostructure, and we took into account that $G(r,r')=G(\rho-\rho';z,z')$.

Finally, the system of equations for the expansion coefficients in (5) takes the form

$$[E_n(-i\nabla)-E]\langle n\beta|\rangle=e^2\sum W_{nn'}(\beta,z_0)\langle n'\beta|\rangle. \tag{9}$$

Solution of system of equations (9) allows us in principle to determine the envelope functions and the energy spectrum of the heterostructure with a donor impurity, with allowance for mixing of states split off from all the $2D$ quantum-well subbands. Here the one-dimensional envelopes $f_n(z)$ and the one-electron spectrum $E_n(k)$ carry information about the profile of the $1D$ potential of the given heterostructure and also about the peculiarities of the band structure of the semiconductors forming the heterostructure or, specifically, about their effective masses and the deviation of their dispersion relation from parabolic at small k. The electrostatic Green's function allows for differences in the dielectric constant in the materials of the quantum wells and the barrier layers.

4. It is easy to see that the diagonal matrix elements in (8) are significantly greater than the nondiagonal one for the same β and z_0: $W_{nn}\gg W_{nn'}$, $n\neq n'$. This inequality, which follows directly from the condition of orthogonality of the one-dimensional envelope functions, becomes even stronger

in the case of substantially asymmetrical heterostructures, in which the envelopes corresponding to different quantum-well subbands are, as a rule, localized (for the most part) in different quantum wells. Therefore, in the zeroth approximation, we may neglect the nondiagonal elements in (9) and solve the now independent equations for each n. In this case, a series of energy levels corresponding (in the adopted approximation) to states localized along the axis of the heterostructure splits off from each subband.[3] Further account of the nondiagonal terms in (9) leads to a certain refinement of the energies of such levels (by removing the degeneracy of some of these levels) and to a conversion of all the levels except for those split off from the lowest subband to quasi-stationary levels.[3]

We write the equation defining the contribution in the zeroth approximation $\langle n\beta|0\rangle$ of the nth subband to the envelope function of the state associated with the donor impurity in the form

$$\left[E_n^{(0)}-\frac{\hbar^2}{2m_n}\nabla^2+V_ne^2W_{nn}(\beta,z_0)-E\right]\langle n\beta|0\rangle=0. \quad (10)$$

Here $E_n^{(0)}$ and m_n are the energy (for $k=0$) and effective mass of an electron in the nth subband. The operator V_n, which allows for the nonparabolicity of the nth subband (for small k), can be written in the k-representation as[14,15]

$$V_n=\frac{\hbar^2}{2m_0}b_n^2k^4, \quad (11)$$

where m_0 is the mass of the free electron, and typical values of the phenomenological parameters b_n lie between 10^{-7} and 10^{-6} cm. It is natural to allow for the influence of the operator V_n as a perturbation since the contribution of the envelope functions of the localized states to the binding energy becomes insignificant with increasing k, starting with $k\approx a_l^{-1}$, where a_1 is the characteristic localization radius of the electron at the impurity center. Such an approach allows us to avoid an increase in the order of the differential equation (10) and, correspondingly, the need to formulate additional conditions for the envelopes at the heteroboundaries.

We will find the solution of Eq. (10) by a variational method. It is natural to choose the test envelope function of the ground state in the form of a $2D$ hydrogen-like orbital

$$\langle n\beta|0\rangle=\sqrt{\frac{2\kappa^2}{\pi}}\exp(-\kappa\beta) \quad (12)$$

with the single variational parameter κ. The ground-state energy is determined by the minimum of a functional whose form can be easily found directly from Eq. (10). Thus, the contribution of the second term in Eq. (10) is obviously equal to $\hbar^2\kappa^2/2m_n$. The contribution of the third term in the form (11) is also easily determined:[14]

$$V_n(\kappa)=\frac{\hbar^2b_n^2\kappa^4}{m_0}\left\{\ln\left[1+\left(\frac{\pi}{\kappa a}\right)^2\right]-\frac{3}{2}\right\}. \quad (13)$$

The logarithm in expression (13) is, as usual, the result of truncating the corresponding integrand function at the boundary of the $2D$ Brillouin zone. A simple means of constructing the electrostatic Green's function[19] used in Refs. 14 and 15 in the treatment of excitons in asymmetrical systems of quantum wells can also be applied to the calculation of the contribution of W_{nn} to the energy functional. Here we restrict, the discussion, as in Ref. 19, to an account of terms not higher than first order in the small parameter $\nu=(\varepsilon_1-\varepsilon_2)/(\varepsilon_1+\varepsilon_2)$, where ε_1 and ε_2 are the dielectric constants of the materials of the quantum wells and the barrier layers. The one-electron envelope functions $f_n(z)$ and effective masses m_n in the $2D$ subbands are determined numerically.[19] The procedure for calculating the Coulomb contribution to the functional being varied simplifies substantially if we introduce the universal function[3,14]

$$F(\varsigma)=\varsigma\left\{\frac{\pi}{2}\left[H_1(\varsigma)-Y_1(\varsigma)\right]-1\right\}, \quad (14)$$

where $Y_1(\varsigma)$ and $H_1(\varsigma)$ are the Bessel and Struve functions, respectively, and the argument ς is a linear combination of the integration variable z and the z coordinates of the heterojunctions.[14,19] Note that contributions of any order in ν to the energy functional can be expressed in terms of $F(\varsigma)$.

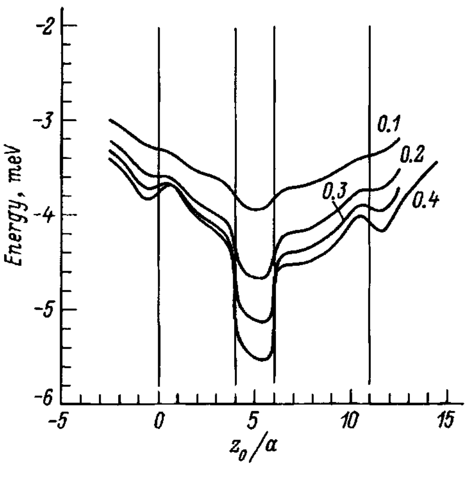

FIG. 1. Dependence of the ground-state energy of the shallow donor on its position in the heterostructure $Al_xGa_{1-x}As$–GaAs 4–2–5. The values of the Al concentration in the barriers (x) is indicated next to the corresponding curves.

5. By (numerically) minimizing the energy functional defined in this way, it is possible to obtain the dependence of the binding energy of a shallow donor on its position z_0 in the heterostructure. The figures presented below gives results of calculations of the binding energy of a shallow donor impurity in the heterostructure $Al_xGa_{1-x}As$–GaAs with two quantum wells separated by a barrier transparent to tunneling; the outer barrier layers are assumed to be semi-infinite. Figure 1 plots the binding energy (in meV) of a shallow donor state that splits off from the lower ($n=1$) $2D$ subband of the conduction band of a 4–2–5 heterostructure (width of the leftmost quantum well equal to $4a$, of the inner barrier, to $2a$, and rightmost quantum well, to $5a$) as a function of the position z_0 of the impurity in the heterostructure. Here and in the following figures the energy is reckoned from the edge of the corresponding subband, each division on the horizontal axis corresponds to the lattice constant $a=5.65$ Å, and the value of the parameter b_n is assumed

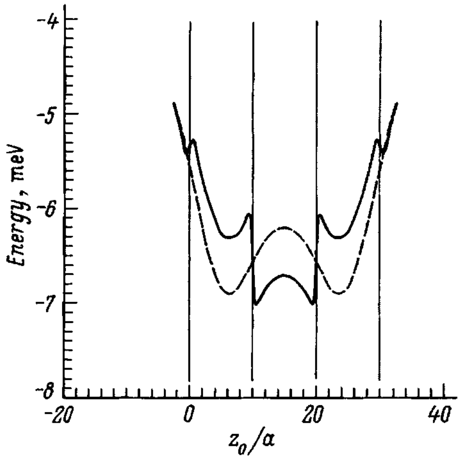

FIG. 2. Dependence of the ground-state energy of the shallow donor on its position in the heterostructure $Al_xGa_{1-x}As$–GaAs 10–10–10. The dashed curve was calculated without allowing for the difference between the dielectric constants of the quantum-well and barrier materials.

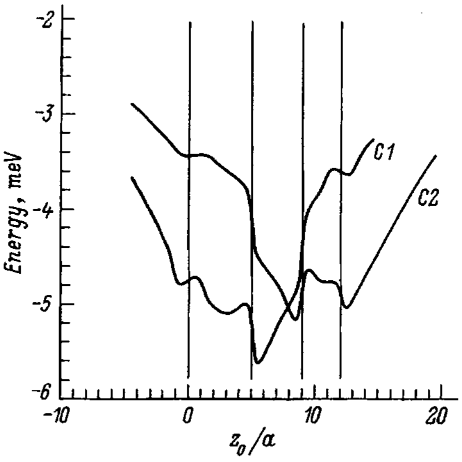

FIG. 3. Dependence of the ground-state energy of the shallow donor on its position in the heterostructure $Al_{0.3}Ga_{0.7}As$–GaAs 5–4–3. The curves $C1$ and $C2$ correspond to the states split off from the first and second quantum-well subbands; the energy in each case is reckoned from the edge of the corresponding subband.

equal to 25 Å. The numbers beside the curves in Fig. 1 indicate the Al concentration in the barrier layers ($x=0.1$, 0.2, 0.3, 0.4). The dependence of the binding energy on z_0 is a complicated nonmonotonic function with a very deep minimum corresponding to the inner barrier. This has to do with the fact that the dielectric constant in the barriers is less than in the quantum wells and with the extremely large value of the one-electron envelope for $n=1$ in the maximally narrow ($2a$) inner barrier. The minima near the outer heterojunctions are due mainly to the spatial dependence of the dielectric constant. The dependence of the binding energy on x is governed by two factors—a deepening of the quantum wells with growth of x accompanied by an increase in the degree of localization of the $1D$ envelope, and a growth of the parameter ν.

The conclusion that the binding energy of an electron at an impurity center located in the barrier can exceed the binding energy of an electron for an impurity center inside one of the quantum wells is not unexpected, and specifically for the reason that in asymmetrical systems of quantum wells the envelope functions in the inner (narrow) barriers can have values comparable with their values in the quantum wells. Therefore, an account of the difference in the dielectric properties of the quantum-well and barrier materials can lead to a considerable change in the binding energy, in particular, if we note that in the heterostructure $Al_xGa_{1-x}As$–GaAs for $x\approx 0.4$ this difference reaches a value of about 10% and cannot, in general, be assumed to be negligible. In this regard, note that in a periodic superlattice[20] as in a symmetrical system of quantum wells (Fig. 2), the envelope function of the lower subband has a noticeable minimum in the barrier region; therefore, an account of the difference in dielectric constants cannot lead to a qualitative change in the nature of the dependence of the binding energy on the position of the impurity in a superlattice or a system of quantum wells.

Figure 3 plots data for a 5–4–3 heterostructure with $x=0.3$. The curves denoted $C1$ and $C2$ correspond to the ground-state energy and are split off from the subbands with $n=1$ and $n=2$. The visible asymmetry of the two curves is clearly linked with the asymmetry of the envelopes $f_1(z)$ and $f_2(z)$: the first of them is concentrated mainly in the left-hand (wider) quantum well, whereas the main extremum of the second curve is located in the region of the narrower quantum well. A heterostructure with still stronger localization of the $1D$ envelopes, 8–4–4, demonstrates a respectively stronger dependence of the binding energy of the donor state on z_0 (Fig. 4).

6. The value of the binding energy found in the zeroth approximation based on Eq. (10) can be refined if we take into account the nondiagonal elements on the right side of Eq. (9) in terms of perturbation theory. Below, for simplicity, we restrict the discussion to the two lower $2D$ subbands with $n=1$ and $n=2$. In this case we can write Eq. (9) as

$$(E-H_1)\psi_1=H_{12}\psi_2, \quad (E-H_2)\psi_2=H_{21}\psi_1. \tag{15}$$

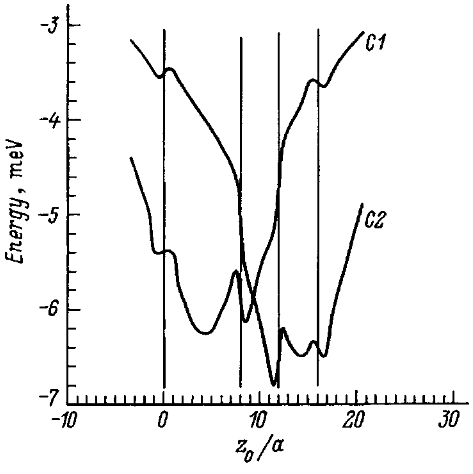

FIG. 4. Dependence of the ground-state energy of the shallow donor on its position in the the heterostructure $Al_{0.3}Ga_{0.7}As$–GaAs 8–4–4. The curves $C1$ and $C2$ correspond to the states split off from the first and second quantum-well subbands; the energy in each case is reckoned from the edge of the corresponding subband.

Here $H_n = E_n(-i\nabla) - e^2 W_{nn}$, $H_{nn'} = -e^2 W_{nn'}$ for $n \neq n'$, $\psi_n \equiv \langle n\beta | \rangle$. Introducing the Green's function operators $G_n(E) = (E - H_n)^{-1}$, we can transform system of equations (15) into the equivalent equation

$$(H_1 + H_{12} G_2(E) H_{21}) \psi_1 = E \psi_1, \tag{16}$$

which formally resembles the Schrödinger equation, but contains an additional energy-dependent term in the potential, $H_{12} G_2(E) H_{21}$. We represent the ground-state energy in the form $E = E_{10}^{(0)} + E_{10}^{(1)}$, where $E_{10}^{(0)}$ is the solution of Eq. (10) for $n = 1$, and the first correction to the energy, $E_{10}^{(1)}$ is found from perturbation theory

$$E_{10}^{(1)} = \langle \psi_1^{(0)} | H_{12} G_2(E_{10}^{(0)}) H_{21} | \psi_1^{(0)} \rangle. \tag{17}$$

Here $\psi_n^{(0)} \equiv \langle n\beta | \rangle$, the argument E in the Green's function operator has been replaced by its zeroth approximation $E_{10}^{(0)}$, and the bracket notation in Eq. (17) denotes integration over β. It is easy to see that $E_{10}^{(1)} < 0$, i.e., that taking account of the second subband leads to some deepening of the donor impurity ground-state energy level that has split off from the first subband. Indeed, the sign of the expression on the right-hand side of Eq. (17) coincides with the sign of the energy denominator of the Green's function. Similar arguments show that the ground-state level split off from the second subband under the influence of the states of the first subbands, in contrast, becomes shallower, i.e., it has a tendency to approach the edge of the subband with $n = 2$. In the case of heterostructures with sufficiently narrow quantum wells and barriers it is easy to make an order-of-magnitude estimate of the level shift due to the intersubband interaction. As was already noted, the magnitude of the matrix element of the operator H_{12} is in any case less than the characteristic Coulomb energy $\mathrm{Ry}^{(n)} = m_n e^4 / 2\varepsilon^2 \hbar^2$, where ε is the average dielectric constant of the structure. The magnitude of the energy denominator of the Green's function in expression (17) can be estimated as $\Delta_{21} = E_2^{(0)} - E_1^{(0)}$ provided that $\Delta_{21} \gg \mathrm{Ry}^{(n)}$. This condition is obviously satisfied in the case of quantum wells and barriers of nanometer dimensions. Therefore,

$$\frac{|E_{10}^{(1)}|}{\mathrm{Ry}^{(1)}} < \frac{\mathrm{Ry}^{(1)}}{\Delta_{21}}; \tag{18}$$

and an analogous inequality holds for $E_{20}^{(1)}$. In this sense, it may be said that in nanostructures the Coulomb series of donor impurity levels are "suspended" from each of the quantum-well subbands.

7. Clearly, allowance for the finite number of quantum-well subbands cannot significantly affect inequality (18). It is necessary, however, to estimate the contribution to the binding energy of the quasi-continuum of states of the conduction band. Toward this end, we can use system of equations (9), which to second order in the nondiagonal matrix elements of the Coulomb interaction operator leads to an equation for the ground-state energy of the donor impurity:

$$(E - E_{10}) = \sum_{n \neq l} \sum_{\nu} \frac{|\langle 10 | W_{\mathrm{ln}} | n\nu \rangle|^2}{E - E_{n\nu}}. \tag{19}$$

Here $|n\nu\rangle$ is the donor-state envelope function which corresponds to the nth quantum-well subband, $\{\nu\}$ is the set of transverse quantum numbers passing over in the continuum to the transverse quasimomentum (just as n passes over in this case to the longitudinal quasimomentum). Note that in the two-subband approximation (15) expression (19) becomes exact.

We restrict the analysis to the case of sufficiently narrow systems of quantum wells, in which their characteristic size $d < a_1$, where a_1 is the effective $2D$ Bohr radius of the donor state split off from the first subband. In addition, we assume that the quantum wells are so deep that their depth $\Delta E_c \gg \hbar^2 / 2 m_c d^2$; here m_c is the effective mass of the conduction band. Under these conditions a rough upper estimate of the contribution of the quasi-continuum in Eq. (19) is

$$(E - E_{10})_{\mathrm{cont}} \sim -\mathrm{Ry}^{(1)} \left(\frac{d}{a_1} \right)^2 \ln \left[1 + \frac{a}{d} \frac{E_c}{\Delta E_c} \right]. \tag{20}$$

Here $E_c \approx \pi \hbar^2 / m_c a^2$ is a characteristic energy of the order of the width of the conduction band, and a is the lattice constant. The logarithmic dependence of the binding energy on the band width of the quasi-continuum of states allows us to ignore the contribution of these states, at least in the case of relatively narrow systems of quantum wells, when $d < z_1$.

8. For uniformly doped heterostructures a certain set of Coulomb level series is associated with the donor impurity, where these levels are due to the impurities located in each monolayer of the heterostructure. This circumstance may be the reason for the broadening and attenuation of the impurity bands in the optical spectra of the heterostructures, and may also limit the possibility of controlling the location of the Fermi quasilevels with the help of an external electric field in comparison with deep impurities.[13]

In conclusion, we note that in heterostructures with maximally narrow quantum wells and barriers [with width in the range $(2-3)a$] the binding energy of a shallow donor, as a rule, is significantly less than its $2D$ limiting value; its magnitude is mainly determined by the geometry of the heterostructure [via the one-electron spectrum $E_n(k)$ and the one-dimensional envelopes f_n] and the difference in the dielectric properties of the components of the heterostructure due to modification of the Coulomb interaction and formation of a charge-image field.

This work was carried out with the support of the Russian Foundation for Basic Research and the Russian Ministry of Scientific and Technological Programs within the scope of the program "Physics of Solid-State Nanostructures." One of the authors (V. Belyavskiĭ) is grateful to ISSEP for support of this work (Grant No. 824-p).

[1] H. Sakaki, Solid State Sci. **97**, 2 (1991).
[2] R. Dingle, H. L. Störmer, A. C. Gossard, and W. Wiegmann, Appl. Phys. Lett. **33**, 665 (1978).
[3] V. A. Chaplik and M. V. Éntin, Zh. Éksp. Teor. Fiz. **61**, 2496 (1971) [Sov. Phys. JETP **34**, 1335 (1971)].
[4] G. Bastard, Phys. Rev. B **24**, 4714 (1981).
[5] R. L. Greene and K. K. Bajaj, Solid State Commun. **45**, 825 (1983).
[6] T. Tanaka, N. Nagaoka, and T. Yamabe, Phys. Rev. B **28**, 7068 (1983).
[7] W. Lu and J. J. Quinn, Phys. Rev. B **31**, 2348 (1985).
[8] C. Mailhot, Y. C. Chang, and T. C. McGill, Phys. Rev. B **26**, 4449 (1982).

[9] S. Fraizzoli, F. Bassani, and R. Buczko, Phys. Rev. B **41**, 5096 (1990).

[10] D. B. Tran Troai, Physica B **175**, 373 (1991).

[11] A. A. Gorbatsevich, V. V. Kapaev, and Yu. V. Kopaev [JETP Lett. **57**, 596 (1993)].

[12] A. A. Gorbatsevich, V. V. Kapaev, Yu. V. Kopaev, and V. Yu. Kremlev, Phys. Low-Dimens. Struct. **5**, 57 (1994).

[13] V. I. Belyavskiĭ, Yu. V. Kopaev, N. V. Kornyakov, and S. V. Shevtsov, [JETP Lett. **61**, 1039 (1995)].

[14] V. I. Belyavskiĭ, Yu. V. Kopaev, S. T. Pavlov, and S. V. Shevtsov, Pis'ma [JETP Lett. **61**, 292 (1995)].

[15] V. I. Belyavsky, Yu. V. Kopaev, and S. V. Shevtsov, Solid State Commun. **94**, 715 (1995).

[16] G. Bastard, J. A. Brum, and R. Ferreira, Solid State Phys. **44**, 229 (1990).

[17] M. Altarelli, Springer Proc. Phys. **25**, 170 (1988).

[18] D. A. Broido and L. J. Sham, Phys. Rev. B **34**, 3917 (1986).

[19] V. I. Belyavskiĭ, Yu. V. Kopaev, N. V. Kornyakov, and S. V. Shevtsov, Fiz. Tverd. Tela **37**, 3147 (1995) [Semiconductors **37**, 1734 (1995)].

[20] E. L. Ivchenko and A. V. Kavokin, Fiz. Tekh. Poluprovodn. **25**, 1780 (1991) [Sov. Phys. Semicond. **25**, 1070 (1991)].

Translated by Paul F. Schippnick

Nonlinear conductivity and current–voltage characteristics of two-dimensional semiconductor superlattices

Yu. A. Romanov and E. V. Demidov

Institute for the Physics of Microstructures, Russian Academy of Sciences,
603600 Nizhniĭ Novgorod, Russia

(Submitted December 25, 1995; accepted for publication May 20, 1996)
Fiz. Tekh. Poluprovodn. **31**, 308–310 (March 1997)

Electron transport and heating in a two-dimensional semiconductor superlattice with arbitrary orientation of the field (current) relative to the crystallographic axes is investigated in the approximation of constant energy and velocity relaxation times with electron–electron collisions taken into account. The nonlinear conductivity, average electron energies, and interrelationship between field direction and the current excited by it in an unbounded superlattice, as well as the current-voltage characteristics and the transverse electromotive force of a superlattice of finite width are found.
[S1063-7826(97)01003-X]

Studies of electron transport in superlattices (SL) usually employ the classical Boltzmann equation with one constant relaxation time of the electron distribution function. In this approximation the motions of the electrons along the crystallographic axes of the superlattice are independent and therefore its electrical characteristics (in the absence of a magnetic field) can be obtained by a simple superposition of the characteristics of one-dimensional superlattices. This, in particular, pertains to the results on self-induced transparency of two-dimensional and three-dimensional superlattices,[1] which are identical in this approximation to the corresponding known results for one-dimensional superlattices.[2–4] This also pertains to the effect of the transverse electromotive force.[5]

However, in real relaxation processes the degrees of freedom of the electron are not independent since its states vary interdependently and mix in all three directions. Therefore, the indicated τ-approximation can even lead to qualitatively inaccurate results. This is the case with the heating of an electron gas. For example, this approximation gives zero electron heating in the direction perpendicular to the field if the latter is directed along the superlattice axis. It does not help to introduce two different relaxation times for the distribution function (i.e., for its symmetric and antisymmetric parts) if they pertain to only one degree of freedom of the electron.[4,6]

The present paper examines transport and heating of the electrons of a two-dimensional superlattice with square symmetry (SL-2) on the basis of the Boltzmann equation with a new model collision integral. The latter contains three relaxation times: $\tau_1(\varepsilon)$ is the randomization time of the direction of the electron momentum, without change of energy ε (the characteristic setup time of the uniform electron distribution on the isoenergy surface due to elastic collisions); $\tau_\varepsilon(\varepsilon)$ is the relaxation time of the electron energy, which describes its transitions between the isoenergy surfaces, and $\tau_{ee}(\varepsilon)$ is the inverse electron–electron collision frequency. In accordance with the abovesaid, we have

$$\frac{\partial f(\mathbf{k},t)}{\partial t}+\frac{e\mathbf{E}}{h}\,\frac{\partial f(\mathbf{k},t)}{\partial k}=-\left(\frac{\partial f}{\partial t}\right)_{\rm col}, \tag{1}$$

$$\left(\frac{\partial f}{\partial t}\right)_{\rm col}=\frac{f(\mathbf{k},t)-\overline{f^s}(\varepsilon,t)}{\tau_1(\varepsilon)}+\frac{f(\mathbf{k},t)-f_0(\varepsilon,T_e)}{\tau_{ee}(\varepsilon)}+\frac{f(\mathbf{k},t)-f_0(\varepsilon,T_0)}{\tau_\varepsilon(\varepsilon)}, \tag{2}$$

where $f(\mathbf{k},t)$ is the field-perturbed electron distribution function, $f^s(\varepsilon,t)$ is the electron distribution function averaged over the equipotential surfaces, $f_0(\varepsilon,T_e)$ and $f_0(\varepsilon,T_0)$ are the equilibrium electron distribution functions with effective temperature T_e and lattice temperature T_0, respectively; $\mathbf{k}$ is the wave vector, and E is the electric field. The temperature T_e is determined by the condition of equality of the mean electron energies described by the distribution $f(\mathbf{k},t)$ and $f_0(\varepsilon,T_e)$. The first and second ($T_e \neq T_0$) terms in Eq. (2) ''mix'' all the degrees of freedom of the electron, which is the fundamental difference between the given approach and that of Refs. 1–6. It is important to emphasize that the electron–electron collisions in superlattices are accompanied, as a rule, by Peierls distortions and therefore lead to randomization of the direction of the momentum and velocity of the electrons (additional resistance), which is reflected in Eq. (2). Such collisions cannot have as their result a momentum shift of the Fermi distribution function.[7] Note that in the case of nonuniform fields the collision integral (2) must be revised to allow for the conservation laws.

The dispersion relation of the electrons of an SL-2 superlattice in the tight-binding approximation has the form

$$\varepsilon(k_1,k_2)=\varepsilon_1(k_1)+\varepsilon_2(k_2)=(\Delta/2)(1-\cos k_1 d)+(\Delta/2)(1-\cos k_2 d), \tag{3}$$

where d is the period of the SL-2 superlattice, $\hbar k_{1,2}$ are the components of the quasimomentum of the electron along its crystallographic axes x_1 and x_2, respectively, and 2Δ is the energy width of the two-dimensional miniband. We assume that electron motion along the x_3 direction (the third degree of freedom) is ''frozen.'' The nonadditive dispersion relation used in Refs. 1 and 5 reduces to the above dispersion relation by rotating the coordinate system through an angle of $\pi/4$ radians.

For simplicity we assume that the times τ_1, τ_ε, and τ_{ee} are independent of the energy. In the stationary case the electric current and electron heating, according to Eqs. (1) and (2), are given by

$$j_{1,2}=\frac{\sigma_0+[1+(E_{2,1}/E_0)^2]E_{1,2}}{1+(1/2)[1+(\tau_\varepsilon/\tau_p)](E/E_0)^2+(\tau_\varepsilon/\tau_p)(E_1E_2/E_0^2)^2}, \tag{4}$$

$$\langle\Delta\varepsilon_{1,2}\rangle\equiv\langle\varepsilon_{1,2}\rangle-\frac{\langle\varepsilon\rangle_0}{2}=\frac{\sigma_0\tau_\varepsilon E^2}{2n}\times\frac{[1+(1/2)(E/E_0)^2\sin^2 2\theta\pm(\tau_p/\tau_\varepsilon)\cos 2\theta]}{1+(1/2)[1+(\tau_\varepsilon/\tau_p)](E/E_0)^2+(\tau_\varepsilon/\tau_p)(E_1E_2/E_0^2)^2}, \tag{5}$$

where $\sigma_0=ne^2d^2\tau_p/2\hbar^2$ $(\Delta-\langle\varepsilon\rangle_0)$ is the linear conductivity of the SL-2 superlattice, $E_0=\hbar/ed\tau_p$ is the effective field, θ is the angle between the field vector and the crystallographic axis x_1, $\tau_p^{-1}=\tau_1^{-1}+\tau_\varepsilon^{-1}+\tau_{ee}^{-1}$ is the inverse relaxation time of the electron velocity, the angle brackets $\langle\rangle$ and $\langle\rangle_0$ denote the averages with respect to the perturbed and equilibrium electron distribution functions, respectively, and n is the electron concentration.

Relation (5) indicates substantial electron heating in the direction transverse to the current. Even in a field directed along a crystallographic axis (e.g., x_1) heating in the direction perpendicular to it and the current (the x_2 direction) is large. The ratio of the corresponding increments of the mean energies in this case is

$$\gamma\equiv\frac{\langle\Delta\varepsilon_2\rangle}{\langle\Delta\varepsilon_1\rangle}=\frac{\tau_\varepsilon-\tau_p}{\tau_\varepsilon+\tau_p}. \tag{6}$$

For $\tau_\varepsilon=3\tau_p$, $\gamma=0.5$. For $\tau_\varepsilon\gg3\tau_p$ heating becomes isotropic. In the limit of strong fields and $\theta\neq0$, $\pi/2$ the electrons are uniformly distributed in the miniband.

In general, the vectors **j** and **E** are noncollinear. Their mutual orientation is given by

$$\tan\varphi=\tan\theta\,\frac{1+(E/E_0)^2\cos^2\theta}{1+(E/E_0)^2\sin\theta}, \tag{7}$$

where φ is the angle between the current density vector **j** and the crystallographic axis x_1. The plots of $\varphi(\theta)$ are shown in Fig. 1. Note that the dependence $\varphi(\theta)$ is a universal function of the dimensionless field E/E_0 and does not depend on the ratio τ_ε/τ_p.

For given $E>\sqrt{2}E_0$, three field directions, one of which is unstable, can correspond to a fixed current direction. The SL-2 symmetric direction $\varphi=\pi/4$ is special. Due to the transverse negative differential conductivity, the field direction with $\theta=\pi/4$ is unstable for $E>\sqrt{2}E_0$, and electric fields transverse to the current arise in the SL-2 superlattice. This effect was considered in Ref. 1 for $\tau_\varepsilon=\tau_p$. From the macroscopic point of view it is analogous to the Erlbach effect[8] in multivalley semiconductors, but is a higher-frequency effect since it is governed not by intervalley scattering, but by the dynamics of the electron in the narrow miniband.

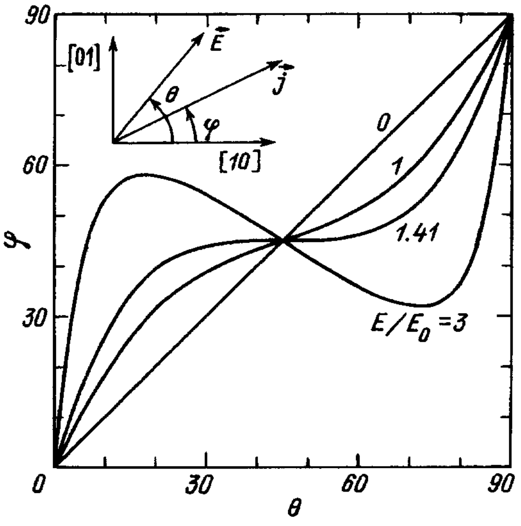

FIG. 1. Dependence of the direction of the current density vector **j** on the direction of the electric field **E**. The numbers next to the curves are the values of E/E_0.

Let us now consider the current–voltage characteristic of an SL-2 superlattice of finite width. Let the x_1 axis make an angle φ with respect to the boundaries of the wafer. For definiteness, we take $|\varphi|<\pi/4$. We will not consider domain formation here; we will assume, therefore, that the field in the sample is homogeneous. The dependence of the current $j(E_\parallel)$ and transverse field $E_\perp(E_\parallel)$ on the stretching field $E_\parallel$ in the sample can be found from Eqs. (4) and (5) and the condition that the transverse current vanishes. These dependences are shown in Figs. 2 and 3. Branches *3* and *3′* are unstable relative to transverse perturbations of the field.

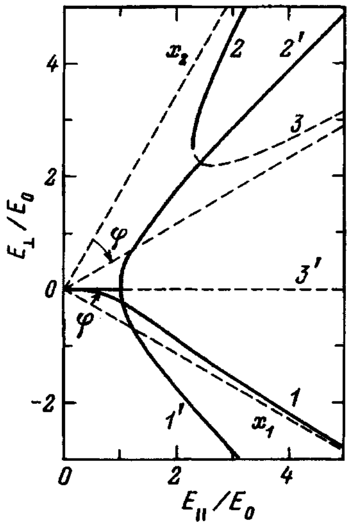

FIG. 2. Dependence of the transverse field $E_\perp$ in a superlattice of finite width on the applied stretching field $E_\parallel$ for $\varphi=30°$ (curves *1–3*) and $\varphi=45°$ (curves *1′–3′*). Asymptotes of the curves are shown for $\varphi=30°$.

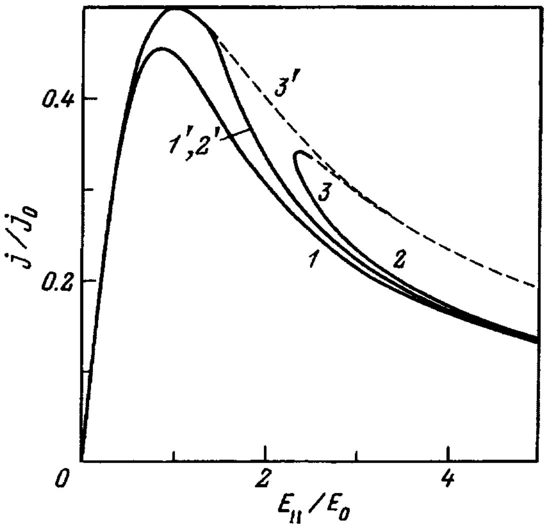

FIG. 3. Current–voltage characteristics of a superlattice of finite width for $\varphi=30°$ (curves *1–3*) and $\varphi=45°$ (curves *1′–3′*); $\tau_\varepsilon/\tau_p=2$.

The orientation $\varphi=45°$ is important and simple to calculate. For it

$$j^{(1,2)}=\frac{2\sigma_0E_0^2}{(1+\tau_\varepsilon/\tau_p)E_\parallel},\qquad E_\perp^{(1,2)}=\pm\sqrt{E_\parallel^2-2E_0^2},\qquad E_\parallel>\sqrt{2}E_0, \tag{8}$$

$$j^{(3)}=\frac{\sigma_0E_\parallel}{1+(\tau_\varepsilon/\tau_p)(E_\parallel/E_0)^2},\qquad E_\perp^{(3)}=0,$$

$$\frac{j_{\max}^{1,2}}{j_{\max}^{(3)}}=\frac{2\sqrt{\tau_\varepsilon/\tau_p}}{1+\tau_\varepsilon/\tau_p}. \tag{9}$$

For this orientation in the field region $\sqrt{2\tau_p/\tau_\varepsilon}<E_\parallel<\sqrt{2}E_0$ there exists only one differential conductivity, and in the region $E>\sqrt{2}E_0$ there exist two—a longitudinal and a transverse conductivity. In the first region $E_\perp=0$ and therefore ordinary strong- and weak-field Gunn domains arise. With an increase in the ratio τ_ε/τ_p, the first region increases in the direction of smaller fields and the splitting of the current-voltage characteristic disappears, but the dependence of the transverse electromotive force on $E_\parallel/E_0$ remains constant. Since the currents in the second region in this case are relatively small, it is difficult to attain the regime of ''skew'' domains.[9,10] Qualitatively, such a situation takes place for all angles φ. Therefore, in the case $\tau_\varepsilon\gg\tau_p$ anisotropy effects, including the transverse electromotive force, are hard to observe since they are suppressed by the longitudinal current instability arising in fields when the anisotropy of the SL-2 conductivity is still small.

This work was carried out with the financial support of the Russian Fund for Fundamental Research.

[1] G. M. Shmelev and É. M. Épshteĭn, Fiz. Tverd. Tela **35**, 494 (1993) [Phys. Solid State **35**, 256 (1993)].
[2] Yu. A. Romanov, Fiz. Tekh. Poluprovodn. **5**, 1434 (1971) [Sov. Phys. Semicond. **5**, 1256 (1971)].
[3] A. A. Ignatov and Yu. A. Romanov, Fiz. Tverd. Tela **17**, 3388 (1975) [Sov. Phys. Solid State **17**, 2216 (1975)].
[4] A. A. Ignatov and Yu. A. Romanov, Phys. Solid State B **73**, 1106 (1977).
[5] G. M. Shmelev and É. M. Épshteĭn, Fiz. Tverd. Tela **34**, 2565 (1992) [Sov. Phys. Solid State **34**, 1375 (1992)].
[6] S. A. Ktitorov, G. S. Simin, and V. Ya. Sindalovskiĭ, Fiz. Tverd. Tela **13**, 2230 (1971) [Phys. Solid State **13**, 1872 (1971)].
[7] X. L. Lei, N. J. M. Horing, and H. L. Cui, Phys. Rev. Lett. **66**, 3277 (1993).
[8] E. Erlbach, Phys. Rev. **132**, 1976 (1963).
[9] Z. S. Gribnikov, Zh. Éksp. Teor. Fiz. **83**, 718 (1982) [Sov. Phys. JETP **56**, 401 (1982)].
[10] M. Ashe, Z. S. Gribnikov, V. V. Mitin, and O. G. Sarbeĭ, *Hot Electrons in Multivalley Semiconductors* [in Russian] (Kiev, 1982).

Translated by Paul F. Schippnick

Fabrication of blocked impurity-band structures on gallium-doped silicon by plasma hydrogenation

V. M. Émeksuzyan, G. N. Kamaev, G. N. Feofanov, and V. V. Bolotov

Institute of Semiconductor Physics, Siberian Branch of the Russian Academy of Sciences,
630090 Novosibirsk, Russia
Institute of Sensor Micro-Electronics, Siberian Branch of the Russian Academy of Sciences,
644077 Omsk, Russia

(Submitted May 22, 1995; accepted for publication May 22, 1996)
Fiz. Tekh. Poluprovodn. **31**, 311–317 (March 1997)

The electrical characteristics of blocked impurity-band structures (BIB-structures) based on gallium-doped silicon ($N_{\mathrm{Ga}} \approx 5 \times 10^{17}$ cm^{-3}) are investigated. The blocking layers were formed by passivation of the gallium impurity by means of treatments in an rf-discharge hydrogen plasma at substrate temperatures $T = 20$–220 °C. It is found that the activation energy E_a of the hopping conductivity with hopping between nearest gallium neighbors decreases from 8.7 meV (before hydrogenation) to 1.3 meV (after hydrogenation at $T = 220$ °C). The current–voltage characteristics and temperature dependence of the dark current of the structures and their change after isochronal ($t = 20$ min) annealing at temperatures $T = 220$–400 °C are determined. The current–voltage characteristics of the structures at low temperatures are calculated. The results of calculations are found to agree with experimental data.
[S1063-7826(97)01103-4]

1. INTRODUCTION

At low temperatures in partially compensated silicon doped with impurities with shallow levels with concentration $N_s \sim 10^{17} - 10^{18}$ cm^{-3}, hopping conductivity is observed with hopping between nearest neighbors or with variable hopping length.[1–4] The presence of hopping conductivity leads to the appearance of large dark currents in photoresistances fabricated in a doped semiconductor, and thereby to a reduction of their detecting power.[5–7] With the aim of suppressing dark currents in semiconductor photodetectors in heavily doped materials, we propose variants of blocked-impurity band (BIB) structures.[5–11]

In a previous paper[12] we proposed a way to attain this goal and considered the electrical characteristics of BIB structures in which the blocking layers were obtained by hydrogenation in boiling distilled water. As is well known,[13–17] passivation of shallow donor and acceptor states and formation of electrically neutral complexes $(\mathrm{A}^-\mathrm{H}^+)^0$ and $(\mathrm{D}^+\mathrm{H}^-)^0$ takes place in such layers. In this paper our goal is to examine the possibility for the formation of structures with blocked hopping conductivity on the surface of gallium-doped silicon by means of hydrogenation in a hydrogen plasma, and to investigate and describe the electrical properties of these structures.

2. EXPERIMENTAL TECHNIQUE

In this work we used p-type silicon wafers of thickness $d = 380$ μm grown by zone melting and doped with gallium $[N_{\mathrm{Ga}} = (2-5) \times 10^{17}$ cm$^{-3}]$. Ohmic contacts on the nonplanar side of the structures were created by implantation of B$^+$ ions with energy $E = 100$ keV and dose $\Phi = 1.9 \times 10^{15}$ cm^{-2} with subsequent thermal annealing at $T = 1000$ °C for $t = 0.3$ h and Cr+Au metallization at 200 °C. The planar side of the wafers was subjected to hydrogenation in a hydrogen plasma under reduced pressure $(0.1 - 0.3$ Torr), obtained by rf-discharge at substrate temperatures $T = 20 - 220$ °C. Exposure time to the plasma varied in the limits $t = 0.2 - 1$ h. Ohmic contacts on the blocking layer side were created by implantation of B$^+$ ions with energy $E = 10$ keV and dose $\Phi = 6.3 \times 10^{15}$ cm^{-2} without subsequent annealing. After the implantation we subjected Cr+Au to undergo a transition to metallic state at $T = 200$ °C. The concentration profiles of the gallium impurity in the electrically active state were determined from room temperature measurements at frequencies $f = 0.14 - 1$ MHz of the current–voltage characteristics of Al–p-Si Schottky diodes fabricated on wafers which were not subjected to boron ion implantation and metallization on the blocking layer side. The concentration of the deep-level centers in the blocking layer was monitored by transient capacitance deep-level spectroscopy (TCDLS) in the constant-voltage regime by the technique described in Ref. 17. The current–voltage characteristics and temperature dependence of the resistance of the structures were measured in the temperature range $4.2 - 50$ K before and after hydrogenation. The thermal stability of the structures was investigated with the help of isochronal ($t = 20$ min) annealing in a dry nitrogen atmosphere in the temperature range $T = 200 - 400$ °C.

3. PASSIVATION OF GALLIUM IMPURITY BY HYDROGENATION OF STRUCTURES IN HYDROGEN PLASMA

Figure 1 shows the concentration profile of the ionized impurity in Si:Ga with initial gallium concentration $N_{\mathrm{Ga}} = 5 \times 10^{17}$ cm^{-3} after hydrogenation in a hydrogen plasma. As can be seen from Fig. 1, after processing at $T = 20$ °C for $t = 20$ min a layer with depth $h \approx 0.5$ μm is

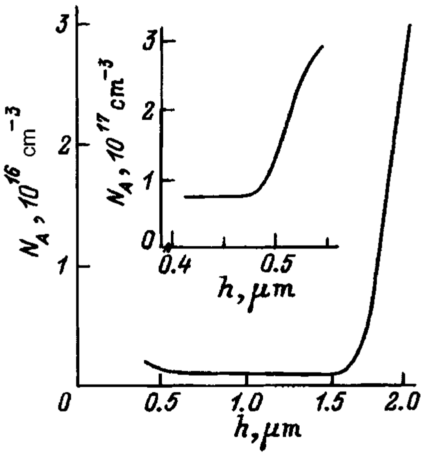

FIG. 1. Concentration profile of the ionized impurity in p-type-Si:Ga with initial concentration $N_{Ga}=5\times10^{17}$ cm^{-3} after hydrogenation in hydrogen plasma. Treatment time $t=20$ min at $T=220$ °C. Inset: the same at $T=20$ °C.

formed with residual ionized impurity concentration of about 7×10^{16} cm^{-3} (see the inset in Fig. 1). Processing at $T=220$ °C for the same length of time leads to the appearance of a high-resistance layer of thickness $h\approx1.7$ μm with residual ionized impurity concentration on the order of 10^{15} cm^{-3}. Thus, the use of hydrogenation in a hydrogen plasma enables a wide variation of the thickness of the passivated layers and the concentration of the residual impurities. These parameters are governed by the temperature dependence of the hydrogen diffusion coefficient (in the temperature range 130−275 °C) $D[\mathrm{cm}^2/\mathrm{s}]=9\times10^{-7}\times\exp(-0.45/kT)$ (see Ref. 18) and by the interaction of the hydrogen atoms with gallium, and also by the decay of the $(\mathrm{Ga}^-\mathrm{H}^+)^0$. Estimation of the hydrogen penetration depth at $T=220$ °C gives $L=(Dt)^{1/2}=1.78$ μm, in good agreement with the experimentally determined value (see Fig. 1).

To study processes of defect formation taking place during hydrogenation in plasma, we performed TCDLS measurements of the defect concentration in the hydrogenated layers. The measurements showed that the concentration of deep centers in the surface layers at depths of the order of 0.1 μm does not exceed 5×10^{13} cm^{-3} and that it falls abruptly with increasing depth, so that at a depth of 1 μm it is already lower than the sensitivity limit of the method ($\sim10^{12}$ cm^{-3}). Another confirmation of the absence of any significant concentration of defects with deep energy levels after hydrogenation follows from an analysis of the magnitude of the current through the structure, which is determined by the conductivity of the blocking layer[12] in the temperature range 4–25 K.

Figure 2 plots the temperature dependence of the current I through a structure fabricated in silicon with an initial gallium concentration $N_{Ga}=5\times10^{17}$ cm^{-3} and through structures fabricated in the same crystal after hydrogenation in plasma at $T=20$ and 220 °C. Here, according to Fig. 1, blocking layers of thickness 0.5 and 1.7 μm, respectively, are formed. According to current theory,[2–4] the temperature dependence of the current in the temperature region below the freeze-out temperature of the gallium level in silicon ($E_{Ga}=E_v+0.065$ eV) is determined by the activation energy of hopping conductivity due to hops between nearest neighbors. The activation energy obtained from the slopes in Fig. 2 is $E_a=8.7$ meV for the unhydrogenated structures, and for the structures hydrogenated in plasma at $T=20$ and 220 °C it drops to $E_a=2.4$ and 1.3 meV, respectively. These values in good agreement with the calculated values of the activation energy of hopping conductivity[2] estimated under the assumption that the degree of compensation is small ($K\ll1$):

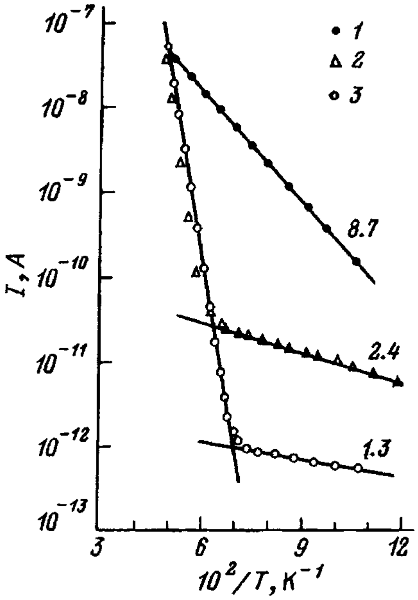

FIG. 2. Temperature dependence of the current I through a structure of area 4×5 mm^2 in p-type-Si:Ga with $N_{Ga}=5\times10^{17}$ cm^{-3}; bias voltage equal to 2 V; 1) before hydrogenation; 2, 3) after hydrogenation in hydrogen plasma for $t=20$ min at $T=20$ °C (2), 220 °C (3). Numbers next to the curves are the activation energy E_a in meV.

$$E_a=0.61E_A(1-0.29K^{1/4})\approx\frac{e^2}{4\pi\varepsilon_0\varepsilon}N_A^{-1/3}, \tag{1}$$

where $E_A=e^2/4\pi\varepsilon_0\varepsilon r_A$ is the energy of the interaction between the acceptor states at mean distance $r_A=(4\pi N_A/3)^{-1/3}$, $\varepsilon_0\varepsilon$ is the dielectric constant, and N_A is the acceptor concentration. For initial structures with $N_A=5\times10^{17}$ cm^{-3} Eq. (1) yields the value $E_a=9.8$ meV, and for hydrogenated layers with residual acceptor concentration $N_A=10^{15}$ cm^{-3} it yields the values $E_a=1.2$ meV. Thus it is clear from Fig. 2 that attendant to hydrogenation of a layer of the structure, the activation energy of hopping conductivity in the layer decreases with decreasing in N_A in accordance with Eq. (1).

4. CURRENT-VOLTAGE CHARACTERISTICS OF BIB STRUCTURES. PHYSICAL MODEL AND COMPARISON WITH EXPERIMENT

Current-voltage characteristics of BIB structures are shown in Fig. 3. As can be seen from the figure, the characteristics are substantially nonlinear in the region 13–20 K, while the current density at bias voltages of the order of

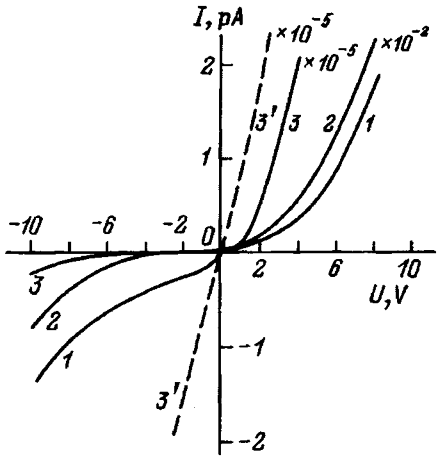

FIG. 3. Current–voltage characteristics of structures with a blocking layer obtained by hydrogenation in hydrogen plasma at $T = 220\,^\circ\mathrm{C}$ for $t = 20$ min (*1–3*), and of the original structure (before hydrogenation) (*3'*). Measurement temperature T_{meas}, K: *1*) 13.6, *2*) 15, *3*) 20, *3'*) 20.

1 V is about 10^{11} A/cm^2 ($T_{\mathrm{meas}} = 15$ K). With increase of the temperature, the dark currents grow and at $T > 30$ K the current–voltage characteristic transforms into a linear dependence. This takes place at temperatures at which valence-band conductivity becomes the predominant transport mechanism.

A. Basic features of the model. System of equations

To describe charge transport processes in BIB structures and also the dark current-voltage characteristic, we propose the following model of dark current flow through a BIB structure. For definiteness, we consider structures based on p-type silicon (Si:Ga) consisting of a heavily doped photoactive layer (the A layer) with doping level $N_{\mathrm{A1}} \simeq 10^{17} - 10^{18}$ cm^{-3} and a lightly doped blocking layer (the B layer) with doping level $N_{\mathrm{A2}} \simeq 10^{14} - 10^{16}$ cm^{-3}. Analysis shows that in the low-temperature region ($T \leqslant 50$ K) charge transport is possible in such structures via the valence band (VB) and the impurity band (IB). The following major physical processes accompanying charge transport are possible:

1. Formation of space charge regions (SCR's) as a result of the accumulation of charge in the layer in the IB states.

2. The nonresistive state of hopping conductivity for large electric fields.

3. The appearance of an avalanche in the valence band and a corresponding additional generation of holes in the valence band and electrons in the impurity band (large electric fields).

4. Recombination of electrons from the impurity band and holes from the valence band.

5. Thermal-field generation of electron–hole pairs (via the Poole–Frenkel' mechanism).

6. Tunneling-field generation of electron–hole pairs.

7. Thermal-field hole injection into the valence bands from the B-layer contact (due to a lowering of the barrier via the Schottky mechanism.

8. Tunneling-field hole injection into the valence bands from the B-layer contact.

9. Size and other effects associated with the fundamental inhomogeneity of conduction via the impurity band (conduction is realized via chains of the ''infinite'' cluster network).

In what follows we will consider the one-dimensional model. We assume homogeneity of the A and B layers and ignore effects of the type mentioned in item 9. We assume electric fields $E \leqslant 10^4$ V/cm for which, as estimates show, the manifestation of the effects indicated in items 3, 6, and 8 is insignificant. We also disregard the effect indicated in item 2, although this can be justified only for the A layer while for the B layer in some cases it can have a substantial effect on the current–voltage characteristics. Within the framework of the formulated assumptions and approximations we can write the following equations.

In the transport of electrons from the impurity band and holes from the valence band the electron (J_n) and hole (J_p) flux densities are

$$J_n = -D_n \frac{\partial n}{\partial x} - \mu_n n E, \tag{2}$$

$$J_p = -D_p \frac{\partial p}{\partial x} + \mu_p p E, \tag{3}$$

where E is the electric field intensity, D is the diffusion coefficient, μ is the mobility, n and p are the electron concentration in the impurity band and the hole concentration in the valence band (the subscripts n and p on the parameters D and μ indicate these quantities for the corresponding particles). The continuity equations for the electrons and holes (the stationary case is considered) have the form

$$\frac{\partial n}{\partial t} = -\frac{\partial J_n}{\partial x} + g_{TE} - r = 0, \tag{4}$$

$$\frac{\partial p}{\partial t} = -\frac{\partial J_p}{\partial x} + g_{TE} - r = 0, \tag{5}$$

where g_{TE} is the coefficient of thermal-field generation of electron–hole pairs, and r is the electron–hole pair recombination coefficient. The Poisson equation takes the form

$$\frac{\partial E}{\partial x} = \frac{e}{\varepsilon_0 \varepsilon} (N_D + p - n), \tag{6}$$

where N_D is the concentration of the (positively charged) compensating donor impurity. The equations for the voltage on the structure and the current through it are

$$U = \int E dx, \tag{7}$$

$$I = e S_g (J_p - J_n), \tag{8}$$

where S_g is the area of the contact electrodes of the structure.

The following boundary conditions are used.

1. At the boundary of the A layer with the contact layer

$$n|_{I1} = n_1, \tag{9}$$

$$p|_{I1} = p_1, \tag{10}$$

where n_1 and p_1 are the thermodynamic-equilibrium values of the electron concentration in the impurity band (IB) and the hole concentration in the valence band (VB) for the equilibrium A layer.

2. At the boundary of the A and B layers

$$[E]|_{l12}=0, \tag{11}$$

$$[J]_p|_{l12}=[J_n]|_{l12}=0. \tag{12}$$

Here the brackets denote the jump at the boundary of the quantity enclosed in brackets.

3. At the boundary of the B layer with the contact layer

$$n|_{l2}=N_{A2}, \tag{13}$$

$$p|_{l2}=0 \tag{14}$$

for positive bias voltage on the B layer, and

$$J_p|_{l2}=J_{TE} \tag{15}$$

for negative bias voltage on it. Here condition (13) corresponds to complete filling of the surface acceptor states with electrons from the contact layer, condition (14) corresponds to complete capture by the contact of the arriving holes for a negative bias on the B layer; and condition (15) corresponds to thermal-field hole injection from the B-layer contact with flux density J_{TE} (Schottky mechanism) for positive bias on the B layer.

Analysis of dark current flow in the BIB structure allows us to distinguish two substantially different mechanisms of current flow. Here, as can be seen from Fig. 2, at some critical temperature T_{cr} (for curves *1*, *2*, and *3* in Fig. 2 $T_{\text{cr}}=20.0$, 15.9, and 14.3 K, respectively) the mechanism of current flow through the structure changes. At temperatures of the structure above T_{cr} it may be assumed that current flows via the A-layer impurity band and the B-layer valence band. At temperatures of the structure below T_{cr} current flows via the impurity bands of both layers (A and B); i.e., the temperature T_{cr} is a transition temperature from the conduction band to the hopping band for the B layer. The region of relatively high temperatures, when the current flow via the valence band predominates in the A layer, is not considered here since in this case blocking of impurity conduction does not take place. Taking into account the points discussed above, we calculated the current–voltage characteristics of BIB structures for the two cases.

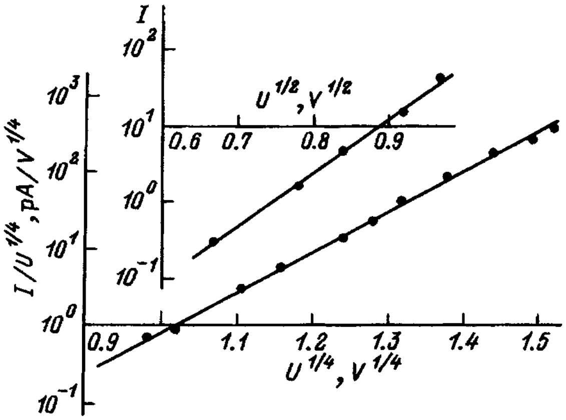

FIG. 4. Comparison of experimental and calculated current–voltage characteristics for positive (inset) and negative bias voltages on the blocking layer at $T_{\text{meas}}=20$ K (above the critical temperature T_{cr}). The points correspond to experiment, and the straight line to calculation.

The case $T>T_{\text{cr}}$. For positive voltages on the B layer the current-voltage characteristic is determined by 1) above-barrier hole injection (with lowering of the barrier via the Schottky mechanism[1]) from the B-layer contact to the valence-band region of the B layer, 2) their drift through the B layer, and 3) recombination with electrons located in acceptor states of the A layer. The electrons flow into the recombination region via the A-layer impurity band from the A-layer contact. Solving system of equations (4)–(15) for this case, for positive bias voltages on the B layer it is possible to obtain an analytical expression for the corresponding current–voltage characteristic in the form

$$I(U)=I_0 \exp(U/U_0)^{1/2}, \tag{16}$$

where

$$I_0=\frac{4\pi S_g e m_p k^2 T^2}{h^3} \exp(-e\varphi_0/kT),$$

$$U_0=\frac{2\pi\varepsilon_0\varepsilon d_2 k^2 T^2}{e^3},$$

m_p is the hole mass, and φ_0 is the change in the potential at the boundary of the electrode with the B layer. As can be seen from Fig. 4, where the dependence $\ln I=f(U^{1/2})$ is shown in the inset, good agreement is observed between the experimental values of the current–voltage characteristic and the values calculated according to Eq. (16).

For negative biases on the B layer, the current–voltage characteristic is governed by thermal generation of holes from the acceptor impurity in the space-charge region of the A layer with lowering of the barrier via the Poole–Frenkel' mechanism[1] and hole drift via the valence band through the B layer onto the negative electrode. The electrons in the acceptor states in the space-charge region of the A layer stream onto the positive electrode via hopping transport. Solving system of equations (4)–(15) for this case, we obtain an expression for the corresponding current–voltage characteristic

$$I(U)=AU^{1/4} \exp(\beta U^{1/4}/\varphi_A), \tag{17}$$

where

$$A=\left(\frac{2}{e}\right)^{1/4} \frac{(\varepsilon_0\varepsilon)^{5/4}\sqrt{\pi} S_g \gamma_p N_{A1} N_v \varphi_T}{2N_{D1}^{3/4}} \exp\left(-\frac{\varphi_A}{\varphi_T}\right),$$

$$\beta=\frac{(2N_{D1})^{1/4}}{\sqrt{\pi}} \left(\frac{e}{\varepsilon_0\varepsilon}\right)^{3/4},$$

$\varphi_T=kT/e$ is the thermal potential, γ_p is the hole–electron recombination coefficient, φ_A is the ionization potential of the acceptor impurity, N_{D1} is the donor impurity concentration in the A layer, and $N_v=a_v T^{3/2}$ is the effective density of states in the valence band. As can be seen from Fig. 4, which shows experimental and calculated [according to Eq. (17)]

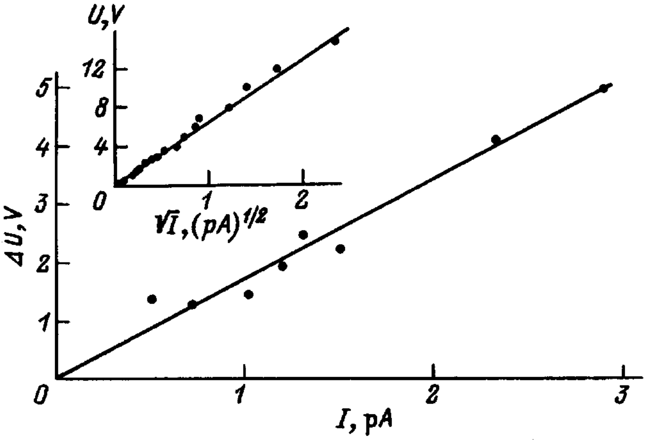

FIG. 5. Comparison of experimental and calculated current–voltage characteristics for positive (inset) and negative bias voltages on the blocking layer at $T_{\text{meas}}=13.6$ K (below the critical temperature T_{cr}). The points correspond to experiment, and the straight line to calculation.

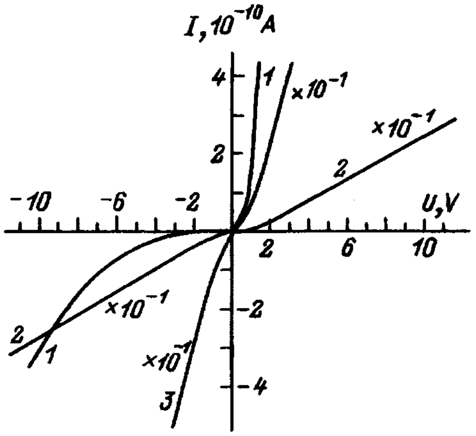

FIG. 6. Variation of the current–voltage characteristics of structures hydrogenated in hydrogen plasma at $T=20$ °C for $t=20$ min during isochronal (20 min) annealing: 1) after hydrogenation, 2, 3) after hydrogenation and annealing at T, °C: 2) 300, 3) 400. Measurement temperature $T_{\text{meas}}=15$ K.

current–voltage characteristics in the coordinates $\ln(I/U^{1/4})=f(U^{1/4})$, good agreement is observed for negative bias voltages on the blocking layer.

The case $T<T_{\text{cr}}$. For positive voltages on the B layer the current-voltage characteristic is determined by 1) hopping transport of electrons through the A layer, 2) electron injection into the B-layer impurity band, where a space-charge region is created on both sides of the layer interface as a result of excess electron charge, and finally by 3) streaming of electrons via hopping conductivity onto the positive electrode. Solving system of equations (4)–(15) for this case, it is possible to obtain an analytical expression for the corresponding current–voltage characteristic. In this case it is more convenient, as will be clear from what follows, to represent the current–voltage characteristic in the form of the dependence $U(T)$:

$$U^+(I)=K^+\sqrt{I}, \tag{18}$$

where

$$K^+=(2d_2)^{3/2}/3\sqrt{\varepsilon_0\varepsilon\mu_2S_g},$$

μ_2 is the electron mobility in the B-layer impurity band. A current–voltage characteristic such as (18) takes the form of a straight line in the coordinates $U=f(U^{1/2})$, which is shown in comparison with experimental data in the inset in Fig. 5.

For negative biases on the B layer, the current–voltage characteristic is determined by electron injection from the electrode in contact with the B layer and by the charge of the B-layer acceptor states, which causes the appearance of a region of excess electron charge. Next, via hopping conductivity the electrons stream into the impurity band of the A layer, where a second space-charge region (exclusion) is formed as a result of the predominance of A-layer conduction over B-layer, and then the electrons escape to the positive electrode. The corresponding current–voltage characteristic for this case, obtained by solution of system of equations (4)–(15), can be represented in the form

$$U^-(I)=K^-I+K^+\sqrt{I}, \tag{19}$$

where

$$K^-=d_2/e\mu_2N_{D1}S_g.$$

It is convenient for analysis to switch to the difference in the positive and negative branches of the current–voltage characteristics:

$$\Delta U(I)=U^-(I)-U^+(I)=K^-I. \tag{20}$$

Dependence (20) takes the form of a straight line in linear coordinates and the corresponding comparison of calculation with experiment is shown in Fig. 5.

5. STABILITY OF HYDROGENATED STRUCTURES TO THERMAL EFFECTS

Studies of the stability of hydrogenated structures to thermal effect have shown that the shape of the current–voltage characteristic typical of BIB structures disappears at 300 °C, and the voltage dependence of the current becomes quasilinear. However, it should be noted that the current through the structure even after annealing at 400 °C (Fig. 6, curve *3*) is still roughly an order of magnitude less than the current that is characteristic of unhydrogenated structures. This difference probably stems from the fact that at temperatures above 200 °C the liberated hydrogen atoms diffuse to greater depths and passivate deep donors, which decreases both the degree of compensation in the structures and the hopping conductivity. This hypothesis is confirmed by the fact that the dissociation energy of the hydrogen-passivated deep donors is greater than 2 eV and that they are stable up to temperatures of 500 °C and higher.[13–16] Consequently, the degree of compensation of p-type material when annealed above 220 °C should decrease, and this should lead to a decrease of the hopping-conductivity current, as is observed experimentally.

6. CONCLUSION

By hydrogenating heavily doped p-type silicon in a hydrogen plasma we have succeeded in creating structures with blocked hopping conductivity via the impurity band (BIB structures) with dark current densities on the order of 10^{-11} A/cm^2 at $T = 15$ K. The electrical characteristics of the plasma-hydrogenated BIB structures are in good agreement with calculation.

We would like to thank V. M. Sutyrin, N. V. Smirnova, and S. N. Klemin for plasma treatment of the structures and for their cooperation in preparing the test structures. We also thank A. V. Karpov for assistance in carrying out some of the measurements.

[1] A. Milis, *Impurities with Deep Levels in Semiconductors* [Russ. trans., Mir, Moscow (1977)].
[2] V. I. Shklovskiĭ and A. L. Efros, *Electronic Properties of Doped Semiconductors* (Springer-Verlag, New York, 1984).
[3] N. F. Mott and E. A. Davis, *Electronic Processes in Non-Crystalline Materials* (Clarendon Press, Oxford, 1971).
[4] J. Bourgoin and M. Lanoo, *Point Defects in Semiconductors* (Springer-Verlag, New York, 1983).
[5] M. D. Petroff and M. G. Stapelbrock, U.S. Patent No. 4568960 (1980).
[6] E. R. Brown and P. E. Tannenwald, SPIE Proceedings Vol. 666, *Far-Infrared Science and Technology* (1986) p. 38.
[7] N. Sclar, Progr. Progr. Quant. Electron. **9**, 149 (1984).
[8] F. Szmulowicz and F. L. Madarsz, J. Appl. Phys. **62**, 2533 (1987).
[9] D. M. Watson and J. E. Huffman, Appl. Phys. Lett. **52**, 1602 (1988).
[10] B. G. Martin, Solid−State Electron. **33**, 427 (1990).
[11] P. R. Norton, Opt. Eng. **30**, 1649 (1991).
[12] V. V. Bolotov, G. N. Kamaev, G. N. Feofanov, and V. M. Émeksuzyan, Fiz. Tekh. Poluprovodn. **24**, 1697 (1990) [Sov. Phys. Semicond. **24**, 1061 (1990)].
[13] S. J. Pearton, J. W. Corbelt, and T. S. Shi, Appl. Phys. A **43**, 153 (1987).
[14] J. Chevallier and M. Ancouturier, Ann. Rev. Mater. Sci. **18**, 219 (1988).
[15] N. M. Johnson, C. Doland, F. Ponce, J. Walker, and G. Anderson, Physica B **170**, 3 (1991).
[16] S. M. Myers, M. I. Baskes, H. K. Birnbaum, J. W. Corbett, G. G. DeLeo, S. K. Estreicher, E. E. Haller, P. Jena, N. M. Johnson, R. Kirchheim, S. J. Pearton, and M. J. Stavola, Rev. Mod. Phys. **64**, 559 (1992).
[17] V. V. Bolotov, G. L. Plotnikov, V. M. Émeksuzyan, and K. Shmal'ts, Fiz. Tekh. Poluprovodn. **26**, 1295 (1992) [Sov. Phys. Semicond. **26**, 723 (1992)].
[18] A. Mogro-Campero, R. P. Love, and R. Schubert, J. Electrochem. Soc. **132**, 2006 (1985).

Translated by Paul F. Schippnick

Shubnikov–de Haas oscillations in HgSe⟨Fe⟩ and HgSe⟨Co⟩ under hydrostatic pressure

É. A. Neĭfel'd, K. M. Demchuk, G. I. Kharus, A. É. Bubnova,
L. I. Domanskaya, G. D. Shtrapenin, and S. Yu. Paranchich

Institute of Metal Physics, Ural Branch of the Russian Academy of Sciences, 620219 Ekaterinburg, Russia

(Submitted November 27, 1995; accepted for publication May 22, 1996)
Fiz. Tekh. Poluprovodn. **31**, 318–322 (March 1997)

Shubnikov–de Haas oscillations have been studied in the gapless semiconductors HgSe⟨Fe⟩ and HgSe⟨Co⟩ under hydrostatic pressure. It is shown that in HgSe⟨Fe⟩ an increase in pressure results in a decrease in the electron density, which fits within the framework of the Kane model with constant Fermi energy. In contrast, in HgSe⟨Co⟩ the electron density is independent of the pressure, i.e., Fermi-level pinning is absent. [S1063-7826(97)01203-9]

1. INTRODUCTION

The $3d$ transition elements form isovalent substitution impurities in II–VI semiconductor crystals. The energy levels of $3d$-electrons play a different role in wideband and gapless semiconductors. In the first case they fall, as a rule, into the band gap. In gapless semiconductors (HgSe, HgTe) they are situated against the background of the continuum of allowed states. If the energy levels of the electrons in the d states fall into the valence band as, for example, in HgSe ⟨Mn⟩, then the Mn impurity atoms will be electrically neutral and the d electrons of the Mn atoms will affect only the magnetic properties of the crystals. But if the energy of the electrons in the d states lies above the bottom of the conduction band, as in HgSe⟨Fe⟩, they can play the role of donors, giving back the d electrons to the band. Such autoionization of iron ions transforms the divalent ions into trivalent: $\mathrm{Fe}^{2+}\rightarrow\mathrm{Fe}^{3+}+e^{-}$. It is energetically favorable only for small iron impurity concentrations N_{Fe} as long as the Fermi level $\varepsilon_F(n)$, where n is the electron concentration, is not comparable with the energy of the d electron ε_d reckoned from the bottom of the conduction band. In HgSe⟨Fe⟩ the energy $\varepsilon_d \simeq 220$ meV and the equality $\varepsilon_F(n_0)=\varepsilon_d$ is achieved for $n_0 \simeq 4.5\times10^{18}\ \mathrm{cm}^{-3}$. For $N_{\mathrm{Fe}}>n_0=N^*_{\mathrm{Fe}}$ the so-called mixed-valence regime arises. In this regime some of the iron atoms remain doubly ionized while the Fermi level is fixed at the resonant iron levels.

Micielski[1] was the first to direct attention to the role of Coulomb repulsion in the mixed-valence regime, which leads to a correlated Fe^{3+} ion distribution. At low temperatures, where scattering of charge carriers takes place at charged centers, correlation in the Fe^{3+} ion distribution leads to an increase in the mean free path of the conduction electrons. This explains the experimentally observed increase in the electron mobility μ with increasing iron concentration in the interval $4\times10^{18}-2\times10^{19}\ \mathrm{cm}^{-3}$.

In gapless semiconductors with an inverted energy spectrum the application of hydrostatic pressure leads to a decrease of the absolute value of the energy gap, $\varepsilon_g=\varepsilon_{\Gamma_6}-\varepsilon_{\Gamma_8}$. This results in a decrease of the effective electron mass and the density of states in the conduction band. The connection between the conduction electron concentration and the Fermi energy in the two-band Kane model is described by the relation

$$(3\pi^2 n)^{2/3}=3\varepsilon_F[\varepsilon_F-\varepsilon_g(P)]/Q, \tag{1}$$

where Q is the matrix element of the kp interaction, $\varepsilon_g(P)=\varepsilon_g^0-\beta P$, and $\beta=\partial\varepsilon_g/\partial P$ is the pressure coefficient. It is clear from relation (1) that for fixed position of the Fermi level in semiconductors with a Kane spectrum the dependence of $n^{2/3}$ on P should be linear. Such behavior has been observed in the gapless solid solution HgCdTa (Ref. 2) in which the Fermi level in the conduction band is fixed at the resonant acceptor states.

Tsidil'kovskiĭ *et al.*[3] found that doping HgSe with the transition elements Cr, Co, and Ni above certain concentration levels N^* is not accompanied by a growth of the concentration of the conduction electrons and, by analogy with HgSe⟨Fe⟩, they assumed that these elements also form resonant donor states, degenerate with the conduction band. Conclusions about stabilization of the Fermi level with growth of the impurity concentration were reached in studies of a series of samples which can have other uncontrollable, electrically active defects, which are attributable to the conditions under which they were fabricated, associated with nonstoichiometry or group-III element impurities. In this regard, a study of the influence of high pressures has substantial advantages since the fabrication history of the sample has no relevance here.

In the present paper we present results of experimental studies of Shubnikov–de Haas oscillations in the solid solutions HgSe⟨Fe⟩ and HgSe⟨Co⟩ under hydrostatic pressure.

2. EXPERIMENTAL RESULTS

The resistance of the samples was measured by the constant-current method. The samples were placed in a high-pressure chamber connected by a capillary to a helium compressor whose design is described in Ref. 4. Discrete resistance measurements were carried out at 4.2 K in a superconducting solenoid with continuous scanning of the magnetic field.

Experimental studies of Shubnikov–de Haas oscillations under conditions of hydrostatic pressure were carried out with two samples of HgSe⟨Fe⟩ with iron concentration

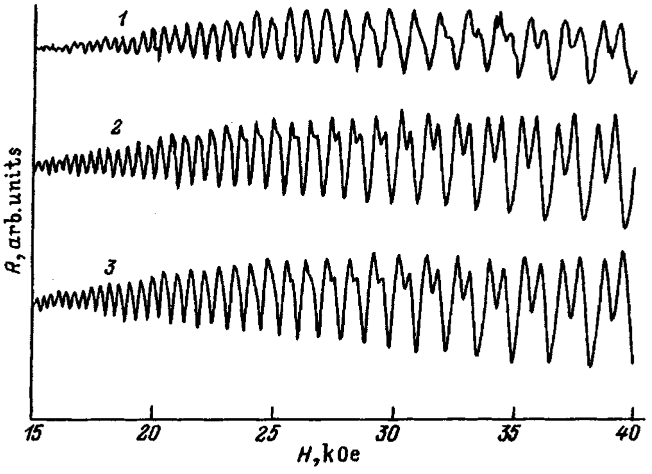

FIG. 1. Oscillations of the longitudinal magnetoresistance at atmospheric pressure (*1*) and under hydrostatic pressure at pressures of 3 kbar (*2*) and 5 kbar (*3*) for a sample of HgSe⟨Fe⟩ with iron concentration $N_{\mathrm{Fe}}=5\times10^{19}$ cm^{-3}.

$N_{\mathrm{Fe}}=5\times10^{19}$ cm^{-3} (sample 1) and $N_{\mathrm{Fe}}=10^{19}$ cm^{-3} (sample 2) and with a sample of HgSe⟨Co⟩ with cobalt concentration $N_{\mathrm{Co}}=5\times10^{18}$ cm^{-3}. The samples of HgSe⟨Fe⟩ were chosen in such a way that the iron concentration in one of them was less than the concentration at which maximum electron mobility is observed,[5] $N_{\mathrm{Fe}}=2\times10^{19}$ cm^{-3}, and in the other the concentration was greater. In both samples of HgSe⟨Fe⟩ $N_{\mathrm{Fe}}>N^*_{\mathrm{Fe}}$, and in the sample of HgSe⟨Co⟩ similarly $N_{\mathrm{Co}}>N^*_{\mathrm{Co}}$ since according to the results of Ref. 3, $N^*_{\mathrm{Co}}\simeq2\times10^{18}$ cm^{-3}.

Figures 1 and 2 plot the oscillating components of the longitudinal magnetoresistance at atmospheric pressure, and also at pressures of 3 and 5 kbar for both samples of HgSe⟨Fe⟩. The position of the extremum in the magnetic field depends on the pressure. The spin splitting of the oscillation maxima for sample 1 increases as the pressure is increased and is observed in smaller fields. Splitting is not observed for sample 2 at atmospheric pressure but shows up at $P=3$ kbar.

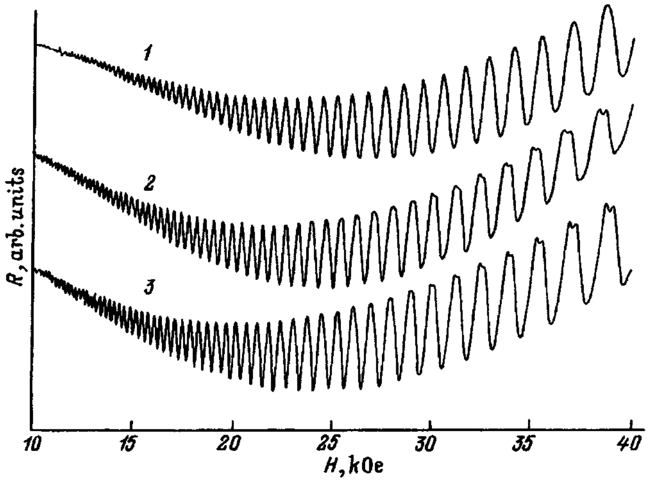

FIG. 2. Same as in Fig. 1, but for a sample of HgSe⟨Fe⟩ with iron concentration $N_{\mathrm{Fe}}=5\times10^{19}$ cm^{-3}.

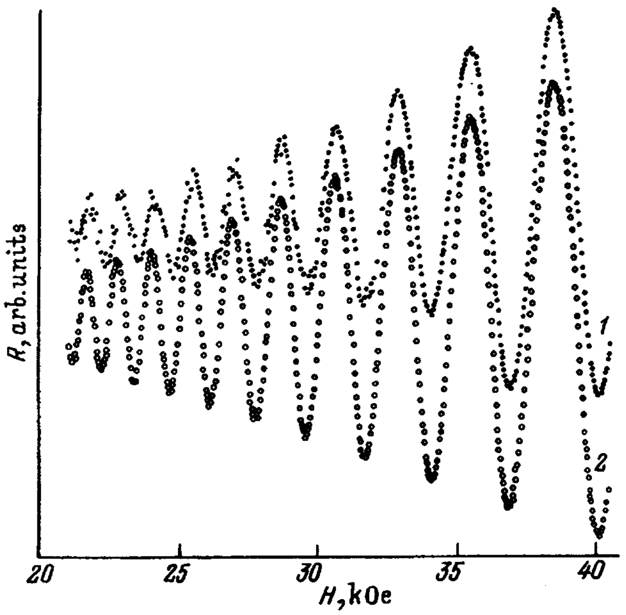

FIG. 3. Oscillations of the longitudinal magnetoresistance at atmospheric pressure (*1*) and under hydrostatic compression at a pressure of 5 kbar (*2*) for a sample of HgSe⟨Co⟩.

Figure 3 shows oscillations of the magnetoresistance for the sample of HgSe⟨Co⟩ at atmospheric pressure and for $P=5$ kbar. It is obvious that in this case hydrostatic pressure has no effect on the position of the extrema in the magnetic field in contrast to the iron-containing samples.

Table I lists values of the conductivity σ, the electron concentration n determined from the period of the Shubnikov–de Haas oscillations, and the electron mobility $\mu=\sigma/ne$ for the investigated samples at different pressures P. Table I also gives the Dingle temperature T_D, calculated from the magnetic-field dependence of the amplitude of the oscillations. For the samples of HgSe⟨Fe⟩ T_D was determined in the field interval 15–25 kOe, where spin splitting is absent. For the sample of HgSe⟨Co⟩ T_D was determined in the interval 20–40 kOe.

3. DISCUSSION OF RESULTS

Figure 4 plots the dependence of the conduction electron concentration for the investigated samples in the form of the dependence $n^{2/3}(P)$. The experimental results for HgSe⟨Fe⟩ are well described by a linear dependence corresponding to Eq. (1) for $\varepsilon_F(P)=\mathrm{const}$. The pressure coefficients β for both samples, determined from these dependences, practically coincide: $\beta=7.7$ meV/kbar (for sample 1) and $\beta=8.0$ meV/kbar (for sample 2); these values agree with the results available in the literature.

In contrast, for HgSe⟨Co⟩ the electron concentration is almost independent of pressure. According to relation (1), the Fermi level in the investigated pressure interval increases from 150 to 163 meV. The qualitative difference in the pressure dependences $n(P)$ for HgSe⟨Fe⟩ and HgSe⟨Co⟩ is ob-

TABLE I.

P, kbar	n, 10^{18} cm^{-3}	σ, 10^4 $\Omega^{-1}\cdot$cm^{-1}	μ, 10^4 cm^2/(V$\cdot$s)	T_D, K
HgSe⟨Fe⟩, $N_{\mathrm{Fe}}=5\times10^{19}$ cm^{-3}				
0	4.80	3.60	4.69	4.73
3	4.50	3.71	5.16	3.45
5	4.21	3.52	5.23	3.35
HgSe⟨Fe⟩, $N_{\mathrm{Fe}}=10^{19}$ cm^{-3}				
0	4.63	5.21	7.03	2.87
3	4.30	5.51	8.05	2.27
5	4.04	5.29	8.17	2.29
HgSe⟨Co⟩, $N_{\mathrm{Co}}=5\times10^{18}$ cm^{-3}				
0	1.68	1.04 ± 0.01	3.87 ± 0.05	13.0
2.3	1.69	1.04 ± 0.01	3.87 ± 0.05	10.8
5.3	1.70	1.04 ± 0.01	3.87 ± 0.05	10.4

vious and testifies to the absence of a resonant level ε_d in HgSe⟨Co⟩ at least up to 163 meV. The authors of Ref. 6 came to just this conclusion after studying the spectra in HgSe⟨Co⟩ and not detecting the presence of Co^{3+} ions. Thus, we may conclude that Co impurity atoms are not donors in the HgSe crystal and that the conduction electrons are generated by other types of defects. It should be noted that although the linear dependence $n^{2/3}(P)$ is well satisfied for both samples of HgSe⟨Fe⟩, the Fermi level is fixed in them at somewhat different values of the energy. This difference $\delta\varepsilon_F\simeq 5-6$ meV reflects the spread of levels ε_d resulting from the influence of random electrostatic fields of the charged centers and lies within the limits of the estimate $\Delta\varepsilon_d\simeq e^2n^{2/3}/\varkappa$.

Figure 3 also presents experimental data for HgSe⟨Fe⟩ samples with $N_{\mathrm{Fe}}=8\times10^{18}$ cm^{-3} from Ref. 7. It can be clearly seen that they fit quite nicely into a linear dependence for $n^{2/3}(P)$, but with a somewhat smaller pressure coefficient, $\beta\simeq 6.3$ meV/kbar. The depressed value of the pressure coefficient β possibly simply reflects the fact that the conditions for fixing the Fermi level in the samples investigated in Ref. 7 were poorly met.

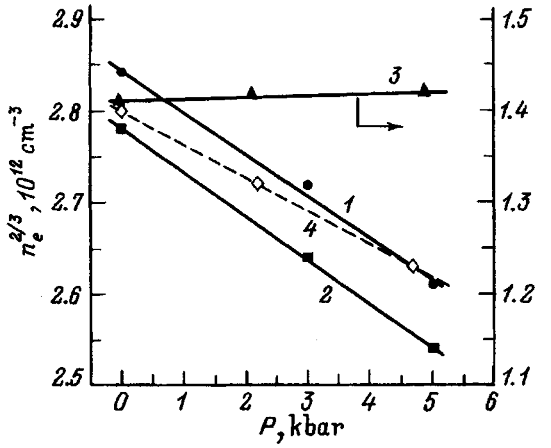

FIG. 4. Pressure dependence of the electron density for samples of HgSe⟨Fe⟩ with iron concentration N_{Fe} in units of 10^{19} cm^{-3} equal to *1* — 5, *2* — 1; *3* — for the sample of HgSe⟨Co⟩ with cobalt concentration $N_{\mathrm{Co}}=5\times10^{18}$ cm^{-3}; *4* — results of Ref. 7.

Let us consider the effect of hydrostatic pressure on the electron mobility and Dingle temperature. The electron relaxation time for scattering from randomly distributed Coulomb centers[8]

$$\tau\sim k_F^3/N_i m_F, \tag{2}$$

where $k_F^3=3\pi^2 n$ and N_i is the concentration of the charged centers. Noting that for uncompensated samples $n=N_i$ from the condition of electrical neutrality, we see that the only quantity that substantially depends on the pressure is the mass at the Fermi level m_F:

$$m_F=\hbar^2\left(k\,\frac{dk}{d\varepsilon}\right)_{\varepsilon=\varepsilon_F}. \tag{3}$$

Using the Kane dispersion relation (1), we obtain

$$\frac{1}{m_F}\,\frac{dm_F}{dP}=-\beta\,\frac{1}{\varepsilon_g+2\varepsilon_F},\quad \varepsilon_F(P)=\mathrm{const} \tag{4a}$$

or

$$\frac{1}{m_F}\,\frac{dm_F}{dP}=-\beta\,\frac{1}{(\varepsilon_g+2\varepsilon_F)^2},\quad n(P)=\mathrm{const.} \tag{4b}$$

It follows from the formulas that for the HgSe⟨Fe⟩ samples with fixed Fermi level the relative decrease of the mass m_F at $P=5$ kbar is 6% and is roughly two times larger than for the sample of HgSe⟨Co⟩ with constant electron concentration. The experimental data presented in the table for the mobility μ ($\mu\sim m_F^{-2}$) are in good agreement with the expected values for HgSe⟨Fe⟩; however, in the case of HgSe⟨Co⟩ as a result of a spread in values of σ, the variation of the mobility could not be determined. It should also be noted that in the sample of HgSe⟨Fe⟩ with $N_{\mathrm{Fe}}=10^{19}$ cm^{-3} the mobility increases more rapidly with the pressure than in HgSe⟨Fe⟩ with $N_{\mathrm{Fe}}=5\times10^{19}$ cm^{-3}. The value $N_{\mathrm{Fe}}=10^{19}$ cm^{-3} lies in the range of iron impurity concentrations in which the mobility $\mu(N_{\mathrm{Fe}})$ grows with increasing N_{Fe} as a result of the correlated distribution of Fe^{3+} ions.[5] The correlation factor is disregarded in Eq. (2), which is suitable for the case of randomly distributed Coulomb centers. Qualitatively, the degree of correlation can be characterized by the parameter α

$= N_{\mathrm{Fe}}^{3+}/N_{\mathrm{Fe}} \simeq n(P)/N_{\mathrm{Fe}}$. For $N_{\mathrm{Fe}} > N_{\mathrm{Fe}}^{*}$, hydrostatic pressure causes a transition of the electrons from the conduction band to the resonant d-states of the Fe^{3+} ions:

$$\mathrm{Fe}^{3+} + e^{-} \rightarrow \mathrm{Fe}^{2+}.$$

Decrease of the parameter α with increasing pressure leads to a stronger growth of the mobility than follows from Eq. (2). This agrees with the results of Ref. 7, in which the pressure dependences of the Hall effect and the conductivity were investigated. On the other hand, in samples with high iron impurity concentration, $N_{\mathrm{Fe}} > 2 \times 10^{19}\ \mathrm{cm}^{-3}$, variations of the correlation parameter α have no effect on the mobility and the change in the effective mass is the main reason for the growth of the mobility.

The decrease in the Dingle temperature T_D with pressure is, no doubt, also mainly due to a decrease in the effective mass of the electrons. The increase in the degree of correlation in the mixed-valence regime plays a smaller role. Unfortunately, T_D is difficult to estimate theoretically since in addition to collisional broadening of the Landau levels $\Gamma \simeq \hbar/\tau$, contributions to T_D can come from other factors, e.g., spatial inhomogeneity of the electron concentration. In addition, an experimental determination of T_D from the magnetic-field dependence of the amplitude of the oscillations can be distorted by the appearance of nodes in the oscillograms, which are due to the presence of small terms in the dispersion relation which are linear in the quasimomentum.[9] Nevertheless, it is clear from the data in the table that for the HgSe⟨Fe⟩ samples the magnitude of T_D varies with pressure more strongly than for the HgSe ⟨Co⟩ samples, which qualitatively confirms the difference in the behavior of $m_F(P)$ in cases (4a) and (4b).

4. CONCLUSIONS

Our studies of the pressure dependence of the electron concentration and mobility and also the Landau temperature allow us to conclude that in the gapless semiconductors HgSe⟨Co⟩ the d electrons of the cobalt atoms do not form a resonant level in the conduction band capable of fixing the Fermi level, in contrast to HgSe⟨Fe⟩, where the Fermi level is clearly fixed in a narrow energy band (of the order of 10 meV), i.e., it does not depend on the pressure. Cobalt impurities in HgSe crystals probably are not electrically active donors (like Mn in HgSe⟨Mn⟩) and electrons are delivered to the conduction band either by nonstoichiometric defects or by shallow impurities of other elements.

It is interesting to discuss the possibility whereby other $3d$ transition elements can be donors with a resonant level in HgSe crystals. An analysis of the positions of the levels of the $3d$ impurities in wideband II–VI semiconductor compounds based on optical studies has shown that in all matrices the energy position of the d level is shifted monotonically upward in energy in the series from Cu to Sc.[10] The exception here is manganese, the element with a half-full d subshell $(5d)$, which is especially stable. The position of the d levels in various matrices of II–VI crystals correlates well with the third ionization potential of the corresponding elements, which indicates a relatively autonomous character of the d electrons and provides grounds for assuming that such a tendency can also be maintained in gapless II–VI crystals, which differ from wideband semiconductors by the inverse sequence of the s- and p-distances. It may then be expected that the cobalt d level is located lower in energy than the Fe level, and the levels of Ti and V and possibly Cr are higher than the Fe level (See Fig. 7 in Ref. 10). Therefore, it may be expected that the elements Ti and V can form a resonant d level in the conduction band if they can be substitution impurities.

[1] J. Mycielski, Solid State Commun. **60**, 165 (1986).

[2] C. T. Elliot, I. Melngailis, T. C. Harman, J. A. Kafalas, and W. S. Kerman, Phys. Rev. B **5**, 2985 (1972).

[3] I. M. Tsidil'kovskiĭ, N. K. Lerinman, L. D. Sabirzyanova, S. Yu. Paranchich, and Yu. S. Paranchich, Fiz. Tekh. Poluprovodn. **26**, 1894 (1992) [Sov. Phys. Semicond. **26**, 1062 (1992)].

[4] N. A. Gorodilov, K. M. Demchuk, and É. A. Neĭfel'd, Dep. VINITI No. 8574-B87 from 09.12.87.

[5] I. M. Tsidil'kovskiĭ, Usp. Fiz. Nauk **162**, 63 (1992) [Sov. Phys. Usp. **35**, 85 (1992)].

[6] S. K. Misra, J. Pescia, M. Averous, G. Ablart, L. Allam, C. Fau, S. Charar, M. Kholdi and M. D. Pace, Solid State Commun. **90**, 273 (1994).

[7] C. Skierbiszewski, T. Suski, E. Litwin-Staszewski, W. Dobrowolski, K. Dybko, and A. Mycielski, Semicond. Sci. Technol. **4**, 293 (1989).

[8] B. M. Askerov, *Electron Transport Phenomena in Semiconductors* [in Russian] (Nauka, Moscow, 1985).

[9] D. G. Seiler, R. R. Galazka, and W. M. Becker, Phys. Rev. B **3**, 4274 (1971).

[10] V. I. Sokolov, Fiz. Tekh. Poluprovodn. **28**, 545 (1994) [Semiconductors **28**, 329 (1994)].

Translated by Paul F. Schippnick

Thermoelectric figure of merit of monopolar semiconductors with finite dimensions

V. S. Zakordonets and G. N. Logvinov

Ternopol State Pedagogical Institute, 282009 Ternopol, Ukraine

(Submitted December 14, 1995; accepted for publication May 30, 1996)
Fiz. Tekh. Poluprovodn. **31**, 323–325 (March 1997)

The figure of merit of monopolar nondegenerate semiconductors is theoretically investigated. The difference between the electron and phonon temperatures, which arises as a result of the action of different surface mechanisms of energy relaxation at the contacts of the sample with the heat reservoir, is taken into account. It is shown in the case of isothermal boundary conditions for the electron subsystem and adiabatic conditions for the phonon subsystem that the thermoelectric figure of merit of the sample increases with decreasing sample's linear dimensions and reaches its maximum in films of submicron thickness. © *1997 American Institute of Physics.* [S1063-7826(97)01303-3]

As is well known, the figure of merit of thermoelectric materials is given by[1]

$$Z=\frac{\alpha^2\sigma}{\varkappa_e+\varkappa_p}, \tag{1}$$

where α, σ, $\varkappa_e$, and $\varkappa_p$ are the thermoelectric power, electrical conductivity, and electron and hole thermal conductivities, respectively. It is also known that Eq. (1) does not take the sample's geometrical dimensions into account. At the same time, in the study of the thermoelectric properties of semiconductors, their geometrical dimensions are the most general and one of the most important factors of approximation to the real situation.[2] It is natural that the electrical (current) and thermal boundary conditions must be formulated in this case. Usually in the formulation of the thermal boundary conditions at the walls, one prescribes the total heat flux associated with the heat transfer in the charge carrier and phonon subsystems. At the same time, as experiments[3,4] and their theoretical generalization[2] show, there is the possibility of controlling these fluxes at the boundaries of the sample separately. This circumstance leads to the result that at distances of the order of the cooling length L (see Ref. 5) from the surfaces in contact with the external heat sinks, the electron (T_e) and phonon (T_p) temperatures differ.[6] Since the numerical values of the electron–phonon cooling length are important for estimates of the thermoelectric figure of merit, values of these quantities are given in Table I for a number of semiconductors and metals at room temperature.[7] In the so-called two-temperature approximation, the thermoelectric figure of merit has been calculated only in submicron layers under the condition $a/L\ll 1$, where $2a$ is the thickness of the sample.[8] In the present paper our objective is to obtain a generalized thermoelectric figure of merit which is valid for semiconductor samples of arbitrary dimensions.

Let an isotropic, monopolar semiconductor sample with a nondegenerate electron gas have the shape of a rectangular parallelepiped, whose end faces $x=\mp a$ are in contact with the heat reserviors at the temperatures T_1 and T_2 ($T_1>T_2$), and whose side faces are adiabatically isolated for all of the quasiparticle subsystems. The sample is connected to an external metallic resistance R_m of length $2b$ in such a way that the thermoelectric current j flows in the circuit. For simplicity, we restrict the discussion to scattering of charge carriers by acoustic phonons. We assume that the boundary conditions for the electron and phonon subsystems satisfy the most general boundary conditions of thermal conductivity.[6]

Within the framework of the chosen model in the approximation that is linear in the quantity $(T_1-T_2)/T^*$, where $T^*=(T_1+T_2)/2$, the thermoelectric current and electron and phonon temperature distributions were studied in detail in Ref. 9. They are given by expressions which can be represented in the form

$$T_{e,p}=T^*-\frac{\Delta T}{2}\times\left\{\frac{x}{a}-\frac{[A_e+\delta A_p(1+\lambda)]\,\dfrac{x}{a}-\gamma_{e,p}[B_e-B_p-\lambda B_p]\,\dfrac{\sinh kx}{ak\cosh ka}}{A_eB_p+\delta A_pB_e}\right\}, \tag{2}$$

where

$$A_{e,p}=1+\frac{\varkappa_{es,ps}}{\varkappa_{e,p}}\frac{\tanh ak}{ak},\quad B_{e,p}=1+\frac{\varkappa_{es,ps}}{\varkappa_{e,p}},$$

$$\varkappa_{es,ps}=a\,\eta_{e,p}.$$

These parameters have the meaning of the surface electron and phonon thermal conductivities; $\eta_{e,p}$ are coefficients which define the rate of heat transfer between the electron and phonon subsystems and the heat reservoir,

$$L=k^{-1}=(k_e^2+k_p^2)^{-1/2}$$

is the electron–phonon cooling length,

$$k_{e,p}^2=P/\varkappa_{e,p},\quad \delta=k_p^2/k_e^2=\varkappa_e/\varkappa_p,$$

$\gamma_e=1$, $\gamma_p=-\delta$, P is a parameter defining the intensity of the interaction of the electron and phonon subsystems,[6] $\Delta T=T_1-T_2$;

$$j=\frac{(1-\beta)\alpha_s+\beta\alpha}{R}\,\Delta T, \tag{3}$$

where $R=R_0+R_\Pi+R_m$ is the total resistance of the thermoelectric circuit, $R_0=2a/\sigma+2/\sigma_s$ is the resistance of the semiconductor sample, σ is its electrical conductivity of the

TABLE I. Inverse cooling lengths of electrons and phonons of some materials.

Material	k, cm^{-1}	Material	k, cm^{-1}
Ge	6.0×10^3	Si	1.7×10^4
GaAs	2.5×10^3	InSb	1.0×10^4
Bi_2Te_3	1.8×10^4	CdS	1.8×10^5
CdSe	3.7×10^4	HgSe	1.1×10^3
GaP	1.4×10^5	InP	4.3×10^3
PbTe	1.3×10^4	HgTe	1.0×10^3
Sn	2.5×10^5	Pb	3.9×10^5
InAs	1.8×10^5	Cu	4.9×10^5
Ag	4.6×10^4	Au	8.1×10^4

metallic segment of the circuit (cross section of the circuit elements at all points is assumed to be unity),

$$\lambda=\frac{2a^*(\alpha-\alpha_s)}{\varkappa_e}\,\frac{(1-\beta)\alpha_s+\beta\alpha}{R},$$

$$R_\Pi=\frac{2aT^*\gamma(\alpha-\alpha_s)^2}{\varkappa_e}, \tag{4}$$

$$\beta=1-\frac{(A_e+\delta A_p)-(B_e-B_p)\tanh(ka)/ka}{A_eB_p+\delta A_pB_e},$$

$$\gamma=\frac{\delta A_p+B_p\,\tanh(ka)/ka}{A_eB_p+\delta A_pB_e}. \tag{5}$$

To determine the figure of merit of semiconductor materials of arbitrary dimensions, we make use of a general expression for the efficiency of a thermal element

$$\eta=\frac{W}{q(x=-a)}, \tag{6}$$

where $W=j^2R_m$ is the useful power liberated in the load, $q=q_e(x=-a)+q_p(x=-a)$ is the total heat flux fed to the hot junction. The electron and phonon components of the heat fluxes are given by the expressions[6]

$$q_e=-\varkappa_e\,\frac{dT_e}{dx}+\Pi(T_e)j, \tag{7}$$

$$q_p=-\varkappa_p\,\frac{dT_p}{dx}, \tag{8}$$

where $\Pi(T_e)=\alpha T_e$ is the Peltier coefficient. Combining Eqs. (2), (7), and (8), we obtain from expression (6) for the efficiency of the thermal element

$$\eta=\frac{\Delta T}{T_1}\left[\frac{4}{Z^*T_1}+\frac{T_e(x=-a)}{T_1}\,\frac{\alpha}{[\alpha_s(1-\beta)+\alpha\beta]}\,\frac{R}{R_m}\right]^{-1}, \tag{9}$$

where

$$Z^*=\frac{8a[\alpha_s(1-\beta)+\alpha\beta]^2R_m}{\varkappa_p(1+\delta)R^2}\left[1-\frac{A_e+\beta A_p(1+\lambda)}{A_eB_p+\delta A_pB_e}\right]^{-1} \tag{10}$$

is the dimensionality parameter of the inverse temperature, which is called the thermoelectric figure of merit. The first term in brackets in (9) is associated with irreversible heat losses due to heat conduction, and the second is associated with the liberation of Peltier heat. Note that the generalized thermoelectric figure of merit (10) is determined by its surface characteristics in addition to the material parameters of the semiconductor material.

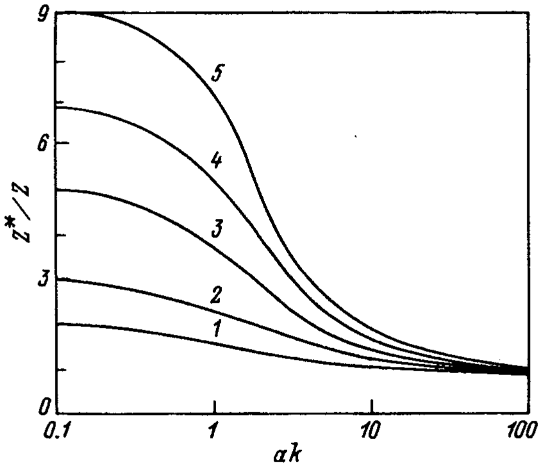

FIG. 1. Dependence of the ratio Z^*/Z on the linear dimensions of the sample for $\varkappa_{es}\gg\varkappa_e$, $\varkappa_{ps}\ll\varkappa_p$ for different values of δ: *1* — 1, *2* — 0.5, *3* — 0.25, *4* — 0.17, *5* — 0.125.

In the limiting case of isothermal contact of the electron and phonon subsystems of the bulk semiconductor sample ($a/L\gg1$) with the heat reservoirs ($\varkappa_{es}\gg\varkappa_e$, $\varkappa_{ps}\gg\varkappa_p$) we have $\gamma=0$, $\beta=1$, $R_\Pi=0$, $T_e(x=-a)=T_1$, and expression (9) for the condition of maximum power ($R_0=R_m$) becomes the standard expression[10]

$$\eta_W=\frac{\Delta T}{T_1}\,\frac{1}{4/Z^*T_1+2}, \tag{11}$$

where $Z^*=Z$.

The most interesting case from the point of view of thermoelectric transformation of energy is the one in which the phonon subsystem is adiabatically isolated, and the electron subsystem is in isothermal contact with the heat reserviors ($\varkappa_{es}\gg\varkappa_e$, $\varkappa_{ps}\ll\varkappa_p$). Expression (9) will then again acquire the form (11) with the difference that now

$$Z^*=Z\left(1+\frac{1}{\delta ak}\right). \tag{12}$$

In semiconductor samples of submicron dimensions ($a/L\ll1$)

$$Z^*=Z\left(1+\frac{1}{\delta}\right), \tag{13}$$

which completely coincides with the results of Ref. 8. The results of calculation are presented in Fig. 1.

Estimates show that in the case under consideration, e.g., for InSb ($\delta=10^{-2}$, Ref. 11), which is not the best thermoelectric material, at $T=300$ K for the linear dimensions of the sample $2a=2$ mm and 10^{-2} mm the figure-of-merit coefficients are $Z\approx10^{-4}$ K^{-1} and $\approx1.5\times10^{-3}$ K^{-1}, respectively. With further decrease of the geometrical dimensions, the figure of merit increases and reaches its maximum value $Z = 7 \times 10^{-3}$ K^{-1} in samples of submicron dimensions. Thus, for $\varkappa_{es} \geqslant \varkappa_e$, $\varkappa_{ps} \leqslant \varkappa_p$, $\delta \ll 1$, and submicron dimensions the thermoelectric figure of merit even of poor thermoelectric materials can surpass the figure of merit of the better thermoelectric materials, in which $\delta \simeq 1$. This result is explained by the fact that in submicron samples the electron–phonon interaction is absent; therefore, the phonon subsystem, being adiabatically isolated, ‘‘shuts itself out’’ of the process of heat transfer from the heater to the refrigerator, thereby increasing the figure of merit of the material.

In reality, ideal heat transfer and complete thermal isolation are idealizations; therefore, in real situations the increase in the figure of merit will be less.

This work was supported in part by the George Soros International Program of Education in the Exact Sciences (ISSEP) and the International Revival Fund (Grant No. APV 062064).

[1] L. I. Anatychuk, *Thermal Elements and Thermoelectric Devices* (Handbook) [in Russian] Dumka Naukova, Kiev (1979).

[2] M. Ya. Granovskiĭ and Yu. G. Gurevich, Fiz. Tekh. Poluprovodn. **9**, 1552 (1975) [Sov. Phys. Semicond. **9**, 1024 (1975)].

[3] A. I. Klimovskaya and O. V. Snitko, Pis’ma Zh. Éksp. Teor. Fiz. **7**, 194 (1968) [JETP Lett. **7**, 149 (1968)].

[4] A. I. Klimovskaya, AutoRef. Candidate’s Dissertation (IPAN [Institute of Physics, Academy of Sciences of the Ukrainian SSR], Kiev, 1972).

[5] Z. S. Gribnikov and V. I. Mel’nikov, Zh. Eksp. Teor. Fiz. **51**, 1909 (1966) [Sov. Phys. JETP **24**, 1282 (1967)].

[6] F. G. Bass, V. S. Bochkov, and Yu. G. Gurevich, Fiz. Tekh. Poluprovodn. **23**, 1895 (1989) [Sov. Phys. Semicond. **23**, 1173 (1989)].

[7] L. P. Bulat, Avtoref. Doctoral Dissertation (LPI [Leningrad Polytechnical Institute], Leningrad, 1989).

[8] G. N. Logvinov, Izv. Vuzov. Fizika, No. 9, 68 (1993).

[9] Yu. G. Gurevich and G. N. Logvinov, Fiz. Tekh. Poluprovodn. **26**, 1945 (1992) [Sov. Phys. Semicond. **26**, 1091 (1992)].

[10] A. R. Regel’ (ed.), *Thermoelectrical Generators* [in Russian] Atomizdat, Moscow (1976).

[11] B. M. Mogilevskiĭ and A. F. Chudnovskiĭ, *Thermal Conductivity of Semiconductors* [in Russian], Nauka, Moscow (1972).

Translated by Paul F. Schippnick

Galvanomagnetic phenomena in p-$Hg_{1-x}Mn_xTe$ solid solutions

R. I. Bashirov, R. R. Bashirov, V. A. Elizarov, and A. Yu. Mollaev

Kh. I. Amirkhanov Institute of Physics, Dagestan Scientific Center, Russian Academy of Sciences, 367003 Makhachkala, Russia

(Submitted August 14, 1995; accepted for publication June 3, 1996)
Fiz. Tekh. Poluprovodn. **31**, 326–328 (March 1997)

Galvanomagnetic effects in homogeneous samples of p-$Hg_{1-x}Mn_xTe$ solid solutions were investigated in stationary and pulsed magnetic fields up to 200 kOe in the temperature range 1.8–300 K. The magnetopolar origin of the anomalous dependence of the Hall coefficient on the magnetic field at liquid-helium temperatures is confirmed. The shift in the inversion point of the Hall coefficient agrees with the model of the bound magnetic polaron. Freezing of holes to acceptor levels in high magnetic fields was observed for all samples. © *1997 American Institute of Physics.* [S1063-7826(97)01403-8]

Dilute magnetic semiconductors have recently been receiving increasing attention. The most studied of this class of substances are manganese–mercury–tellurium (MMT) solid solutions. They form a continuous series of substitution solutions in which the the magnetic manganese ions replace the mercury ions in the crystalline lattice of mercury telluride. In a magnetic field the exchange interaction of the free current carriers with the manganese d-electrons leads to a renormalization of the energy spectrum of the electrons and holes and to the appearance of singularities in the field and temperature dependences of the kinetic coefficients. Galvanomagnetic effects in hole-type MMT samples of gapless and narrow-gap compositions were investigated in Refs. 1–6 (see also the bibliography cited in Ref. 7). A number of problems in the physics of semimagnetic semiconductors require more experimental data for their solution; of especial importance here are measurements of high-quality samples. We have therefore focused special attention on the selection of homogeneous samples.

The samples for study were cut from untouched single-crystal blocks, polished, etched with a butyl alcohol (95%)–bromine (5%) mixture, and rinsed with isobutyl alcohol and distilled water. Point contacts were indium-soldered. The degree of homogeneity in composition was determined with an x-ray microanalyzer from measurements of the manganese distribution. The samples selected in this way were examined for homogeneity of their electrical parameters with length and for symmetry of the field dependence of the magnetoresistance and Hall voltage for both (opposite) directions of current and magnetic field in the temperature interval 4.2–300 K. All of these data, taken together, allowed us to select out homogeneous samples for study.

The measurements were performed in stationary (up to 20 kOe) and pulsed (up to 200 kOe) magnetic fields with direct recording of the magnetic-field dependence of the voltages. The samples investigated in stationary magnetic fields had dimensions $10\times4\times0.6\ \mathrm{mm}^3$, and the samples investigated in pulsed fields had dimensions $6\times0.9\times0.4\ \mathrm{mm}^3$.

Table I gives the main characteristics of the samples. They can be divided into two groups according to the nature of the field dependence and sign of the Hall constant. The samples whose Hall coefficient R was positive at liquid-helium temperatures and fell off in magnitude with growth of the magnetic field remained positive in the investigated range of magnetic fields. This group included samples 4–6.

Figure 1 plots the results of measurements on sample 5. It follows from the field-dependence of the Hall coefficient $R(H)$ that at temperatures $T<6$ K the Hall effect owes its existence entirely to holes and the Fermi level is located in the valence band. With growth of the magnetic field and temperature, the Hall coefficient decreases and at large magnetic fields tends to the value

$$R_\infty=[e(N_A-N_D)]^{-1}.$$

When both holes and electrons take part in conduction and $\mu_n\gg\mu_p$ (μ_n and μ_p are the electron and hole mobilities), a magnetic field region is reached with growth of the magnetic field, where $\gamma_n\gg1$ but $\gamma_p\ll1$ ($\gamma_n=\mu_nH$, $\gamma_p=\mu_pH$). In this region $\sigma_{xy}^{(n)}$ falls off as $1/H$ and $\sigma_{xy}^{(p)}$ grows as H ($\sigma_{xy}^{(n)}$ and $\sigma_{xy}^{(p)}$ are the components of the conductivity tensor for the electrons and the holes, respectively); as a result, at some magnetic field H_i the quantity σ_{xy}, like the Hall coefficient, vanishes. The field H_i, according to Eq. (A.11) in Ref. 8, is given by

$$H_i=(1/\mu_p)(n/p)^{1/2}, \tag{1}$$

where n and p are the electron and hole concentrations. The contribution of the electrons to the Hall effect is manifested as the temperature approaches 10 K, and Hall voltage is observed to change sign in weak magnetic fields. With growth of the temperature, the contribution of the electrons to the Hall effect grows and the sign-inversion point of the Hall coefficient shifts toward higher magnetic fields as a result of the growth of the electron concentration.

It is customary to call the decrease of the Hall coefficient with growth of the magnetic field at liquid-helium temperatures an anomalous effect that is characteristic of MMT. There are a few explanations for this effect, but at present the following explanation is the preferred one.[4] The exchange interaction of the free charge carriers with the localized magnetic moments of the Mn^{++} ions leads to the appearance of bound magnetic polaron states. In this model the free hole concentration increases with increasing magnetic field; this

TABLE I. Main parameters of the investigated samples of p-$Hg_{1-x}Mn_xTe$ at 4.2 K.

Sample No.	Composition, x	$\|R_0e\|^{-1}$, cm^{-3}	$\|R_0\|\sigma$, $cm^2/(V\cdot s)$
1	0.080	$1.6\cdot 10^{15}$	270000
2	0.076	$4.8\cdot 10^{15}$	162000
3	0.066	$2.2\cdot 10^{15}$	24000
4	0.049	$3.0\cdot 10^{17}$	1620
5	0.057	$1.2\cdot 10^{16}$	7700
6	0.040	$2.3\cdot 10^{16}$	2630

increase is especially noticeable at low temperatures. In the described model the hole concentration may be found from the relation $p=(eR_0)^{-1}$, and $\mu_p=\sigma R_0$, where R_0 is the Hall coefficient in the limit $H\rightarrow 0$. For sample 5 these values for $T=1.8$ K are $p=10^{16}\,cm^{-3}$, $\mu_p=7800\,cm^2/(V\cdot s)$, and for $T=4.2$ K they are given in the table. Note that the values of the mobility and concentration for this sample fit quite nicely the theoretical dependence (see Ref. 3, Fig. 5) of the hole mobility μ_p on the concentration of scattering centers for scattering by impurity ions if it is assumed that the uncompensated semiconductor model is realized in sample 5. When the temperature is lowered from 4.2 to 1.8 K, a binding of the holes to the magnetic polaron is observed in samples 4–6, and a ''destruction'' of the magnetic polaron takes place in higher magnetic fields. For example, in sample 4 this happens at $H>7$ kOe, and in sample 6 it occurs at $H>5$ kOe. Below these fields the Hall coefficient does not depend on the magnetic field, but a region of ordinary positive magnetoresistance $\Delta\rho/\rho_0>0$ does appear in the magnetic-field dependence of the transverse magnetoresistance. The experimental data correspond to the model of the bound magnetic polaron.[4]

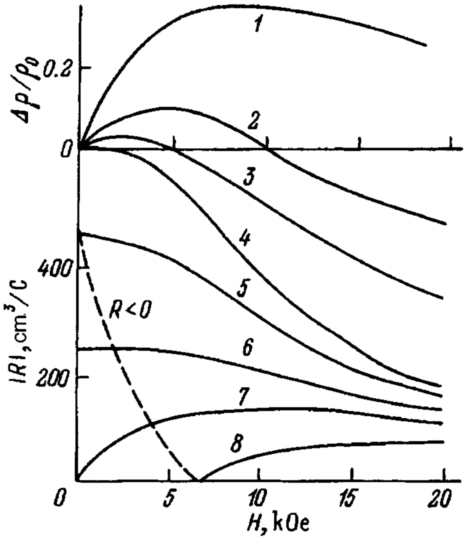

FIG. 1. Sample 5 (from Table I). Curves of the transverse magnetoresistance $\Delta\rho/\rho_0$ (*1–4*) and Hall coefficient R (*5–8*) versus magnetic field at T (K) equal to 20 (*1,8*), 10 (*2,7*), 6 (*3,6*), 4.2 (*4,5*).

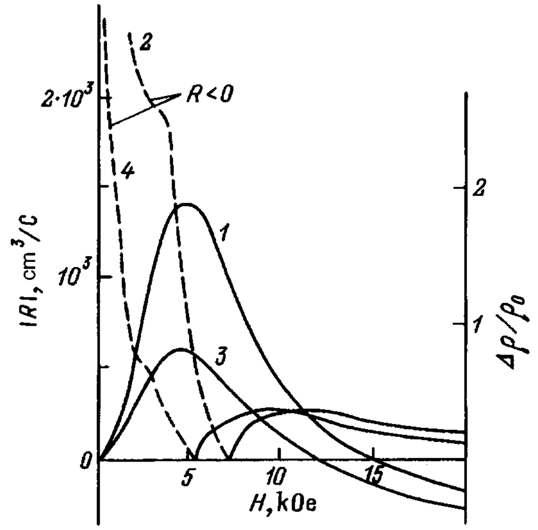

FIG. 2. Sample 3 (from Table I). Curves of the transverse magnetoresistance $\Delta\rho/\rho_0$ (*1,3*) and Hall coefficient R (*2,4*) versus magnetic field at T (K) equal to 1.8 (*1,2*) and 4.2 (*3,4*).

Let us consider the experimental data for the samples for which the Hall coefficient at liquid-helium temperatures in weak magnetic fields is negative, and in strong magnetic fields is positive; they include samples 1–3. Figure 2 plots these values for sample 3 (see the table). From the dependence of the Hall coefficient on the magnetic field $R(H)$ it follows that both electrons and holes take part in conduction here. At liquid-helium temperatures in weak magnetic fields the Hall constant has a negative sign. For this sample $n=(eR_0)^{-1}=8.7\times 10^4$ cm^{-3} and $\mu_n=\sigma R_0=8\times 10^4$ $cm^2/(V\cdot s)$ at $T=1.8$ K. When the temperature is varied above and below the interval $4.2-6$ K, the sign-inversion point of the Hall coefficient shifts to higher fields due to a change in the ratio of the electron and hole contributions to the conductivity, i.e., consistent with Eq. (1). While this behavior is attributable to an increase in the free electron concentration at $T>6$ K, when the temperature is lowered from 4.2 to 1.8 K the holes become bound, the free hole concentration decreases, and the H_i transition also shifts to higher fields. The maximum in the transverse magnetoresistance curve is explained by the fact that the contribution to the conductivity

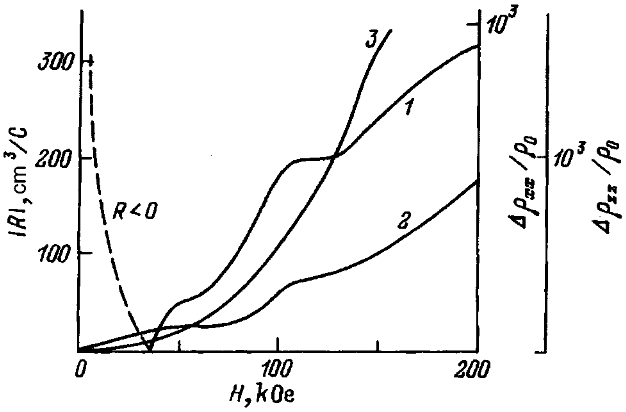

FIG. 3. Sample 1 (from Table I). Curves of the Hall coefficient R (*1*) and longitudinal (*2*) and transverse (*3*) magnetoresistance versus magnetic field at 4.2 K.

of the free holes varies with magnetic field. For $H > H_i$ the electrons are excluded from the conduction process and the hole concentration increases as a result of destruction by the magnetic field of the bound polaron state. For a narrow-gap MMT (sample 2) the maximum of the transverse magnetoresistance is located at the magnetic field $H = 6$ kOe, which corresponds to sign-inversion of the Hall coefficient. The maximum of the longitudinal magnetoresistance is shifted upward in magnetic field to $G = 10$ kOe.

The greatest magnetic freezing occurs in sample 1, in which the composition is close to the transition from a gapless to a narrow-gap semiconductor (Fig. 3). In this sample as the magnetic field is increased from $H < 40$ kOe to $H > 40$ kOe, one passes from a region where conduction is mediated mainly by electrons to one in which conduction is mediated by holes, and at higher magnetic fields to the frozen region, at which an abrupt increase in the magnetoresistance, by roughly a thousandfold, is observed.

In all of the investigated samples freezing of holes to the acceptor levels is observed, although in Ref. 4 freezing of holes was observed only in samples in which the the electron contribution to the conductivity predominated.

This work was carried out with the financial support of the Russian Fund for Fundamental Research (Grant No. 94-02-03910).

[1] A. B. Davydov, B. B. Ponikatov, and I. M. Tsidil'kovskiĭ, Fiz. Tekh. Poluprovodn. **15**, 881 (1981) [Sov. Phys. Semicond. **15**, 504 (1981)].

[2] N. B. Brandt, V. V. Moshchalkov, A. O. Orlov, L. Skrbek, I. M. Tsidil'kovskiĭ, and S. M. Chudinov, Zh. Éksp. Teor. Fiz. **84**, 1059 (1983) [Sov. Phys. JETP **57**, (1983)].

[3] A. V. Germanenko, L. P. Zverev, V. V. Kruzhaev, G. M. Min'kov, O. É. Rut, N. P. Gavaleshko, and V. M. Frasunyak, Fiz. Tverd. Tela **26**, 1754 (1984) [Sov. Phys. Solid State **26**, 1062 (1984)].

[4] A. V. Germanenko, L. P. Zverev, V. V. Kruzhaev, G. M. Min'kov, and O. É. Rut, Fiz. Tverd. Tela **27**, 1857 (1985) [Sov. Phys. Solid State **27**, 1114 (1985)].

[5] A. V. Germanenko, L. P. Zverev, V. V. Kruzhaev, G. M. Min'kov, and O. É. Rut, Fiz. Tekh. Poluprovodn. **20**, 80 (1986) [Sov. Phys. Semicond. **20**, 46 (1986)].

[6] A. V. Germanenko, V. V. Kruzhaev, and G. M. Min'kov, Fiz. Tekh. Poluprovodn. **20**, 141 (1986) [Sov. Phys. Semicond. **20**, 85 (1986)].

[7] Yu. Furdina and Ya. Kosut, *Semimagnetic Semiconductors* [Russ. trans., Mir, Moscow (1992) [translation of *Diluted Magnetic Semiconductors*, edited by J. K. Furdyna *et al.* (Semiconductors and Semimetals Series, Vol. 25, Academic Press, San Diego, 1988)].

[8] I. M. Tsidil'kovskiĭ, G. I. Kharus, and N. G. Shelushinina, *Impurity States and Transport Phenomena in Gapless Semiconductors* (Sverdlovsk, Ural Scientific Center, Academy of Sciences of the USSR, 1987).

Translated by Paul F. Schippnick

Lattice vibrations in $CuInSe_2$ crystals

N. N. Syrbu and M. Bogdanash

Kishineu Technical University, 277012 Kishineu, Moldova

V. E. Tezlevan

Institute of Applied Physics, Moldavian Academy of Sciences, 277028 Kishineu, Moldova

(Submitted October 26, 1995; accepted for publication June 4, 1996)
Fiz. Tekh. Poluprovodn. **31**, 329–334 (March 1997)

Infrared reflection spectra of $CuInSe_2$ crystals are investigated for the polarizations **E**∥**c** and **E** ⊥ **c**. Contours of the reflection spectra are calculated and phonon parameters and dielectric constants are determined. The effective charges of the Cu, In, and Se ions in these materials are determined. The two-phonon absorption spectra in $CuInSe_2$ are investigated and the absorption bands are identified from the selection rules. © *1997 American Institute of Physics.* [S1063-7826(97)01503-2]

1. INTRODUCTION

The ternary semiconductor $CuInSe_2$ has shown promise for use in solar cells. The vibrational properties of $CuInSe_2$ crystals have been investigated in a number of works.[1–9] However, results of studies of the infrared reflection spectra and Raman spectra do not agree. The infrared reflection spectra and Raman spectra were found to be lacking some of the vibrational modes. The infrared reflection spectra for the polarizations **E**∥**c** and **E**⊥ **c**, in which three *E* modes (**E**⊥ **c**) were identified instead of the expected six, are presented in Ref. 7. In Raman scattering studies at 300 and 100 K (Ref. 9) only the *A* mode has been visually identified, although the authors assert that they identified all the vibrational modes.

In the present study we have investigated infrared reflection spectra of $CuInSe_2$ crystals in the polarizations **E**∥**c** and **E** ⊥ **c**, in which we have found all the expected vibrational modes and also new information about the phonon parameters.

2. EXPERIMENTAL PROCEDURE

Single crystals of $CuInSe_2$ were grown by the Bridgman method in the form of bars 3 cm in diameter and 6–7 cm in length. Wafers of dimensions 1.5×2.5 cm were then cut from the bars. The reflection spectra were measured on a computer-controlled KSDI-82 vacuum spectrometer. The spectral width of the gap was equal to $0.2\ \mathrm{cm}^{-1}$ in the frequency range $50-250\ \mathrm{cm}^{-1}$ and $1\ \mathrm{cm}^{-1}$ in the range $200-4000\ \mathrm{cm}^{-1}$.

The reflection spectra were also calculated in the many-oscillator model of the dispersion relations

$$\varepsilon(\omega)=\varepsilon_1+i\varepsilon_2=\varepsilon_\infty+\sum_{j=1}^{N}\frac{4\pi f_j\omega_{TOj}^2}{(\omega_{TOj}^2-\omega^2+i\omega\gamma_j)},$$

$$\varepsilon_0=\varepsilon_\infty+\sum_{j=1}^{N}4\pi f_j,$$

$$f_i=\varepsilon_\infty\frac{(\omega_{LOj}^2-\omega_{TOj}^2)}{(4\pi\omega_{TOj}^2)}\prod_{i\neq j}\frac{(\omega_{LOi}^2-\omega_{TOj}^2)}{(\omega_{TOi}^2-\omega_{TOj}^2)},$$

$$\varepsilon_\infty=\left|\frac{1-\sqrt{R}}{1+\sqrt{R}}\right|^2,$$

where ε_∞ and ε_0 are the high-frequency and low-frequency dielectric constants, ω_{LOj} and ω_{TOj} are the longitudinal and transverse phonon frequencies, γ_j is the damping factor, f_j is the jth oscillator strength, and R is the reflection coefficient in the frequency range $3000-4000\ \mathrm{cm}^{-1}$.

3. EXPERIMENTAL RESULTS

In the reflection spectra of $CuInSe_2$ crystals in the polarization **E** ⊥ **c** we identified six vibrational modes with *E*

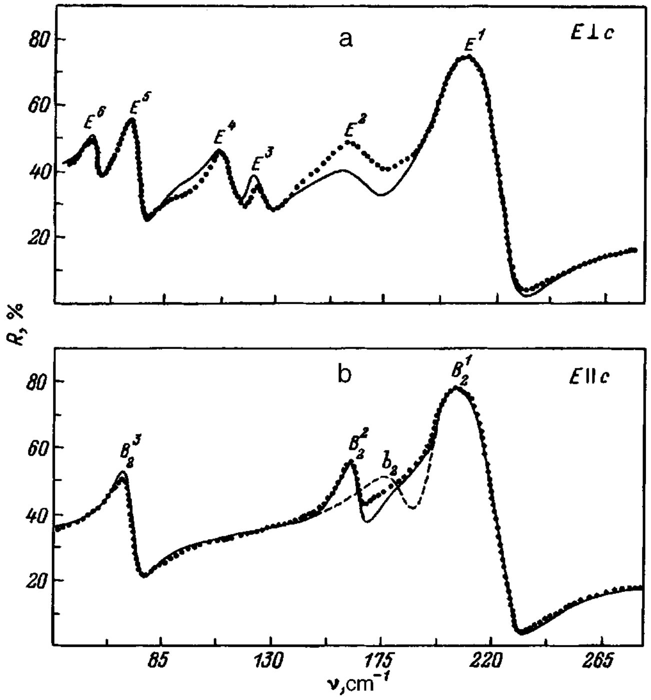

FIG. 1. Reflection spectra of $CuInSe_2$ crystals for polarizations **E**∥**c** (a) and **E**⊥ **c** (b); solid line—calculation, points—experiment, dashed line—see text.

TABLE I. Parameters of the B_2 and E modes in $CuInSe_2$ crystals.

	Data obtained from published papers							
	Refs. 6 and 7*		Ref. 9					
	mode frequency ν, cm^{-1} at temperature T, K				Results of our study			
Mode	300	100	300	100	ν_{LO}, cm^{-1}	ν_{TO}, cm^{-1}	γ	$4\pi f_1$
$B_2^{(1)}$	232	214	233–215	233−217	228.6	208.6	6.0	1.40
$B_2^{(2)}$	193	181	198	200−177	169	163	20	2.33
$B_2^{(3)}$	65	64	71−70	72−70	78.8	70.5	6.5	2.36
E^1	229	213	230−217	233−217	227.5	204	8.0	2.10
	212	207						
E^2	183	179	-	230−227	174	162	10	1.54
E^3			211	216−211	128.5	122	8.0	1.07
E^4			-	188−288	116	108	9.0	1.24
E^5			77−77	78−78	77.5	71.0	6.0	2.54
E^6			60−58	60−61	57.0	55.5	4.0	1.28

*Note: these data were obtained in the infrared.

symmetry (Fig. 1a, here $\nu = 1/\lambda$, λ is the wavelength of the light), i.e., as many modes as expected from the group-theory analysis

$$\Gamma_{\mathrm{opt}} = 1A_1 + 2A_2 + 3B_1 + 3B_2 + 6E.$$

The macroscopic electric field produced by the longitudinal optical vibrations splits each of the polar vibrations of B_2 and E symmetry into longitudinal (LO) and transverse (TO) modes. The values of the LO and TO phonon parameters and dielectric constants obtained are listed in Table I. The points in Fig. 1 indicate experimental values, and the solid curve corresponds to calculated values of the reflection coefficient. The modes E^1 and E^5 possess the largest oscillator strengths. The damping factors vary in the limits 4–10. The reflection spectra in Fig. 1a are in satisfactory agreement with the data of Ref. 7. We assume that the reflection peak E^1 which we have identified and the peaks $E^1(E^2)$ identified in Ref. 7 are due to a single vibrational mode. The reflection maximum E^2(174/162) corresponds to the reflection peak E^3 in Ref. 7. In the long-wavelength region ($40-120\,cm^{-1}$) we have identified the previously unrevealed vibrational modes E_4–E_6 (Fig. 1a, Table I). Calculations of the reflection spectra show that the contours of nearly all the oscillators are satisfactorily described by the dispersion relations.

In the polarization **E**∥**c** we identified the three expected vibrational modes of B_2 symmetry (Fig. 1b, Table I). The high-frequency B_2 mode is the strongest mode in this polarization. These modes agree with the data of Refs. 6 and 7. Note that the vibrational mode B_2 is observed at different frequencies for samples of different preparation history, as is shown by the dashed line in Fig. 1b. Apparently, some samples have a violation of stoichiometry (selenium vacancies), which affects this vibrational mode. The parameters of the vibrational modes of the $CuInSe_2$ crystals are compared with the corresponding parameters for $CuGaSe_2$ and $CuInS_2$ in Table II. As can be seen, the frequency ratios for $CuGaSe_2$ and $CuInSe_2$ exhibit only insignificant variation. Here for all the vibrational modes with E and B_2 symmetry with the exception of $B_2^{(2)}$ and E^2, the frequency ratios vary in the limits 1.18–1.28. For E^2 and $B_2^{(2)}$ the frequency ratio stands at 1.09–1.12. These data reflect the fact that in $CuInSe_2$ crystals the vibrational modes $B_2^{(2)}$ and E^2 are found

TABLE II. Frequencies of active vibrational modes in the infrared and their ratios in $CuGaSe_2$, $CuInSe_2$, and $CuInS_2$.

	$CuGaSe_2$ Ref. 11		$CuInSe_2$ our data		$CuInS_2$ Refs. 6 and 7		Ratios of mode frequencies			
							$\nu_{CuGaSe_2}/\nu_{CuInSe_2}$		$\nu_{CuInS_2}/\nu_{CuInSe_2}$	
Polarization of mode	ν_{LO}, cm^{-1}	ν_{TO}, cm^{-1}	ν_{LO}, cm^{-1}	ν_{TO}, cm^{-1}	ν_{LO}, cm^{-1}	ν_{TO}, cm^{-1}	LO	TO	LO	TO
E^1	277	255	227.5	204	338	324	1.22	1.25	1.49	1.59
E^2	186	180	174	162	312	294	1.09	1.11	1.83	1.82
E^3	149	145	128.5	122	258	244	1.19	1.18	2.06	1.98
E^4	135	129.8	116	108			1.19	1.18		
E^5	90.9	82.2	77.5	71			1.20	1.17		
E^6	68	64.5	57	55.5			1.19	1.16		
$B_2^{(1)}$	273	257	228.6	208.6	352	328	1.19	1.28	1.54	1.64
$B_2^{(2)}$	188	177.9	169	163	265	238	1.12	1.1	1.58	1.47
$B_2^{(3)}$	89.6	83.0	78.8	70.5			1.18	1.21		

$M_1 = m_{\mathrm{In}} + m_{\mathrm{Se}} = 193.78$, $M_2 = m_{\mathrm{Ga}} + m_{\mathrm{Se}} = 148.66$, $M_3 = m_{\mathrm{In}} + m_{\mathrm{S}} = 146.88$

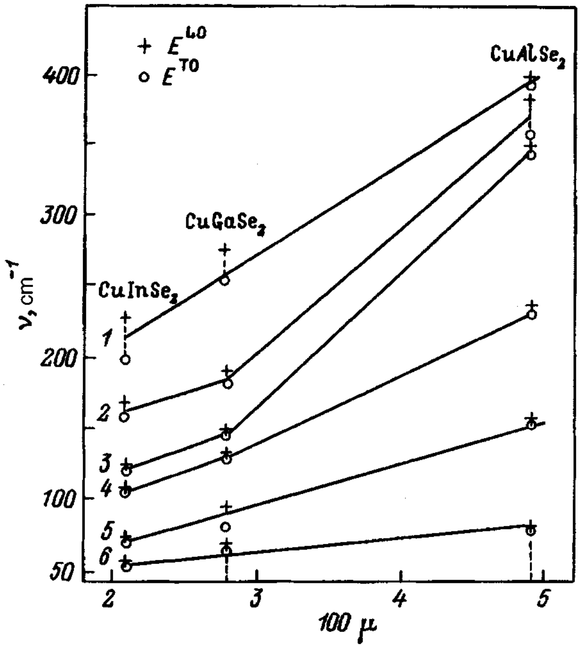

FIG. 2. Dependence of the frequencies of the vibrational modes E_i ($i=1,2\ldots6$) on the reduced mass of the ions In–Se, Ga–Se, and Al–Se in crystals of $CuInSe_2$, $CuGaSe_2$, and $CuAlSe_2$. The numbers next to the curves correspond to the number of the mode.

at higher frequencies than they should be according to Figs. 1a and 1b. The frequency ratios of the vibrational modes of $CuInSe_2$ and $CuInS_2$ vary to a greater extent. This is as it should be since there is less difference between the reduced mass of the Ga–Se_2 and In–Se_2 complexes than between the In–Se_2 and In–S_2 complexes. The mass ratio of the ions In–Se(M_1) to the mass of the ions Ga–Se(M_2) is equal to 1.30. The $CuGaSe_2$/$CuInSe_2$ frequency ratio, which varies in the range 1.09–1.28, is in completely satisfactory agreement with the square root of the mass ratios of the ions $(M_1/M_2)^{1/2}=1.14$ (see Table II). The frequency ratios for $CuInS_2$ and $CuInSe_2$ differ more significantly than the ratio $(M_1/M_3)^{1/2}$ of the mass of the ions In–Se(M_1) to the mass of the ions In–S(M_3 (Table II). In $CuInS_2$ crystals the inter-

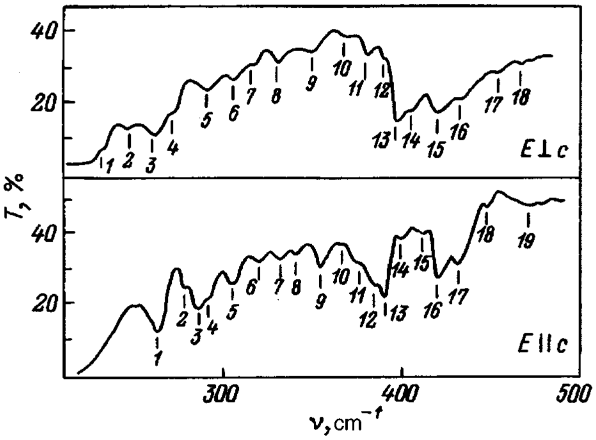

FIG. 3. Two-phonon absorption spectra of $CuInSe_2$.

TABLE III. Frequencies and combinations of modes in the two-phonon absorption (transmission) spectrum for $CuInSe_2$ crystals in the polarization $\mathbf{E}\perp\mathbf{c}$; $A_1\otimes E, A_2\otimes E, B_1\otimes E, B_2\otimes E$.

		Results of our study		
Number of structure	Data from Ref. 7 ν, cm^{-1}	Experiment ν, cm^{-1}	Combination of modes	Calculation ν, cm^{-1}
1		224	$B_1^{(2)}(165^{a})+E_6^{LO}(57)$,	222
			$B_2^{(2)LO}(169)+E_6^{TO}(55.5)$	224.5
2		250	$E_2^{LO}(174)+B_2^{(3)LO}(78.8)$	252.8
			$A_1(178)+E_5^{TO}(71)$	249
3		263	$B_2^{(1)TO}(208.5)+E_6^{TO}(55.5)$	264.1
4		271	$B_2^{(2)TO}(163)+E_4^{TO}(108)$	271
5		291	$E_3^{TO}(112)+B_2^{(2)LO}(169)$,	291
			$B_2^{(1)TO}(208.5)+E_6^{TO}(55.5)$	264.1
6	300	305	$A_1(178^{a})+E_3^{LO}(128.5)$	306.5
7		316	$E_4^{TO}(108)+B_2^{(1)TO}(208.6)$	316.6
8	332	326	$B_2^{(2)TO}(163)+E_2^{TO}(162)$,	325
			$E_2^{TO}(162)+B_1^{(2)(165)}$	327
9	347	344	$B_2^{(2)LO}(169)+E_2^{LO}(174)$	343
10		368	$E_1^{TO}(204)+B_2^{(2)TO}(163)$	367
11	385	382	$A_1(178^{a})+E_1^{TO}(204)$	382
12		390	$B_2^{(1)LO}(228.6)+E_2^{TO}(162)$	390
13		397	$E_1^{LO}(227.5)+B_2^{(2)LO}(169)$	396.5
14	405	405	$E_1^{LO}(227.5)+A_1(178)$	405.5
15		423	$E_1^{LO}(227.5)+A_2^{(1)}(196)$	423.5
16	428	432	$E_1^{TO}(204)+B_2^{(1)LO}(228.6)$	432.6
17		457	$B_2^{(1)LO}(228.6)+E_1^{LO}(227.5)$	456.1
18	465	467	$B_1^{(1)}(239)+E_1^{LO}(227.5)$	466.5

Note: Here the subscript i in the mode notation $E_i^{LO,TO}$ corresponds to the superscript in the mode notation for E_i in the text.

TABLE IV. Frequencies and combinations of modes in the two-phonon absorption (transmission) spectrum for $CuInSe_2$ crystals in the polarization $\mathbf{E}\|\mathbf{c}$; $A_1 \otimes B_2$, $A_2 \otimes B_1$, $E \otimes E$.

		Results of our study		
Number of structure	Data from Ref. 7 ν, cm^{-1}	Experiment ν, cm^{-1}	Combination of modes	Calculation ν, cm^{-1}
1		263	$E_1^{TO}(204)+E_6^{LO}(57)$	261
2		278	$E_2^{TO}(162)+E_4^{LO}(116)$	278
3		285	$E_1^{LO}(227.5)+E_6^{LO}(57)$	284.5
4		291	$E_3^{LO}(128.5)+E_2^{TO}(162)$	290.5
5		305	$E_1^{LO}(227.5)+E_5^{LO}(77.5)$	305
6	316	320	$E_1^{TO}(204)+E_4^{LO}(116)$	320
7		334	$E_1^{LO}(227.5)+E_4^{TO}(108)$	335.5
8	340	343	$E_1^{LO}(227.5)+E_4^{LO}(116)$	244.5
9	349	355	$E_1^{LO}(227.5)+E_3^{LO}(128.5)$	356
10		367	$E_1^{TO}(204)+E_2^{(2)TO}(162)$	366
11		378	$E_1^{TO}(204)+E_2^{LO}(174)$	378
12		386	$A_2(178)+B_2^{(1)TO}(208.6)$	386.6
13	395	392	$E_2^{TO}(162)+E_1^{LO}(227.5)$	389.5
14		401	$E_2^{LO}(174)+E_1^{LO}(227.5)$	401.5
15	411	411	$E_1^{TO}(204)+E_1^{TO}(204)$	408
16	427	426	$E_1^{LO}(227.5)+E_1^{TO}(204)$	431.5
17	438	435	$B_1^{(1)}(239^{a})+A_2^{(2)}(196^{a})$	435
18	443	450	$2E_1^{LO}$	455

Note: Here the subscript i in the mode notation $E_i^{LO,TO}$ corresponds to the superscript in the mode notation for E_i in the text.

atomic distances also vary since the sulfur ions have smaller radii than the selenium ions.

Figure 2 compares the frequencies of the vibrational E modes of $CuInSe_2$, $CuGaSe_2$, and $CuAlSe_2$ (the data for $CuAlSe_2$ and $CuGaSe_2$ are taken from Ref. 11) as functions of the reduced mass μ of the ions In(Ga,Al)–Se. For $CuAlSe_2$ the high-frequency vibrational modes E_i with $i=1,2,3$ depend on μ to a greater extent than the low-frequency vibrational modes with $i=4,5,6$. Comparing the mode frequencies for $CuInSe_2$ and $CuGaSe_2$, we also notice a shift of all vibrational frequencies of $CuGaSe_2$ toward higher energies. This occurs because the heavier indium ions have been replaced here by lighter gallium ions. In $CuAlSe_2$ the still lighter aluminum atom appears in place of the gallium atom. The increase in the frequency of the vibrational modes $i=1$, 2, 3, as one goes from $CuGaSe_2$ to $CuAlSe_2$ (i.e., the heavier Ga ion is replaced by the lighter Al ion), confirms that these modes are internal vibrational modes.

4. TWO-PHONON ABSORPTION IN $CuInSe_2$ CRYSTALS

The two-phonon absorption spectra of $CuInSe_2$ crystals were analyzed in Ref. 7. But since we have obtained new data about the vibrational mode spectra in the one- and two-phonon regions, we will here again discuss two-phonon absorption on the basis of our results. The absorption (transmission) spectra in the region 250–500 cm^{-1} were measured in samples 20–30 μm thick (Fig. 3). We identified 18 absorption bands in each of the polarizations $\mathbf{E}\|\mathbf{c}$ and $\mathbf{E}\perp\mathbf{c}$. Our spectra agree for the most part with the absorption spectra of Ref. 7. The small thickness of the crystals allowed us to carry out measurements almost up to the one-phonon region ($\sim 250\ cm^{-1}$) and obtain a larger number of absorption bands than are presented in Ref. 7.

According to the selection rules, in $CuInSe_2$ crystals in the polarization $\mathbf{E}\perp\mathbf{c}$ the phonon combinations $A_1\otimes E$, $A_2\otimes E$, $B_1\otimes E$, and $B_2\otimes E$ are active, and in the polarization $\mathbf{E}\|\mathbf{c}$ the combinations $A_1\otimes B_2$, $A_2\otimes B_1$, and $E\otimes E$ are active. Tables III and Tables IV list the frequencies of the absorption lines we have identified, the results of Ref. 7, and also calculated values of the frequencies of the two-phonon combinations responsible for these absorption bands. Nearly all of the identified two-phonon bands are described by a combination of LO and TO vibrational modes of the corresponding symmetry, allowed by the selection rules. The difference between the experimentally identified and calculated bands does not exceed a few inverse centimeters. In the $\mathbf{E}\|\mathbf{c}$ polarization all the identified bands are described by the combination $E\otimes E$, with the exception of bands 12 and 17. Band 17 (identified in Ref. 7) is described by the combination $A_2^{(2)}\otimes B_1^{(1)}$.

5. EFFECTIVE IONIC CHARGES AND THEIR ISOTROPY

The parameters of the effective ionic charges of $CuInSe_2$, $CuGaSe_2$, and $CuAlSe_2$ are found from the following relations:

$$4\pi c^2\sum_{j=1}^{N}(\omega_{LOj}^2-\omega_{TOj}^2)=\frac{4\pi e^2 N}{V}\left|\frac{(Z_a e^*)n_a}{m_a}+\frac{(Z_b e^*)n_b}{m_b}+\frac{(Z_c e^*)n_c}{m_c}\right|,$$

$$n_aZ_ae+n_bZ_be-n_cZ_ce=0,$$

TABLE V. Parameters of the effective ionic charge in $CuGaSe_2$, $CuInSe_2$, and $CuAlSe_2$ crystals.

Crystal	Polarization and modes	ε_0	ε_∞	$\frac{e_s^*}{Z_{\text{eff}}e}=x$, calculated according to Eq. (1)	$e_s^*/Z_{\text{eff}}e=\frac{3\sqrt{\varepsilon_\infty}}{\varepsilon_\infty+2}$	Z/Z_{eff}	$\Delta Z=Z_{\text{eff}}^{\mathbf{E}\parallel\mathbf{c}}-Z_{\text{eff}}^{\mathbf{E}\perp\mathbf{c}}$	e_B^*/Z_{eff}
$CuGaSe_2$	$\mathbf{E}\parallel\mathbf{c}$					$Cu\sim0.63$		
	B_2	7.3	4.2	0.44	0.99	$Ga\sim0.25$	$Cu\sim0.25$	2.05
						$Se\sim-0.44$		
	$\mathbf{E}\perp\mathbf{c}$					$Cu\sim0.38$		
	E	12.83	5.13	0.36	0.95	$Ga\sim0.34$	$Se\sim0.08$	2.25
						$Se\sim-0.36$		
$CuInSe_2$	$\mathbf{E}\parallel\mathbf{c}$					$Cu\sim0.21$	$Cu\sim0.04$	
	B_2	12.09	6.0	0.31	0.92	$In\sim0.33$		2.45
						$Se\sim-0.31$	$In\sim-0.04$	
	$\mathbf{E}\perp\mathbf{c}$					$Cu\sim0.17$		
	E	16.63	6.86	0.27	0.91	$In\sim0.37$	$Se\sim0.04$	2.69
						$Se\sim-0.27$		
$CuAlSe_2$	$\mathbf{E}\parallel\mathbf{c}$					$Cu\sim0.40$	$Cu\sim0.20$	
	B_2	6.67	5.2	0.35	0.95	$Al\sim0.30$		2.28
						$Se\sim-0.35$	$Al\sim-0.12$	
	$\mathbf{E}\perp\mathbf{c}$					$Cu\sim0.20$		
	E	8.28	6.0	0.31	0.92	$Al\sim0.42$	$Se\sim0.04$	2.59
						$Se\sim-0.31$		

where V is the volume of the unit cell; N is the number of atoms per unit cell; n_a, n_b, and n_c are the stoichiometric coefficients; and m_a, m_b, and m_c are the atomic masses of the elements making up the crystal.

To determine the effective charges of the ions of the three-component material we used the condition

$$x=\frac{e_s^*}{Z_{\text{eff}}},\quad \varepsilon_\infty-1=\frac{2}{x^2+x}, \tag{1}$$

which was proposed in Ref. 12–14. This condition is essentially satisfied in all the investigated materials. The effective ionic charges we obtained for $CuInSe_2$ differ slightly from the results of Ref. 9 since the frequencies of the LO and TO phonons also differ, and the effective charges are calculated on the basis of these frequencies. The dielectric constant parameters $(\varepsilon_\infty,\varepsilon_0)$ and effective ionic charges of $CuInSe_2$, $CuGaSe_2$, and $CuAlSe_2$ differ substantially for the two polarizations $\mathbf{E}\parallel\mathbf{c}$ and $\mathbf{E}\perp\mathbf{c}$ (see Table V).

To describe the results for different crystals, we introduced the anisotropy parameter of the effective ionic charges $\Delta Z=Z_{\text{eff}}^{\mathbf{E}\parallel\mathbf{c}}-Z_{\text{eff}}^{\mathbf{E}\perp\mathbf{c}}$, where $Z_{\text{eff}}^{\mathbf{E}\parallel\mathbf{c}}$ and $Z_{\text{eff}}^{\mathbf{E}\perp\mathbf{c}}$ are the effective ionic charges of the corresponding atom (ion) in the polarization $\mathbf{E}\parallel\mathbf{c}$ and $\mathbf{E}\perp\mathbf{c}$, respectively. The parameter ΔZ can have both positive and negative values, which characterize the electron cloud of the ion shell and its deviation from a perfectly spherical shape.[15] For positive ΔZ the cloud is elongated along the $\mathbf{c}$ axis, and for negative ΔZ it is compressed. As can be seen, the shape of the electron cloud is different for all the ions in the three compounds considered.

In summary, replacing indium by gallium or aluminum in $CuInSe_2$ not only alters the frequencies of the vibrational modes, but also redistributes the electron cloud relative to the principal axes of the crystal.

[1] I. N. Gan, I. Tauc, V. G. Lambrecht, and M. Robbins, Phys. Rev. **13**, 3610 (1976).

[2] V. Riede, H. Sobotta, H. Neumann, H. X. Nguyen, W. Müller, and G. Kühn, Solid State Commun. **28**, 449 (1978).

[3] H. Neumann, R. D. Tomlinson, W. Kissinger, and N. Avgerinos, Phys. Status Solidi B **118**, K51 (1983).

[4] I. V. Bondar, A. G. Karoza, B. V. Korzun, and G. F. Smirnova, Zh. Prikl. Spectrosk. **36**, 451 (1982).

[5] P. M. Nicolic, S. M. Stojikovic, Z. Petrovic, and P. Dimitrijevic, Fizica **10**, Suppl. 2, 98 (1978).

[6] H. Neumann, H. Sobotta, V. Riede, B. Schumann, and G. Kühn, Cryst. Res. Technol. **18**, K90 (1983).

[7] H. Neumann, Solar Cells **16**, 399 (1986).

[8] H. Tanino, H. Deal, and H. Nakanishi, *Proceedings of the Ninth International Conference on Ternary and Multinary Compounds*, Yokohama, 1993 [Jpn. J. Appl. Phys. **32**, Suppl. 32-3, 436 (1993)].

[9] H. Tanino, T. Maeda, H. Fujikake, H. Nakanishi, S. Endo, and T. Irie, Phys. Rev. B **45**, 13,323 (1992).

[10] H. Neumann, W. Kissinger, H. Sobotta, and V. Riede, Czechoslovak J. Phys. **84**, 69 (1984).

[11] A. M. Andriesh, N. N. Syrbu, M. S. Iovu, and V. E. Tezlevan, Phys. Status Solidi B **187**, 83 (1995).

[12] K. Wakamura and T. Ogawa, Jpn. J. Appl. Phys. **19**, 249 (1980).

[13] M. Wakaki, Jpn. J. Appl. Phys. **24**, 1471 (1985).

[14] G. Lutz, G. Waschenlach, G. Kelche, and H. Haenseier, Solid State Chem. **44**, 196 (1983).

[15] N. N. Syrbu, Opt. Spektrosk. **79**, 249 (1995) [Opt. Spectrosc. **79**, 227 (1995)].

Translated by Paul F. Schippnick

Anomalies in the low-temperature thermoelectric power of p-Bi_2Te_3 and Te associated with topological electronic transitions under pressure

E. S. Itskevich, L. M. Kashirskaya, and V. F. Kraĭdenov

L. F. Vereshchagin Institute of High-Pressure Physics, Russian Academy of Sciences, 142092 Troitsk, Russia

(Submitted January 9, 1996; accepted for publication June 4, 1996)
Fiz. Tekh. Poluprovodn. **31**, 335–337 (March 1997)

Thermoelectric power measurements have been carried out for the narrow-band semiconductors p-Bi_2Te_3 and Te under pressures up to 2.5 GPa at liquid-helium temperatures. The dependences observed correlate with the data obtained by oscillation methods. These correlations allow one to use the thermoelectric power to search for topological electronic transitions in semiconductors. © *1997 American Institute of Physics.* [S1063-7826(97)01603-7]

We have placed before ourselves the task of extending the range of methods for searching for topological electronic transitions (TET's) in narrow-band semiconductors under pressure, not for the usual purpose of studying details of the band structure guided by quantum oscillations of the resistance (the Shubnikov–de Haas effect), but in order to apply it to the goal of studying the thermoelectric power.

Oscillation methods for finding TET's require, as their main condition, high-quality single crystals and a complicated experimental technique. The use of a model for the behavior of the thermoelectric power in TET's developed for the case of semimetals and alloys under conditions of uniaxial deformation, as Minina *et al.*[1–4] have shown, is quite effective. In these papers they demonstrated the possibility of using the thermoelectric power to search for the principal modifications of the topological electronic transition in semimetals and alloys under conditions of uniaxial deformation. We solved the analogous problem for cadmium under conditions of hydrostatic pressure in Ref. 5. We demonstrated the existence of a correlation between direct observations of TET's by the use of oscillation methods employing anomalies in the pressure dependence of the thermoelectric power of cadmium.

The authors of Refs. 6 and 7 in a study of Shubnikov–de Haas oscillations under conditions of hydrostatic pressure observed topological electronic transitions of the type ''formation (or breaking) of bridges joining isolated isoenergy cavities'' of the Fermi surface for p-Bi_2Te_3 and Te. In this case the Fermi energy E_F is observed to pass smoothly through the critical points of the charge carrier spectrum E^* at which the topological electronic transition takes place by varying the hydrostatic pressure. This is held to be one of the most informative and refined methods for studying topological electronic transitions. The combination of observing the passage of the Fermi energy through the critical points in this way and using the thermoelectric-power method to search for the topological electronic transitions is especially effective since the entire experiment is carried out with the same sample.

The Fermi surface of p-Bi_2Te_3 for $E_F < E^* = 18$ meV consists of six quasi-ellipsoids, between which linkages form under pressure which are similar to those present in the Fermi surface of arsenic.[7] Tellurium has a shallow ($E^* = 2.3$ meV) saddle point in the spectrum of its valence band which is forced out, i.e., it moves up, under pressure, which in samples with $E_F < E^*$ leads at first to the appearance of a linkage or bridge between the two existing ellipsoids, i.e., to the appearance of a dumbbell–shaped Fermi surface, and then, after the disappearance of the saddle point at $P \simeq 2.7$ GPa, to the reappearance of the original ellipsoidal Fermi surface.[7,8]

1. Our experiment was carried out at liquid-helium temperatures in a hydrostatic high-pressure chamber similar to that described in Refs. 6 and 7. The samples were cut by electric spark from single-crystal bars and processed with polishing chrome etchant. The C_3 axis was determined visually from the cleavage planes. A temperature gradient was created along the C_3 axis ($\nabla T \| C_3$) for Te and perpendicular to the C_3 axis ($\nabla T \perp C_3$) for p-Bi_2Te_3 and Te. The technique used for measuring the thermoelectric power in the samples, which had the shape of rectangular parallelepipeds with dimensions $1 \times 1 \times 6$ mm^3, is described in Ref. 9.

2. Figure 1 plots the pressure dependence of the thermoelectric power for three samples of p-Bi_2Te_3 with E_F below the critical value $E^* = 18$ meV. For the sample that was measured in the most detail (sample 1) with $E_F = 6$ meV, a complex picture of the pressure dependence is observed with two minima and two maxima. On the basis of the model that has been proposed for the Fermi surface of p-Bi_2Te_3 (Refs. 6 and 10), such a picture can be explained by the ''fine'' structure of formation of the bridge. Specifically, at first a hole-type cavity is formed. This creates the first anomaly in the pressure dependence of the thermoelectric power at the critical pressure P_{c1}. With increasing pressure, this cavity then joins up with the principal hole-type ellipsoids, creating a second anomaly at P_{c2}. A sketch of the evolution of the topological electronic transition is given in Fig. 2. The picture of the evolution of the Fermi surface of p-Bi_2Te_3 under hydrostatic pressure obtained from measurements of the thermoelectric power makes it possible not only to unambiguously reconfirm, but also refine, the earlier proposed model of the Fermi surface for this crystal.

The anomalies of the pressure dependence of the thermoelectric power, which are due to the rearrangement of the spectrum, can be assumed to be the two maxima and two minima at the corresponding pressures, P_{c1} and P_{c2}. Using

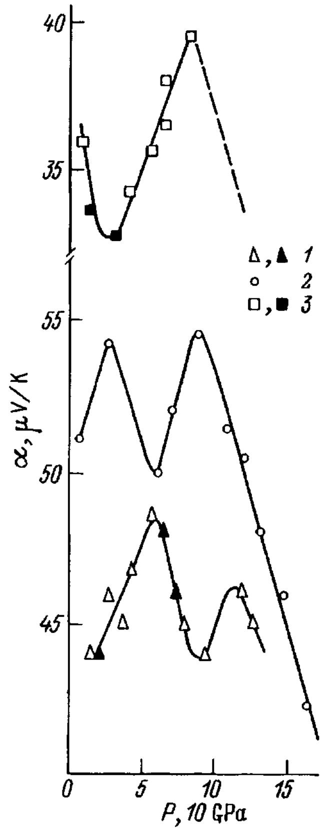

FIG. 1. Dependence of the thermoelectric power of p-Bi_2Te_3 on the pressure P at $T=4.2$ K. Hole concentration p, 10^{17} cm^{-3}: *1*) 7, *2*) 8, *3*) 20. Filled symbols indicate the values of α measured upon release of pressure.

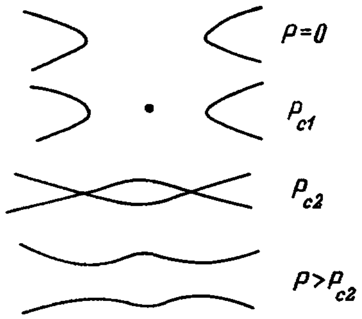

FIG. 2. Diagram of sequence of appearance of linkages between two hole-type ellipsoids in p-Bi_2Te_3 under pressure.

the pressure coefficient of variation of the energy gap obtained from data on the Shubnikov–de Haas effect, $dz/dP=-2.7$ meV/kbar (Ref. 6) $(z=E^*-E_F)$, we can estimate the pressure at which $z=0$, i.e., at which the first TET of the type ''formation of a new isoenergy cavity'' takes place, creating the first anomaly in the thermoelectric power. Thus, for sample 1 with $z=12$–13 meV this value is $P_{c1}=4.5$–5 kbar, for sample 2 with $z=10$–11 meV, $P_{c1}=3.5$–4 kbar, and for sample 3 with $z=6$–5 meV, $P_{c1}=1.5$–2 kbar. The first maximum corresponds satisfactorily with these estimates. Thus, the sign of the thermoelectric power anomalies in p-Bi_2Te_3 is positive.

It follows from Ref. 11, in which the thermoelectric power and the thermal conductivity of samples of Bi_2Te_3 similar to ours were investigated over a wide temperature range, that the thermoelectric power in our samples at 4 K has a predominantly phonon character (α_{ph}). At this temperature we clearly observed anomalies in $\alpha(P)$. The conclusion of Abrikosov and Pantsulaya[12] that there are no anomalies in α_{ph} associated with the topological electronic transitions was based on the assumption of isotropic scattering of the charge carriers. Allowing for the anisotropy of the relaxation time that is present in noncubic crystals, in particular Bi_2Te_3 and Te, enabled Suslov[13] to provide a theoretical basis for the appearance of anomalies in α_{ph} connected with the topological electronic transitions. The magnitude of α is determined not only by the hole concentration, but also by the number of structural defects, especially dislocations, which by scattering phonons can strongly lower α. The reason for the appearance of dislocations may be a breach of hydrostatic conditions in the high-pressure chamber caused by cooling it down to liquid-helium temperatures. Each pressure change is accompanied by annealing and the appearance of new dislocations. Most likely, this is also the reason for the almost twofold decrease in α for sample 3 in comparison with the analogous sample of p-Bi_2Te_3 in Ref. 11 at 4.2K, and also for the fact that the value of α for sample 1 is slightly lower than the value of α for sample 2.

Thus, a topological electronic transition in p-Bi_2Te_3, reliably identified by oscillation methods, shows up as an anomaly in the dependence of the thermoelectric power on the hydrostatic pressure at the point at which E_F passes through the critical point E^*.

3. Our measurements of the thermoelectric power of tellurium samples with hole concentration $p=4\times10^{14}$ cm^{-3} for $\nabla T \| C_3$ and $p=2\times10^{15}$ cm^{-3} for $\nabla T \perp C_3$ under pressures up to 25 kbar at liquid-helium temperatures are plotted in Fig. 3. The solid and dashed curves plot the calculated variation of the thermoelectric power of Te with growth of the pressure on the assumption that the measured thermoelectric power is either purely diffusional (α_D) or completely phonon in character (α_{ph}). In the investigated samples at 4.2 K a hole gas is nondegenerate; i.e., $\alpha_D \sim \ln[(m^*)^{1.5}]$, $\alpha_{\mathrm{ph}} \sim m^*$, and the effective hole mass $m^*(P)=m^*(0)\exp(-0.006P)$ (Ref. 14). Thus, the overall trend of the functional dependence $\alpha(P)$ can be satisfactorily explained by a diminution with growth of the pressure of the effective hole mass m^*.

If we compare the values of the thermoelectric power for our samples at 4 K extrapolated to $P=0$ with the values in the literature for similar samples,[15] then we may conclude that the phonon component of the thermoelectric power of our samples at 4 K, which gives the main contribution to α, is significantly smaller (more than sixfold) than for the samples of Ref. 15. We measured the temperature dependence (from 16 to 300 K) of the thermoelectric power of tellurium with hole concentration $p=2\times10^{15}$ cm^{-3} at $P=0$. At $T=200$ K, where the main contribution to α comes from the diffusional component α_D, our value $\alpha \approx 700$ μV/K is close to the value of α for the analogous sample 2 of Ref. 15. As was shown in Ref. 16, cooling a

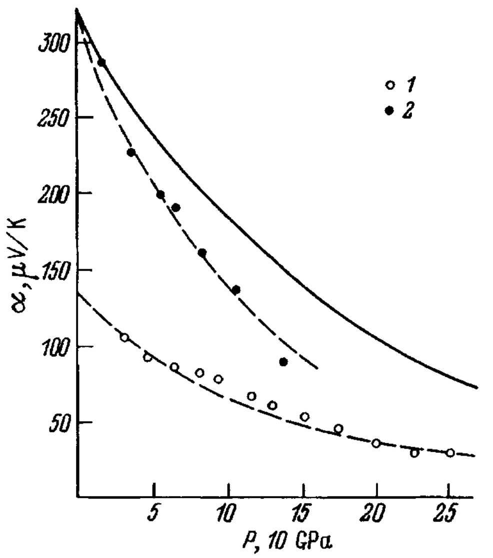

FIG. 3. Dependence of the thermoelectric power of Te on the pressure P at $T=4.2$K. Hole concentration p, 10^{14}cm^{-3}: *1)* 4, *2)* 20. Calculations shown by curves: α_D — dashed, α_{ph} — solid.

tellurium sample under pressure gives rise to a strong growth of the number of dislocations (by a factor of 3–4). Phonon scattering by dislocations should strongly decrease the effect of an increase in the number of holes and, consequently the magnitude of α_{ph}, which would then lead to a significantly smaller value of the thermoelectric power for our samples.

It is hard to distinguish any clearly pronounced anomalies in $\alpha(P)$, but a definite irregularity at 7 kbar for Te with $p=2\times10^{15}$ cm^{-3} ($\nabla T\perp C_3$) and at 12 kbar for Te with $p=4\times10^{14}$ cm^{-3} ($\nabla T\| C_3$), and a tendency toward saturation of the thermoelectric power at the highest pressures are quite clear. Such a character of the dependence is in satisfactory agreement with theoretical conclusions and with our experimental data obtained from measurements of Shubnikov–de Haas oscillations under pressure. According to the calculation carried out by Lyapin,[8] complete disappearance of the saddle point in the valence band of Te and, consequently, the transition from a dumbbell–shaped Fermi surface to an ellipsoidal Fermi surface is expected at $P_c=27$ kbar. This topological electronic transition may be responsible for the flattening out of $\alpha(P)$ at pressures $P>20$ kbar. It is entirely possible that the first observed irregularity is connected with the topological electronic transition caused by the coalescence of the two hole-type quasi-ellipsoids into a dumbbell.[7] The small volumes of the isoenergy surfaces ($E_F<2.3$ meV) may be one of the reasons for the weakly expressed anomalies.

In summary, it may be stated that for all of the investigated types of topological electronic transitions reliably identified from the Shubnikov–de Haas oscillations, anomalies are present in the thermoelectric power which are uniquely linked with a change in the topology of the Fermi surface. It can also be asserted that the presence of anomalies in the pressure dependence of the low-temperature thermoelectric power is indicative of topological electronic transitions in semiconductors, semimetals, and metals.

This work was carried out with the financial support of the Russian Foundation for Basic Research (Project No. 93-02-14235).

[1] N. B. Brandt, V. S. Egorov, M. Yu. Lavrenyuk, N. Ya. Minina, and A. M. Savin, Zh. Éksp. Teor. Fiz. **89**, 1157 (1985) [*sic*].

[2] M. Yu. Lavrenyuk, N. Ya. Minina, and A. M. Savin, Pis'ma Zh. Éksp. Teor. Fiz. **46**, 224 (1987) [JETP Lett. **46**, 282 (1987)].

[3] N. B. Brandt, M. Yu. Lavrenyuk, N. Ya. Minina, and A. M. Savin, Zh. Éksp. Teor. Fiz. **94**, 235 (1988) [Sov. Phys. JETP **67**, 1867 (1988)].

[4] L. A. Kirakozova, M. Yu. Lavrenyuk, N. Ya. Minina, and A. M. Savin, Fiz. Tverd. Tela **30**, 666 (1988) [Sov. Phys. Solid State **30**, 381 (1988)].

[5] V. F. Kraĭdenov, E. S. Itskevich, and A. G. Gapotchenko, Fiz. Tverd. Tela **37**, 405 (1995) [Phys. Solid State **37**, 218 (1995)].

[6] V. V. Sologub, M. L. Shubnikov, E. S. Itskevich, L. M. Kashirskaya, R. V. Parfen'ev, and A. D. Goletskaya, Zh. Éksp. Teor. Fiz. **79**, 2374 (1980) [Sov. Phys. JETP **52**, 1203 (1980)].

[7] V. B. Anzin, M. S. Bresler, I. I. Farbstein, E. S. Itskewich, Yu. V. Kosichkin, V. A. Sukhoparov, A. S. Telepnev, and V. G. Veselago, Phys. Status Solidi B **48**, 531 (1971).

[8] S. G. Lyapin, AutoRef. Candidate's Dissertation (Moscow, 1988), p. 78.

[9] S. L. Bud'ko, A. G. Gapotchenko, E. S. Itskevich, and V. F. Kraĭdenov, Prib. Tekh. Éksp., No. 2, 205 (1977).

[10] V. V. Sologub, R. V. Parfen'ev, and A. D. Goletskaya, Pis'ma Zh. Éksp. Teor. Fiz. **21**, 711 (1975) [JETP Lett. **21**, 337 (1975)].

[11] A. D. Goletskaya, V. V. Sologub, and S. S. Shalyt, Fiz. Tekh. Poluprovodn. **5**, 477 (1971) [Sov. Phys. Semicond. **5**, 416 (1971)].

[12] A. A. Abrikosov and A. V. Pantsulaya, Fiz. Tverd. Tela **28**, 2140 (1986) [Sov. Phys. Solid State **28**, 1195 (1986)].

[13] I. M. Suslov, Pis'ma Zh. Éksp. Teor. Fiz. **46**, 26 (1987) [JETP Lett. **46**, 30 (1987)].

[14] V. B. Anzin, M. I. Eremets, Yu. V. Kosichkin, A. I. Nadezhdinskii, and A. M. Shirokov, Phys. Status Solidi A **42**, 385 (1977).

[15] I. N. Timchenko and S. S. Shalyt, Fiz. Tekh. Poluprovodn. **4**, 934 (1962).

[16] M. V. Glushkov, E. S. Itskevich, Yu. V. Kosichkin, A. N. Tolmachev, and A. M. Shirokov, Fiz. Tverd. Tela **19**, 3580 (1977) [Sov. Phys. Solid State **19**, 2092 (1977)].

Translated by Paul F. Schippnick

Formation of a quasi-periodic boron distribution in silicon, initiated by ion implantation

A. M. Myasnikov, V. I. Obodnikov, V. G. Seryapin, E. G. Tishkovskiĭ, B. I. Fomin, and E. I. Cherepov

Institute of Semiconductor Physics, Siberian Branch of the Russian Academy of Sciences, 630090 Novosibirsk, Russia

(Submitted November 8, 1995; accepted for publication June 24, 1996)
Fiz. Tekh. Poluprovodn. **31**, 338–341 (March 1997)

The temperature range in which oscillating impurity distributions are formed in heavily boron-doped silicon irradiated with boron ions B^+ is found. It is hypothesized that the effect is associated with boron clustering processes which proceed more efficiently in the region of the maximum of the implanted impurity distribution and at the boundaries of the ion irradiation region. © *1997 American Institute of Physics.* [S1063-7826(97)01703-1]

1. INTRODUCTION

In Ref. 1 we established that as a result of annealing samples of heavily boron-doped silicon at 900 °C, where these samples were later irradiated by a 10^{16} cm^{-2} dose of 180-keV $^{10}B^+$ ions, a quasi-periodic structure is formed in the concentration profiles of both boron isotopes in the region subjected to boron implantation, consisting of five maxima.

Our goal was to determine the temperature interval in which the formation of oscillating distributions of boron atoms can be observed.

2. EXPERIMENT

As the starting samples we used samples that were prepared by a method that is completely analogous to the one described in Ref. 1. Boron diffusion was caused to take place in a KEF-7.5 silicon wafer with (100) surface orientation at 1150 °C so as to create a region of uniform doping to a depth of a few microns with boron concentration $\approx 2\times 10^{20}$ cm^{-3}. Both isotopes were deposited in the doped region—^{10}B and ^{11}B in their natural abundances $\approx$20 and $\approx$80%. Then, using an HVEE-400 setup, a 10^{16} cm^{-2} dose of 400-keV $^{10}B^+$ ions were implanted. The irradiated samples were annealed for 60 min at temperatures in the range 700–1150 °C.

The distribution of the ^{10}B and ^{11}B isotopes with depth was investigated by secondary-ion mass spectroscopy using an MIQ-256 setup by CAMECA-RIBER. The constancy of the etching rate was monitored by the yield of secondary silicon ions.

A. Experimental results

The measurements show that heating the samples to 700 °C has little effect on the initial impurity profiles shown in Fig. 1a. In the case of annealing at 800 °C, however, peculiarities in the boron isotope profiles in the form of dips begin to appear, and in the temperature interval 900–1075 °C five maxima are formed in the profiles of both isotopes (Figs. 1b and 1c).

The quasi-periodic structure is not formed when the samples are heated to 1150 °C—only weakly expressed distortions of the now flat impurity profiles are observed along with a lowering of the total boron concentration in comparison with its initial value, due to diffusive spreading (Fig. 1d).

In Fig. 2 the oscillating impurity profile, shown in Fig. 1b, is compared with the profile obtained in Ref. 1, where the conditions of the experiment differed only in the ion energy (180 keV). The central maxima are aligned to facilitate the comparison. Such a comparison of the impurity profiles shows that increasing the energy of the bombarding ions does not substantially alter the characteristics of the arising quasi-periodic structures. Only the depth varies at which they are found. The average modulation period of these structures is 95 nm (with a maximum value of 109 nm and a minimum value of 88 nm).

The width of the region in which the formation of quasi-periodic structures is observed correlates with the size of the region containing the main fraction of implanted boron. Its characteristic width varies insignificantly as the energy of the impinging boron ions is increased from 180 to 400 keV (in particular, the spread of the projected mean free path ΔR_p increases by roughly a factor of[2] 1.2). The nearly identical initial conditions in these two cases lead to identical results after annealing.

The above experimental facts, in conjunction with the fact that in all cases similar variations in the impurity distribution were not observed in the continuations of the flat segments of the initial diffusion profiles with depth, indicate that side by side with a high initial level of doping, implantation is a determining factor in the formation of quasi-periodic distributions as a result of heat processing.

3. DISCUSSION

Our results show that neither the number nor the spatial positions of the concentration peaks depend on temperature. Since it is known that migration of boron atoms has an activation character in the investigated temperature range, the apparent activation-free character of the processes which leads to the appearance of spatially separated sites of boron atom accumulation, necessarily requires a consideration of processes involving the participation of other components of the defect–impurity subsystem, specifically, vacancies and interstitial silicon atoms.

The mobility of the vacancies and interstitials is activated at temperatures substantially lower than those used in

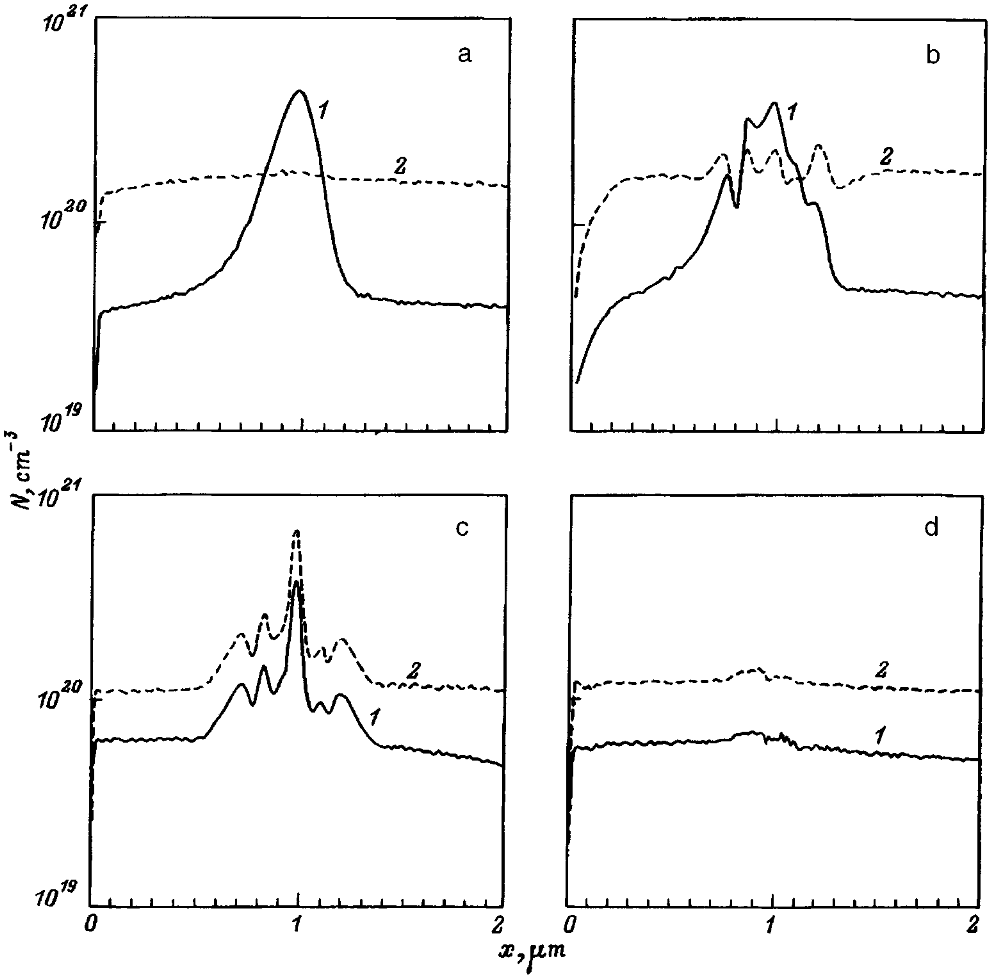

FIG. 1. Concentration profiles of boron isotopes (*1*—^{10}B, *2*—^{11}B) in silicon with an initial boron concentration of 2×10^{20} cm^{-3}, obtained by implantation of ^{10}B ions ($E=180$ keV, $D=10^{16}$ cm^{-2}) and annealing for 60 min at different temperatures: a) without annealing, b) 900 °C, c) 1075 °C, d) 1150 °C.

the experiment. High temperatures are needed only to free elementary defects from defect–impurity associations.

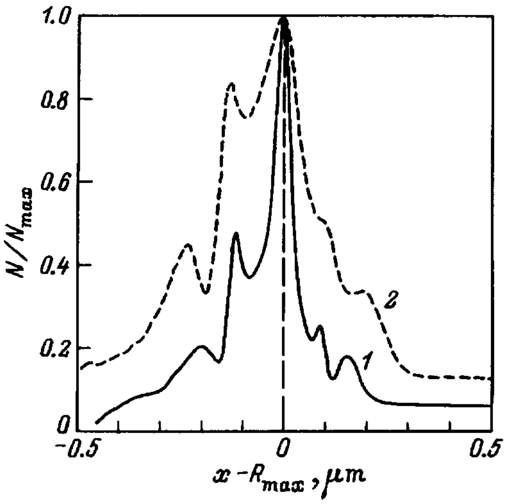

FIG. 2. Concentration profiles of the boron isotope ^{10}B in silicon with an initial boron concentration of 2×10^{20} cm^{-3}, obtained by implantation of ^{10}B ions ($D=10^{16}$ cm^{-2}) and annealing for 60 min at 900 °C: 1) $E=180$ keV, 2) $E=400$ keV.

Calculations which used the program TRIM-94 show that the coordinates of the maxima of the implanted boron distribution and of the energy losses to elastic collisions virtually coincide; i.e., most of the implanted impurity atoms are located in the same region of the semiconductor as the irradiation-generated defects, and it is in a segment of this region that all of the processes analyzed in the present paper take place.

In Ref. 1 we established that the spatial characteristics of the quasi-periodic structures in the boron atom distribution arising as a result of annealing at 900 °C for 10–240 min do not depend on the duration of heating. Consequently, the formation of these sites of boron accumulation should occur during times shorter than the lower limit of the indicated interval since for these features to appear in the impurity profile, time is required for the impurity to migrate into these spatially separated sites.

Thus, the quasi-periodic structure forms, as it were, in two stages. In the first (fast) stage, sites form in which boron accumulates and the comparatively slow process of boron accumulation at these sites occurs in the second stage.

In our experiments the fast stage proved to be essentially unobservable. However, on the basis of an analysis of the initial conditions and character of the localized features arising in the impurity distribution it is possible to construct a consistent (in our view) hypothesis of how this happens.

Upon the implantation of boron ions in the region adjoining R_p, simultaneous with the accumulation of defect complexes containing interstitial silicon atoms and vacancies there also takes place an accumulation of boron atoms not occupying regular sites of the crystalline lattice. Their number is made up from a significant fraction of the boron atoms introduced by irradiation and from a fraction of the boron atoms that were located at regular lattice sites before irradiation. In addition to the boron atoms which show up at arbitrary sites due to collision mechanisms, these sites can also have boron atoms that have been dislodged from regular lattice sites as a result of reactions with the intrinsic interstitials (the Watkins reaction[3,4]) directly upon ion implantation. An indication of the efficiency of such a process in heavily doped silicon is given in Ref. 5, where the displacement reaction is used to explain the substantially lower (in comparison with the case in lightly doped silicon) concentration of $\{113\}$ defects in silicon samples doped with boron up to concentrations $N_{\mathrm{B}} \geqslant 10^{19}$ cm^{-3} and irradiated with electrons; i.e., the main fraction of the boron atoms in the implantation region adjoining R_p is found at irregular sites and consists of not only the implanted fraction of boron atoms, but also a significant fraction of the boron atoms introduced by diffusion.

Note also that under the conditions of our experiment for the temperatures at which the appearance of quasi-periodic structures is observed, the total boron concentration exceeds its limiting value at the displacement sites[6,7] both inside the implantation region and outside it.

In the initial stage of annealing (possibly already as the samples are being heated up from room temperature in the furnace) the defect–impurity associations release their constituent interstitial silicon atoms, vacancies, and boron atoms, which show up at the interstitial sites.

Inside the irradiation region the excess boron atoms that cannot dissolve in the regular sites of the silicon lattice accumulate into clusters. The process of spontaneous clusterization proceeds most efficiently at the center of this region—in the vicinity of the maximum of the implanted boron distribution. The formed clusters serve as sinks for the free boron component, which ensures the accumulation of the impurity in the vicinity of R_p upon subsequent heating due to its migration from neighboring regions. It should be noted that contraction of the impurity upon annealing into the region of the maximum of the implanted boron distribution was observed earlier[8,9] and takes place if the implanted boron concentration in this region is not high enough.

The relaxation of the nonequilibrium defect subsystem takes place at the same time as the processes described above. Vacancies that have freed themselves from the defect–impurity associations participate in reactions associated with setting up boron atoms at lattice sites, and in annihilation reactions with the intrinsic interstitials. The intrinsic interstitial atoms, in addition to taking part in the annihilation reactions, also take part in displacement reactions in which the boron atoms are dislodged from regular lattice sites.

The fraction of boron atoms occupying regular lattice sites in the implantation region in the initial stage of annealing is small. As a result, the unreacted intrinsic interstitial atoms, which diffuse out of it in numbers significantly exceeding those of the vacancies, reach the nominal boundaries of this region, show up at displacement sites in silicon samples with high boron concentration and in such samples displace boron from the regular lattice sites.

Since none of the boron atoms at these sites, which have been displaced from the regular lattice sites, can again occupy regular lattice sites of the silicon lattice as a result of the high initial doping level, the boron atom excess created at the interstitial sites is removed at subsequent times by a chain of spontaneous clusterization reactions. The boron clusters formed at the boundaries of the irradiation region, just like the clusters at the center of the implantation region, begin to function like sinks for the free boron component.

If these three regions of nascent clusters (at the center and at the edges of the irradiation region) are so widely separated that diffusive migration of mobile boron atoms cannot substantially lower the boron concentration in the space between them, then spontaneous clusterization of boron will also lead to cluster formation in these intervening spaces. Of course, the probability of survival of these additional sinks in competition with the sinks located in the regions considered above will be higher in the centers of the intervening spaces. These additional sinks will show up in the concentration profiles as intermediate maxima.

If the samples are held at high temperatures for a longer time (in the second stage), the processes will proceed in the system of formed sinks—mobile boron atoms will escape to the clusters.

4. CONCLUSIONS

1. We have established that quasi-periodic structures are formed in the boron atom distribution as a result of irradiation of heavily boron-doped silicon by a 10^{16} cm^{-2} dose of 400-keV B^+ ions with subsequent annealing for one hour in the temperature interval 900–1075 °C.

2. We assume that the formation of a quasi-periodic structure takes place in two stages and that it is associated with clusterization of boron atoms dislodged from regular lattice sites with subsequent runoff to already formed clusters of the free boron component. The spatial inhomogeneities owe their existence to the fact that the clusterization process proceeds more efficiently in the vicinity of a maximum of the implanted impurity distribution and at the edges of the region containing the main fraction of implanted atoms. Cluster formation is accompanied by a runoff of the mobile boron atoms to these clusters.

We thank L. I. Fedina and B. A. Zaĭtsev for many useful remarks made in the course of this work. We also thank G. A. Kachurin for a discussion of the results.

[1] A. M. Myasnikov, V. I. Obodnikov, V. G. Seryapin, E. G. Tishkovskiĭ, B. I. Fomin, and E. I. Cherepov, Pis'ma Zh. Éksp. Teor. **60**, 96 (1994) [JETP Lett. **60**, 102 (1994)].

[2] H. Ryssel and I. Ruge, *Ionenimplantation* [in German] (Teubner, Stuttgart, 1978).

[3] G. D. Watkins, *Radiation Damage in Semiconductors* (Dunod, Paris,

1964), p. 97.
[4] G. Watkins, *Lattice Defects in Semiconductors*, Conference Series No. 23 (Institute of Physics, London–Bristol, 1975), p. 1.
[5] L. I. Fedina and A. L. Aseev, Fiz. Tverd. Tela **32**, 60 (1990) [Sov. Phys. Solid State **32**, 33 (1990)].
[6] H. Ryssel, K. Muller, K. Haberger, R. Henkelmann, and F. Jahnel, Appl. Phys. **22**, 35 (1980).
[7] V. E. Borisenko and S. G. Yudin, Phys. Status Solidi A **101**, 123 (1987).
[8] W. K. Hofker, H. W. Werner, D. P. Oostkoek, and H. A. M. de Grefte, Appl. Phys. **2**, 265 (1973).
[9] M. G. Dowsett, E. A. Clark, and M. N. Lewis, *Proceedings of the Sixth International Conference SIMS-VI* (1988), p. 725.

Translated by Paul F. Schippnick

Influence of elastic stresses on the character of epitaxial crystallization of (Hg, Mn)Te

S. V. Kavertsev and A. E. Belyaev

Institute of Semiconductor Physics, Ukrainian National Academy of Sciences, 252650 Kiev, Ukraine

(Submitted May 12, 1996; accepted for publication June 24, 1996)
Fiz. Tekh. Poluprovodn. **31**, 342–346 (March 1997)

Available experimental data on the composition and conditions for crystallization of semiconductor $Hg_{1-z}Mn_zTe$ solid-state solutions epitaxially grown on Cd(Zn)Te substrates reveal a number of peculiarities, which indicate that the substrate strongly affects the character of crystallization of the solid phase. In this paper we discuss data on liquid-phase epitaxy of $Hg_{1-z}Mn_zTe$ which suggest the possibility that elastic stresses caused by the mismatch between the crystal lattice parameters of the substrate and the epitaxial layer can influence the composition and conditions for crystallization of these layers. An important tool in our investigation is a thermodynamic analysis of the metastable equilibrium between the stressed solid phase and the supersaturated solution of components. © *1997 American Institute of Physics.* [S1063-7826(97)01803-6]

1. INTRODUCTION

One of the fundamental factors that determine the particular features of epitaxial growth of semiconductor solid-state solutions by the method of liquid-phase epitaxy (LEP) is how the character of the phase equilibria changes when the substrates used are mismatched to the layers with respect to lattice parameter. Thus, for example, epitaxial films of $Hg_{1-z}Mn_zTe$ are usually grown on substrates of CdTe material, whose crystal lattice parameter is larger than that of the solid solutions for any composition (Table I). Because of this circumstance, the composition of the epitaxial layer can be affected not only by the interdiffusion of metals, but also by the following processes. First of all, the mismatch in crystal lattice parameters can hinder the formation of nuclei of the new phase on the surface of the substrate when it is brought into contact with the growth melt. This in turn makes it necessary to supercool the melt beforehand in order to start crystallization. If the required supercooling is not provided, the substrate partially dissolves, which depletes the melt of tellurium. This partial dissolution of the substrate continues until the equilibrium temperature for crystallization of the melt is no longer higher than the substrate temperature at the given value for supercooling. Furthermore, the value of the supercooling itself (i.e., the supersaturation of the melt) is determined by elastic stresses that arise between the substrate and the epitaxial layer at the beginning of the crystallization. From a thermodynamic point of view, as long as the layer thicknesses are small (less than 1 μm) these stresses can be relieved by the formation of a network of mismatch dislocations in the growing layer, after which the supercooling becomes more than sufficient; further crystallization is largely determined by diffusion processes in the liquid phase. However, in view of the relatively low growth temperature and the fact that interdiffusion of the components can wash out the boundary between the substrate and the epitaxial layer, it is easy to argue that the stressed state of the crystal is preserved over distances of tens of microns. Since the elastic interaction energy is included in the total crystal energy additively, it could well cause the concentrations of materials in the solid phase to decrease. The goal of our paper is to estimate the actual role played by these substrate factors during the epitaxial growth of $Hg_{1-z}Mn_zTe/CdTe$.

As material for our investigation we have taken the experimental data on liquid phase epitaxy of $Hg_{1-z}Mn_zTe$ given in Refs. 2 and 3. Danilov *et al.*[2] carried out a detailed analysis of phase equilibria in the Hg–Mn–Te system using the method of fully associated solutions (FAS). They compared the experimental data on LEP with calculations based on the FAS method, in which the parameters of the calculations were partially chosen from theoretical considerations and partially from analysis of the phase diagram for the binary systems Hg–Te and Mn–Te along with points on the phase diagram of the Hg–Mn–Te system determined by the method of visual-thermal analysis. They conducted their liquid-phase epitaxy on CdTe substrates at temperatures 5–7 degrees lower than the expected liquidus temperature of the equilibrium system. Danilov *et al.* note that under these conditions there is practically no tendency for the substrate to dissolve. Our goal in Ref. 3 was to obtain material with composition $z = 0.08$ corresponding to a band gap of ~0.1 eV at 300 K. We grew epitaxial films on a substrate of $Cd_{0.96}Zn_{0.04}Te$; the composition of each batch was determined from the dependence of z on the liquid-phase composition given by Zhovnir *et al.*,[4] who in turn obtained this dependence while attempting to relate the liquidus surface of the Hg–Mn–Te system to the crystallization temperature of

TABLE I. Crystal lattice parameters of several binary compounds with the sphalerite structure (Ref. 1).

Compound	a, Å
CdTe	6.482
HgTe	6.4605
MnTe	6.345*
ZnTe	6.1037

*Note: Value obtained from analysis of composition dependence of the lattice parameter of $Hg_{1-x}Mn_xTe$.

TABLE II. Experimental data on liquid-phase epitaxy of $Hg_{1-x}Mn_xTe$.

	Liquid-phase composition (batch)			Solid-phase composition		
				expected	microanalysis results	
Substrate	Mn fraction	Te fraction	T, K	Mn fraction	Mn fraction	Cd fraction
CdTe (Ref. 2)	0.01	0.75	781	>0.1	0.06	
	0.015		789	0.17	0.09	
	0.0175		793	0.17	0.105	
	0.01875		799	0.17	0.14	
	0.025		802	>0.17	0.165	
	0.032	0.6	923	>0.17	0.14	
$Cd_{0.96}Zn_{0.04}Te$ (Ref. 3)	0.2425	0.75	793	0.08	0.04	0.02
	0.33775	0.65	848	0.08	0.07	0.04

epitaxially grown crystals on a substrate of CdTe. Note that they also used the FAS approximation in their calculations.

The results listed in Table II reveal that in all the experiments the values of manganese concentration were smaller than expected. Andrukhiv *et al.*,[5] noted an analogous disagreement between calculations based on the FAS method and experiment, which they attributed to the elastic stresses during epitaxial growth of the $Hg_{1-z}Zn_zTe$ compound.[5] Furthermore, in Ref. 3 we noted the presence of cadmium in the epitaxial layer, in quantities proportional to the quantity of manganese, which at first glance could also be a manifestation of the stabilizing effect on the period of the crystal lattice.

In order to estimate quantitatively the possible effect of elastic stresses on the composition and crystallization conditions of the solid phase, we, like the authors of Refs. 2 and 4, will use the method of quasichemical reactions. In other words, we assume that the equilibrium state of the system is determined by the relation between activities of the quasichemical components that are forming the system. By analogy with Hg–Cd–Te,[6] we assume that the liquid phase contains not only free mercury, manganese, and tellurium, but also the associates $HgTe^l$ and $MnTe^l$, and that the solid phase can be treated as a solid solution in the binary HgTe of the compound MnTe analogous to it. Let us denote the relative concentrations and activity coefficients of these components by y_i, γ_i, $i=1...5$, and $z_j \gamma_j^s$, $j=1, 2$ respectively.

In this approximation, the state of the liquid-phase system is described by the system of equations

$$y_1\gamma_1 y_3\gamma_3 = k_{a1} y_4 \gamma_4,$$

$$y_2\gamma_2 y_3\gamma_3 = k_{a2} y_5 \gamma_5,$$

$$y_1 = x_1(1+y_4+y_5) - y_4,$$

$$y_2 = x_2(1+y_4+y_5) - y_5,$$

$$y_3 = x_3(1+y_4+y_5) - y_4 - y_5, \tag{1}$$

and equilibrium between the liquid phase and the crystal is described by the equations

$$y_1\gamma_1 y_3\gamma_3 = k_{f1} z_1 \gamma_1^s,$$

$$y_2\gamma_2 y_3\gamma_3 = k_{f2} z_2 \gamma_2^s, \tag{2}$$

where x_i, $i=1...3$ are the initial (total) concentrations of mercury, manganese, and tellurium, respectively; and k_{ai} and k_{fi} are certain thermodynamic parameters. The rigorous meaning of these parameters may be different, depending on their intended use. When elastic stresses are present, the total energy of the system is increased by an amount $G^{ei} = \sigma a(a-a_s)^2$, where a_s and a are the crystal lattice parameters of the substrate and epitaxial layer, and σ is a parameter that takes into account the elastic properties of the material.[7] The temperature dependence of σ is weak. Assuming that $a = \Sigma a_j z_j$, where a_j are lattice parameters of the binary compounds that generate the solid solution, we find that the system of equations (2) should be replaced by equations of the type

$$RT\ \ln(Y_1\gamma_1 y_3\gamma_3 / k_{f1} z_1) = W(T)(1-z_1)^2 + \sigma(a_1(a-a_s)^2 + 2a(a-a_s)(a_1-a)), \tag{3.1}$$

and

$$RT\ \ln(Y_2\gamma_2 y_3\gamma_3 / k_{f2} z_2) = W(T)(1-z_2)^2 + \sigma(a_2(a-a_s)^2 + 2a(a-a_s)(a_2-a)), \tag{3.2}$$

where W is a solid-phase interaction parameter in the usual approximation that the solution is quasiregular. Then since we know the temperatures at which the stressed solid phase is in metastable equilibrium with the supersaturated solution of components, when the fraction of the substrate that dissolves is insignificant, it is sufficient to identify the contribution of elastic stresses by calculating $RT\ \ln(y_1\gamma_1 y_3\gamma_3 / k_{1f})$ for each experimental point from (1).

TABLE III. Liquidus temperature (computed) for the HgTe system in the tellurium sector.

Atomic fraction of Te in the liquid phase	Calculated liquidus temperature, K	
	according to Ref. 2	according to Ref. 6
0.6	880.3	908.8
0.65	853.0	869.9
0.7	821.4	825.1
0.75	781.4	779.8
0.8	728.6	735.2

TABLE IV. Computed quantities that characterize the state of the system Hg–Te at the point of three-phase equilibrium; solution enriched by tellurium.

T, K	Activity of tellurium in the liquid phase, a_3	Vapor pressure above pure Te (Ref. 6) $p^0_{\mathrm{Te2}}=4.7191-59960.2/T$, atm	Vapor pressure of Te in equilibrium in the liquid phase, atm	
			$p_{\mathrm{Te2}}=a_3^{1/2}\cdot p^0_{\mathrm{Te2}}$	experiment (Ref. 8)
934.4	0.1052	2.190×10^{-2}	2.42×10^{-4}	1.91×10^{-3}
925.3	0.1992	1.896×10^{-2}	7.52×10^{-4}	2.4×10^{-3}
915.2	0.2858	1.609×10^{-2}	1.32×10^{-3}	2.67×10^{-3}
905.7	0.3530	1.375×10^{-2}	1.71×10^{-3}	2.71×10^{-3}
890.2	0.4392	1.056×10^{-2}	2.04×10^{-3}	2.68×10^{-3}
875.1	0.5023	8.095×10^{-3}	2.04×10^{-3}	2.59×10^{-3}

In order to calculate this quantity, the so-called state function of the liquid phase, it is necessary to know the degree of association k_{f1}, and also the interaction parameters of the components within the framework of a thermodynamic model of the multicomponent solution. As a first approximation we assume that the concentration of free material in the solution is much smaller than the concentration of the associate MnTe^l; i.e., the condition $y_2 \ll y_5$ holds. In this case, from system (1) we derive the system

$$y_4^2 x_3(1-x_3)-y_4(1+k_{a1}\gamma_4/(\gamma_1\gamma_3)(1-x_2)^2-x_2)$$

$$+x_3(1-x_3)-x_2(1-x_2)=0. \tag{4}$$

$$y_1=((1-x_3)-x_3y_4-x_2)/(1-x_2)$$

$$y_3=(x_3-(1-x_3)y_4-x_2)/(1-x_2)$$

Furthermore, at small manganese concentrations we can neglect the contribution due to interaction between Mn and the associate MnTe^l in the activity coefficient for the primary components of the solution. Consequently, the state function for the liquid phase can be computed exclusively in terms of thermodynamic parameters of the Hg–Te system. We will use this approximation and the data of Ref. 6, thereby eliminating the need to use MCT thermodynamic parameters computed within the FAS approximation. The reason for this latter precaution is the sizable discrepancy in the liquidus temperature of the Hg–Te system computed from the data of Refs. 2 and 6 (Table III). In this case the use of values of the free-tellurium activity in enriched-tellurium solutions calculated by the FAS method leads to a considerable error when the vapor pressure of tellurium in equilibrium with the liquid is computed (Table IV).

The results of the calculations which we performed are listed in Table V. We see that the cumulative quantity $\Omega=RT\ \ln(y_1\gamma_1y_3\gamma_3/k_{f1})-RT\ln(z_1)$ which characterizes the ‘‘nonideality’’ of the solid phase is positive, large and increases rapidly with decreasing manganese concentration, as does the value of the factor $f=a_1(a-a_s)^2+2a(a-a_s)\times(a_1-a)$, which determines the elastic component to Eq. (3.1). This allows us to consider our points as actual points of metastable ‘‘mixed’’ equilibrium. However, for a quantitative comparison the parameter σ should have values of order 10^{34} cal/mole, which is much larger than the value calculated from the data of Refs. 5 or 9. We associate this discrepancy with a less-than-adequate description of the state of the liquid phase, and also with the choice of supercoolings made in Ref. 1, which we consider to be slightly premature.

As for the four-component system, the data of Ref. 3 cannot be unambiguously explained within the framework of our analysis. On the one hand, the data in Table VI imply that both temperatures used in Ref. 3 are too small to initiate crystallization over the almost isoperiodic substrate $\mathrm{Cd_{0.96}Zn_{0.04}Te}$. Since the data of Ref. 4 characterize epitaxial crystallization on a CdTe substrate, this seems natural, and underlines the important role of elastic stresses in epitaxial crystallization. Under conditions where the supercooling choice is incorrect, the composition of the grown crystals may reflect a depletion of manganese in the region of the melt adjacent to the substrate, which increases with decreasing original concentration of manganese in the melt. In this case, however, the presence of a certain fraction of cadmium in the epitaxial layer must be explained primarily by metallic interdiffusion. It was noted in Ref. 3 that the concentration of Cd in grown films is nearly constant and that the thickness of the transition region is rather small compared to the thickness of the film (10 versus 100 microns). Consequently, we must assume that under certain conditions the diffusion profile of cadmium in the growing layer can have a rather nonstandard form. On the other hand, the presence of cad-

TABLE V. Computed quantities that characterize the contribution of elastic stresses to epitaxial crystallization of (Hg, Mn)Te/CdTe.

T, K	$RT\ \ln(y_1\gamma_1y_3\gamma_3/k_{f1})-RT\ln(z_1)$, cal/mole		$W(1-z)^2$, cal/mole, according to Ref. 2	$a_1(a-a_s)^2+2a(a-a_s)(a_1-a)$, 10^{34} m^3
	FAS (Ref. 2)	our calculations		
781	68.80	49.15	0.516	26.79
789	39.65	18.72	1.16	22.95
793	24.58	3.63	1.58	20.46
799	36.32	18.56	2.81	13.17
802	28.91	8.23	3.90	6.694
923	-1.894	28.72	2.81	13.17

TABLE VI. Expected temperature for the start of crystallization for epitaxial growth of (Hg, Mn)Te on matched and mismatched substrates.

	Original composition liquid phase		Metal fraction in sublattice, microanalysis		Liquidus temperature, K		
Substrate	$x_2/(1-x_3)$	x_3	Mn	Cd	experiment (Ref. 3)	expected from Ref. 4	our estimate
$Cd_{0.96}Zn_{0.04}Te$	0.03	0.75	0.04	0.02	793		798
CdTe	0.03	0.75				793	793
$Cd_{0.96}Zn_{0.04}Te$	0.035	0.65	0.07	0.04	848		892
CdTe	0.035	0.65				870	887

mium in the epitaxial layer can be viewed as a sign that the substrate is dissolving. This shows that our estimates of the liquidus temperature of the system may be overestimates, which to some extent assists the resolution of the contradiction between calculated values of f and Ω. Furthermore, it is worth emphasizing the difference between the data of Ref. 4, which were obtained based on the method of differential-thermal analysis, and the data of Ref. 2; this also says that the points of Ref. 2 are more likely points of metastable equilibrium.

2. CONCLUSIONS

We have shown that both the change in phase equilibrium conditions due to elastic stresses and the interdiffusion of components can have a considerable effect on the composition of epitaxially grown $Hg_{1-z}Mn_zTe$ samples. In particular, the use of a CdTe substrate that is mismatched with respect to lattice parameter greatly decreases the concentration of manganese in the epitaxial layer. Furthermore, under certain conditions cadmium diffusion and (or) dissolving of the substrate lead to the formation of a uniform four-component compound (Hg, Mn, Cd)Te on a cadmium-containing substrate. The conditions for formation of high-quality four-component structures requires further investigation.

[1] N. N. Berchenko, V. E. Krebs, and V. G. Sredin, *Semiconductor Solid Solutions and Applications: Handbook Tables* (Voenizdat, Moscow, 1982).

[2] M. A. Danilov, A. M. Litvak, and K. E. Mironov, Inorg. Mater. **28**, 1860 (1992) [in Russian].

[3] A. E. Belyaev, S. A. Vitusevich, S. M. Komirenko, S. V. Kavertsev, G. I. Zhovnir, and L. V. Raskovetskiĭ, Ukr. Fiz. Zh. **41**, 340 (1996) [in Russian].

[4] G. I. Zhovnir, S. V. Kletskiĭ, N. V. Sochinskiĭ, and V. M. Frasunyak, Inorg. Mater. **25**, 1216 (1989) [in Russian].

[5] A. M. Andrukhiv, A. M. Litvak, and. E. Mironov, Inorg. Mater. **29**, 492 (1993) [in Russian].

[6] T. Tung, C.-H. Su, P.-K. Liao, and R. F. Brebrick, J. Vac. Sci. Technol. **21**, 117 (1982).

[7] V. V. Kuznetsov, P. P. Maskvin, and V. S. Sorokin, *Nonequilibrium Phenomena during Heteroepitaxy of Semiconductor Solid Solutions* (Metallurgiya, Moscow, 1991).

[8] C.-H. Su, P.-K. Liao, T. Tung, and R. F. Brebrick, High Temp. Sci. **14**, 181 (1981).

[9] R. Dornhaus and G. Nimtz, in *Narrow gap semiconductors*, R. Dornhaus, G. Nimtz, and B. Schlicht eds., p. 121 (Springer-Verlag, Berlin e.a., 1983).

Translated by F. Crowne

Effect of illumination time on the annealing of optically created metastable defects in *p*-type *a*-Si:H

A. G. Kazanskiĭ

M. V. Lomonosov State University, 119899 Moscow, Russia

(Submitted May 20, 1996; accepted for publication June 24, 1996)
Fiz. Tekh. Poluprovodn. **31**, 347–349 (March 1997)

The effect of illumination time on the relaxation of the concentration of optically created metastable defects in films of boron-doped a-Si:H in the temperature range 360–400 K is discussed. The concentration relaxes according to a stretched exponential law $\sim\exp[-(t/\tau_r)^\beta]$. In the region of temperatures under study and for illumination times of 0.1 –7.0 s, the coefficient β is equal to 0.55–0.65; furthermore, the temperature dependence of the effective time τ_r was activated, with an activation energy E_a of 0.97–1.07 eV. As illumination increased, a weak increase in E_a and β is observed. The quantity τ_r increases as the illumination time increases, in accordance with a law that is close to logarithmic. The experimental results obtained are compared with the existing microscopic models for the formation and annealing of metastable defects in a-Si:H films. *© 1997 American Institute of Physics.* [S1063-7826(97)01903-0]

The generation of nonequilibrium carriers in amorphous hydrogenated silicon (a-Si:H) is known to lead to the creation of defects of the dangling-bond type, which disappear after annealing at temperatures of 100–180 K (depending on the type and level of doping). Despite the fact that metastable states in a-Si:H have been studied for almost 15 years, the microscopic processes that lead to their appearance remain unclear. Recently, two classes of models have been proposed to explain the kinetics of the time-varying defect concentration as these defects appear and are annealed away. According to the first class of models,[1] the process that determines the rate of change of the defect concentration is diffusion of the hydrogen that participates in the processes of defect formation and annealing. Support for this model comes from a correlation between the diffusion coefficient and the rate of change of the defect concentration in undoped, n-type, and p-type materials.[2] According to the other class of models, the rate of the transient processes is determined by the defects themselves, in particular the distribution of energy barriers corresponding to their formation and annealing.[3] These models[3] predict that the effective relaxation (or annealing) time τ_r for the optically generated defect concentration should depend on the illumination time t_{ill}. For the other type of models, in which the rate of transient processes is determined by hydrogen diffusion, this dependence is not expected.[3]

The existing data[4–6] indicate that large values of t_{ill} correspond to high values of τ_r; however, to our knowledge the dependence of τ_r on t_{ill} has not been studied.

In this paper we discuss the results of such investigations for films of p-type a-Si:H. These investigations reveal that the largest observed rates for transient processes are in undoped films. The measurements were made on films of a-Si:H obtained by decomposing mixtures of the gases monosilane (SiH_4) and diborane (B_2H_6) in a glow discharge at a substrate temperature (quartz) of 250 °C. The bulk ratio of B_2H_6 to SiH_4 in the reactor chamber was $k=10^{-5}$. Optical degradation of the samples was brought about by illumination from a filament lamp passed through a thermal filter; the lamp intensity was 60 mW/cm^2. Before the measurements, the films were annealed in a vacuum of 10^{-3} Pa for 30 minutes at a temperature of 180 °C. The change in conductivity (σ) after switching off the illumination was recorded with the help of a C9-8 memory digital oscilloscope. Light pulses with durations within the limits 0.05–10 s were generated by a chopper.

Figure 1 shows the effect of illumination time on the relative magnitude of the conductivity σ_B/σ_A at various temperatures, where σ_A and σ_B are respectively the conductivities of an annealed sample and of a sample after illumination. The measurements were made three seconds after the illumination was switched off. It is clear that the function $\sigma_B(t_{ill})$ is nonmonotonic in character: σ_B decreases for short times but increases for longer illumination times. The time t_m corresponding to the minimum value of σ_B decreases with increasing temperature. Such dependences suggest that there are two processes competing to determine the change in σ_B. The first process, which determines the decrease in σ_B at short times, is associated with an increase in the defect concentration and a shift in the Fermi level (E_F) towards the middle of the mobility gap.[7,8] As for the process that causes the increase in σ_B, there is no unified point of view. In the opinion of the authors of Ref. 7, the increase in σ_B is connected with an increase in the concentration of electrically active boron atoms under the influence of light. In contrast, in Ref. 8 the increase in σ_B is explained in terms of the formation of defects as a result of the illumination in the oxide layer at the film's surface, which leads to band bending near the film's surface and creation of a carrier accumulation layer.

It is clear from Fig. 1 that for a correct investigation of the effect of t_{ill} on τ_r under conditions where only dangling bonds are created, measurements for $t_{ill}<t_m$ are needed.

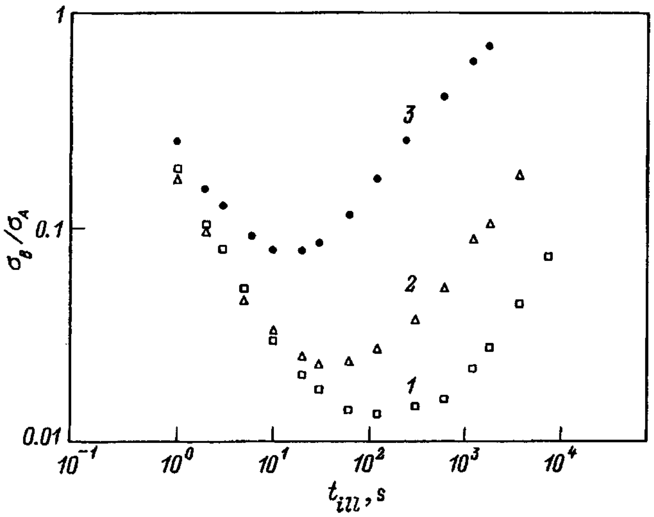

FIG. 1. Dependence of the relative conductivity (σ_B/σ_A) for a-Si:H films doped with boron on the illumination time (t_{ill}) at various temperatures T, K: *1*—360, *2*—380, *3*—400.

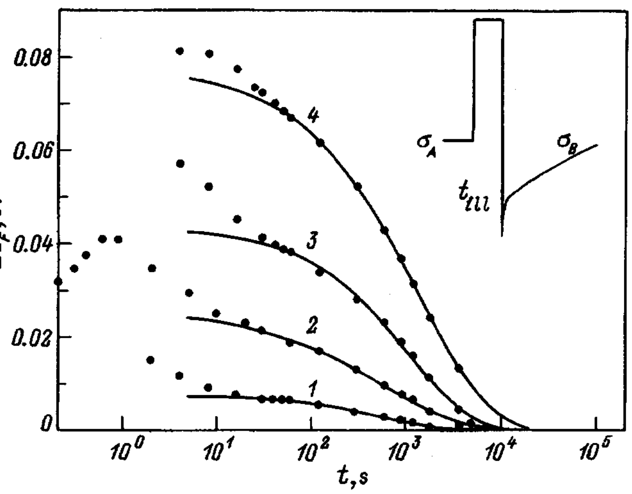

FIG. 2. Relaxation of the shift in Fermi level (ΔE_F) after illumination of the film at $T=360$ K over various times. The solid curves were obtained by the method of nonlinear regression for stretched exponentials. t_{ill}, s: *1*—0.14, *2*—0.52, *3*—1.1, *4*—3.3.

The inset in Fig. 2 shows the relaxation of the conductivity after the film is illuminated for a time t_{ill}. After the light is switched off, a decrease in σ, which is connected with the relaxation of the photoconductivity down to values smaller than σ_A, is observed. The value of σ then increases and approaches that of σ_A, which is attributable to the annealing of the optically created defects and to an accompanying shift in the Fermi level toward the valence band edge. This shift in the Fermi level relative to its position in an annealed sample (E_F^A) is determined by the expression $\Delta E_F = E_F^B - E_F^A = kT\cdot\ln(\sigma_A/\sigma_B)$. Figure 2 also shows the relaxation of ΔE_F corresponding to the region of increasing σ (i.e., the region where the defects have been annealed) for various illumination times of the film. For $t_{ill}=0.52$ s a portion of the change in ΔE_F corresponding to relaxation of the photoconductivity is also shown.

If the density of states is independent of energy over the range where E_F shifts, we may assume that $\Delta N \sim \Delta E_F$, where ΔN is the change in defect concentration leading to the shift in E_F. The relaxation of ΔE_F in the region where σ increases must therefore reflect the relaxation of the optically created defect concentration.

A look at Fig. 2 reveals that two segments can be distinguished on the relaxation curve for ΔE_F (corresponding to the region where σ increases)—a segment where ΔE_F increases rapidly, and a segment on which the variation of ΔE_F can be described by a stretched exponential $(\Delta E_F F \sim \exp[-(t/\tau_r)^\beta])$. Computed curves for the second segment are shown in Fig. 2. As the illumination time increases, the contribution of the first segment to the relaxation of ΔE_F decreases. It is noteworthy that the authors of Refs. 9 and 10 measured the transient capacitance of $p-n$ structures based on a-Si:H in order to study the relaxation of concentrations of defects in p-type a-Si:H created by carrier injection arising from voltage pulses of various durations. These authors also observed two characteristic segments on the relaxation curve. The first, which is described by a power law, disappears as the duration of the injection pulse increases, while the second is satisfactorily described by a stretched exponential. They invoked the Adler model of defect formation,[11] in which the configuration changes during the formation of the metastable defect, to explain the presence of the first segment. The second segment of the relaxation they associated with annealing of the metastable defects.

In the temperature range 360–400 K and for illumination times in the range 0.1–7.0 s, the coefficient β is in the range 0.55–0.65; the activation energy E_a for the temperature dependence τ_r was found to be 0.97–1.07 eV, which corresponds to activation energies for annealing defects obtained in other papers.[3] With an incrase in t_{ill} a slight increase in E_a and β was observed.

Figure 3 shows the dependence of τ_r on t_{ill} obtained by

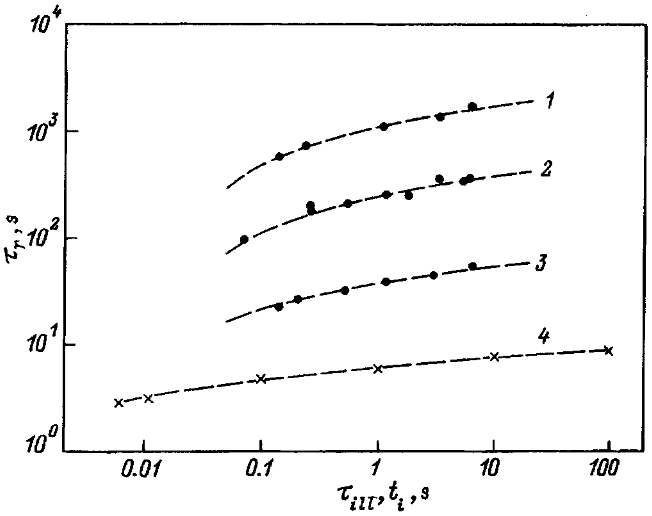

FIG. 3. Dependences of the relaxation time τ_r on illumination time t_{ill} at various temperatures (*1*–*3*) obtained in the present work, and on the injection time (t_i) at $T=439$ K obtained in Ref. 4. The dashed curves correspond to a logarithmic dependence T, K: *1*—360, *2*—380, *3*—400.

analyzing the second segment of the relaxation curve for ΔE_F at various temperatures. In this same figure, the dependence of τ_r on t_i obtained for $T = 439$ K in Ref. 10 is shown for weakly doped p-type a-Si:H. According to Ref. 10, $\tau_r \sim \ln(t_i)$. The data obtained here for τ_r are also described satisfactorily by a logarithmic dependence on t_{ill} (see Fig. 3). The dependence $\tau_r(t_{ill})$ turns out to be considerably weaker than that described by theory developed in Ref. 3 ($\tau_r \sim t_{ill}$), where it is assumed that the concentration of defects is exponentially distributed with respect to formation energy. The difference observed here may be connected with a dependence of the defect concentration on the formation energy that is weaker than exponential. Nevertheless, these results indicate that the rates of formation and annealing of metastable defects are to a considerable degree directly associated with the defects themselves, and are determined by a two-step process consisting of trapping of a carrier at a state which is the source of the dangling bond, and then the breaking of the bond.

The author is sincerely grateful to Professors Fus and Dr. H. Mell for providing the p-type a-Si:H films.

This work was carried out with the financial support of Goskombuz, Russian Federation (Grant No. 97-0-7.I-153) and INTAS (Grant No. 93-1916).

[1] W. B. Jackson and J. Kakalios, Phys. Rev. B **37**, 1020 (1988).
[2] W. B. Jackson, J. M. Marshall, and M. D. Moyer, Phys. Rev. B **39**, 1164 (1989).
[3] R. S. Crandall, Phys. Rev. B **43**, 4057 (1991).
[4] T. J. McMahon and R. Tsu, Appl. Phys. Lett. **51**, 412 (1987).
[5] T. Kumeda, H. A. Morimoto, and T. Shimizu, Jap. J. Appl. Phys. **25**, L654 (1986).
[6] R. S. Crandall, Phys. Rev. B **36**, 2645 (1987).
[7] J. Jang, S. C. Park, S. C. Kim, and C. Lee, Appl. Phys. Lett. **51**, 1804 (1987).
[8] A. G. Kazanskiĭ, Bull. Moscow State Univ., Ser.3, Phys. and Astron. **33**, 70 (1992).
[9] M. W. Carlen, Y. Xu, and R. S. Crandall, Phys. Rev. B **51**, 2173 (1995).
[10] R. S. Crandall and M. W. Carlen, J. Non-Cryst. Sol. **190**, 133 (1995).
[11] D. Adler, Solar Cells **9**, 133 (1982).

Translated by F. Crowne

Recombination mechanisms in doped *n*-type $Hg_{1-x}Cd_xTe$ crystals and properties of diffusion p^+-n junctions based on them

V. V. Teterkin, S. Ya. Stochanskiĭ, and F. F. Sizov

Semiconductor Physics Institute, Ukrainian National Academy of Sciences, 252620 Kiev, Ukraine

(Submitted May 23, 1996; accepted for publication June 24, 1996)
Fiz. Tekh. Poluprovodn. **31**, 350–354 (March 1997)

We made p^+-n-type photodiodes for the 3–5 and 8–12 μm wavelength regions by diffusing As into single-crystal n-$Hg_{1-x}Cd_xTe$ substrates, and investigated their electrical and photoelectric properties. Analysis of the temperature dependences of the differential resistance and current-voltage characteristics led us to conclude that charge-carrier transport is predominately due to the generation-recombination mechanism at a temperature of 77 K. As the temperature increases, a contribution from the diffusion component also appears. We obtained values of the product $R_0A \cong 0.3-1.0$, 1–10, and $(1-10)\times 10^4\ \Omega\cdot cm^2$ for diodes with long-wavelength photosensitivity cutoffs $\lambda_c \cong 11.5$, 10.5, and 6.0 μm, respectively, indicating that they could operate in the regime where performance is limited by background radiation fluctuations. © *1997 American Institute of Physics.* [S1063-7826(97)02003-6]

1. INTRODUCTION

The majority of previously published papers, in which $Hg_{1-x}Cd_xTe$ n^+-p-type photodiodes were investigated, have dealt with devices made by ion implantation and diffusion. Because of their longer diffusion lengths for minority carriers (electrons) and also their potential for achieving longer lifetimes[1–4] than for p^+-n-type diodes, n^+-p-type photodiodes have attracted the most interest. However, it has recently been proved, both theoretically and experimentally, that p^+-n-type diodes can be obtained with high values of differential resistance, especially in the infrared (IR) wavelength region of the spectrum ($\lambda > 10\mu$m). These new results, which have led to intense studies of these diodes,[5–8] are of significance to designers of multielement photoreceivers in which signals are extracted by commutators based on charge-coupled devices.[7,8]

Additional advantages of these photodiodes flow from the peculiar physical properties of single crystals of $Hg_{1-x}Cd_xTe$ solid solutions. In particular, it is advantageous to use substrates with electronic (n-type) conductivity from the point of view of obtaining starting material with optimal and reproducible electrical characteristics; such substates are obtained by doping $Hg_{1-x}Cd_xTe$ with various impurities.[9] When substrates with n-type conductivity are used, it is relatively easy to obtain doped single crystals with carrier concentrations of $10^{14}-10^{15}\ cm^{-3}$, concentrations that are nearly impossible to achieve for single crystals with hole (p-type) conductivity. However, a number of donor impurities are known to form deep levels in the band gap of $Hg_{1-x}Cd_xTe$, which turn out to have a considerable influence on the carrier lifetime, dark current, and differential resistivity of photodiodes.[9–12] This statement is also true for intrinsic lattice defects, i.e., mercury vacancies. Therefore, the inference that a given single crystal is suitable for making photodiodes should be based on more that its electrical characteristics: the possible influence of impurities on the carrier lifetimes should be considered as well. It is noteworthy that the predominant mechanisms for recombination in pure and perfect single crystals of undoped n-$Hg_{1-x}Cd_xTe$ are interband Auger and radiative recombination.[1,13] At the same time, at a temperature of 77 K the predominant mechanism for current flow in diodes based on $Hg_{1-x}Cd_xTe$ is generation-recombination,[1] in which the nature of the generation-recombination centers is still unclear for the most part.

It is also known that the intrinsic oxide has been used successfully to passivate the surfaces of n-$Hg_{1-x}Cd_xTe$ crystals. It is likely that the lowest values of surface recombination velocity have been achieved by using this oxide.[14] For n^+-p-type diodes this method of passivating the substrate surface is not suitable, since it leads to the formation of inversion layers.[14,15] This is yet another reason why diodes of p^+-n-type are preferable.

2. EXPERIMENT AND DISCUSSION OF RESULTS

The literature contains descriptions of the properties of p^+-n-type photodiodes prepared by molecular-beam and liquid-phase epitaxy of layers of narrow-gap $Hg_{1-x}Cd_xTe$ onto substrates of CdTe and CdZnTe.[5–8] Recently, photodiodes have been made by the relatively simple method of diffusing As into bulk single-crystal $Hg_{1-x}Cd_xTe$ substrates with n-type conductivity and compositions $x \cong 0.195$, 0.205 and 0.265. Table I lists the characteristics of several of these substrates.

The substrates are first doped with indium. Since indium exhibits a high electrical activity in $Hg_{1-x}Cd_xTe$, in order to obtain a substrate with an electron concentration of $\sim 10^{15}-10^{16}\ cm^{-3}$ it is necessary to introduce roughly the same number of impurity atoms.[16]

In order to determine how impurities and intrinsic defects affect the lifetime of the carriers, we studied the mechanisms for their recombination in the initial substrates. To this end we prepared samples with thickness $\approx 300\ \mu$m with surfaces passivated by the intrinsic oxide. We measured the relaxation of photoconductivity due to carriers excited by a Nd^{3+}-YAG laser ($\tau_{pulse} \approx 8-15$ ns). The relaxation curves

TABLE I. Electrical characteristics of several initial single-crystal films of n-type $\mathrm{Hg}_{1-x}\mathrm{Cd}_x\mathrm{Te}$, and values of R_0A for $p^+ - n$-type photodiodes.

No P.P.	Composition x	$N\cdot 10^{-15}$, cm^{-3}	$\mu\cdot 10^{-5}$, $\mathrm{cm}^2/\mathrm{V}\cdot\mathrm{s}$	λ_c, μm	R_0A, $\Omega\cdot\mathrm{cm}^2$
1	0.205	2.4	1.2	10.4	0.95
2	0.205	2.4	1.2	10.4	1.76
3	0.205	2.05	1.4	10.5	0.78
4	0.205	1.1	2.0	10.0	2.0
5	0.265	3.6	0.2	6.0	2×10^4
6	0.265	1.4	0.6	6.0	6×10^4
7	0.265	6.6	0.3	6.0	3×10^4
8	0.265	1.2	0.45	6.0	1.5×10^5

are described by an exponential function with the time constant τ. The quantity to be measured τ_{eff} depends on bulk and surface recombination.

The contribution from surface recombination can be estimated as follows. If there is no capture of carriers at capture centers, the lifetime of minority carriers is the same as that of majority carriers.[13,17] If we assume that $\tau_n = \tau_p \cong 10^{-6}$ s at $T = 77$ K, then the minority-carrier diffusion length is $L_p \ll d$. When this condition is satisfied, the time constant τ_{eff} differs from the bulk lifetime of the semiconductor τ_n by a factor of $(1+S)^{-1}$,[13,17] where the dimensionless parameter $S = s\tau_p/L_p$ takes into account the contribution of surface recombination. The surface recombination velocity s depends on the method of surface passivation, and in n-$\mathrm{Hg}_{1-x}\mathrm{Cd}_x\mathrm{Te}$ varies over the range 10^2–10^4 cm/s. For surfaces passivated by the intrinsic oxide, the quantity s has typical values of $\sim 10^2$ cm/s.[6,13,14] Estimates of the parameter S for these values of the surface recombination velocity 10^2 cm/s imply that the bulk lifetime can differ from the measured lifetime by no more than 10%. Therefore, within this error, we can identify τ_{eff} with the bulk lifetime τ_n.

Figure 1 shows a typical dependence of τ_n on inverse temperature for n-$\mathrm{Hg}_{1-x}\mathrm{Cd}_x\mathrm{Te}$ ($x \cong 0.265$). We can identify two characteristic segments on the experimental curves. In the temperature ranges $T \geqslant 200$ K, which corresponds to intrinsic conductivity, τ_n decreases like $\exp(\Delta E/kT)$, and the activation energy $\Delta E \approx E_{g0}$, where E_{g0} is the zero-temperature width of the band gap for the solid solution. Its dependence on composition and temperature is given by the expression[18]

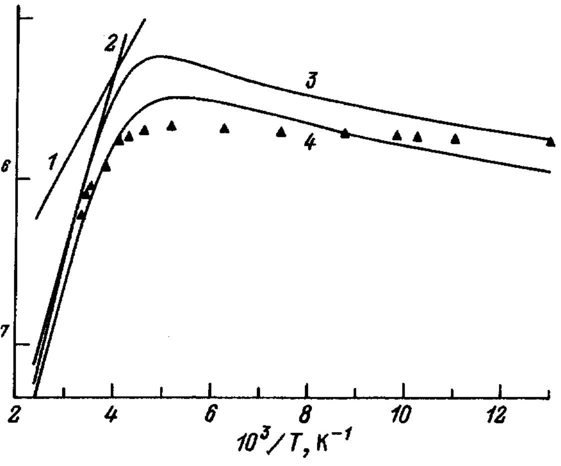

FIG. 1. A typical temperature dependence of the carrier lifetime in n-$\mathrm{Hg}_{1-x}\mathrm{Cd}_x\mathrm{Te}$. The solid curves are calculations of the lifetimes for intrinsic radiative (*1* and *2*) and Auger recombination for values of the product $|F_1F_2|$ equal to 0.2 and 0.3 (*3* and *4*). The dots are experiment for n-$\mathrm{Hg}_{1-x}\mathrm{Cd}_x\mathrm{Te}$, with $n = 2.1\times 10^{15}$ cm^{-3}.

$$E_g = -0.302 + 1.93x - 0.81x^2 + 0.832x^3 + 5.32\times 10^4 \times (1-2x)\left[\frac{-1822 + T^3}{255.2 + T^2}\right]. \tag{1}$$

In the region of impurity conductivity ($T < 200$ K), τ_n decreases insignificantly as the temperature falls. We found that for electron concentrations $n \leqslant 10^{16}$ cm^{-3} the lifetime has a typical value of $\sim 10^{-6}$ s in this temperature range. In the past, similar temperature dependences of the lifetime were obtained for single crystals of undoped n-$\mathrm{Hg}_{1-x}\mathrm{Cd}_x\mathrm{Te}$ ($x = 0.195$ and 0.205).[13] The fact that the activation energy $\Delta E \approx E_{g0}$ indicates a contribution from interband Auger recombination. Figure 1 also shows the results of calculations of the lifetime for radiative and Auger recombinations using the expressions[1,13]

$$\tau_R = \frac{2n_i\tau_{Ri}}{n_0 + p_0}, \tag{2}$$

$$\tau_A = \frac{2n_i\tau_{Ai}}{n_0(n_0 + p_0)}, \tag{3}$$

$$\tau_{Ri} = 5.8\cdot 10^{-13}\varepsilon_\infty^{1/2}\left(\frac{m_0}{m_e^* + m_h^*}\right)^{3/2}\left(1 + \frac{m_0}{m_e^*} + \frac{m_0}{m_h^*}\right) \times \left(\frac{300}{T}\right)^{3/2} E_g^2, \tag{4}$$

$$\tau_{Ai} = \frac{7.6\cdot 10^{-18}\varepsilon_\infty^2(1+\mu)^{1/2}(1+2\mu)\exp\left[\left(\frac{1+2\mu}{1+\mu}\right)\frac{E_g}{kT}\right]}{\frac{m_e^*}{m_0}\,|F_1F_2|^2\left(\frac{kT}{E_g}\right)^{3/2}}. \tag{5}$$

Here τ_{Ri} and τ_{Ai} are the corresponding lifetimes in intrinsic material, n_0 and p_0 are the equilibrium electron and hole concentrations, n_i is the intrinsic carrier concentration, and $\mu = m_e/m_{hh}$ is the ratio of the electron and heavy hole effective masses. The effective mass of electrons is calculated in the Kane model

$$\frac{m_0}{m_e^*} = 1 + \left(\frac{2m_0P^2}{3h^2}\right)\left(\frac{2}{E_g} + \frac{1}{E_g + \Delta}\right), \tag{6}$$

where $\Delta = 0.9$ eV, $P = 8.49\times 10^{-8}$ eV·cm.[19] Equation (6) was verified experimentally in Ref, 20 for the solid solutions n-$\mathrm{Hg}_{1-x}\mathrm{Cd}_x\mathrm{Te}$ used in this work. For the heavy-hole mass we used a value $m_{hh} = 0.45m_0$. A fitting parameter in the calculations is the product of overlap integrals $|F_1F_2|$. In the compounds $\mathrm{Hg}_{1-x}\mathrm{Cd}_x\mathrm{Te}$ this product varies in the range[1] 0.1–0.3. It is clear from Fig. 1 that the best agreement between the experimental and computed curves is obtained for the mechanism of Auger recombination, and for the value $|F_1F_2| = 0.3$. Based on the results of our calculations and

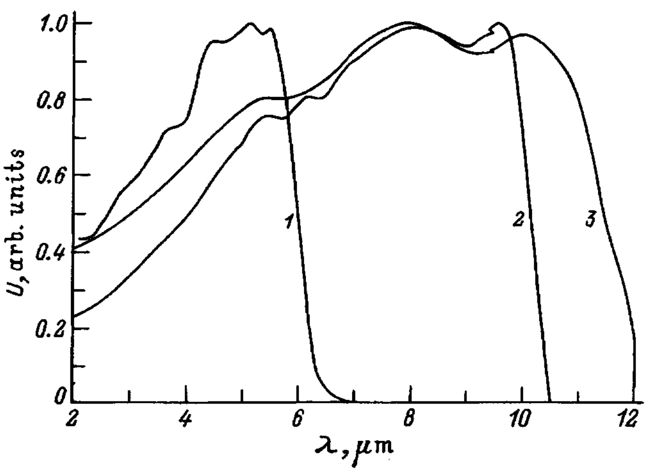

FIG. 2. Spectral dependence of the photoresponse in p^+-n-type $Hg_{1-x}Cd_xTe$ diodes. The composition x of the substrate was: 0.265 (*1*), 0.205 (*2*), 0.915 (*3*).

experimental studies, we conclude that for n-$Hg_{1-x}Cd_xTe$ substrates doped with In localized states in the band gap do not have a significant effect on the lifetime of carriers at those concentrations, $n=10^{15}$ to 10^{16} cm^{-3}, which are optimal for fabricating photodiodes.

We fabricated p^+-type layers by diffusing As into an n-type-substrate at temperatures close to 400 °C for a period of 2 to 12 h. After diffusion, the samples were subjected to annealing in mercury vapor at a temperature of 230–250 °C for 24 h. Measurements of the differential Hall effect established that the concentration of holes in this layer was $\sim 10^{17}$ cm^{-3}, and its thickness was found to be between 1 and 3 μm. Mesa structures with area $A=(2-6)\times 10^{-4}$ cm^2 were isolated from the p^+ layer by chemical etching to a depth of 2–4 μm. From measurements of the barrier capacitance it was established that the impurities in the base of the diodes were broadly distributed [the capacitance could be rectified when plotted in the coordinates $C^{-2}(U)$]. This result is atypical for the methods of diode fabrication used in this work. However, if we take into account that As in $Hg_{1-x}Cd_xTe$ has a low diffusion coefficient, it is clear that the diffusion profile can be rather sharp (see, e.g., the results of studies of the Auger profile of As in epitaxial films[7,8]). Note that the electron concentration we found by measuring the barrier capacitance nearly coincides with the Hall concentration of electrons in the original substrate.

The spectral dependence of the diode photoresponse is shown in Fig. 2. At $T=80$ K the photodiodes intended for the mid-IR spectral region ($x=0.265$) have a long-wavelength photosensitivity cutoff (based on a level of $0.5\cdot I_{ph}$) λ_c equals 6.0 μm. In photodiodes designed for the long-wavelength IR region of the spectrum ($x=0.205$ and 0.265), λ_c is equal to 10.5 and 11.5 μm, respectively.

We investigated the charge transport mechnisms by measuring the current-voltage characteristics and the values of the product R_0A (where R_0 is the differential resistivity at zero bias, and A is the diode area) as a function of temperature. Long-wavelength and mid-wavelength diodes were studied in the temperature ranges 77–150 K and 77–300 K, respectively. At $T\cong 77$ K, the forward branches of the current-voltage characteristics of photodiodes for both spectral regions are given by the expression

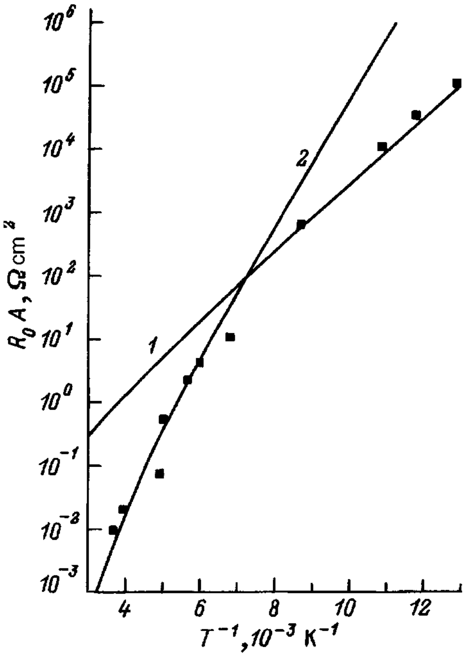

FIG. 3. Temperature dependences of the product R_0A for p^+-n-type diodes, $x=0.265$. The solid curves are calculations of the diffusion (*1*) and generation-recombination (*2*) components, the points are from experiment. The diode area $A=4\times 10^{-4}$ cm^2.

$$I=I_0\left[\exp\left(\frac{qU}{\beta kT}\right)-1\right], \tag{7}$$

where the constant $\beta\cong 2.0$. This is evidence that generation-recombination is the dominant mechanism for charge transport. For diodes in the long-wavelength region this mechanism was dominant over the entire temperature interval investigated. Figure 3 shows a typical temperature dependence of the product R_0A for photodiodes for the mid-IR spectral region ($x\cong 0.265$). The measured slope of the experimental curve in the temperature range 120–140 K implies a change in the charge transport mechanism. The activation energies for high-temperature and low-temperature segments coincides with the values E_{g0} and $E_{g0}/2$ calculated using Eq. (1). On this same figure we show calculated curves for the diffusion and generation-recombination current components:

$$(R_0A)_D=\frac{1}{q}\frac{N_p}{n_i^2}\left(\frac{kT}{q}\frac{\tau_h}{\mu_h}\right)^{1/2}, \tag{8}$$

$$(R_0A)_{GR}=\frac{U_{bi}\tau_0}{qn_iW}. \tag{9}$$

In Eqs. (8) and (9) the primary contribution to the temperature dependence R_0A comes from the intrinsic carrier concentration n_i. To calculate it we use the approximate expression given in Ref. 18. The diffusion potential U_{bi}, the width of the space-charge region W, and the carrier concentration

$n=N_D$ are determined experimentally by measuring the barrier capacitance at $T=77$ K. In the calculations of $(R_0A)_{GR}$, the effective lifetime τ_0 was a fitting parameter.

It follows from Eq. (8) that the value of the product $(R_0A)_D$ depends on the lifetime of minority carriers (in this case holes) and their mobilities. For these calculations we assumed that the ratio of mobilities of minority and majority carriers in the substrates equaled 0.01.[21] Agreement between calculated and experimental values of R_0A was obtained for $\tau_h \cong \tau_n$, where τ_n is the Auger-recombination lifetime calculated from Eqs. (3) and (5). Equality of the quantities τ_h and τ_n confirms the assumption made above regarding absence of trapping processes for minority carriers and capture centers.

The generation-recombination component of the current consists of bulk and surface contributions. The contribution of the bulk component is given by Eq. (9). In order to estimate the surface component, it is necessary to know the surface recombination velocity, and also the ratio of the area of the $p-n$ junction to its perimeter P:

$$(R_0A)_{GR}^{\text{surf}}=\frac{U_{bi}A}{n_iQWsP}. \tag{10}$$

From (10) it follows that the importance of the surface component increases as the area of the junction decreases. Estimates show that for the photodiodes under study in this paper, with relatively large areas and ratios $P/A \leqslant 160\ \text{cm}^{-1}$, as s changes from 10^2 to 10^4 cm/s, the contribution of the surface component does not exceed 10% (see also the results of experimental studies of R_0A reported in Ref. 5).

3. CONCLUSIONS

The values of the product R_0A which were obtained by us are higher than those in n^+-p-type diodes made by diffusion or ion implantation into bulk single-crystal and epitaxial film substrates.[1,3] They are also higher than the values given in Ref. 22, in which photodiodes made by using the technology described above on bulk single-crystal substrates were investigated for the first time. We probably can also conclude that defects in our diodes, which determine the generation-recombination mechanism for charge transport at low temperatures, arise primarily from the process of fabricating the diodes themselves; therefore, it may be possible to further improve their characteristics by perfecting the corresponding technologies.

It is also easy to verify (see, e.g., Ref. 1) that the photodiodes studied in this paper have values of the product R_0A corresponding to operating regimes that are background-limited; thus, they can be used as effective IR photodetectors in the mid-wave and long-wave spectral regions.

We are sincerely grateful to K. R. Kubanov and Ya. Rutkovskiĭ for providing samples, for help in preparing the diodes, and for useful discussions.

[1] A. Rogalski and J. Piotrowski, Prog. Quant. Electron. **12**, 87 (1988).
[2] *Photodetectors in the Visible and Infrared Regions*, P. G. Kiess, ed. (Radio i Svyaz', Moscow, 1985).
[3] N. L. Bazhenov, S. I. Gasanov, V. K. Ogorodnikov, and V. I. Protsyk, Foreign Electrical Engineering, Vol. 8, (303) 3 (1986) [in Russian].
[4] P. R. Norton, Opt. Eng. **30**, 1649 (1991).
[5] C. C. Wang, J. Vac. Sci. Technol. **9**, 1740 (1991).
[6] G. N. Pultz, W. Peter, P. W. Norton, E. E. Kruger, and M. B. Reine. J. Vac. Sci. Technol. **9**, 1724 (1991).
[7] J. M. Arias, J. G. Pasko, M. Zandian, L. J. Kozlowski, and R. E. DeWames, Opt. Eng. **33**, 1422 (1994).
[8] J. M. Arias, J. G. Pasko, M. Zandian, S. H. Shin, G. M. Williams, L. O. Bubulas, R. E. DeWames, and W. E. Tennant, J. Electron. Mater. **22**, 1049 (1993).
[9] P. Gapper, J. Vac. Sci. Technol. B **9**, 1667 (1991).
[10] M. B. Reine, A. K. Sood, and T. J. Tredwell, *Photovoltaic Detectors*, in *Semiconductors and Semimetals* **18**, R. K. Willardson and A. C. Beer eds. (N. Y., Academic Press, 1981).
[11] D. Rosenfeld and G. Bahir, IEEE Trans. Electron. Dev. **39**, 1638 (1992).
[12] C. E. Jones, V. Nair, J. Lindquist, and D. L. Polla, J. Vac. Sci. Technol. **21**, 187 (1982).
[13] M. A. Kinch, M. J. Brau, and A. Simmons, J. Appl. Phys. **44**, 1649 (1993).
[14] D. E. Lacklison and P. Capper, Semicond. Sci. Technol. **2**, 33 (1987).
[15] R. Dornhaus and G. Nimtz, *The Properties and Applications of the* $Hg_{1-x}Cd_xTe$ *Alloy System*, in Springer Tracts in Modern Physics **98**, 119 (1985).
[16] V. I. Ivanov-Omskiĭ, K. E. Mironov, K. D. Mynbaev, and V. V. Bogoboyashchiĭ, Fiz. Tekh. Poluprovodn. **25**, 1423 (1991) [Sov. Phys. Semic. **25**, 857 (1991)].
[17] V. L. Bonch-Bruevich and S. G. Kalashnikov, *Physics of Semiconductors* (Nauka, Moscow, 1977).
[18] J. R. Lowney, D. G. Seiler, C. L. Littler, and I. T. Yoon, J. Appl. Phys. **71**, 1235 (1992).
[19] M. H. Weiler. *Magnetooptical properties of* $Hg_{1-x}Cd_xTe$ *Photovoltaic Detectors*, in *Semiconductors and Semimetals* **16**, R. K. Willardson and A. C. Beer eds. (N.Y., Academic Press, 1981).
[20] V. V. Bogoboyashchiĭ, A. I. Elizarov, V. A. Petryakov, and F. F. Sizov, Kvant. Elektron. (Kiev) **34**, 70 (1988).
[21] J. Piotrowski, $\text{Hg}_{1-x}\text{Cd}_x\text{Te}$ *Detectors*, in *Infrared Photon Detectors*, edited by A. Rogalski (SPIE Optical Engineering Press, 1995).
[22] J. Rutkowski, A. Rogalski, J. Piotrowski, and J. Pawluczyk, Proc. SPIE **1845** (1993).

Translated by F. Crowne

Influence of the X-valley on the tunneling and lifetime of electrons in GaAs/AlAs heterostructures

E. V. Demidov

Microstructure Physics Institute, Russian Academy of Sciences, 603600 Nizhniĭ Novgorod, Russia

(Submitted March 11, 1996, accepted for publication June 26, 1996)
Fiz. Tekh. Poluprovodn. **31**, 355–357 (March 1997)

The effective-mass approximation is used to calculate the probability for tunneling of an electron through a triangular barrier and its lifetime in the triangular quantum well formed by a GaAs/AlAs heterojunction and a strong electric field. It is shown that for such structures the tunneling probability into the X-valley can exceed the probability for tunneling into the Γ-valley by several orders of magnitude. The lifetime of an electron in the quasistationary state formed by the triangular heterobarrier is also essentially determined by tunneling to the X-valley and comes to $\sim 10^{-13} - 10^{-11}$ s in fields $E \sim 10^5 - 10^6$ eV/cm. © *1997 American Institute of Physics.* [S1063-7826(97)02103-0]

1. INTRODUCTION

Negative differential resistance (NDR) and rapid current switching in multilayer semiconductor heterostructures, including GaAs/AlAs structures, have been widely investigated in recent years.[1,2] The mechanism for NDR in these systems is connected with switching between a low-conductivity state, where the current is determined by tunneling of electrons through a barrier, and a high-conductivity state caused by heating of carriers which transfers them to the upper L-and X-valleys and projects them over the heterobarrier. The switching rate for such structures is a function of the lifetime for carrier heating by electron-electron collisions and the lifetime of electrons in the quasistationary state formed by the barrier τ. A distinctive feature of structures with a GaAs/AlAs heterobarrier grown on the (100) plane is the fact that the broken translational invariance at the heterojunction leads to mixing of the states of the Γ- and X-valleys. An electron from the Γ-valley tunneling through the barrier can transfer either to the Γ-valley or to one of the X-valleys. Transfers to the L- or the other two X-valleys is forbidden by the law of conservation of momentum along the barrier (in what follows we will set this momentum equal to zero). Usually the probability for tunneling into the X-barrier is quite small. However, if the barrier in the Γ valley is sufficiently high and its transparency is small, then the X-valley tunneling can give a substantial contribution. Liu[3] discussed resonant tunneling of electrons through a quantum state in the X-valley for structures with a single GaAs/AlAs/GaAs barrier using the effective-mass approximation. The lifetime of the quasistationary state in structures with a thin barrier was discussed by Zhang *et al.*[4] Stovneng *et al.*[5] calculated the tunneling current through a thick barrier using the tight-binding approximation.

In this paper we discuss the tunneling of electrons through the triangular barrier formed by a uniform electric field and a GaAs/AlAs heterostructure (see the inset in Fig. 1). In the effective-mass approximation we will calculate the probabilities D_Γ and D_X for tunneling of an electron from the Γ valley of GaAs to the Γ- and X-valleys of AlAs, and also the lifetime of an electron in the triangular quantum well formed by the heterobarrier. The escape of electrons into the X-valley was not considered in Refs. 3 and 4, since for thin layers this usually is forbidden or insignificant. Furthermore, the structure under consideration here contains only one heterojunction; therefore, in contrast to Refs. 3–5, comparatively simple analytic expressions are obtained for $D_{\Gamma,X}$ and τ and their asymptotic estimates. In these calculations the following parameters are used:[4] $U_\Gamma = 0.861$ eV is the magnitude of the energy discontinuity at the heterobarrier for the Γ-valley, $U_{X1} = 0.46$ eV is the position of the bottom of the X valley in GaAs (region 1 to the left of the barrier) and $U_{X2} = 0.185$ eV is the position of the bottom of the X valley in AlAs (region 2 to the right of the barrier) with respect to the Γ-valley in GaAs. For the respective effective masses we use the following values: $m_{\Gamma 1} = 0.067 m_e$, $m_{\Gamma 2} = 0.15 m_e$, $m_{X1} = 1.3 m_e$, and $m_{X2} = 1.1 m_e$, where m_e is the mass of an electron.

The mixing of the Γ- and X states in the heterostructure is taken into account using the following boundary conditions for the wave function at the heterojunction:[3]

$$\Psi_{\Gamma 1} = \Psi_{\Gamma 2}, \quad \frac{1}{m_{\Gamma 2}} \frac{d\Psi_{\Gamma 2}}{dz} - \frac{1}{m_{\Gamma 1}} \frac{d\Psi_{\Gamma 1}}{dz} = \alpha \Psi_{X1},$$

$$\Psi_{X1} = \Psi_{X2}, \quad \frac{1}{m_{X2}} \frac{d\Psi_{X2}}{dz} - \frac{1}{m_{X1}} \frac{d\Psi_{X1}}{dz} = \alpha \Psi_{\Gamma 1}, \tag{1}$$

where $\alpha = 2\alpha_1/\hbar^2$, $\alpha_1 = 0.1$ eV-Å, is taken from Ref. 3.

The transmission coefficient of an electron through the triangular barrier $D_{\Gamma,X}$ is calculated from the expressions

$$D_\Gamma = \frac{m_{\Gamma 1}}{\pi m_{\Gamma 2} k_\Gamma x_{\Gamma 2}} \, |b|^2, \tag{2}$$

$$D_X = \frac{m_{\Gamma 1}}{\pi m_{X2} k_\Gamma x_{X2}} \frac{\alpha^2 |E_\Gamma b|^2}{\left| \frac{k_X}{m_{X1}} \, E_X + \frac{1}{m_{X2} x_{X2}} \, E_X' \right|^2}, \quad \varepsilon \leqslant U_{X1}, \tag{3}$$

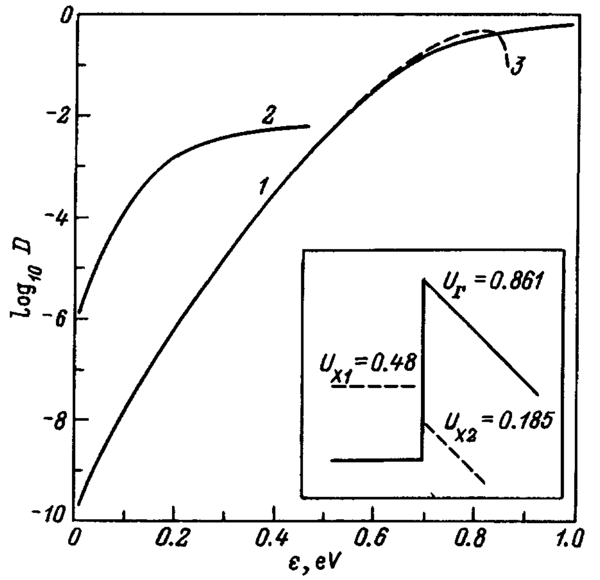

FIG. 1. Dependence of $D_\Gamma(\varepsilon)$ (*1*) and $D_X(\varepsilon)$ (*2*) for $E = 10^6$ eV. For comparison $D_\Gamma(\varepsilon)$, computed using the approximate formulas (6) and (3), is also shown.

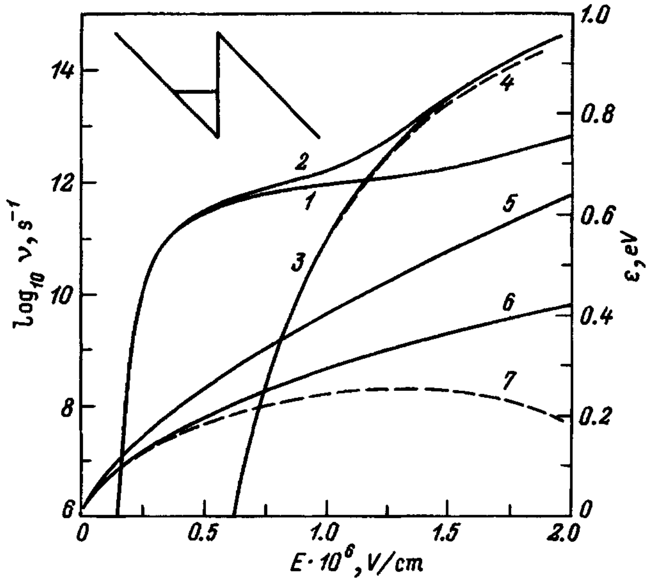

FIG. 2. Dependence of the inverse lifetime (*1–4*) and ε_0, Re(ε), Re($\varepsilon_0 + \delta\varepsilon$) (*5–7*) on the applied electric field for the quasistationary state of an electron in the heterostructure. *1*—Exact value for the inverse lifetime, *2*—ν calculated according to (8), taking into account $\Gamma - X$-tunneling, *3*—ν calcuated without including the X valley, *4*—inverse lifetime calculated using the approximate expression (9).

$$b = 2\left[E_\Gamma + i\,\frac{m_{\Gamma 1} E'_\Gamma}{m_{\Gamma 2} k_\Gamma x_{\Gamma 2}} - i\,\frac{\alpha^2 m_{\Gamma 1} E_\Gamma}{k_\Gamma\left(\dfrac{k_X}{m_{X1}} + \dfrac{E'_X}{m_{X2} x_{X2} E_X}\right)} \right]^{-1}, \tag{4}$$

where $k_\Gamma(\varepsilon) = \sqrt{2 m_{\Gamma 1}\varepsilon}/\hbar$, $k_X(\varepsilon) = \sqrt{2 m_{X1}(U_{X1} - \varepsilon)}/\hbar$, $F = eE$, $x_{(\Gamma,X)2} = (\hbar^2 / 2 m_{(\Gamma,X)2} F)^{1/3}$,

$$E_\Gamma(\varepsilon) = \mathrm{Bi}\left(\frac{U_\Gamma - \varepsilon}{F x_{\Gamma 2}}\right) + i\,\mathrm{Ai}\left(\frac{U_\Gamma - \varepsilon}{F x_{\Gamma 2}}\right)$$

$$E_X(\varepsilon) = \mathrm{Bi}\left(\frac{U_{X2} - \varepsilon}{F x_{X2}}\right) + i\,\mathrm{Ai}\left(\frac{U_{X2} - \varepsilon}{F x_{X2}}\right), \tag{5}$$

e is the electron charge, E is the electric field, ε is the energy of an electron incident on the barrier measured from the bottom of the conduction band of GaAs, $\hbar$ is Planck's constant, and Ai and Bi are Airy functions. According to Eq. (5), $E'_{\Gamma,X}$ can be expressed by replacing Ai, Bi by Ai$'$, Bi$'$.

The third term in Eq. (4), which is proportional to α^2, measures the influence of the X-valley on the tunneling of electrons into the Γ-valley. Because α is small, the correction associated with this term does not exceed 0.3% for the structure under consideration in the entire energy interval, and this term can be dropped in Eq. (4).

If the condition $(U_\Gamma - \varepsilon)/F x_{\Gamma 1} \gg 1$ holds (i.e., the transparency of the barrier is small), then for D_Γ it is not difficult to obtain the approximate expression

$$D_\Gamma \simeq \frac{4\sqrt{m_{\Gamma 1} m_{\Gamma 2}\varepsilon(U_\Gamma - \varepsilon)}}{(m_{\Gamma 2} - m_{\Gamma 1})\varepsilon + m_{\Gamma 1} U_\Gamma} \times \exp\left(-\frac{4}{3}\,\frac{\sqrt{2 m_{\Gamma 2}(U_\Gamma - \varepsilon)^3}}{\hbar F} \right), \tag{6}$$

which for $m_{\Gamma 1} = m_{\Gamma 2}$ coincides with Ref. 6.

Figure 1 shows the functions $D_\Gamma(\varepsilon)$ and $D_X(\varepsilon)$ calculated using Eqs. (2)–(5) (curves *1* and *2*) when $E = 10^6$ V/cm. For comparison we also show $D_\Gamma(\varepsilon)$ calculated using the approximate expression (6) (curve *3*). As is clear from the figure, curves *1* and *3* are in good agreement for $D_\Gamma \leqslant 0.1$. At small energies, for which the transparency of the barrier for Γ-electrons is small, the tunneling probability to the X-valley exceeds the probability for tunneling to the Γ-valley by four orders of magnitude. As the energy, and accordingly the transparency of the barrier to the Γ-valley, increase, the role of the $\Gamma - X$-transitions decreases due to their relatively small probability.

The lifetime for the quasistationary state in the triangular potential well is found from the imaginary part of its complex energy

$$\tau^{-1} = \nu = -2\,\mathrm{Im}(\varepsilon)/\hbar, \tag{7}$$

where ε is determined from the condition that the wave function to the right of the barrier have the form of an outgoing wave at $+\infty$, while infinitely far to the left of the barrier it decays exponentially. By analogy with the stationary case, these conditions for ε, together with the boundary conditions (1), give a transcendental equation for ε. If the potential well is sufficiently deep, then ε can be written in the form $\varepsilon = \varepsilon_0 + \delta\varepsilon$, where $\varepsilon_0 = 2.34 F x_{\Gamma 1}$ is the energy of the ground state in the triangular well with an infinite barrier. Substituting this expression for ε into the transcendental equation and expanding the latter with respect to $\delta\varepsilon$ (when the condition $\delta\varepsilon \ll \varepsilon_0$ holds), we obtain the approximate expression

$$\delta\varepsilon \simeq -\frac{F}{m_{\Gamma 1}}\left(\frac{E'_{\Gamma}}{m_{\Gamma 2}x_{\Gamma 2}E_{\Gamma}}+\frac{\alpha^2}{\frac{1}{m_{X1}x_{X1}}A_0-\frac{E'_X}{m_{X2}x_{X2}}E_X}\right)^{-1}, \tag{8}$$

where $A_0 = \mathrm{Ai}[(U_{X1}-\varepsilon_0)/Fx_{X1}]/\mathrm{Ai}'[(U_{X1}-\varepsilon_0)/Fx_{X1}]$ and ε must everywhere be replaced by ε_0.

If we disregard tunneling through the X valley in (8) (the term proportional to α^2), when the condition $(U_\Gamma-\varepsilon_0)/Fx_{\Gamma 1} \gg 1$ holds, we obtain the simple expression

$$\delta\varepsilon_\Gamma \simeq \frac{-\hbar m_{\Gamma 2}F}{m_{\Gamma 1}\sqrt{2m_{\Gamma 2}\varepsilon_0(U_\Gamma-\varepsilon_0)}} \times\left[1+i\exp\left(-\frac{4}{3}\frac{\sqrt{2m_{\Gamma 2}(U_\Gamma\varepsilon_0)^3}}{\hbar F}\right)\right], \tag{9}$$

where the real part $\delta\varepsilon$ determines the energy shift connected with finiteness of the height of the barrier U_Γ, while the imaginary part of the complex energy determines the lifetime of the quasistationary state.

The dependence of the inverse lifetime of an electron on the applied electric field (curve *1*) is shown in Fig. 2. Here we plot the functions calculated using Eq. (8): curve *2* was plotted with $\Gamma - X$ tunneling included, curve *3* without including the X tunneling. For comparison we also show the inverse lifetime calculated using the approximate expression (9) (curve *4*). In this figure we also show the dependences of ε_0, $\mathrm{Re}(\varepsilon)$ and $\mathrm{Re}(\varepsilon_0+\delta\varepsilon)$ on E (curves *5–7*, respectively). The overestimated value of ν obtained from Eqs. (8) and (9) for $E > 10^6$ V/cm is associated with the fact that in these fields ε_0 overestimates ε somewhat.

As is clear from this figure, the effect of tunneling into the Γ-valley gives rise to an increase of $\nu(E)$ only for electric fields $E > 1.5\times 10^6$ V/cm; therefore, inclusion of the X valley in calculating the lifetime is very important. For $E > 5\times 10^5$ V/cm, where the quasistationary state is lifted above the X-valley in AlAs, the inverse lifetime is a rather weak function of the field and varies in the range $\nu \sim 10^{11} - 10^{13}\ \mathrm{s}^{-1}$.

The author wishes to thank Yu. A. Romanov for discussing the results of the paper. This work was carried out with the financial support of MNTP (project 1-030), MNF, (project NOL300) and RFFI.

[1] K. Hess, T. K. Higman, M. A. Emanuel, and J. J. Coleman. J. Appl. Phys. **60**, 3775 (1986).

[2] A. M. Belyantsev and Yu. Yu. Romanov, Fiz. Tekh. Poluprovodn. **29**, 1408 (1995) [Sov. Phys. Semic. **29**, 728 (1995)].

[3] H. C. Liu, Appl. Phys. Lett. **51**, 1019 (1987).

[4] Yu Zhang and H. Zheng, Appl. Phys. Lett. **65**, 1036 (1994).

[5] J. A. Stovneng and P. Lipavsky, Phys. Rev. B **49**, 16494 (1994).

[6] V. M. Galitskiĭi, B. M. Karnakov, and V. I. Kogan, *Problems in Quantum Mechanics*(Nauka, Moscow, 1981) p.177 [in Russian].

[7] A. I. Baz', Ya. B. Zel'dovich, and A. M. Perelomov, *Scattering, Reactions and Decay in Nonrelativistic Mechanics* (Nauka, Moscow, 1966) p.162 [in Russian].

Translated by F. Crowne

Auger recombination in strained quantum wells

A. D. Andreev and G. G. Zegrya

A. F. Ioffe Physicotechnical Institute, Russian Academy of Sciences, 194021 St. Petersburg, Russia

(Submitted May 12, 1996; accepted for publication June 26, 1996)
Fiz. Tekh. Poluprovodn. 31, 358–364 (March 1997)

A nonthreshold mechanism for Auger recombination of nonequilibrium carriers in quantum wells with strained layers is investigated theoretically. It is shown that the dependence of the Auger recombination rate on the magnitude of the strain and the height of the heterobarriers for electrons and holes can be analyzed only by calculating the overlap integrals between initial and final particle states microscopically. In quantum wells with strained layers the presence of strain affects qualitatively and quantitatively the electron-hole overlap integral. The dependence of the Auger recombination rate on the quantum well parameters, the magnitude of the stress, and temperature are analyzed for heterostructures based on InGaAsP/InP and InGaAlAs/InP. © *1997 American Institute of Physics.* [S1063-7826(97)02203-5]

1. INTRODUCTION

Semiconductor heterostructures—isolated heterojunctions, quantum wells, and quantum dots—are primary objects of investigation in semiconductor physics. Many different optoelectronic devices have been created using semiconductor heterostructures, among them lasers based on double heterojunctions and quantum wells.[1,2] The lowest laser threshold currents are for semiconductor quantum-well lasers.[2] In the majority of these devices, the semiconductor heterostructure quantum wells contain strained layers. It is well known[3,4] that the presence of elastic strain in a semiconductor heterostructure strongly affects the elementary recombination processes that occur there. In long- wavelength lasers ($\lambda > 1.3\mu$m) nonradiative Auger recombination processes must be considered along with radiative recombination processes. Nonradiative recombination processes decrease the internal quantum yield and increase the threshold current of lasers at high temperatures. In order to fabricate long-wavelength lasers with improved characteristics, it is important to suppress these Auger recombination processes. One way to do this is to create structures with strained layers.[3,4]

Zegrya *et al.*[5] were the first to show theoretically that the Auger recombination process has no threshold in semiconductor heterostructures, and that the Auger recombination rate is a power-law function of temperature. The existence of a nonthreshold channel for Auger recombination was demonstrated experimentally by various groups for type-I (see Ref. 6) and type-II heterostructures (see Refs.7 and 8). The main features of the nonthreshold Auger recombination channel are: 1) the Auger electron receives the momentum necessary for a transition to a highly excited state by interacting with the heterojunction boundary rather than from other particles; 2) because there is no conservation law for the component of momentum perpendicular to the plane of the heterostructure, the Auger processes is one without a threshold, and the rate at which it proceeds is a nonexponential (power-law) function of temperature; 3) the excited Auger electron is ejected in the direction perpendicular to the plane of the heterostructure. It is noteworthy that calculations of the Auger recombination rate for quantum wells in the literature up to now have proceeded by analogy with bulk semiconductors, i.e., the Auger process is assumed to have a threshold while the Auger recombination rate in the quantum well retains its exponential dependence on temperature.[1,2,9]

In our previous papers we investigated the nonthreshold Auger process in unstrained type-I and type-II quantum wells.[10–12] We showed that the Auger recombination rate depends significantly on the parameters of the quantum well (the height of the heterobarriers for electrons and holes, and the width of the quantum well). It is obvious that for strained heterostructures the rate for the nonthreshold Auger recombination process depends significantly on the magnitude of the strain.

Our goal was to study the effect of elastic strain on the Auger recombination rate in a quantum well with strained layers. We will show that the Auger recombination rate is a strong function of the parameters of the quantum well and the magnitude of the strain.

2. AUGER RECOMBINATION RATE

In heterostructures with quantum wells there are two important Auger recombination channels: CHCC and CHHS.[10] In this paper we restrict the discussion to the CHCC Auger process (Fig. 1).

According to the standard rules of the theory of Auger processes, the Auger recombination rate is calculated using first-order perturbation theory with respect to the electron-electron interaction[5,12,13]:

$$G=\frac{2\pi}{\hbar}\frac{1}{S}\sum_{1,2,3,4}|M|^2\delta(E_1+E_2-E_3-E_4)\times f_c(E_1)f_c(E_2)f_h(E_3)[1-f_c(E_4)]. \tag{1}$$

Here $f(E_i)$ is the Fermi distribution function of the ith particle ($i=1,2,3,4$); E_1 and E_2 are the initial, and E_3 and E_4 the final energies of electrons; S is the area of the heterojunction; and M is the matrix element of the electron-electron interaction computed with allowance for the antisymmetrization of the electron-wave functions in the initial

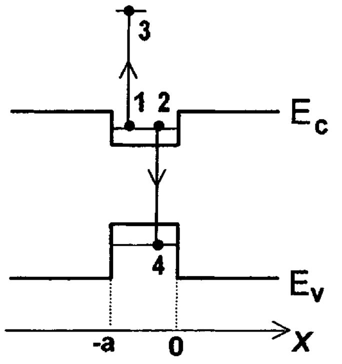

FIG. 1. Schematic representation of the band diagram of a heterostructure with a single quantum well. The numbers 1 and 2 denote initial states of a particle, 3 and 4 denote final states. The arrows point to transitions of a particle from initial states 1 and 2 to final states 3 and 4 during the Auger recombination process.

and the final states. After statistical averaging over the initial spin states of the electrons, the square of the matrix element has the form

$$\langle |M|^2\rangle = |M_I|^2 + |M_{II}|^2 - M_I M_{II}^*, \tag{2}$$

$$M_I = \int \psi_1^*(\mathbf{r})\psi_3(\mathbf{r}) \frac{e^2}{\kappa_0|\mathbf{r}-\mathbf{r}'|} \psi_2^*(\mathbf{r}')\psi_4(\mathbf{r}') d^3\mathbf{r} d^3\mathbf{r}', \tag{3}$$

where κ_0 is the static dielectric constant permittivity of the medium; M_{II} is obtained from M_I by the replacement $1 \leftrightarrow 2$. To calculate the matrix element for an Auger transition, it is necessary to find the wave function of the carriers that participate in the recombination process. It was shown previously that the wave functions of carriers (both holes and electrons) should be computed in the multiband approximation.[5,12,13] In this case the choice of an effective Hamiltonian for the multiband model is very important. This Hamiltonian should describe the basic features of the spectrum and wave functions of carriers in the quantum well (the mixing of light and heavy holes, the nonparabolicity of the spectrum). In our paper we have used the Kane model, because this model gives a good description of the band structure of narrow-gap semiconductors. Within the framework of this model the basis wave functions for the bottom of the conduction band and the top of the valence band are chosen in the form $|s\rangle$- and $|\mathbf{p}\rangle$-functions (the X axis is directed perpendicular to the plane of the quantum well). The wave functions of electrons and holes are superpositions of the basis states

$$\psi = u(\mathbf{r})|s\rangle + \mathbf{v}(\mathbf{r})|\mathbf{p}\rangle, \tag{4}$$

where $u(\mathbf{r})$ and $\mathbf{v}(\mathbf{r}) \equiv (v_x, \mathbf{v}_\parallel)$ are smooth envelopes of Bloch functions. The system of equations for the envelopes has the form

$$\begin{gathered}
\left[E - \frac{E_g}{2} - V_c(x) - d_c\right] u - \gamma \hat{\mathbf{k}}\mathbf{v} = 0, \\
\left[E + \frac{E_g}{2} + V_v(x) - d_x + \frac{\hbar^2 \hat{\mathbf{k}}^2}{2m_{hh}}\right] v_x - \gamma \hat{k}_x u = 0, \\
\left[E + \frac{E_g}{2} + V_v(x) - d_\parallel + \frac{\hbar^2 \hat{\mathbf{k}}^2}{2m_{hh}}\right] \mathbf{v}_\parallel - \gamma \hat{k}_\parallel u = 0.
\end{gathered} \tag{5}$$

Here $\hat{\mathbf{k}} = -i\nabla$; γ is the Kane matrix element; E_g is the width of the band gap of the narrow-gap semiconductor (without including strain); m_{hh} is the heavy-hole effective mass of the bulk material; and $V_c(x)$ and $V_v(x)$ are the heights of the heterobarriers for electrons and holes, respectively, in the absence of strain. The quantities d_c, d_x, and $d_\parallel$ are expressed in terms of the deformation potential constants a_c, a_v, and b: $d_c = a_c(e_x + 2e_\parallel)$; $d_x = 2e_\parallel(a_x - b) + e_x(a_v + 2b)$; $a_\parallel = (a_v - b)(e_x + e_\parallel) + (a_v + 2b)e_\parallel$. In the case we are studying, i.e., an unstrained barrier, we have for the strain tensor components: $e_\parallel = (a_B - a_W)/a_W$, $e_x = -2C_{12}e_\parallel/C_{11}$, where a_B and a_W are the lattice constants of the barrier and quantum well materials, respectively; C_{11} and C_{12} are elastic constants. The system of equations (5) does not contain terms that describe the spin-orbit coupling and its variation in the presence of strain. The effect of the spin-orbit coupling on the Auger recombination process is taken into account only through the Kane matrix element γ:

$$\gamma^2 = \frac{\hbar^2 E_g(E_g + \Delta_{so})}{2m_c(E_g + 2\Delta_{so}/3)},$$

where Δ_{so} is the magnitude of the spin-orbit splitting. At the heterojunction boundary the wave functions determined from the system (5) satisfy certain boundary conditions.[12] We note that in calculating the wave functions and spectrum of the holes it is necessary to take into account the mutual conversion of light and heavy holes. As we already noted above, of the mixing of light and heavy hole states gives qualitatively and quantitatively incorrect results for the overlap integrals and consequently for the Auger recombination rate.

3. AUGER TRANSITION MATRIX ELEMENT

The fundamental problem in calculating the Auger recombination rate is computation of the Auger- transition matrix element. Expanding the Coulomb interaction potential in a Fourier integral, we obtain

$$M_I = \frac{4\pi e^2}{\kappa_0} \int \frac{d^3q}{(2\pi)^3} \frac{1}{q^2} I_{13}(\mathbf{q}) I_{24}(-\mathbf{q}), \tag{6}$$

$$I_{ij}(\mathbf{q}) = \int d^3r\, \psi_i^*(\mathbf{r}) \psi_j(\mathbf{r}) e^{i\mathbf{qr}}. \tag{7}$$

Here I_{ij} is the overlap integral between states of particles i and j. Using the explicit expressions for the wave functions of electrons and holes determined from the system (5), we can obtain analytic expressions for the overlap integrals and matrix element. In this case it is convenient to use the following computational scheme. We first calculate the overlap integral $I_{13}(\mathbf{q})$ between states ''1'' and ''3'' (see Fig. 1).

Then we integrate over q_x in M_I, using the residue theorem. In this case it turns out that in the complex q_x plane there exist two kinds of poles: 1) a pole corresponding to low momentum transfer $q_x^{(1)} = |\mathbf{q}_1 - \mathbf{q}_4|$ (where $\mathbf{q}_i$ is the longitudinal momentum of particle i); 2) a pole corresponding to large momentum transfer $q_x^{(2)} \sim Q$, where $Q \sim (m_c E_g/\hbar^2)^{1/2}$. As a result, the matrix element splits into two parts:

$$M = M^{(1)} + M^{(2)},$$

where $M^{(1)}$ and $M^{(2)}$ are the contributions to the matrix element corresponding to small $q_x^{(1)}$ and large $q_x^{(2)}$ momentum transfers.

It has been shown previously[5,12] that the overlap integrals entering into the Auger recombination matrix element must be calculated within the framework of the multiband Kane model, taking into account the nonparabolicity of the carrier spectrum. For the overlap integral I_{14} between states of the localized (''1'') and highly excited (''4'') electrons this is important for the following reasons. First of all, the wave function of a highly excited electron in the conduction band contains a significant admixture of $|p\rangle$ states of the valence band (i.e., $u_3 \sim v_{x3}$). Secondly, this overlap integral consists of contributions from three regions of integration with respect to X: two regions of below-barrier motion of electron ''1'' ($x < -a$ and $x > 0$; see Fig. 1) and the quantum well region $(-a < x < 0)$. In the summation, contributions from the regions of below-barrier motion compensate for the contribution from the quantum-well region, leading to an additional smallness in the matrix element of order $\widetilde{V}_c/E_g$, where $\widetilde{V}_c$ is the effective height of the barrier for electrons (taking strain into account). Note that in type-II heterostructures an analogous compensation leads to the suppression of the Auger recombination process for certain heterostructure parameters.[11]

In computing the electron-hole overlap integral I_{24}, it is necessary to take into account the mutual conversion of light and heavy holes and the strongly nonparabolic dependence of the hole spectrum on the longitudinal momentum q_4. It is possible to do this on the basis of the multiband Kane model. In this model the wave functions for holes consist of superpositions of light- and heavy-hole states. The interaction with the heterojunction causes a strong mixing of these states, which depends strongly on the longitudinal hole momentum q_4. In Fig. 2a, we show the dependence of the amplitudes of light L and heavy H hole states in the quantum well region $(-a < x < 0)$ as a function of the longitudinal momentum q_4. The effect of mutual conversion of light and heavy holes on the amplitudes H and L leads to a nonmonotonic dependence of the overlap integral for electrons and holes I_{24} on the hole momentum q_4 (see Fig. 2*b*). For $q \sim \pi/a$ the primary contribution to the electron- hole overlap integral comes from light-hole states (see Fig. 2). It is especially important to emphasize that the dependence of the overlap integral I_{24} on the momentum transfer $|\mathbf{q}_2 - \mathbf{q}_4|$ is strongly nonlinear. For an unstrained quantum well a linear dependence of I_{24} on the momentum transfer is obtained only for small momentum transfers $q < \pi/a$, where a is the width of the quantum well; in the region $q > \pi/a$, the overlap integral I_{24} is a weak decreasing function of the momentum transfer (Fig. 3a). In Fig. 3b we show the same function for a strained quantum well. Our analysis shows that strain affects the dependence of the electron-hole overlap integral on momentum transfer, both qualitatively and quantitatively.

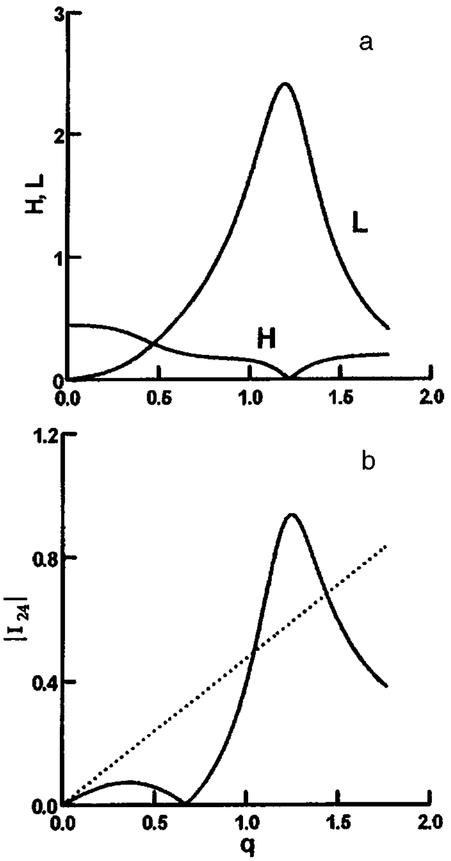

FIG. 2. a—Dependence of the amplitudes of light L and heavy H hole states on the longitudinal momentum q in a strained InGaAsP quantum well, $a = 60$Å, $\xi = 1.5\%$. *b*—Dependence of the overlap integral for electrons and holes I_{24} $(q_x = 0)$ on the longitudinal hole momentum $q \equiv q_4$ for $q_2 \equiv 0$, calculated from the exact expression (7)—the solid curve; the dashes are the linear approximation $I_{24} = \gamma|\mathbf{q}_2 - \mathbf{q}_1|/|E_2 - E_4|$ used in papers by other authors (see Ref. 9). The parameters of the structure were taken from Ref. 14.

Wang *et al.*[9] computed the Auger recombination rate by using a phenomenological expression to calculate the electron-hole overlap integral $|I_{24}|^2 = \alpha |q_2 - q_4|^2/E_g$; i.e., they assumed that I_{24} is a linear function of the momentum transfer (where α is a certain fitting parameter). In their calculations the value of the fitting parameter α does not depend on the quantum well parameters or the magnitude of the strain. In our paper we show that this phenomenological approach is inapplicable, in general, and cannot be used to analyze the dependence of the Auger recombination rate on the quantum well parameters, the magnitude of the strain, or the temperature. Thus, in order to calculate the overlap integrals of the particles that participate in the Auger recombination process, it is necessary to use wave functions calculated on the basis of the multiband Kane model.

In order to evaluate the Auger recombination rate, we must subsutitute into Eq. (1) the matrix element, which is calculated analytically according to the scheme described

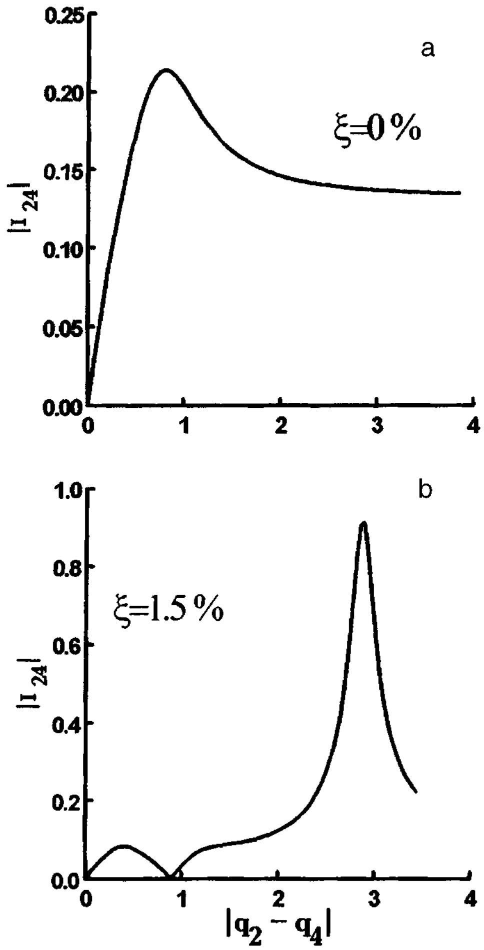

FIG. 3. Dependence of the overlap integral for electrons and holes I_{24} ($q_x=0$) on the momentum transfer $|\mathbf{q}_2-\mathbf{q}_4|$ for an unstrained (*a*) and strained (*b*) quantum wells based on InGaAsP; $E_g^{\mathrm{eff}}=$ 0.83 eV, $a=60$Å, with band structure parameters taken from Ref. 14.

above. From here on we will use the standard scheme for these computations. Transforming to polar coordinates (q_i, φ_i) in the plane of longitudinal momentum q, we have for the Auger recombination rate

$$G=\frac{1}{4\pi^5\hbar}\sum_{n_1,n_2,n_4}\int_0^\infty\int_0^\infty\int_0^\infty q_1 dq_1 q_2 dq_2 q_4 dq_4$$

$$\times\int_0^{2\pi}\int_0^{2\pi} d\varphi_1 d\varphi_2 |M(q_1,q_2,q_4,\varphi_1,\varphi_2)|^2$$

$$\times f_c(q_1) f_c(q_2) f_h(q_4)\left|\frac{E_3}{\partial k_3}\right|^{-1}.$$

For further calculations of the Auger recombination rate we will calculate numerically the five fold integral (8). Analysis of Eq. (8) allows us to conclude that the Auger recombination rate has a nonexponential dependence on temperature; i.e., the Auger recombination process is a nonthreshold process.[5,10]

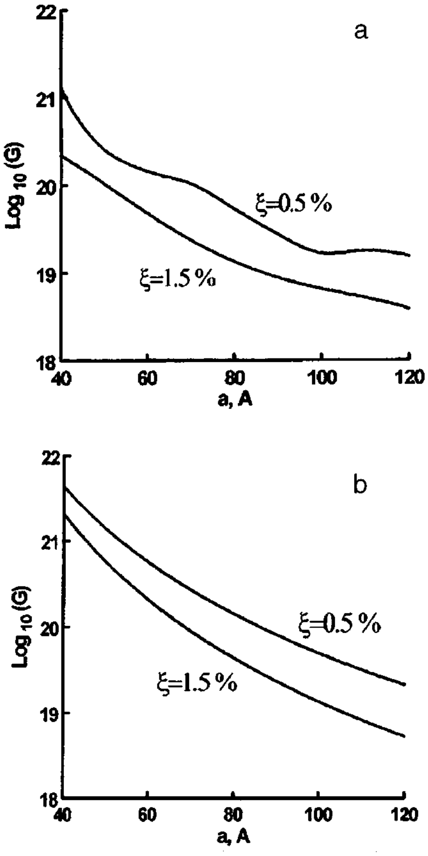

FIG. 4. Dependence of the logarithm of the Auger recombination rate $\log_{10}(G)$ on the quantum well width a for two values of elastic strain ξ for quantum wells based on InGaAsP (*a*) and InGaAlAs (*b*). For both structures $E_g^{\mathrm{eff}}=$ 0.8 eV, $n=p=2\times10^{12}$ cm^{-2}, with band structure parameters calculated according to Ref. 14.

4. DISCUSSION AND RESULTS

As a demonstration of the dependence of the Auger recombination rate on the quantum well parameters, we will discuss two heterostructures based on $\mathrm{In}_{1-x}\mathrm{Ga}_x\mathrm{As}_y\mathrm{P}_{1-y}$ and $\mathrm{In}_{1-x-z}\mathrm{Ga}_x\mathrm{Al}_z\mathrm{As}$. The composition of the quaternary solutions determined from the condition $E_g^{\mathrm{eff}}=\mathrm{const}$ for these values of the strain ξ and the quantum well width (here, E_g^{eff} is the effective width of the band gap). In this case the values of the strain ξ that correspond to real structures can vary only with specific limits that depend on E_g^{eff} and a. The choice of these structures is motivated by the fact that they are widely used to make long- wavelength lasers in the range 1.3–1.5 μm. In making lasers that emit in this wavelength range it is important to choose structure parameters (while keeping the value of E_g^{eff} fixed) such that the Auger recombination current is minimal and the quantum yield maximal. Our primary task was to carry out qualitative and quantitative analyses of the dependence of the Auger recombination rate on the structure parameters.

We have analyzed theoretically the dependence of the Auger recombination rate on the quantum well width a, the height of the heterobarriers for electrons V_c and holes V_v, the magnitude of the strain ξ, and the temperature T. Our

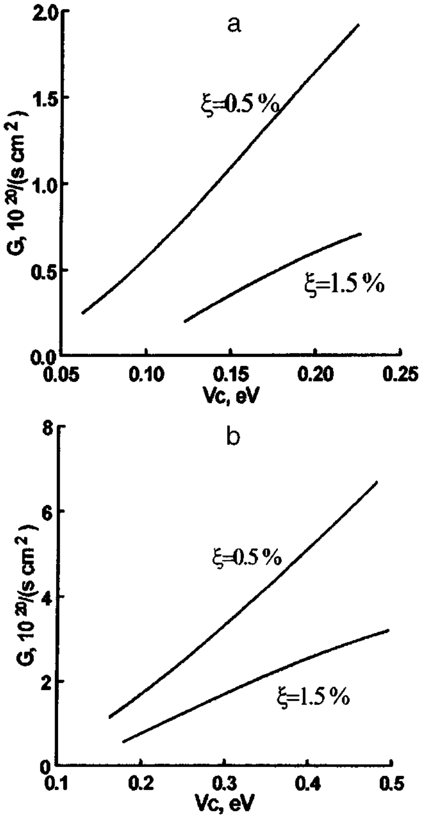

FIG. 5. Dependence of the Auger recombination rate G on the height of the heterobarrier for electrons V_c for two values of the elastic strain ξ and quantum wells based on InGaAsP (*a*) and InGaAlAs (*b*). For both structures $E_g^{\text{eff}} = 0.8$ eV, $n = p = 2 \times 10^{12}$ cm^{-2}, with band structure parameters calculated using the data from Ref. 14.

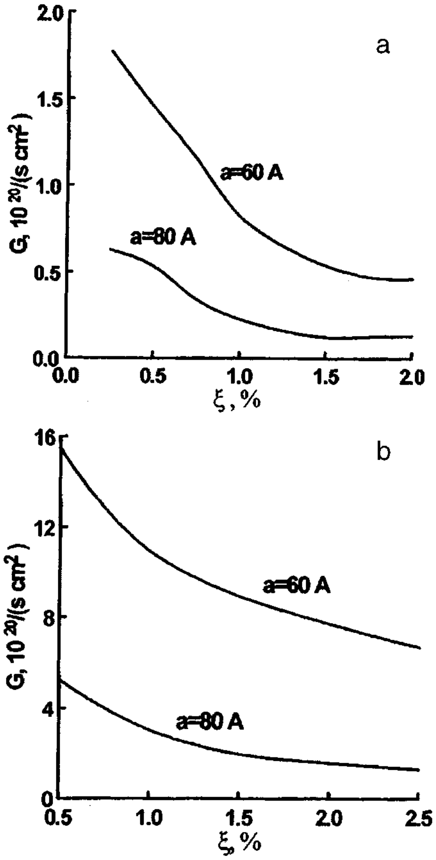

FIG. 6. Dependence of the Auger recombination rate G on the magnitude of the elastic strain for two values of the quantum well width a and heterojunctions based on InGaAsP (*a*) and InGaAlAs (*b*). For both structures $E_g^{\text{eff}} = 0.8$ eV, $n = p = 2 \times 10^{12}$ cm^{-2}, with band structure parameters calculated using the data from Ref. 14.

analysis shows that the Auger recombination rate depends strongly on these quantum well parameters.

Figure 4 shows the dependence of the Auger recombination rate on the quantum well width for the two structures described above. As the quantum well width increases, the Auger recombination rate falls off strongly. For example, when the quantum well width changes from 40 to 120 Å, the rate G drops by more than two orders of magnitude. For the two structures mentioned above, the dependences of the Auger recombination rate on a differ qualitatively. In the structure $\text{In}_{1-x-z}\text{Ga}_x\text{Al}_z\text{As}$, the height of the heterojunction barrier for electrons V_c is larger than the height of the heterojunction barrier for holes V_v, in the ratio $V_c/V_v = 7/3$. Therefore, the quantum well for electrons is deep and the number of electron levels that participate in the Auger recombination process does not change as the width of the quantum well a changes. Hence, $G(a)$ is a monotonically decreasing function of a for this structure. As the magnitude of the strain ξ increases, the dependence of G on a becomes sharper (Fig. 3). The situation is quite different for a quantum well based on $\text{In}_{1-x}\text{Ga}_x\text{As}_y\text{P}_{1-y}$. For this structure the depth of the quantum well for electrons is smaller than that for holes, the ratio between them is $V_c/V_v = 4/6$. In this case, as a increases, the number of electronic levels that participate in the Auger recombination process increases as well. The appearance of a new level for electrons gives an appreciable contribution to the Auger recombination rate. Consequently, the curve for the dependence of G on a exhibits a slight increase in the Auger recombination rate at the appearance of each new level; as a increases further, the Auger recombination rate decreases as before. At low temperatures the function $G(a)$ is a decreasing function with rather small oscillations for those values of a at which new levels appear. As the value of the strain increases, the dependence $G(a)$ becomes weaker, because in this case the effective height of the heterojunction barrier for electrons decreases. However, as V_c decreases, the Auger recombination rate decreases as well.

As was shown previously,[5]the nonthreshold Auger recombination mechanism at heterostructures is caused by the interaction of a charge carrier with the heterojuncton barrier. For unstrained quantum wells, the Auger recombination rate increases with increasing height of the electron heterobarrier. In Fig. 5 we show the dependence of the Auger recombination rate on the heterobarrier height for a strained quantum well. In the presence of strain the dependence of the Auger recombination rate on the height of the heterobarrier is weaker than in the absence of strain.

Figure 6 shows the dependence of the Auger recombination rate on the magnitude of the strain ξ; in this case the

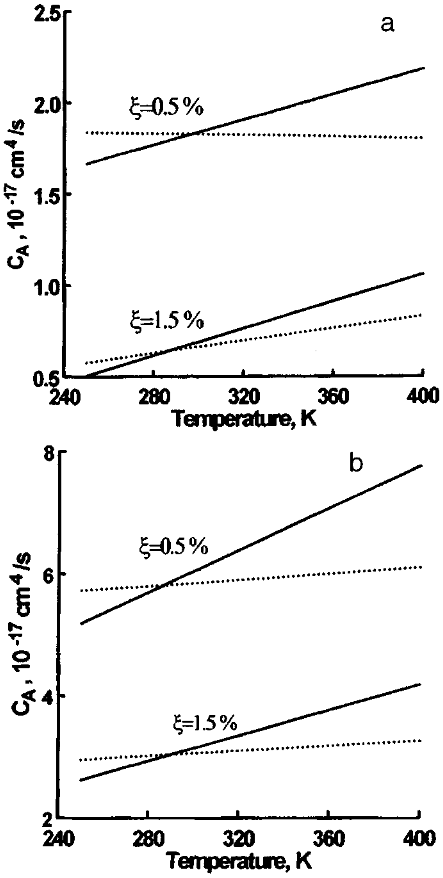

FIG. 7. Dependence of the Auger recombination coefficient C_a on temperature T for two values of the elastic strain ξ and two heterostructures: InGaAsP (*a*) and InGaAlAs (*b*). For both structures $E_g^{\mathrm{eff}} = 0.8$ eV, $n = p = 2 \times 10^{12}$ cm^{-2}, with band structure parameters calculated according to Ref. 14. The dotted curves correspond to the function $C_A(T)$ when $E_g = \mathrm{const}$. The solid curves are the same function for $E_g = E_g(T = 300\mathrm{K}) - \alpha(T - 300\mathrm{K})$, where $\alpha = 4 \times 10^{-4}$ eV/K.

range of variation of possible values of ξ depends on the quantum well parameters. For values of ξ corresponding to real structures, the Auger recombination rate decreases with increasing ξ. As the width of the quantum well decreases, the dependence of the Auger recombination rate on the magnitude of the strain becomes stronger. The dependence of the Auger recombination rate on the strain is determined by the dependence of the overlap integrals I_{13} and I_{24} on ξ [see (6) and (7)]. With increasing ξ, the effective value of the heterobarrier height for electrons decreases. This leads to a decrease in the electron-(highly excited electron) overlap integral I_{13}. The electron-hole overlap integral I_{24} changes significantly as a function of strain: for a large momentum transfer $q < \pi/a$, I_{24} decreases with increasing ξ, while for $q > \pi/a$ it has a maximum (Fig. 3). As a result, the Auger recombination rate decreases with increasing magnitude of the strain ξ.

As we already noted above, in uniform semiconductors, the fact that Auger processes have a threshold causes the Auger recombination coefficient

$$C_A = G/(\hbar^2 p)$$

to depend on temperature according to an exponential law: $C_A \propto \exp(-E_{th}/T)$, where E_{th} is the threshold energy ($E_{th} \propto E_g$), and n and p are electron and hole concentrations, respectively. In quantum wells, as we already noted above, the Auger process has no threshold, and the Auger recombination coefficient depends only weakly on temperature. Our exact analysis shows that over a wide range of quantum well widths the Auger recombination coefficient is virtually temperature-independent. In this case the temperature dependence of C_A is determined by the dependence of the width of the band gap on temperature. In Fig. 7 we show the dependence of the Auger recombination coefficient on temperature for the case where E_g is temperature independent, and for the case where E_g is a function of temperature.

5. CONCLUSION

We have carried out a theoretical first- principles calculation of the rate for CHCC Auger processes in quantum wells with strained layers. Our theoretical analysis shows that the Auger recombination rate in a strained quantum well depends strongly on the height of the heterobarriers for electrons and holes, on the width of the quantum well, and on the magnitude of the strain. We have shown that the qualitative and quantitative analysis of the dependence of the Auger recombination rate on these parameters of the quantum well requires a microscopic calculation of the overlap integrals based on the multiband Kane model. This approach is important for investigating the threshold characteristics of semiconductor quantum-well lasers. In optimizing the parameters of these laser structures it is necessary to know the dependence of the threshold current density on the quantum well parameters, which in turn is determined by processes of Auger recombination and radiative recombination.

This work was supported in part, by the Russian Fund for Fundamental Research (Grant 96-02-17952) and the state program ''Physics of Solid-State Nanostructures.'' The work of A. D. Andreev was supported by stipends from the INTAS grant 93-2492 and was carried out within the framework of the research program of the International Center for Fundamental Physics in Moscow.

[1] G. P. Agrawal and N. K. Dutta, *Long- Wavelength Semiconductor Lasers* (Van Nostrand Reinhold Company, N. Y., 1986).

[2] *Quantum Well Lasers*, Peter S. Zory, Ed. (Academic Press, Inc., 1993).

[3] A. R. Adams, Electron. Lett. **22**, 249 (1986).

[4] P. J. Thijs, L. F. Tiemeijer, and T. van Dongen, IEEE J. Quant. Electron. **QE-30**, 477 (1994), and references therein.

[5] G. G. Zegrya and V. A. Kharchenko, Zh. Éksp. Teor. Fiz. **74**, 173 (1992) [*sic*].

[6] G. G. Zegrya, V. P. Evtikhiev, I. V. Kudryashov, A. D. Andreev, A. B. Komissarov, D. V. Prilutskiĭ, and V. E. Tokranov, *Abs. of Reports of the Second Russian Conf. on Semiconductor Physics*, [in Russian], Zelenogorsk (1996) V. 2, p. 125.

[7] G. G. Zegrya, P. Voisin, D. K. Nelson, A. N. Starukhin, and A. N. Titkov, *Abstract Int. Symp. Nanostructure Physics and Technology* [in Russian] St. Peterburg, (1994), p.101.

[8] M. P. Mikhailova, G. G. Zegrya, K. D. Moiseev, I. N. Timchenko, I. A. Andreev, and Yu. P. Yakovlev, Proc. SPIE, **2397**, 166 (1995).

[9] Jin Wang, P. von Allmen, J.-P. Leburton, and K. J. Linden, IEEE J. Quant. Electron. **QE- 31**, 864 (1995).

[10] G. G. Zegrya, A. D. Andreev, N. A. Gun'ko, and E. V. Frolushkina, Proc. SPIE **2399**, 307 (1995).

[11] G. G. Zegrya and A. D. Andreev, Appl. Phys. Lett. **67**, 2681 (1995).

[12] G. G. Zegrya and A. D. Andreev, Zh. Éksp. Teor. Fiz. **109**, 615 (1996) [Sov. Phys. **82**, 328 (1996)].

[13] B. L. Gel'mont, Zh. Éksp. Teor. Fiz. **75**, 536 (1978) [Sov. Phys. JETP **48**, 258 (1978)].

[14] T. Ishikawa and J. E. Bowers, IEEE J. Quant. Electron. **QE-30**, 562 (1994).

Translated by F. Crowne

Luminescence of porous silicon in the infrared spectral region at room temperature

G. Polisskiĭ and F. Koch

Technical University, Munich, D-85747 Garching, Germany

O. M. Sreseli and A. V. Andrianov

A. F. Ioffe Physicotechnical Institute, Russian Academy of Sciences, 194021 St. Petersburg, Russia

(Submitted June 17, 1996; accepted for publication July 1, 1996)
Fiz. Tekh. Poluprovodn. **31**, 365–369 (March 1997)

A method for preparing mesoporous silicon on *n*-type substrates has been developed. The material exhibits two intense bands of photo- and electroluminescence at room temperature: a primary one in the range 1.4–1.8 eV, and a low-energy infrared band near 1–1.2 eV. It is shown that the position of the primary emission maximum and the intensity of the band can be controlled. The properties of the primary band are explained in terms of a quantum-size model for formation of porous silicon, while the low-energy band is explained as radiative recombination in larger non-quantum-size crystallites. © *1997 American Institute of Physics.* [S1063-7826(97)02303-X]

INTRODUCTION

In recent years there has been much interest in a novel semiconductor material—porous silicon. Its photoluminescence (PL) in the visible region of the spectrum is a well-known phenomenon that has been studied extensively.[1–3] The position of the PL peak in porous silicon made on *p*-type substrates is rather easily shifted over a wide range from the blue-green to the dark red and infrared spectral regions by varying the time and density of the anodization current,[4,5] and also by additional etching after the anodization process.[6]

In all the PL spectra, the intense primary band in the visible is accompanied by a broad, weak, low-energy band between 0.8 and 1.2 eV, primarily at low temperature.[1,7] An infrared band is also observed in electroluminescence (EL) spectra of samples of *n*-type porous silicon in contact with a liquid electrolyte, but at room temperature instead.[8]

The reason for the appearance of the infrared band in the EL and its relation to the infrared band in the PL is unclear. Nowhere in the literature is a method described for controlling the position and intensity of this band.

In this paper we report our efforts to modernize the technology for making *n*-type porous silicon with the goal of obtaining intense low-energy PL and EL bands at room temperature.

EXPERIMENTAL METHOD

All of the samples of porous silicon we investigated were made on *n*-type conducting substrates (the specific resistivity was $2-4\,\Omega\cdot\text{cm}$, orientation (100)) by anodization in standard solutions of hydrofluoric acid (40% or 50% HF:Et$=1:1$) for 10 to 180 min at current densities of $5-80\,\text{mA/cm}^2$ and illumination. The samples were illuminated by a 300-W halogen or xenon lamp through various filters. The optical power was in the range $0.1-0.2\,\text{W/cm}^2$.

In order to excite the PL, we used the 441 and 325-nm lines of a He-Cd laser. The spectrum was dispersed by a SPEX-22 grating monochromator and recorded by a photomultiplier (Hamamatsu) or a cooled germanium detector (North Coast).

EL was excited by current pulses with durations of 0.5–10 ms and repetition rates of 10–100 Hz. The amplitude of the pulses was varied from $1\,\text{mA/cm}^2$ to a few hundred mA/cm^2. The samples were placed in an electrochemical cell with a quartz window and a platinum counter electrode. We used an electrolyte based on potassium or sodium persulfate in a $0.1M$ D_2SO_4 solution. Heavy water was used in the electrolyte because of the considerable absorption of light by ordinary water at wavelengths longer than 1200 nm, whereas D_2O, according to our data, is transparent at least out to 1500 nm.

RESULTS AND DISCUSSION

Photoluminescence. During anodization we used filters that absorbed the high-energy part of the spectrum (low-pass filters), allowing to limit the energy of the light quanta used in the illumination. It is expected that this will lead to a decrease in the energy of the photogenerated carriers, and consequently to an increase in the size of the crystallites of porous silicon. The statistical distribution of crystallites with respect to size in the porous layer that forms under illumination by longer-wavelength light should shift in the direction of larger-scale crystallites. This is because no electron-hole pairs are generated in microcrystallites, for which the effective width of the band gap exceeds the energy of quanta from the illumination source, so that these crystallites are not subject to any further dissolving. Thus, bounding the illumination energy on the high-frequency side should lead to a ‘‘red’’ shift of the PL maximum of the porous layer.

Figure 1 shows PL spectra of samples of porous silicon. Actually, use of the longer-wavelength illumination during the etching process shifts the maximum of the PL toward the low-energy region. The maximum shift of the primary PL peak was 1.38 eV, obtained by illumination through a silicon filter ($E < 1.12$ eV); i.e., the light quanta were close in en-

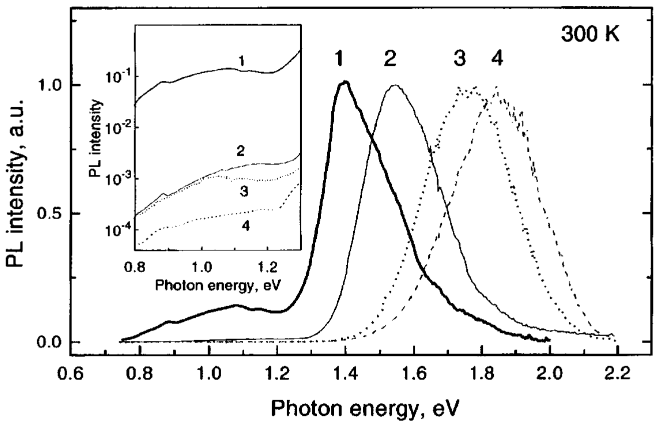

FIG. 1. PL spectra of samples at room temperature. $E_{\text{ex}} = 3.81$ eV. Anodization during illumination by light quanta of various energies, eV: *1*—<1.12, *2*—<1.77, *3*—<2.06, *4*—<2.38. The inset shows the high-energy band of these samples on a semilogarithmic scale.

ergy to the width of the band gap of silicon (Fig. 1, curve *1*). It is noteworthy that the intensity of the PL peak in this case changes only slightly. The intensity of the PL from samples of porous silicon obtained by illumination through a silicon filter depends strongly on the water content in the electrolyte and is minimal when an electrolyte of 50% HF:Et$=1:1$ is used.

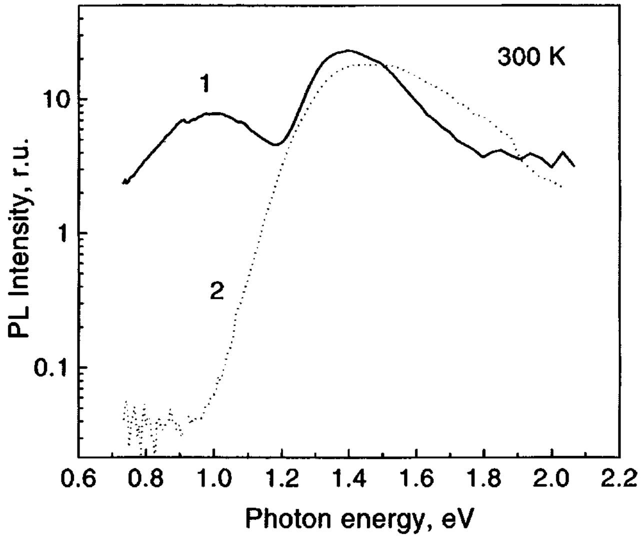

FIG. 2. Photoluminescence spectra of mesoporous samples at room temperature. *1*—on a n-type substrate, obtained by anodization under illumination by quanta with energy <1.12 eV; *2*—on a p^+-type substrate (anodization in the dark).

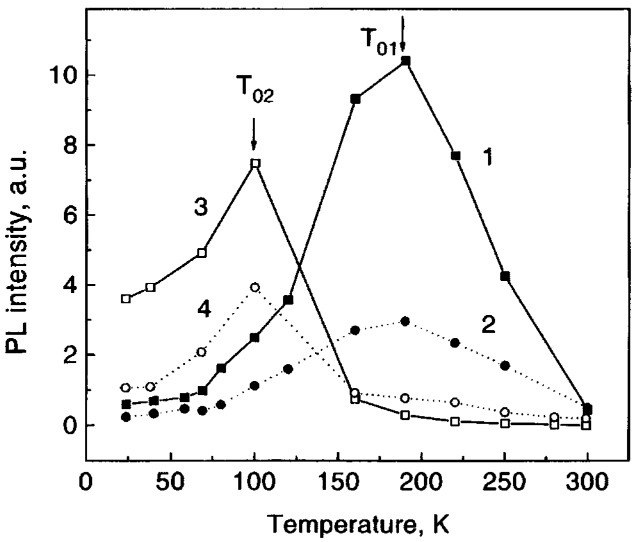

FIG. 3. Temperature dependence of the PL of n-type porous silicon samples. Anodization under illumination by quanta with energy <1.12 eV in different solutions: sample A (*1* and *2*)—40% HF+standard (1:1) sample B (*3* and *4*)—50% HF+standard (1:1). *1,3*—position of the maxima of the primary band for samples A and B, *2,4*—position of the maximum of the low-energy band of these samples. Scale: *1*—×1, *3*—×2, *2,4*—×100

It is clear from Fig. 1 that the shift of the primary PL peak toward the long-wavelength region of the spectrum is accompanied by a growth in intensity of the low-energy peak, while its position is practically unchanged. This behavior differs from that of the infrared peaks observed at low temperatures, and is connected with dangling bonds. As is well known, when the conditions for preparing the porous silicon are changed, these infrared peaks shift ‘‘in sympathy’’ with the shift of the primary peak.[9] Figure 2 shows the PL spectra of a sample on a n-type substrate obtained using the method described above (in what follows these will be n-type samples) and mesoporous silicon prepared on a p^+ substrate. Even when there is fairly good agreement between the position and intensity of the primary PL bands, the low-energy bands differ profoundly. The n-type sample is characterized by a distinct broad band with a maximum at about 1 eV and an intensity more than two orders of magnitude larger than the PL intensity of a mesoporous sample of p^+-Si in this region of the spectrum.

Figure 3 shows the temperature dependence of both PL bands for n-type porous silicon. The temperature dependence of the intensity of the low-energy band is nonmonotonic and analogous to the temperature dependence of the intensity of the high-energy band. The temperature maxima of the curves coincide, although they differ from sample to sample (samples A and B in Fig. 3). The temperature at which maximum intensity is achieved is lower for samples with weaker PL intensity at room temperature.

Electroluminescence. Figure 4 shows the EL spectra of samples of n-type porous silicon in contact with a liquid electrolyte for a cathode bias (minus at the semiconductor). Sample 1 was obtained using a red filter ($E < 1.77$ eV) in the anodization process, while sample 2 was illuminated by white light following the method described in Ref. 8. The changes in EL as the conditions of anodization change correlate with changes in the PL spectrum. The intensity of the infrared band with respect to the visible increases by more than an order of magnitude in samples made using red filters (Fig. 4, curve *1*) compared with the intensity of bands in samples illuminated during anodization by white light (curve *2*). In Fig. 5 we show EL spectra (curves *1* and *2*) and PL spectra (curve *3*) of porous silicon n-type samples. The position of the visible EL band in the samples under study was

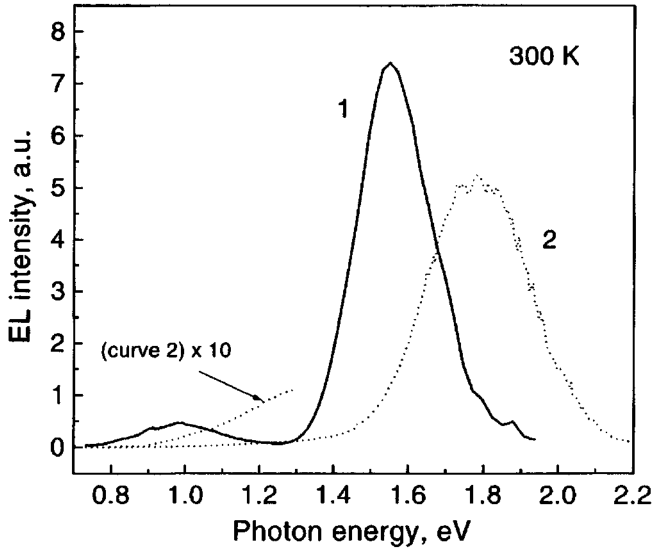

FIG. 4. EL spectra of n-type porous silicon samples. Anodization during illumination by quanta with energies <1.77 eV (*1*) and for illumination by white light (*2*). The current density in a pulse $i=40$ mA/cm^2, $\tau=5$ ms, $f=40$ Hz.

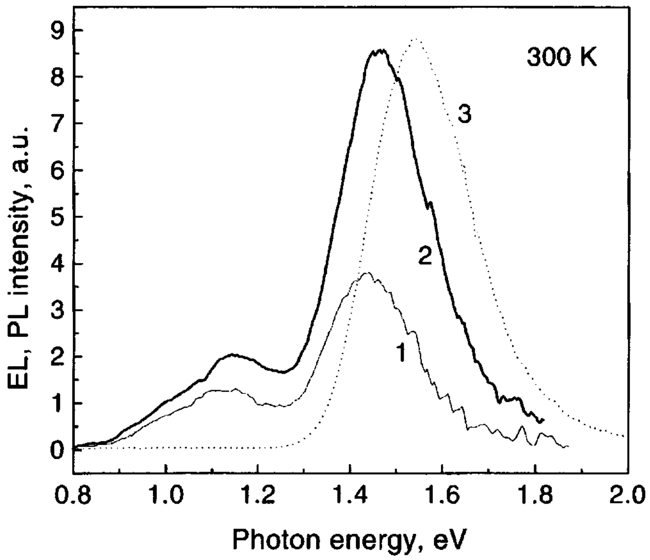

FIG. 5. EL (*1,2*) and PL (*3*) spectra of the same sample. PL excitation at $E_{\mathrm{ex}}=3.81$ eV, EL at $\tau=5$ cm. Current density in the pulse, mA/cm^2: *1*—30, *2*—40.

usually shifted toward the low-energy region compared with the position of the PL band. In accordance with the ideas advanced by Bsiesy *et al.*,[10] this shift can be explained by the small applied fields and currents in the cell. In our experiments we also observed shifts in the EL band that depend on the value of the current (see curves *1* and *2* in Fig. 5); however, they were considerably smaller than the difference between the PL and EL maxima. The wide low-energy band in the EL spectrum has a complex structure; on different samples its maxima could be located in the range from 1 to 1.2 eV. It should be noted that at this time it is difficult to decide what controls these shifts. However, the EL of a polished n-Si substrate in contact with the same electrolyte is characterized by a much weaker and narrower peak with a maximum for 1.1 eV.

MODEL

In explaining these results we assume that the position of the PL peak is determined by the size of the crystallites,[1] while the PL intensity depends significantly on the ratio of radiative and nonradiative recombination channels in the bulk and at the crystallite surface.

The appearance of quantum-well crystallites (nanocrystallites) during the etching of silicon weakens the bulk nonradiative recombination, because the number of defectless and ''undoped'' crystallites in which there are virtually no impurity atoms increases.

In addition, the degree of passivation of the porous silicon surface affects the PL intensity, where this latter depends on the composition of the etchant and the anodization conditions. It is clear from Fig. 3 that when we use an electrolyte with an increased amount of water, the PL intensity at room temperature increases severalfold. According to the data of Ref. 11, this is explained by an improvement in the passivation of the porous silicon surface due to the formation of stretched Si–O–Si bonds, whose presence in small quantities enhances the ordinary hydride passivation of porous silicon.

The shift of the primary PL peak toward lower energies is explained by the increased sizes of the nanocrystallites. This confirms our original assertion that decreasing the energy of electron-hole pairs generated by the light during anodization leads to an increase in the crystallite sizes. The number of these crystallites in this case decreases, naturally leading to a decrease in the intensity of the primary peak for both PL and EL.

We assume that the low-energy PL band of the samples under study is determined by radiative recombination in the non-quantum-size crystallites. The existence of radiative recombination in these crystallites at room temperature can be explained by fluctuations in the potential at the strongly profiled surface of the latter, leading to localization of carriers. In our case, the considerable increase in the intensity of the low-energy PL band is determined either by an increase in the number of non-quantum-size crystallites, a decrease in the porosity, or a lower level of doping of the original silicon, which allows us to assume the existence of a larger number of ''undoped'' and defectless crystallites than in porous silicon obtained on a strongly doped substrate, and also a high degree of surface passivation.

The effect of low-energy illumination, while increasing the nanocrystallite size, at the same time increases the number of non-size-quantized crystallites, which preserve the properties of bulk Si. The number of these crystallites increases not only in the porous silicon itself, which becomes practically mesoporous, but also in the macroscopic n-Si sublayer,[12] whose thickness increases with increasing absorption depth of the light used during anodization. We also note that when a longer-wavelength laser is used to excite the PL (0.441 nm in place of 0.325 nm), the intensity of the low-energy band increases more strongly than that of the high-energy band. This confirms the existence of an n-type macro-underlayer in porous silicon which contributes to the low-energy emission band.

The fact that the low-energy band is caused by radiative recombination in macrocrystallites is also confirmed by our observation of temperature maxima in the photoluminescence of this band, which differ significantly from those that are well known in the literature,[13] and also a temperature variation identical with the primary band for PL. The distinctive features of the EL are explained by analogy with the same features for the PL. The shift in the maximum of the high-energy EL band toward longer wavelengths with respect to the PL peak (Fig. 5) is attributable to the different methods for exciting luminescence. In the case of EL the nonuniformity of the crystallites leads to nonuniformity of the current distribution in the porous silicon layer; naturally, a larger current flows through the larger crystallites, causing an enhancement of the EL intensity and shifting the EL band toward longer wavelengths. The origin of the low-energy EL band is connected, as in the case of PL, with radiative recombination in macrocrystallites.

Thus, we have developed a method for preparing mesoporous silicon on n-type substrates with two intense PL and EL bands at room temperature: one in the range 1.4–1.6 eV, and a low-energy infrared band near 1–1.2 eV. We have shown that it is possible to control both the position of the primary emission maximum and the band intensity. The properties of the primary band are explained on the basis of a quantum-well model for formation of porous silicon, while the low-energy part is explained by radiative recombination in large-scale non-quantum-sized crystallites.

This work was carried out with the financial support of INTAS (grant No. 93-3325). O. M. Sreseli and A. V. Andriyanov also acknowledge with gratitude the support by the Russian Fund for Fundamental Research (Grant No. 96-02-17903), while G. Polisskiĭ and F. Koch are grateful to the BMBT.

[1] L. T. Canham, Appl. Phys. Lett. **57**, 1046 (1990).
[2] *Porous Silicon*, edited by Zhe Chuan Feng *et al.* (World Scientific, 1994).
[3] *Microcrystalline Semiconductors: Materials, Science, & Devices*, edited by P. M. Fauchet *et al.* (Pittsburgh, PA, Mater. Res. Soc. Proc., 1993) V. 283; *Silicon-Based Optoelectronic Materials*, edited by M. A. Tischler *et al.* (Pittsburgh, PA, Mater. Res. Soc. Proc., 1993) v. 289.
[4] H. Koyama and N. Koshida, J. Appl. Phys. **74**, 6365 (1993).
[5] T. Asano, K. Higa, S. Aoki, M. Tonouchi, and T. Miyasato, Jpn. J. Appl. Phys. **31**, 373 (1992).
[6] A. Nikolov, V. Petrova-Koch, G. Polisski, and F. Koch, in Nanocrystalline Semiconductors, edited by L. Brus *et al.* (Boston, USA, Mater. Res. Soc. Symp. Proc., 1994) v. 358, p. 423.
[7] C. H. Perry, F. Lu, F. Namavar, N. M. Kalkhoran, and R. A. Sofer, Appl. Phys. Lett. **60**, 3117 (1992).
[8] O. Sreseli, V. Petrova-Koch, D. Kovalev, T. Muschik, S. Hofreiter, and F. Koch, *Proc. 22th Int. Conf. on the Physics of Semiconductors* (Vancouver, Canada, 1994), edited by D. Lockwood (World Scientific, 1994) V. 3, p. 2117.
[9] V. Petrova-Koch, T. Muschik, G. Polisski, and D. Kovalev, in *Microcrystalline and Nanocrystalline Semiconductors*, edited by L. Brus *et al.* (Boston, USA, Mater. Res. Soc. Symp. Proc., 1994) V. 358, p. 483.
[10] A. Bsiesy, F. Muller, M. Ligeon, F. Gaspard, R. Herino, R. Romestain, and J. C. Vial, Phys. Rev. Lett **71**, 637 (1993).
[11] L. Tsybeskov and P. M. Fauchet, Appl. Phys. Lett. **64**, 1983 (1994).
[12] F. Kozlowsky and W. Lang, J. Appl. Phys. **72**, 5401 (1992).
[13] S. Gardelis and B. Hamiltom, J. Appl. Phys. **76**, 5327 (1994).

Translated by F. Crowne

Negative differential resistivity of a nonideal Schottky barrier based on indium arsenide

A. V. Kalameĭtsev, D. A. Romanov, A. P. Kovchavtsev, G. L. Kuryshev, K. O. Postnikov,
and I. M. Subbotin

*Institute of Semiconductor Physics, Siberian Department of the Russian Academy of Sciences, 630090
Novosibirsk, Russia*

(Submitted January 1996, accepted for publication April 4, 1996)
Fiz. Tekh. Poluprovodn. **31** 370–376 (March 1997)

The process of elastic tunneling is investigated theoretically and experimentally for MOS structures with Schottky barriers based on p^+-InAs. At liquid-helium temperatures, current-voltage characteristics are obtained with negative differential resistivity segments. Using the quasiclassical approximation, analytic expressions are obtained for the tunneling transmission coefficient with carrier conversion. It is shown that the decreasing segments of the current-voltage characteristic are connected with participation in the tunneling process of high-lying quantum-well levels in the n-channel. The calculated current-voltage characteristics are in good agreement with the results of experiment. [S1063-7826(97)02403-4]

INTRODUCTION

Metal-semiconductor and metal-thin-layer insulator-semiconductor structures with Schottky barriers are widely used to investigate tunneling phenomena. Their attractiveness is due to the relative ease with which the barrier parameters can be changed. With regard to electrical properties, structures based on InAs are particularly unusual representatives of these structures. Their peculiarities are normally connected with the fact that the Fermi level at the surface of indium arsenide is located near the edge of the conduction band, irrespective of the position in the crystal bulk.[1–4] For this reason, a n-type conductivity channel arises near the surface of InAs, which is accumulating for n-type material and inverting for p-type material. In such a structure, charge carriers are forced to tunnel through a barrier of complex shape (Fig. 1) and in the case of inversion they can convert not at the semiconductor boundary, but rather in the depletion layer. This complexity of the tunneling process is reflected in complexity of the current-voltage characteristics. Mead and Spetzer[1] reported the first observation of a segment of negative differential resistance on the current-voltage characteristics of a Schottky barrier based on gold-degenerate, p-type indium arsenide at liquid-nitrogen temperatures. Later on, analogous current-voltage characteristics were reported by Esina *et al.*[2]

So far, the existence of a decreasing section of the current-voltage characteristics has not been satisfactorily explained. Esina *et al.*[2], assumed that the reason for the negative differential resistance was the competing dependences of the tunneling transparencies through the thin dielectric barrier and through the bandgap of the semiconductor on external voltage (it is clear from Fig. 1 that the first of these transparencies decreases with increasing voltage, whereas the second increases). However, quantitative calculations showed that the effect of this competition is not always sufficient for negative differential resistance to occur. Thermally stimulated tunneling currents with participation of the conduction band, or inelastic tunneling currents with participation of phonons, can also affect the value of the negative differential resistance.

In this paper we describe a combined experimental and theoretical investigation of tunneling-induced negative differential resistivity of a Schottky barrier with an ultrathin dielectric sublayer between metal (Au) and degenerate p-InAs. Structures are used with controllable thickness of the sublayer. In order to eliminate the effect of thermally stimulated phenomena, the current-voltage characteristics were taken at liquid-helium temperature. We show that the falling portion of the current-voltage characteristic is connected with a specific quantum effect: inelastic tunneling of electrons from the metal to the valence band of the semiconductor, which is strongly affected by a higher-lying, quantum-well level in the inversion channel. Using the quasiclassical approximation, we find analytic expressions for the transmission coefficient, which are used to calculate current-voltage characteristics for specific values of the system parameters. They are in good agreement with experimental results.

1. EXPERIMENTAL RESULTS

As substrates we used polished films of p-InAs with acceptor concentrations of $(1-5)\times10^7\,\mathrm{cm}^{-3}$ and $\langle 111\rangle$ orientation. Three groups of samples were prepared. For samples of the first group, the substrates were etched in lactic acid (80% $C_3H_6O_3$ and 20% H_2O), and then washed in deionized water. After chemical processing of the substrates, gold contact pads were deposited on the surface of the crystals through a mask in a vacuum of 10^{-6} Torr with diameters of 100 μm. For samples of the second group the substrates were etched in KOH, then oxidized in a stream of dry oxygen at a temperature of 200 °C for 2 h; gold contact pads were then deposited with a thickness of 0.2 μm. In order to make ohmic contact, a solid indium coating was deposited on the nonplanar side of the substrates with a thickness of 0.5 μm. According to data from ellipsometry and tunneling spectroscopy,[5,6] an insulating film is present on the surfaces of the substrates of samples from the first and second groups, with a thickness of 20–30 Å, consisting of a mixture of

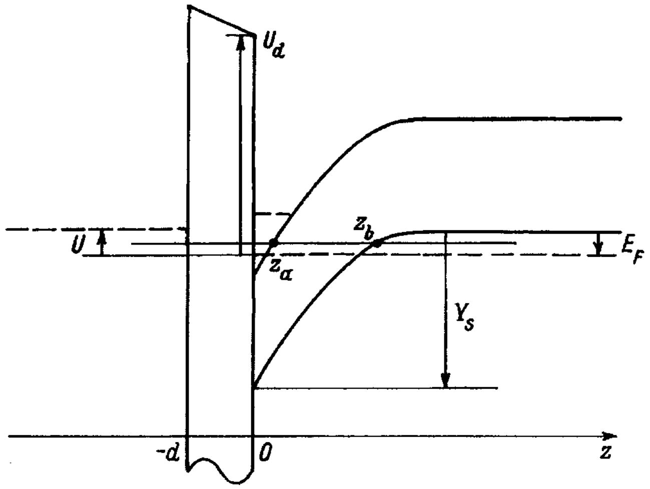

FIG. 1. Band diagram of an MOS structure with an applied external voltage U. d and U_d are the thickness of the insulating layer and height of the energy barrier in it; Y_s is the band bending.

oxides of indium and arsenic for samples of the second group and remnants of lactic acid molecules in an ultrathin insulating film for the first group. Samples of the first and second groups acted like nonideal Schottky barriers with a sublayer, or metal-insulator-semiconductor structures with an ultrathin insulating layer.

The current-voltage characteristics were measured at a temperature of 4.2 K, using a sawtooth voltage signal with a ramp rate of 4 mV/s. In this case, the forward and reverse current-voltage characteristic plots exhibited no hysteresis phenomena. Figure 2 shows the measured current-voltage characteristic for a sample from the second group. A region of negative differential resistance is clearly evident. Current-voltage characteristics from a sample of the first group also have well-marked regions of negative differential resistance, but they differ somewhat with regard to the magnitude of the current. Samples from a third group were prepared in an ultrahigh vacuum using a Riber 250 setup. Before being placed in the chamber, the samples were processed in a mixture of hydrochloric acid and isopropyl alcohol. In an ultrahigh vacuum the surface of the indium arsenide film was cleaned by heating to a temperature of 200 °C until atomic cleanness was achieved.[7] On the InAs surface that was cleaned of its oxide, platinum contacts were deposited using an electron beam through a mask with diameter 100 μm. According to data on tunneling spectroscopy,[8] there was no ultrafine insulating film on the substrate surface and the semiconductor structure was close to an ideal Schottky barrier. There were no regions of negative differential resistance on the current-voltage characteristics of these semiconductor structures from the third group; rather, the current-voltage characteristics were close to calculated ones (in calculating the current-voltage characteristics, the thickness of the insulating layer was assumed to equal zero).

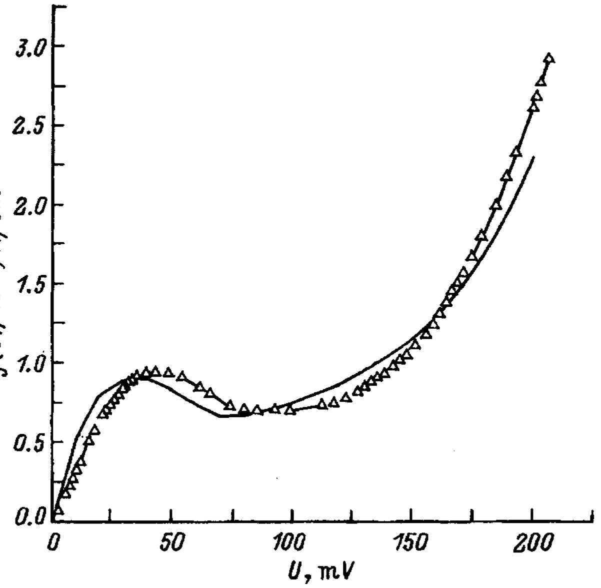

FIG. 2. Current-voltage characteristics in a model with constant built-in charge. The solid curve is theoretical. $d=11.2$ Å, $Y_s=0.49$ eV, $\varepsilon_d=10$ (dielectric constant).

2. THEORETICAL DISCUSSION

1. *Model*. The ultimate goal of our investigation was to obtain the dependence of the elastic tunneling current on the voltage across the MOS structure and to compare this function with experimental current-voltage characteristics. In this case the main difficulty was finding the transmission coefficient for charge carriers through the metal to the valence band of the semiconductor.

The situation we are discussing is one of broad theoretical interest, e.g., for tunneling of carriers through multilayer structures in one of whose layers the carriers can be converted. Actually, the results of the classical paper[9] were directed toward finding the coefficient of interband tunneling in an electric field in the bulk of a sample. However, one of these quantities turns out to be clearly insufficient to describe the process of coherent transport in a layered system. On the other hand, contemporary papers that treat tunneling through layered structures (see, e.g., Ref. 10) are limited to situations where conversion of the carriers takes place at the layer boundary and is taken into account with the help of phenomenological boundary conditions. The approach we will propose here fills in the gap between these limiting cases. It is based on a quasiclassical variant of the transfer-matrix method and can serve as a basis for investigating more complicated tunneling structures with ‘‘conversion’’ layers.

The band diagram of the structure under discussion is shown in Fig. 1. When a doping level of $\sim 2\times 10^{17}$ cm^{-3} is used, the thickness of the depletion layer is $\sim 6.2\times 10^{-6}$ cm. Calculations show that the quantum-well level in the inversion channel of the n-band is located within the bandgap of bulk InAs and lies close to the edge of the valence band in the latter. This position of the state, as we will show below, gives rise to the distinctive features in the transmission coefficient and, accordingly, in the current-voltage characteristics.

The relative smoothness of the depletion layer potential and the large thickness of the interband barrier allows us to remain within the framework of the Dirac model in describing the motion of carriers in the semiconductor, i.e., we disregard the exponentially small contribution of heavy holes to the interband tunneling.[11] The four-component carrier wave function Ψ is determined from the equation

$$\hat{H}\boldsymbol{\Psi}=E\boldsymbol{\Psi} \tag{1}$$

with the matrix Hamiltonian

$$H=\begin{pmatrix} \epsilon_0+V(z) & v\,\hat{\boldsymbol{\sigma}}\hat{\boldsymbol{p}} \\ v\,\hat{\boldsymbol{\sigma}}\hat{\boldsymbol{p}} & -\epsilon_0+V(z) \end{pmatrix} \tag{2}$$

where $\hat{\boldsymbol{p}}$ is the momentum operator, σ_i is a Pauli matrix, v is the interband velocity matrix element, and ϵ_0 is the half-width of the band gap.

On the other hand, the smoothness of the potential $V(z)$ makes it possible to use the quasiclassical approximation in (1). The quasiclassical wave functions obtained in the appendix essentially recall the quasiclassical solution to the Schrödinger equation.[12] In particular, the form of the exponent turns out to be $\int p_z(z)dz$, where p_z is found from the dispersion relation in the corresponding semiconductor band.

2. *Transmission coefficient*. In order to derive a transmission coefficient based on the quasiclassical wave functions found in the appendix, we will reason by analogy with well-known transfer-matrix methods.[9] In each of the classically accessible regions (within the metal and semiconductor, and also in the surface inverted region of the latter), the wave function consists of a sum of two oscillating terms corresponding to oppositely directed currents. In the classically bandgap regions (the insulating layer and the band gap of the semiconductor), the wave functions are growing and decaying exponentials. We will find 2×2 matrices that connect pairs of coefficients for these fundamental solutions on different sides of the classical turning point between each neighboring pairs from the regions listed above. Let us specify that in the vector of coefficients the upper element will correspond to the amplitude of a wave carrying a current from left to right, or to the coefficient of a growing exponential.

For definiteness let us begin the discussion with the turning point at the boundary of the band gap and the valence band of the semiconductor z_b. According to the appendix, the two-component wave functions on the right and left of this point are written in the form

$$\begin{aligned}\tilde{\boldsymbol{\Psi}}_c(z_b,z)&=\frac{A}{\sqrt{|p_z|}}\,\tilde{\boldsymbol{\Phi}}_{c+}e^{i/\hbar\int_{z_b}^{z}|p_z|dz}\\&\quad+\frac{B}{\sqrt{|p_z|}}\,\tilde{\boldsymbol{\Phi}}_{c-}e^{-i/\hbar\int_{z_b}^{z}|p_z|dz},\qquad z>z_b,\\ \tilde{\boldsymbol{\Psi}}_b(z_b,z)&=\frac{C}{\sqrt{|p_z|}}\,\tilde{\boldsymbol{\Phi}}_{b+}e^{1/\hbar\int_{z_b}^{z}|p_z|dz}\\&\quad+\frac{D}{\sqrt{|p_z|}}\,\tilde{\boldsymbol{\Phi}}_{b-}e^{-1/\hbar\int_{z_b}^{z}|p_z|dz},\qquad z<z_b.\end{aligned} \tag{3}$$

The connection between vectors (C,D) and (A,B) is obtained by using a circuit around the turning point $(p_z=0)$ in the complex z plane. It can be shown that on the basis of our model, and for our choice of the functions $\tilde{\boldsymbol{\Phi}}$, the connection matrix is the same as in the case of the Schrödinger equation:[13]

$$\begin{pmatrix} C \\ D \end{pmatrix}=\begin{pmatrix} \frac{1}{2}e^{\pi i/4} & \frac{1}{2}\,e^{-\pi i/4} \\ -ie^{-\pi i/4} & ie^{-\pi i/4} \end{pmatrix}\begin{pmatrix} A \\ B \end{pmatrix}. \tag{4}$$

In an analogous fashion, if we consider a turning point at the boundary between the conduction band and the band gap z_a, we find the connection matrix between vectors of coefficients in the functions $\tilde{\boldsymbol{\Phi}}_a(z_a,z)$ and $\tilde{\boldsymbol{\Phi}}_b(z_a,z)$:

$$\begin{pmatrix} \frac{1}{2i}\,e^{\pi i/4} & e^{\pi i/4} \\ -\frac{1}{2i}\,e^{-\pi i/4} & e^{-\pi i/4} \end{pmatrix}. \tag{5}$$

Note that in deriving (4) and (5) the wave functions in the same region of the band gap were written in different forms. The connection between $\tilde{\boldsymbol{\Phi}}_a(z_a,z)$ and $\tilde{\boldsymbol{\Phi}}_b(z_a,z)$ is obviously given by the trivial diagonal matrix

$$\begin{pmatrix} e^{-1/\hbar\int_{z_a}^{z_b}|p_z|dz} & 0 & \\ 0 & e^{1/\hbar\int_{z_a}^{z_b}|p_z|dz} & 0 \end{pmatrix}. \tag{6}$$

Analogous matrices with obvious replacements at the limits of integration are obtained for the regions within the insulating barrier, and with replacement of $|p_z|$ by $i|p_z|$ for the classically accessible regions in the inversion channel.

It remains for us to obtain the connection matrix for the boundaries. In general, at the boundary of an insulator and a semiconductor we must establish boundary conditions that connect the single-component wave function in the insulator with a two-component wave function in the semiconductor. However, since under the conditions of our problem an electron at $z=0$ has an energy close to the conduction band edge, $|\Psi_2|\ll|\Psi_1|$ and the pre-exponential factor is $\sim 1/\sqrt{p}$. We therefore have the same matching conditions for single-component wave functions at a sharp boundary as those at the boundary between metal and insulator: equality of the quasiclassical wave functions on the right and left of the boundary and equality of their first derivatives normalized by the corresponding masses. Simple calculations give the required connection matrix for the metal-insulator and insulator-semiconductor boundaries in the form

$$\begin{pmatrix} \alpha & \alpha^* \\ \alpha^* & \alpha \end{pmatrix};\quad \begin{pmatrix} \beta & \beta^* \\ \beta^* & \beta \end{pmatrix};$$

$$\begin{aligned}\alpha&=\frac{1}{2}\left(\sqrt{\frac{p_m}{p_d}}-i\,\frac{m_m}{m_d}\,\sqrt{\frac{p_d}{p_m}}\right),\\ \beta&=\frac{1}{2}\left(\sqrt{\frac{p_d}{p_s}}+i\,\frac{m_d}{m_m}\,\sqrt{\frac{p_s}{p_d}}\right),\end{aligned} \tag{7}$$

where p_m,p_d, and p_s are wave vectors in the metal, the insulator, and the semiconductor, and m_m,m_d, and m_s are the corresponding effective masses.

The resulting transport mass

$$\begin{pmatrix} a_{11} & a_{12} \\ a_{21} & a_{22} \end{pmatrix}, \tag{8}$$

which connects the coefficients for plane electron waves in the metal and valence band of the semiconductor, is a product of the matrices listed above, multiplying from left to right in the sequence corresponding to Fig. 1.

Let us now find the transmission coefficient for a charge carrier from the metal to the valence band of the semiconductor. For this formulation of the problem the vector (A,B) in the valence band should be located at $(1,0)$, i.e., only a transmitted wave should be present. Multiplying this vector by the resulting transfer matrix, we obtain the value of the coefficients for incident and reflected waves in the metal. The coefficient for transmission through the structure is defined as the ratio of the fluxes of the transmitted and incident waves. In the case where the energy of an electron passing through the valence band turns out to be close to the top of the latter, this coefficient is

$$D=\frac{m_m}{m_s}\frac{1}{|a_{11}|^2}. \tag{9}$$

Using the matrices obtained above, we can find explicit analytic expressions for the transmission coefficient. In particular, if the energy of an electron lies above the bottom of the surface inversion channel,

$$\begin{aligned} D^{-1}=2|\alpha\beta|^2(&\cosh I(A,b)\cosh I(-d,0) \\ &+\sinh I(a,b)\sin I(0,a)\cos\varphi_\alpha+\sinh I(a,b) \\ &\times(\cosh I(-d,0)\sin I(0,\alpha)\cos\varphi_\beta+\sinh I(-d,0) \\ &\times\cos I(0,a)\sin\varphi_\beta)+\cosh I(a,b)\cos\varphi_\alpha\cos\varphi_\beta \\ &-\sin\varphi_\alpha\sin\varphi_\beta), \end{aligned}$$

where

$$I(z_l,z_r)=\frac{1}{\hbar}\int_{z_l}^{z_r}p_z(z)dz, \tag{10}$$

z_l and z_r give the limits of integration and are denoted in the figure, and α and β are defined in (7).

3. *Expression for the tunneling current.* In order to calculate the current-voltage characteristics we use the standard expression for the dependence of the elastic tunneling current density on the difference in potentials at the boundary of the tunneling structure:[9]

$$j(U)=\frac{2|e|}{h^3}\int D(E,p_\parallel)[f(E+U)-f(E)]dEd^2p_\parallel, \tag{11}$$

where $f(E)$ and $f(E+U)$ are Fermi distribution functions (which for liquid-helium temperatures and the values of U which we used in our experiments can be replaced by step functions); $p_\parallel$ is the longitudinal component of an electron's momentum; and $D(E,p_\parallel)$ is the transmission of an electron through the MOS structure.

Because the spectrum of charge carriers in the metal is described by a parabolic dispersion relation, it is convenient to transform (11) from an integration over the total energy and longitudinal momentum to an integration over the two terms of the total energy in the metal connected with the transverse and longitudinal motion. After some simple transformations we obtain

$$j(U)=\frac{2\pi|e|m}{h^3}\int D(E_\perp,E_\parallel)[f(E+U)-f(E)]dE_\perp dE_\parallel, \tag{12}$$

where $E_\perp$ and $E_\parallel$ are the transverse and longitudinal energies in the metal $(E=E_\perp+E_\parallel)$. The limits of integration are determined by the Fermi level in the metal and the semiconductor and the edges of the band gap in the semiconductor. The dependence of the transmission coefficient on the component of the wave vector along the boundary, i.e., on $E_\parallel$, plays an important role in our subsequent calculations.

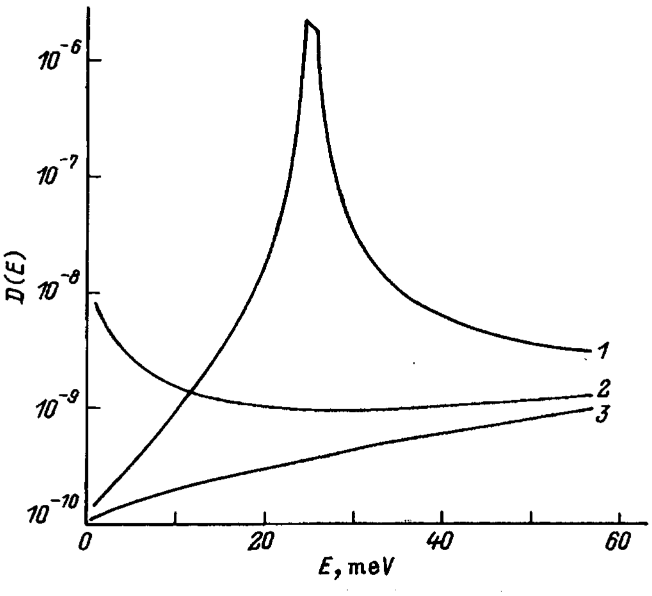

FIG. 3. Transmission coefficient $D(E)$ for various band bendings: $Y_s=0.49$ eV (*1*), 0.46 eV (*2*), 0.43 eV (*3*). The insulator parameters correspond to Fig. 2.

3. RESULTS OF NUMERICAL CALCULATIONS AND DISCUSSION

1. *Transmission coefficient.* Figure 3 shows the dependence of the transmission coefficient on the energy obtained in the previous section. The parameters of the structure corresponding to an actual experiment are shown in the insets to the figure. Different curves correspond to different values of the surface band bending in the semiconductor, while the remaining parameters are fixed.

Using curve *1,* we illustrate a case in which the quantum-well level in the inversion channel is set against the background of the bulk valence band of the semiconductor. The peak in transmission coefficient exactly corresponds to resonant tunneling through this quasistationary level. For smaller values of the band bending (curve *2*) the surface level ''looks into'' the band gap of the semiconductor. Nevertheless, the transmission coefficient increases considerably near the top of the valence band, because the tunneling near the threshold for transmission is suppressed in an energy region that is considerably narrower than the width of the tail of the resonance peak. Further reduction in the band bending involves driving the level into the interior of the band gap, which eliminates its influence on the transmission (curve *3*).

Estimates show that in our experiments the sample parameters correspond to the case illustrated by curve *2*. Therefore, in what follows distinctive features of the computed current-voltage characteristics are associated with tunneling of carriers through the tail of the resonance level.

2. *Current-voltage characteristics*. For the numerical calculation of current-voltage characteristics based on (12) the following two circumstances are important.

First of all, inclusion of the dependence of the transmission coefficient on the longitudinal wave vector (which along with the energy is conserved during an elastic tunneling process). According to Eq. (A7), allowing for the longitudinal momentum of an electron leads to an effective increase in the width of the band gap. This causes a strong dependence of the transmission on the longitudinal wave vector of the carrier.

Secondly, at doping levels of $\sim 10^{17}-10^{18}$ cm^{-3} for the semiconductor the impurity level is washed out into an impurity band and merges with the valence band.[14] We include this effect semiqualitatively by effectively shifting the top of the valence band by the width of the impurity band, i.e., by ~ 50 meV.

The shape of the potential in the depletion layer of the semiconductor is assumed to be quadratic, i.e., created only by charged acceptors. There are no electrons in the inversion channel because the quantum-well level is located above the Fermi level and at low temperatures is unoccupied. The potential drop across the insulator and the semiconductor is determined by the Poisson equation and the condition that the total charge of the MOS structure be zero, taking into account surface-state charges.

The results of our numerical calculations and comparison with experimental data for two different cases are shown in Figs. 2 and 4. The broad peak in the current-voltage characteristic is connected with the close-to-resonant tunneling described earlier as follows. On the initial voltage segment the tunneling current increases for two reasons. The first reason is trivial: as the difference between the Fermi levels of the metal and semiconductor increases, the number of accessible final states for the tunneling carriers increases. The second reason is more specific: the increase in voltage across the structure leads to a flattening of the surface band bending, i.e., a decrease in the electric field intensity in the inversion channel. As a result, the Fermi level in the metal approaches the quantum-well level, which leads to a considerable increase in the tunneling through the near-resonance tail.

A decrease in current takes place when the Fermi level of the metal reaches the top of the semiconductor valence band, after which the number of electrons that participate in the tunneling no longer increases. In this case, the size-quantized level continues to be repelled into the depth of the band gap and withdraws further from the energy gap in which the tunneling takes place. The resulting decrease in tunneling through the near-resonance tail also leads to the fall-off in the current-voltage characteristics. Any further increase in the voltage causes the current to increase, but only until the bottom of the conduction band at the boundary of the semiconductor and insulator is above the top of the valence band in the semiconductor bulk. The reason for this increase in the current is the obvious decrease in transparency of the tunnel barrier connected with the band gap of the semiconductor.

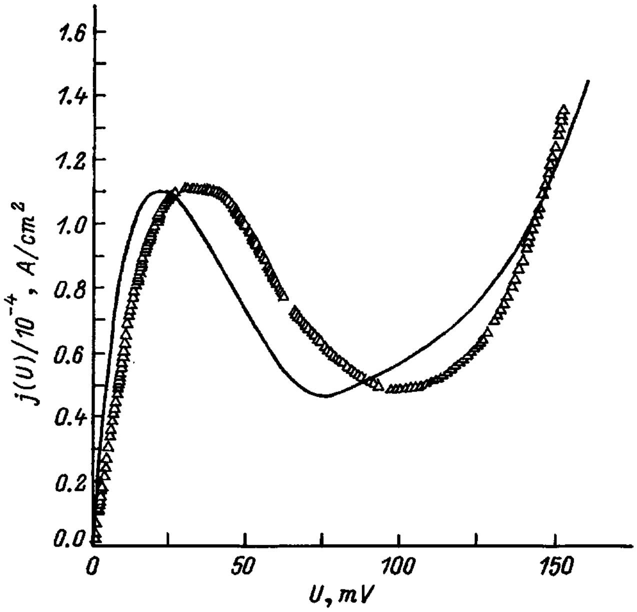

FIG. 4. Current-voltage characteristics in a model with pinned bands. The solid curve is theory. $d=11.6$ Å, $Y_s=0.51$ eV.

The fitting parameters of the insulating layer, for which we in obtained good agreement between experimental and theoretical curves, are listed in the figure captions. Note that the curves in Figs. 2 and 4 are successfully matched for considerably different assumptions about the character of occupation of surface states at the semiconductor-insulator boundary. Figure 2 corresponds to the assumption that all the surface states are empty, which is equivalent to a constant built-in charge at the boundary. Figure 4 corresponds to the assumption that the value of the surface-state density is high; in this case their occupation is determined by the Fermi level in the metal. This implies that all the voltage applied to the structure is dropped entirely within the space-charge region.

It is clear that the results of numerical calculations using these expressions give good agreement with the experimental data. However, there are several discrepancies between theory and experiment: the rather small shift (~ 10 meV) in the position of the current maximum and the somewhat more rapid increase in the experimental curves compared to the theoretical as the voltage increases. This disagreement may be connected with several simplifications and assumptions made in our model. First of all, incorrect use of the quasiclassical principle in narrow regions of energy close to the top of the valence band ($\sim 5-10$ meV). Secondly, the potential profile in the space-charge region, which was chosen to be quadratic, corresponds to the potential created by a uniform distribution of charged acceptors. However, in the real situation we should take into account the nonuniformity of the doping in the skin layer and the influence of the degenerate hole gas on the shape of the potential near the space-charge region's edge. These inadequacies, however, should not affect the qualitative picture of the effect and can be taken into account in a more detailed model.

In this paper we have described theoretical and experimental investigations of the effects of negative differential resistance for MOS structures based on p^+-InAs. Current-voltage characteristics were obtained at liquid-helium temperatures for samples with differing thicknesses of the insulating sublayer. Theoretical dependences of the magnitude of the tunneling current on the structure parameters were calculated using a quasiclassical analog of the transfer matrix method. The presence of a falling portion of the current-voltage characteristics is explained by peculiarities of tunneling through a near-resonant tail of the quantum-well level lying outside the energy region of interest. Theoretical curves are in good agreement with the experimental ones.

We wish to thank E. M. Baskin and M. V. Entin for useful discussions. This work was carried out with the partial support of the Russian Fund for Fundamental Research (Grant No. 96-02-19028) and a Grant from the Russian University No. 95-0-7.2-151.

APPENDIX

Let us find the quasiclassical wave functions for Eq. (1) with the Hamiltonian (2). In our problem the potential depends only on z, which allows us to reduce the number of components of the spinor wave function $\boldsymbol{\Psi}$. Following Ref. 15, we look for a solution to the Dirac equation in the form $\boldsymbol{\Psi}(z)\exp(i/\hbar)\mathbf{pr}$, where $\mathbf{p}$ is the component of momentum in the (x,y) plane. A unitary transformation

$$U=\frac{1}{\sqrt{2}}\begin{pmatrix} \hat{I}+i\,\dfrac{\hat{\boldsymbol{\sigma}}\mathbf{p}}{p} & 0 \\ 0 & \hat{I}+i\,\dfrac{\hat{\boldsymbol{\sigma}}\mathbf{p}}{p} \end{pmatrix} \tag{A1}$$

transforms the Hamiltonian (2) to the form

$$\hat{H}=\begin{pmatrix} \epsilon_0+V(z) & v(\hat{\sigma}_z\hat{p}_z+ivp) \\ v(\hat{\sigma}_z\hat{p}_z-ivp) & \epsilon_0+V(z) \end{pmatrix}, \tag{A2}$$

which obviously commutes with the projection of the spin onto the $z\hat{\sigma}_z$ axis. Consequently, as eigenfunctions of (A2) we may choose eigenfunctions of the operator $\hat{\sigma}_z$. They consist of spinors $\boldsymbol{\Psi}=(\boldsymbol{\Psi}_1,0,\Psi_2,0)$ for the eigenvalue $\sigma_z=+1$ and $\boldsymbol{\Psi}=(0,\Psi_1,0,\Psi_2)$ for $\sigma_z=-1$. Thus, the problem reduces to finding a two-component wave function $\tilde{\boldsymbol{\Psi}}=(\Psi_1,\Psi_2)$. Turning to the sum and difference of components $f_1=\Psi_1+\Psi_2$ and $f_2=\Psi_1-\Psi_2$, we obtain the system of equations

$$\begin{aligned} &(V(z)-E+\sigma_z v\hat{p}_z)f_1+(\epsilon_0-ivp)f_2=0, \\ &(\epsilon_0+ivp)f_1+(V(z)-E-\sigma_z v\hat{p}_z)f_2=0. \end{aligned} \tag{A3}$$

In order to construct quasiclassical wave functions we transform from (A3) to separate second-order differential equations for the functions f_1 and f_2. Expressing one function in terms of the other, we obtain

$$v^2\hbar^2\,\frac{d^2 f_k}{dz^2}+\left((-1)^{k-1}\sigma_z v\hbar\,\frac{dV}{dz}+(E-V)^2 -(\epsilon_0')^2\right)f_k=0, \tag{A4}$$

where $(\epsilon_0')^2=\epsilon_0^2+(vp)^2$. Applying to (A4) the standard WKB approximation

$$f_k=C_k\exp\left(\frac{i}{v\hbar}\left(S_{k0}+\frac{v\hbar}{i}\,S_{k1}+\dots\right)\right), \tag{A5}$$

we obtain the equations for S_{k0} and S_{k1}

$$\begin{aligned} &-\left(\frac{dS_{k0}}{dz}\right)^2+(E-V(z))^2-(\epsilon_0')^2=0, \\ &\frac{d^2S_{k0}}{dz^2}+2\,\frac{dS_{k0}}{dz}\,\frac{dS_{k1}}{dz}+(-1)^{k-1}\sigma_z\,\frac{dV}{dz}=0. \end{aligned} \tag{A6}$$

Substituting these solutions (A5) into the original system (A3), we obtain the relation between the constants C_k.

The resulting quasiclassical wave functions are

$$\begin{aligned} &a)\tilde{\boldsymbol{\Psi}}_{a\delta}=\frac{C}{\sqrt{|p_z|}}\,\boldsymbol{\Phi}(|p_z|)e^{i/\hbar\,\delta\int|p_z|dz'}, \\ &b)\tilde{\boldsymbol{\Psi}}_{b\delta}=\frac{C}{\sqrt{|p_z|}}\,\boldsymbol{\Phi}(-i|p_z|)e^{i/\hbar\,\delta\int|p_z|dz'}, \\ &c)\tilde{\boldsymbol{\Psi}}_{c\delta}=\frac{C}{\sqrt{|p_z|}}\,\boldsymbol{\Phi}(-|p_z|)e^{-\,i/\hbar\,\delta\int|p_z|dz'}, \\ &\boldsymbol{\Phi}(|p_z|)=\frac{\alpha^{-(\sigma_z\delta)/2}}{2\sqrt{\epsilon_0(E-V+|p_z|)}} \\ &\qquad\times\begin{pmatrix} E-V+v|p_z|+(\epsilon_0+i\sigma_z\delta vp) \\ \sigma_z\delta(E-V+v|p_z|-(\epsilon_0+i\sigma_z\delta vp)) \end{pmatrix}, \end{aligned} \tag{A7}$$

where $p_z^2=((E-V)^2-(\epsilon_0')^2)/v$, and $\alpha=\epsilon_0'/(\epsilon_0-ivp)$. The value of $\delta=\pm1$ determines two linearly independent solutions corresponding to waves propagating in opposite directions. a), b), c) are solutions in the conduction band, the band gap, and the valence band, respectively. The constants are chosen in such a way that the wave functions $\tilde{\boldsymbol{\Psi}}_{n\delta}$ transform one into the other (up to a phase factor) as a result of passing around the turning point in the complex z plane.

[1] C. A. Mead and W. G. Spetzer, Phys. Rev. Lett. **10**, 471 (1963).

[2] N. P. Esina, N. V. Zotova, S. A. Karandyshev, and G. M. Filaretova, Fiz. Tekh. Poluprovodn. **17**, 991 (1983) [Sov. Phys. Semicond. **17**, 624 (1983)].

[3] M. F. Millea and A. H. Silver, J. Vac. Sci. Techn. **15**, 1362 (1972).

[4] D. C. Tsui, Phys. Rev. B **4**, 4438 (1971).

[5] A. P. Kovchavtsev, G. L. Kuryshev, K. O. Postnikov, and S. A. Biryuchkov, Fiz. Tekh. Poluprovodn. **19**, 2187 (1985) [Sov. Phys. Semicond. **19**, 1348 (1985)].

[6] A. P. Kovchavtsev, G. L. Kurishev, and K. O. Postnikov, Phys. Status Solidi **97**, 421 (1986).

[7] Yu. G. Galitskiĭ, Surface **5**, 108 (1992) [in Russian].

[8] L. S. Braginsky, E. M. Baskin, A. P. Kovchavtsev, G. L. Kuryshev, K. O. Postnikov, and I. M. Subbotin, Phys. Rev. B **52**, 17 718 (1995).

[9] *Tunnelling Phenomena in Solids*, E. Burstein and S. Lundqvist, Eds., p. 424 (Russ. trans., Mir, Moscow, 1973).

[10] V. Ryshii and A. Zhakharova, Semicond. Sci. Technol. **8**, 377 (1993).

[11] O. E. Kane, J. Phys. Chem. Sol. **12**, 181 (1959).

[12] L. D. Landau and E. M. Lifshits, *Quantum Mechanics*, (Nauka, Moscow, 1989) p. 768.

[13] D. Bohm, *Quantum Theory*, (GIFML, Moscow, 1961) p. 728.

[14] W. Baltensperger, Phil. Mag. **44**, 1355 (1953).

[15] M. de Dios Leyva, R. P. Alvarez, and J. L. Gondar, Phys. Status Solidi B **125**, 221 (1984).

Translated by F. Crowne

Luminescence of copper-aluminum diselenide

V. A. Savchuk, B. V. Korzun, N. A. Sobolev, and L. A. Makovetskaya

Institute of Solid State Physics and Semiconductors, Belarus Academy of Sciences, 220072 Minsk, Belarus

(Submitted December 1, 1995)
Fiz. Tekh. Poluprovodn. **31**, 377–380 (March 1997)

The results of a multifaceted investigation of the luminescence properties of single crystals of copper-aluminum diselenide $CuAlSe_2$ are presented. The luminescence spectrum of undoped single crystals of this compound with homogeneous composition was found to have a complex structure. The luminescence properties were modified by annealing the compound in various atmospheres. The nature of the radiative transitions in this semiconductor was analyzed.

The I–II–VI_2 ternary semiconductor compounds, which crystallize in the chalcopyrite structure, are of enormous interest as potential base materials for use in fabricating devices for the transfer and processing of information, solar energy, and optoelectronics. Copper-aluminum diselenide $CuAlSe_2$, whose optical activity has already been exploited to make narrow-band, light-controlled, optical filters[1] and other devices for controlling light by light in the picosecond regime,[2] exhibits an intense luminescence in the visible region of the spectrum.[3] Because of its rather wide band gap (the width $E_g = 2.67$ eV at room temperature[4]), this material can be used to make light-emitting structures in the blue-green region of the spectrum. However, because it is technologically difficult to obtain high-quality optically uniform single crystals, data on the optical properties of this compound is extremely fragmentary in the literature. In this paper we present the results of a multifaceted investigation of cathodo- and photoluminescence of $CuAlSe_2$.

The crystals which we studied were grown by the method of chemical transport reactions (CTR) using iodine as the transporter from elementary copper, aluminum, and selenium, taken in the ratios 1.1:0.9:1.9, since the region of homogeneity for the compound $CuAlSe_2$ is displaced from the quasibinary line compound Cu_2Se–Al_2Se_3 toward the composition Cu_2Se, and corresponds to the composition $Cu_{1.1}Al_{0.9}Se_{1.9}$.[5] X-ray-phase analysis shows that the crystal structure of the samples is a chalcopyrite lattice with parameters $a = 5.597$ Å, $c = 10.98$ Å, and $c/a = 1.96$. Lamellar samples, which were yellow in color with dimensions $5 \times 5 \times 1$ mm^3, were subjected to annealing in various atmospheres (Zn, Cd, Cd+Al) at temperatures 873 to 923 K for 15 to 20 h. The vacuum anneal takes place at temperatures 773 to 973 K for 12 to 24 h. Shutters for the doping components were designed so as to create saturated vapor pressures only at the initial stage of the process, which eliminates the possibility of formation of secondary phases of type II–VI based on them. All the samples, both the original ones and those subjected to thermal processing, had p-type conductivity. Cathodoluminescence (CL) spectra were recorded at a sample temperature $T = 77$ K. The luminescence was excited by an electron beam with energy 35 eV and a maximum excitation level of up to 15 W/mm^2. In order to prevent local heating by the electron beam, the samples were enclosed in indium, with an aperture of area 0.5×0.1 mm^2 exposing a single facet as the emitting surface. The excitation power density L used to create the cathodoluminescence could be decreased by defocusing the electron beam; the ratio of maximum to minimum excitation power density was $L_{max}/L_{min} = 10^3$. The spectral resolution did not exceed ± 0.2 nm. The luminescence was uniform over the entire volume of the doped samples. Stationary photoluminescence (PL) was excited at $T = 4.2$ K from those fractions normal to the most developed and perfect natural facet (112) of the sample by light from an argon laser (photon energy $E_{ex} = 2.54$ eV) or an ultraviolet xenon high-pressure lamp combined with a UFS-2 filter with a transmission maximum at 330 nm; the emission was analyzed with a grating monochromator and recorded by a cooled photomultiplier with a type-S-1 photocathode. The spectral resolution was 0.25–1.0 eV. The excitation power density L could be decreased by using neutral optical filters such that $L_{max}/L_{min} = 2 \times 10^3$.

Typical cathodoluminescence spectra of unannealed single crystals of copper-aluminum diselenide with uniform composition at $T = 77$ K show a broad orange peak A with half-width $\Delta E = 0.35$ eV and a maximum at 1.94 eV (Fig. 1, curve *1*). In the high-energy tail of the band A there is a band B_1 with a maximum at 2.07 eV. As the level of excitation of cathodoluminescence decreases, the band A broadens, decreases in intensity, and separates into two bands with maxima at 1.91 and 1.96 eV (Fig. 1, inset). The position of band B_1 does not change in this case.

Annealing of the single crystals in the presence of the group II elements of the periodic table Zn, Cd, or Cd+Al leads to a significant transformation of the spectrum. The dominating feature in the spectrum becomes band C (Fig. 1, curves *2–4*); the position of its maximum is determined by the type of alloy formed, while the intensity of the orange band A decreases by a factor of 10^2–10^4, or is not even detectible (for Cd+Al). In this case the color of the visible luminescent emission changes from yellow for Cd+Al to green for Cd and sky-blue for Zn. The intensity of cathodoluminescence is significantly weakened by thermal processing of crystals of this compound in vacuum: processing reveals a broad ($\Delta E \simeq 0.5$ eV), washed-out red peak, whose wings overlap the entire visible range, while the intensity is

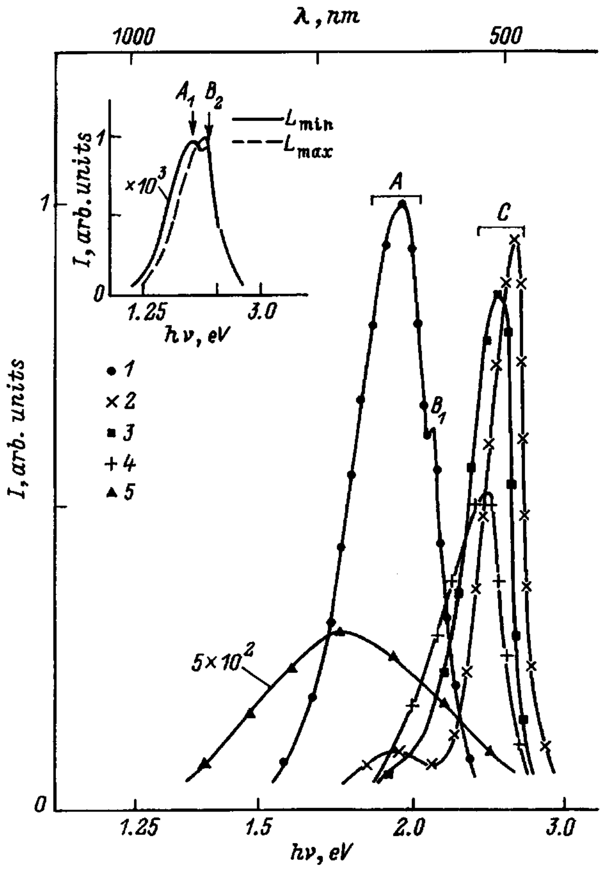

FIG. 1. Cathodoluminescence spectra of single crystals of $CuAlSe_2$ grown by CTR (*1*) and annealed in the presence of zinc (*2*), cadmium (*3*), cadmium plus aluminum (*4*), and vacuum (*5*). $T = 77$ K. Spectral positions of maxima, eV: *1*—1.94 (*A*), 2.07 (B_1); *2*—1.94 (*A*), 2.58 (*C*); *3*—1.94 (*A*), 2.445 (*C*); *4*—2.34 (*C*); *5*—1.65–1.75 (*A*). The inset shows the dependence of the structure of the band *A* on excitation power density.

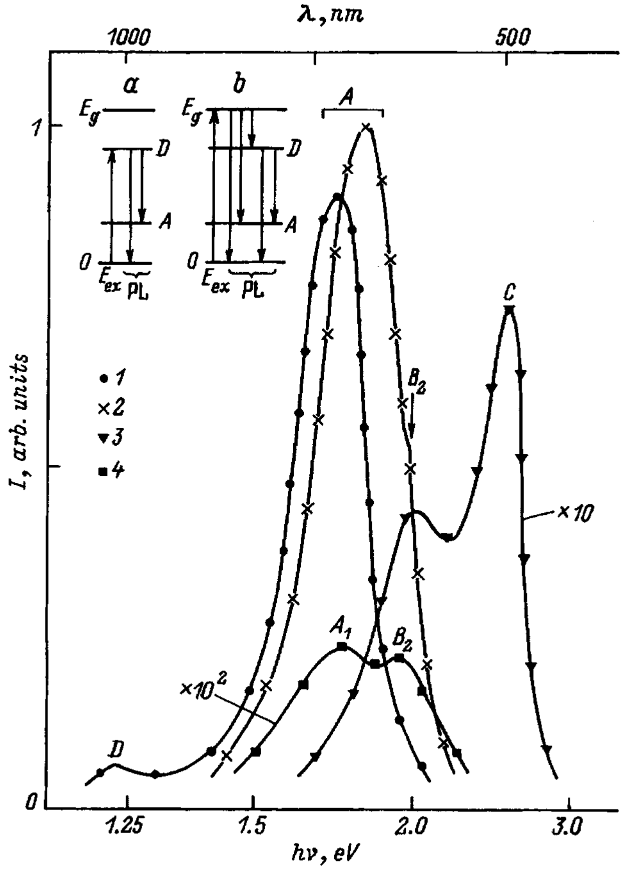

FIG. 2. Spectral dependence of the photoluminescence (PL) of single crystals of $Cu_{1.1}Al_{0.9}Se_{1.9}$—undoped (*1,2*), annealed in the presence of zinc (*3*) and for decreased power density (*4*). $T = 4.2$ K. Excitation energy E_{ex}, eV: *1*—2.54, *2*–*4*—3.76. Spectral positions of maxima, eV: *1*—1.74 (*A*), 1.24 (*D*); *2*—1.81 (*A*), 1.97 (B_2); *3*—1.96 (*A*), 2.53 (*C*); *4*—1.76 (*A*), 1.97 (B_2). The inset shows the energy diagram for transitions with photon excitation energies $E_{ex}<E_g$ (*a*) and $E_{ex}>E_g$ (*b*).

decreased by a factor of $\sim 10^3$ compared with undoped samples (Fig. 1, curve *5*). The position of the band maximum depends on the thermal processing conditions: increasing the working volume of the cell in which the annealing takes place, and shifting the temperature and duration of the anneal, shift the maximum toward lower energies until the luminescence is entirely quenched.

Figure 2 shows PL spectra of single crystals of copper-aluminum diselenide with uniform composition at a temperature 4.2 K. It is clear from the figure that the magnitude of the energy of the excitation photons E_{ex} affects the position of the primary band *A*: as E_{ex} increases, the maximum shifts to higher energies of the spectrum (Fig. 2, curves *1,2*). The position of the maximum also depends on the PL excitation density. In the PL spectra of samples annealed in the presence of zinc, excitation from a xenon lamp leads to two bands, *A* (1.96 eV) and *C* (2.53 eV), with an intensity ratio $I_A : I_C = 1:2$.

Analysis of the spectra shown in these figures indicates that the same recombination mechanisms operate in these compounds for all methods of luminescence excitation, since the spectral content of the radiation does not undergo any significant change. It is obvious that the primary orange band in the spectrum of the undoped compound is complex in structure, consisting of a superposition of bands corresponding to different recombination mechanisms. Evidence of this is the fact that as the excitation power density for the luminescence decreases, we are able to spectrally resolve the peak *A* (Fig. 1, inset; Fig. 2, curve *4*). In this case peak A_1 can be associated with radiative transitions with the participation of donor-acceptor pairs $(D-A)$, because the position of its maximum is sensitive to the change in excitation power density and shifts toward the high-energy region of the spectrum when the latter is decreased.[6] The luminescence band B_2 (like the band B_1), can be related to band-localized level transitions, since its position does not depend on the excitation power density. As the excitation photon energy increases from 2.54 eV (Ar^+ laser) to 3.76 eV (xenon lamp), the maximum of band *A* shifts toward the high-energy region (Fig. 2, curves *1,2*). However, the magnitude of this shift is smaller than the fixed value 0.23 eV assigned by Chichibu *et al.*,[7] who associated it within the framework of a configuration-coordinate model with radiative transitions from deep levels to subbands *A* and *C* of the valence band; the energy gap between these bands is equal to 0.23 eV.

According to our picture, the presence of this shift is explained by the dependence of the recombination light on excitation energy. When the excitation photon energy is smaller than the width of the band gap of the compound ($E_{\mathrm{ex}}<E_g$), the dominant recombination mechanism is the interaction of donor-acceptor pairs (Fig. 2a), which we call L-luminescence by analogy with Ref. 3. As the excitation energy increases ($E_{\mathrm{ex}}>E_g$), the probability of more high-energy transitions increases, including localized level-band and band-band type transitions (Fig. 2b), a redistribution of the band intensities takes place to form the band A, and the resulting maximum shifts toward larger values of the energy, which corresponds to H-luminescence. Analogous considerations apply in discussing the band D, which is recorded only at small photon energies ($E_{\mathrm{ex}}<E_g$), implying that it can be assigned to $D-A$ recombination.

Investigation of the width of the donor and acceptor levels in multicomponent semiconductors is a complicated problem, because even a discussion of the simplest defects in the crystal structure in I–III–VI$_2$ compounds, such as vacancies, substitutional and interstitial atoms, leads to twelve types of point defects, each of which can form optically active levels in the band gap. We recalled above that the region of homogeneity for copper-aluminum diselenide corresponds to $Cu_{1.1}Al_{0.9}Se_{1.9}$, i.e., is shifted toward an excess of Cu atoms and a deficit of Se and Al atoms compared to the ideal stoichiometric compound $CuAlSe_2$. In light of this circumstance, we can assume that the main contribution to the recombination in undoped crystals comes from intrinsic defects connected with an excess of copper and aluminum and selenium vacancies. The excess copper atoms act in two ways: either to occupy the space between lattice sites, which gives rise to donors, or to replace cation vacancies in the aluminum sublattice, since the closeness of the metallochemical properties of Al and Cu implies that the probability of forming Cu_{Al} exceeds manifold the probability of forming Cu_{Se}. The fact that the grown crystals exhibit only p-type conductivity suggests that the preferred mechanism is formation of V_{Al} and Cu_{Al}, which leads to the appearance of acceptor levels. Depending on the characteristics of the chemical bonds in I–III–VI$_2$ compounds (ionic or covalent), a chalcogen vacancy can be either a donor or an acceptor.[8] Since the chemical bond in the semiconductor $CuAlSe_2$ is intermediate between homopolar (covalent) and heteropolar (ionic), the presence of a selenium vacancy can lead to donor and acceptor levels in the band gap, whose mutual electrical compensation decreases their contribution to the electrical conductivity mechanism. Therefore, increasing the number of anion vacancies V_{Se} does not lead to $p-n$ inversion of the conductivity type. Furthermore, by virtue of the high vapor pressure of the chalcogen in the growth process, an autodoping of the compound by Se atoms takes place. As a result, weakly bound interstitial selenium appears in the lattice, which is an acceptor impurity. Therefore, the primary orange band A of the luminescence can be viewed as arising from the participation of a large number of donor and acceptor levels. The character of interaction between these levels also determines the spectral structure of this band. It is also obvious that there is an interrelation between the mechanisms of formation of the orange band A and the band C, which appears in the spectrum as a result of doping. Since the position of this band depends on the intensity of the excitation light, the mechanism that determines its nature is $D-A$ recombination. This fact can explain the participation of V_{Al} and V_{Se} impurity levels in the formation of the two bands. In the annealing process, the closeness of the covalent radii of aluminum, zinc, and cadmium (1.23, 1.225, and 1.405 Å, respectively[7]), causes a replacement of the V_{Al} vacancy by atoms of the doping impurity, with the formation of acceptor levels N_{Al} (where N is Zn, Cd). In favor of this assumption is the impossibility of obtaining material with n-type conductivity by doping with Zn and Cd; i.e., in this case the probability of replacement of a vacancy by atoms of Zn and Cd in the aluminum sublattice is larger than the probability for formation of interstitial defects, which are donors. Depending on the degree of doping, the concentrations of V_{Al} and N_{Al} and, consequently, the intensity of interaction of $V_{Al}-V_{Se}$ and $N_{Al}-V_{Se}$ donor-acceptor pairs, can change. As a result, a redistribution of the relative intensities of bands A and C takes place (Fig. 1, curves *2* and *3*; Fig. 2, curve *3*). When the crystals are annealed in the presence of cadmium with aluminum, due to the diffusion of aluminum atoms from the gas phase to the crystal, there occurs a decrease in the concentration of vacancies V_{Al} and, consequently, a decrease in the probability for formation of Cd_{Al} defects. Cadmium atoms occupy the primary interstitial site, which leads to the appearance in the band gap of yet another level which opens a new recombination channel; the resulting maximum in this case is displaced toward lower energies (Fig. 1, curve *4*). Annealing of the samples in vacuum leads to an increase in the number of intrinsic defects. Meanwhile, the most probable event is formation of new vacancies V_{Se} and V_{Al}, since studies of the composition of the vapor phase above the ternary compound indicate the presence of chalcogen atoms, along with gas-like molecules of type III$_2$–VI.[9] On the other hand, the range of homogeneity of the compound is very small (less than 0.02 mole fraction.[5] Therefore, even a minimal decrease in the amount of host elements Al and Se inevitably leads to the formation of a two-phase region and, consequently, to quenching of the visible luminescence. Therefore, we see no photoluminescence from samples annealed in vacuum. Band B_1 is caused by transitions of the band-localized level type. It is recorded only in the luminescence spectra of starting crystals, and appears even in samples with stoichiometric composition; in this case its relative intensity does not change. For this reason, it is assumed that the formation of the band B_1 involves the participation of defects caused by association of oxygen atoms with doubly ionized copper atoms Cu^{++}. The Cu^{++} ions are formed as the result of an oxidation reaction between Cu^{+} ions of the primary lattice and impurity oxygen atoms, which enter the crystal during the growth process.[10] Annealing in vacuum should lead to a decrease in the concentration of these defects and to the disappearance of the band B_1, which is indeed observed experimentally (Fig. 1, curve *5*). The band B_2 is clearly distinguishable in the PL spectrum only for $E_{\mathrm{ex}} > E_g$. Annealing in the presence of Al leads to quenching of the band B_2. Consequently, we can assume that the formation of the band B_2 is caused by transitions between the conduction band and an acceptor level generated by aluminum vacancies.

While studying the spectral dependence of optical transmission in unpolarized light, we estimated the width of the band gap E_g of the compound, whose value was 2.69 eV at 77 K and 2.61 eV at room temperature.

Thus, the luminescence properties of copper-aluminum diselenide are determined primarily by intrinsic defects. Annealing in various atmospheres leads to a considerable modification of these properties, due to changes in the concentration of intrinsic defects and impurities in the single-crystal compounds, which accompany the thermal processing.

This work was financially supported by the Fund for Fundamental Research of the Republic of Belarus (Project T94-150).

[1] L. A. Makovetskaya, B. V. Korzun, S. A. Grutsko, G. P. Popel'nyuk, N. I. Zheludev, and V. V. Tarasenko, Bull. Acad. Sci. Belarus, Ser. Phys. Math. **3**, 50 (1991) [in Byelorussian].

[2] S. V. Popov, A. S. Semenikhin, V. V. Tarasenko, N. I. Zheludev, Yu. P. Svirko, and L. A. Makovetskaya, Opt. Lett. **15**, 993 (1990).

[3] N. Yamamoto, Japan. J. Appl. Phys. **15**, 1909 (1976).

[4] M. Bettini, Solid State Commun. **13**, 599 (1973).

[5] B. V. Korzun, L. A. Vakovetskaya, V. A. Savchuk, V. A. Rubtsov, G. P. Popelnyuk, and A. P. Chernyakova, J. Electron. Mater. **24**, 903 (1995).

[6] Zh. Pankov, *Optical Processes in Semiconductors* (Moscow, 1979).

[7] S. Chichibu, M. Shishikura, J. Ino, and S. Matsumoto, J. Appl. Phys. **70**, 1648 (1991).

[8] H. Neumann, Cryst. Res. & Techn. **18**, 483 (1983).

[9] L. I. Berger, S. A. Bondar', V. V. Lebedev, A. D. Molodyk, and S. S. Strel'chenko, *The Chemical bond in Semiconductor and Semimetal Crystals* (Nauka i Tekhnika, Minsk, 1973).

[10] I. A. Aksenov, I. R. Gulakov, V. I. Lipnitskii, A. I. Lukomskii, and L. A. Vakovetskaya, Phys. Status Solidi A, **115**, K113 (1989).

Translated by F. Crowne

The electrical activity of isoelectronic germanium impurities in lead chalcogenides

V. F. Masterov, F. S. Nasredinov, S. A. Nemov, P. P. Seregin, A. V. Ermolaev, and
S. M. Irkaev

St. Petersburg State Technical University, 195251 St. Petersburg, Russia

(Submitted June 17, 1996; accepted for publication July 1, 1996)
Fiz. Tekh. Poluprovodn. **31**, 381–383 (March 1997)

The method of Mössbauer spectroscopy of the isotope ^{119}Sn is used to show that in PbS and PbSe an isoelectronic germanium impurity is a two-electron donor, and that the energy levels of germanium lie above the levels formed by tin impurity atoms in these semiconductors.
[S1063-7826(97)02603-3]

In a previous paper, using the method of Mössbauer spectroscopy of ^{119}Sn, we established that isoelectronic tin impurities in lead chalcogenides (PbS, PbSe) are two-electron donors: doping of the solid solutions $Pb_{1-x}Sn_sS$ and $Pb_{1-x}Sn_xSe$ by acceptor impurities (sodium, thallium) is accompanied by conversion of a portion of the tin atoms from divalent Sn^{2+} state to the quadrivalent Sn^{4+} state.[1] In PbSe the energy levels connected with tin centers are found in the lower half of the band gap, while in PbSe they are in the valence band.[1] We can expect analogous behavior for isoelectronic germanium impurities in the lead chalcogenides. The most natural way to observe this effect in PbS and PbSe would be to use Mössbauer spectroscopy of ^{73}Ge. However, due to experimental difficulties in carrying out such an investigation, we have decided to study the electrical activity of germanium impurities in PbS and PbSe by the method of Mössbauer spectroscopy of ^{119}Sn. The main idea here is that in lead chalcogenides that are simultaneously doped with tin, germanium, and acceptors (e.g., $Pb_{1-x-y}Sn_{x-z}Ge_zA_yS$, $Pb_{1-x-y}Sn_{x-z}Ge_zA_ySe$), the presence of electrically active germanium donor centers should, under certain conditions, change the ratio of intensities of the neutral and ionized center lines of tin in the Mössbauer spectrum of ^{119}Sn compared to samples that are doped only with tin and acceptor impurities.

We synthesized our samples using the method described in Ref. 1; we studied single-phase samples for which $N(\mathrm{Sn})+N(\mathrm{Ge})=N(A)$ [here $N(\mathrm{Sn})$, $N(\mathrm{Ge})$, and $N(A)$ are the concentrations of tin, germanium, and acceptors, respectively]. Mössbauer spectra of ^{119}Sn were measured at 80 K using a SM 2201 spectrometer with a $Ca^{119mm}SnO_3$ source. Typical spectra are shown in Figs. 1 and 2.

Mössbauer spectra of a PbS sample containing only tin and an acceptor consist of a superposition of two lines with roughly the same intensity, corresponding to Sn^{2+} (a neutral tin center) and Sn^{4+} (a doubly ionized tin donor center) (see Fig. 1a). The ratio of the concentrations $N(Sn^{2+})$ and $N(Sn^{4+})$ can be determined from the ratio of areas S under the corresponding spectra:

$$S(Sn^{2+})/S(Sn^{4+})=[f(Sn^{2+})/f(Sn^{4+})]\times[N(Sn^{2+})/N(Sn^{4+})]. \qquad (1)$$

According to Ref. 1, the ratio of the Mössbauer coefficients f for Sn^{2+} and Sn^{4+} centers at 80 K is 0.93(1). In particular, for the spectra in Fig. 1a taken at 80 K we obtain $R=N(Sn^{4+})/N(\mathrm{Sn})=0.50(2)$, which corresponds to ionization of half the tin atoms, as we should expect for a two-electron donor.

The gradual replacement in PbS of impurity atoms by germanium leads to a decrease in the intensity of the Sn^{4+} spectrum (see Fig. 1, curve *b*), while in the spectra of samples for which $N(\mathrm{Ge})>N(\mathrm{Sn})$ we observe only the line Sn^{2+} (Fig. 1c). This obviously attests to the donor activity of impurity germanium atoms.

The equation for electrical neutrality for the solid solutions $Pb_{1-x-y}Sn_{x-z}Ge_zA_yS$ can be written as follows:

$$2N(Sn^{4+})+nN(\mathrm{Ge})+p-N(A)=0, \qquad (2)$$

where n is the charge of the germanium centers, and p is the concentration of holes. For the compounds we investigated with $x=y$ we can then write the expression for R as follows:

$$R=1/2+(1-n)z/2(x-z)=p/2(x-z). \qquad (3)$$

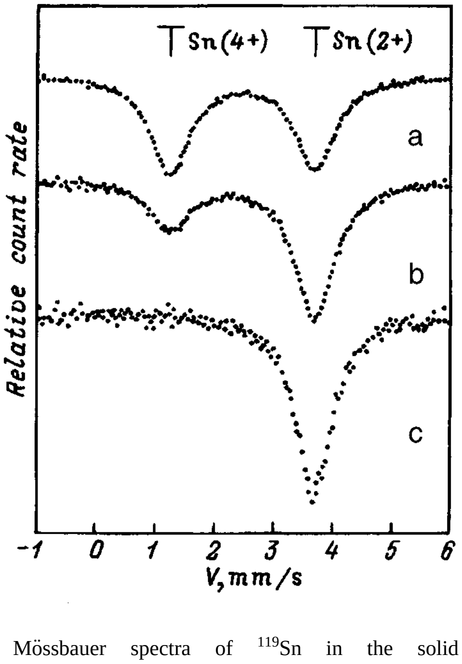

FIG. 1. Mössbauer spectra of ^{119}Sn in the solid solutions $Pb_{0.96}Sn_{0.02-z}Ge_zNa_{0.01}Tl_{0.01}S$: $z=0$ (a), 0.005 (b), 0.01 (c). The positions of the Sn^{2+} and Sn^{4+} spectra are shown.

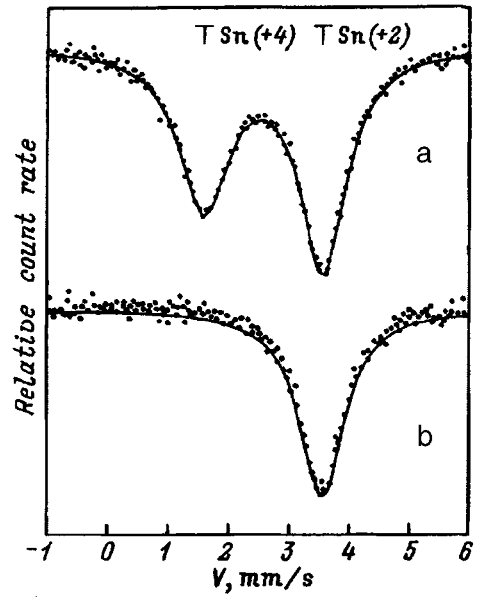

FIG. 2. Mössbauer spectra of ^{119}Sn in the solid solutions $Pb_{0.96}Sn_{0.02-z}Ge_zNa_{0.01}Tl_{0.01}Se$: $z=0$ (a), 0.01 (b).

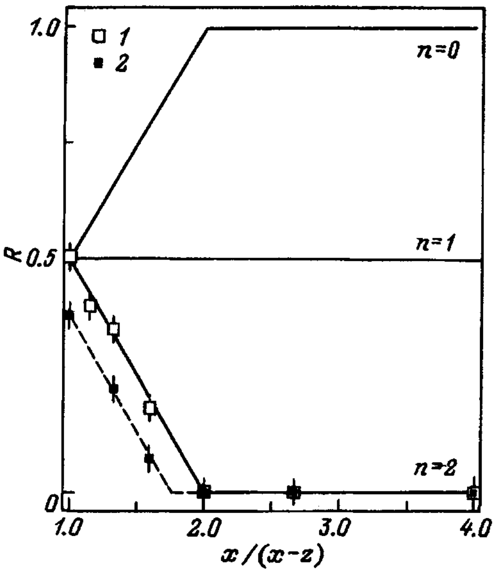

FIG. 3. Computed dependences of R on the ratio of the germanium and tin concentrations $z/(x-z)$ (solid curves). Points—experimental values of R for $Pb_{0.96}Sn_{0.2-z}Ge_zNa_{0.01}Tl_{0.01}S$ (*1*) and for $Pb_{0.96}Sn_{0.2-z}Ge_zNa_{0.01}Tl_{0.01}Se$ (*2*).

In Fig. 3 we show the computed dependence of R on the ratio of the germanium and tin concentrations $z/(x-z)$ in PbS for equal charges of the germanium centers. In the calculations we take into account that for $R<1$ the concentration of holes can be disregarded, because the Fermi level is located in the band gap. If $n=0$ (the germanium is electrically inactive or its energy level lies below the level of tin), then the increase in germanium concentration should lead to an increase in R as long as we have not reached complete ionization of all the tin centers for $z/(x-z)=1$. If $n=1$ (the germanium is a single-electron donor, and its level is above the tin level), then R will not change as the germanium concentration changes. If $n=2$ (germanium, like tin, is a two-electron donor, with a level above the tin donor level), then R will decrease as the concentration of germanium increases as long as all of the tin has not converted to the neutral state for $N(\mathrm{Ge})=N(\mathrm{Sn})$ $[z/(x-z)=1]$. However, we should also take into account the decrease in n due to the incomplete ionization of the germanium centers. The placement of experimental values of R in Fig. 3 for the solid solutions $Pb_{0.96}Sn_{0.2-z}Ge_zNa_{0.01}Tl_{0.01}S$ shows that the isoelectronic germanium impurity in PbS is a two-electron donor and that its energy levels lie below the tin levels.

Impurity atoms of germanium in PnSe also exhibit electrical activity. As is clear from Fig. 2, curve *a*, doping of PbSe by tin alone plus an acceptor impurity leads to the appearance of lines in the Mössbauer spectrum which correspond to Sn^{2+} and Sn^{4+}. The considerable difference in intensities of these lines is explained by the fact that energy levels connected with the tin centers lie in the valence band, so that the value R depends not only on the acceptor concentration (as was true for PbS), but also on the hole concentration. Replacement of tin by germanium is accompanied by a decrease in the intensity of the Sn^{4+} line, and for $N(\mathrm{Ge})>N(\mathrm{Sn})$ only the Sn^{2+} line remains in the spectrum (see Fig. 2, curve *b*). The experimental points shown in Fig. 3 for the solid solutions $Pb_{0.96}Sn_{0.2-z}Ge_zNa_{0.01}Tl_{0.01}Se$ in the region $N(\mathrm{Ge})<N(\mathrm{Sn})$ are located on a curve (shown by dots) which passes above the curve for $Pb_{0.96}Sn_{0.2-z}Ge_zNa_{0.01}Tl_{0.01}S$ due to the effect of holes, but with a very similar slope. This obviously indicates that the isoelectronic germanium impurity even in PbSe is a two-electron donor, and that the energy levels of germanium lie above the tin levels.

All appearances suggest that germanium forms centers with negative correlation energy in both PbS and PbSe, like tin, which requires a special investigation.

This work was carried out with the financial support of the Russian Fund for Fundamental Research (Grant No. 96-02-16957a).

[1] V. M. Masterov, F. S. Nasredinov, S. A. Nemov, and P. P. Seregin, Fiz. Tekh. Poluprovodn. **30**, 840 (1996) [Semiconductors **30**, 450 (1996)].

Translated by F. Crowne